School of Natural Sciences

Habilitation Thesis

Search for New Physics in the Production of Di-Boson Resonances with the ATLAS Detector at the Large Hadron Collider

Dr. Dominik Duda

September 2024

Habilitation Thesis:

"Search for New Physics in the Production of Di-Boson Resonances with the ATLAS Detector at the Large Hadron Collider"

Abstract:

Despite all its success, the Standard Model of particle physics cannot explain some of the phenomena seen in Nature. Long-standing open questions, including the hierarchy problem, dark matter and electroweak baryogenesis motivate searches for new (heavy) particles. With the large amount of data collected during Run-2 of the Large Hadron Collider, searches for new particles predominantly decaying into pairs of bosons provide high sensitivity to physics beyond the Standard Model. The discovered Higgs boson is an example of a massive particle with significant branching fractions for decays into pairs of bosons. Its properties, are measured with increasing precision. Thus, the Higgs boson has become an ideal tool to conduct new-physics searches. This thesis, highlights recent searches by the ATLAS collaboration for diboson resonances and anomalies in the Higgs boson couplings.

Field of study: Experimental High Energy Particle Physics

Habilitation period: October 2020 - October 2024

Defended on: 30th June 2022

Submitted for review: April 2024

Final submission: September 2024

- Habilitation committee:
  - Prof. Dr. Hubert Kroha (Max-Planck-Institut für Physik, München and Technische Universität München, Chair)
  - Prof. Dr. Stephan Paul (Technische Universität München, Member)
  - Prof. Dr. Gregor Herten (Universität Freiburg, Member)

Acknowledgements

First and foremost, I would like to express my sincere gratitude to the chair of my Habilitation committee, Hubert Kroha (Max-Planck-Institut für Physik München and Technische Universität München), for mentoring me during the time of my Habilitation and providing guidance on how to navigate the (administrative) requirements of this process. In addition, I would like to express my gratitude to the other members of my Habilitation committee: Stephan Paul (Technische Universität München) and Gregor Herten (Universität Freiburg) for their support and advice during this intense period of time.

I would like to thank Wade Fisher, Nora Pettersson, Makayla Vessella, Tong Qiu, Tong Li, Ulla Blumenschein, and in particular my two Ph.D students Andreas Huber (formally Hönle) and Stefan Maschek for the great and fun collaboration on our searches for heavy resonances decaying into a Z or W boson and a Higgs boson in final states with leptons and b-jets. In particular, I want to thank Andreas and Nora for their impressive work on the development of our analysis framework, Stefan for his willingness to repeat the mind-numbing task of re-deriving the modelling uncertainties every time we had to changed some detail in the analysis, and Wade for all our discussions on the fit model (the knowledge I gained during these discussions were super helpful for finalising fit models of other analyses and for my convernerships).

For the great (ongoing) collaboration on the search for charged Higgs bosons decaying into a W boson and a 125 GeV Higgs boson in final states with leptons and b-jets, I would like to thank Tatjana Lenz, Shubham Bansal, Raphael Hulsken, Adrian Salvador Salas, Luke Baines, Ulla Blumenschein, and in particular my Ph.D student Simon Grewe, who played a crucial role in almost all aspects of the analysis and provided an impressive amount of work to ensure that the analysis eventually reached the ATLAS approval stage.

I would like to thank Pamela Ferrari, Carsten Burgard, Ralf Gugel, Magdalena Slawinska, Lucrezia Bruni, Remco Castelijn, and Federica Pasquali for the successful collaboration on the search for CP violation in the Higgs plus two jets production and the study of Higgs boson couplings to longitudinally and transversely polarised vector bosons.

The teams that have been working on the cross section measurements in $H \to WW^*$ and the combination of heavy resonance searches are simply too large to acknowledge individual contributions. Hence, I just want to say that I am extremely thankful for the successful collaboration.

A special thanks goes to Ines Ochoa for her exceptional collaboration in leading the ATLAS DBL subgroup alongside me. Furthermore, I want to thank Bill Murray, Viviana Cavaliere, Katharine Leney, and Arnaud Ferrari, who were the coordinators of the ATLAS HDBS group during various phases of my mandate. Working alongside all of you on these efforts has been a truly enriching experience. I also want to take this opportunity to thank Bingxuan Liu and Kun Liu for the fruitful collaboration in coordinating the calibration of ATLAS flavor-tagging algorithms, and the development and calibration of photon identification algorithms, respectively (even if neither of these efforts is detailed in this thesis).

Of course, I also want to thank all my former colleagues at the Max-Planck-Institut für Physik, where I spent most of my time during this Habilitation, and my current colleagues at the University of Edinburgh, as well as everyone who I have forgotten to acknowledge.

Finally, I would like to thank my wife Xiaoli for her support, patience, and understanding throughout this process.

Contents

1 Introduction

The Standard Model (SM) of particle physics describes the production, interaction and decays of Nature's smallest constituents, the elementary particles. Over time and through many experiments, the SM has become one of the most extensively tested theories in physics. Its predictions have been experimentally validated with impressive precision. The most striking example is the agreement between the SM prediction and the experimental measurement of the electron magnetic moment. The electron magnetic moment is the most precisely determined property of an elementary particle, and it agrees with the SM's prediction to within 1 part in 10^{12} [1]. Other success stories of the SM include the predictions of the top quark and the Higgs boson many decades before they were discovered.

With the discovery of the Higgs boson, h, in 2012 by the ATLAS and CMS collaborations at the Large Hadron Collider (LHC) [2, 3], one missing link in the SM was finally revealed. The discovery ended an almost fifty year long saga of searches and was one of the most important milestones for the entire discipline. The Higgs boson is not just another elementary particle. Instead, it plays a central role in the SM being the excitation of a spinless, i.e. scalar, quantum field that permeates the Universe and gives masses to all elementary particles coupling to it.

Despite all its success, the SM can not be the ultimate theory of particle physics as it fails to provide answers to some of the phenomena seen in Nature. Some of the most compelling shortcomings of the SM are the lack of a description for dark matter, the large asymmetry between matter and antimatter in the observable universe, fermion masses and their hierarchy, as well as the necessity for "fine tuning" the Higgs boson mass, referred to as the "naturalness problem". These and other considerations motivate the expectation that physics beyond the Standard Model (BSM) must exist.

Many BSM theories have been proposed to address the open questions of the SM. A common feature of many BSM theories is the existence of new particles with masses at the TeV scale. Heavy resonances that dominantly decay into two bosons (such as ZZ, $W^{\pm}W^{\mp}$, $W^{\pm}Z$, Zh, $W^{\pm}h$, hh, or $\gamma\gamma$) are predicted by many BSM theories. Prominent examples are models with dynamical electroweak symmetry breaking or models with extra dimensions. These models are theoretically well motivated as they offer solutions to the naturalness problem. Di-boson resonances are also predicted in models with an extended scalar sector, which are common in many BSM theories. These models can provide dark matter candidates or explain the matter-antimatter asymmetry.

One of the main goals of the experiments at the LHC is to find and characterise BSM physics. Therefore, the LHC experiments have an extensive programme of direct and indirect searches for new heavy particles. Direct searches for new particles are typically performed by probing for excesses in the distributions of characteristic kinematic observables, such as the invariant mass of specific final state particles. Indirect searches are performed by precision measurements of the properties of known particles, such as their decay rates or production cross sections. The presence of BSM particles can significantly alter these observables. If new particles are too heavy to be directly produced at the LHC, indirect searches are the only way to find hints of their existence. Hence, indirect searches are an important complement to direct searches.

The Higgs boson is the first elementary particle that was discovered through its decay into pairs of Z bosons, W bosons and photons. Ten years after its discovery at the LHC, the Higgs boson has become an indispensable tool to probe for new physics. This is due to its unique role in the SM as it couples to other SM particles proportionally to their mass. This fact motivates the assumption that new heavy particles tend to decay into intermediate states including Higgs bosons, and that Higgs bosons decay into so far unobserved particles. Therefore, searches for new heavy particles that decay into Higgs bosons or searches for exotic decays of the Higgs boson are well-suited to probe for new physics. Precise measurements of the Higgs boson properties, on the other hand, are a sensitive approach to indirectly search for new physics and are an integral part of the physics programme for the current and next generation collider experiments.

In this thesis, searches for new physics in the production of di-boson resonances with the ATLAS detector at the LHC are presented, including both direct searches for new heavy particles and indirect searches probing the properties of the Higgs boson. A common theme of these searches is the attempt to perform them as model independent as possible.

This document is structured as follows: Section 2 provides a brief overview of the experimental setup, including the LHC and the ATLAS detector. It also introduces the relevant techniques for reconstructing and identifying particles with the ATLAS detector. This section serves as a foundation for the following content, providing the necessary background information to understand how direct and indirect searches for BSM physics are done with the ATLAS detector. The main part of the document is in Sections 3 and 4. Section 3 details recent Higgs boson property measurements, while Section 4 describes direct searches for heavy di-boson resonances. These sections focus on analyses efforts with strong personal contributions from myself, but also briefly discuss related work to give a better perspective of how my work extends and/or complements the work done in the field. Section 5 provides a brief recapitulation of the presented work and discusses their relevance for the community. The Appendix A outlines my other academic activities in the course of my habilitation, while Appendix B contains the journal publications from my habilitation work.

2 Experimental techniques

2.1 The Large Hadron Collider

The Large Hadron Collider (LHC) [4] at the European Organisation for Nuclear Research, referred to as CERN (Conseil européen pour la recherche nucléaire), is a 27-kilometre ring of superconducting magnets and high-frequency acceleration cavities dedicated to accelerating and colliding hadron bunches. It first started operation on the 10th of September 2008, and remains the latest addition to CERN's accelerator complex, which is depicted in Figure 1. The LHC is the world's largest and most powerful particle accelerator designed to collide protons with centre-of-mass energies, $\sqrt{s}$, of up to 14 TeV, and luminosities exceeding $10^{34}\,\mathrm{cm}^{-2}\,\mathrm{s}^{-1}$. The LHC can also collide heavy ions with an energy of up to 2.8 TeV per nucleon and a luminosity of up to $10^{27}\,\mathrm{cm}^{-2}\,\mathrm{s}^{-1}$ [4].

Collisions occur at up to 40 MHz, corresponding to a bunch crossing time of 25 ns, at four interaction points, each instrumented with a large detector: ATLAS (A Toroidal LHC Apparatus) [5] and CMS (Compact Muon Solenoid) [6] are general-purpose experiments, ALICE (A Large Ion Collider Experiment) [7], which focuses on heavy-ion collisions, and LHCb (Large Hadron Collider beauty) [8], which is dedicated to studying B-hadrons and their properties.

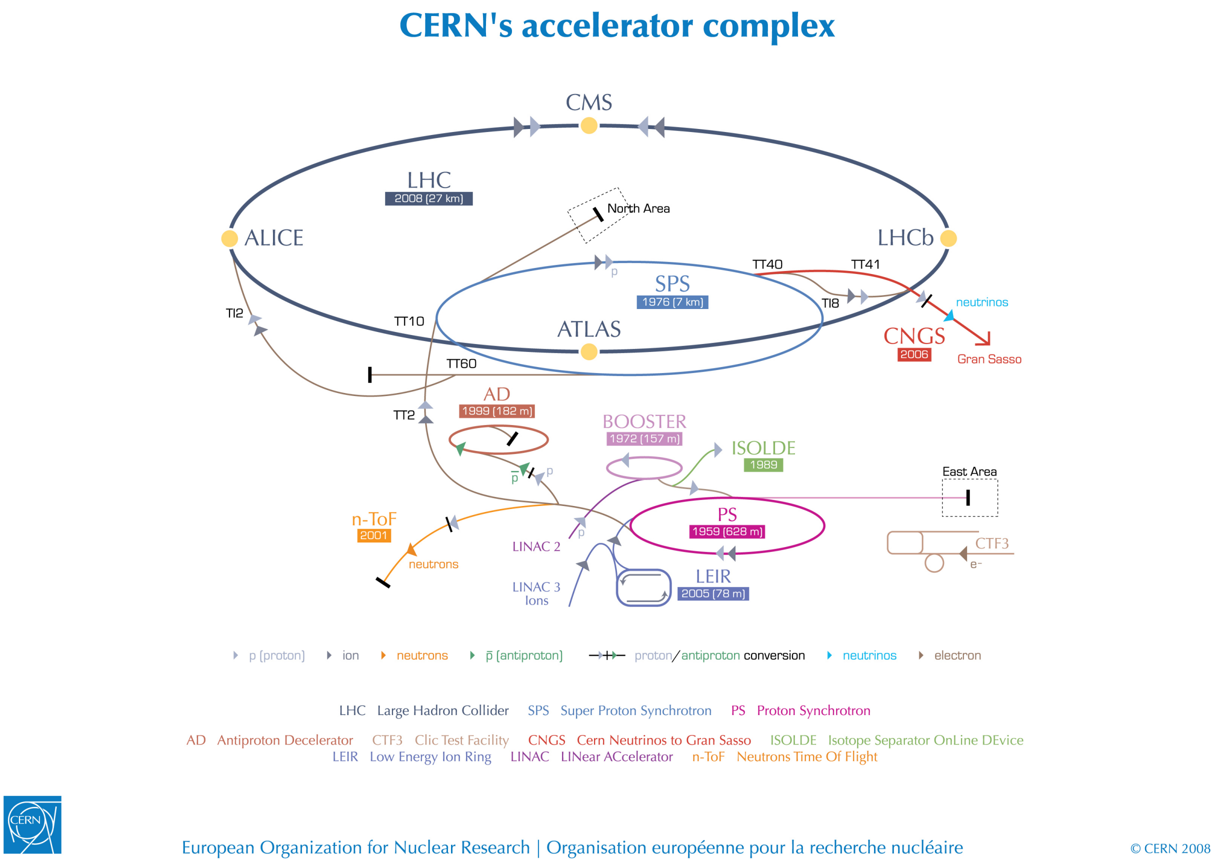

Figure 1: Schematic view of the CERN accelerator complex [9].

The LHC began operations in 2010 with proton–proton (pp) collisions at a center-of-mass energy of 7 TeV. Run 1 continued in 2011 at the same energy. However, in 2012 the center-of-mass energy was increased to 8 TeV. In Run 2, lasting from 2015 to 2018, the LHC was operated with a center-of-mass energy of 13 TeV. Currently in Run 3, which started in July 2022, the LHC collides protons at 13.6 TeV, with operations expected to continue until November 2025. Following a scheduled shutdown, the high-luminosity phase of the LHC (HL-LHC) [10] is scheduled to begin around 2029, which is expected to last until 2041.

2.2 The ATLAS Experiment

The ATLAS experiment [5] at the LHC is a multipurpose particle detector. It has a forward–backward symmetric cylindrical geometry and a near 4π coverage in the solid angle.[1] ATLAS is comprised of a variety of subdetectors: an inner tracking detector (ID), electromagnetic and hadron calorimeters, and a muon spectrometer (MS) incorporating three large superconducting air-core toroidal magnets. A computer-generated image of the ATLAS detector is depicted in Figure 2.

The tracking system is immersed in a 2 T axial magnetic field generated by a surrounding thin superconducting solenoid. and enables precise tracking of charged particles within the range $|\eta| < 2.5$. The ID is comprised of several components: A high-granularity silicon pixel detector, covering the vertex region and typically providing four measurements per track, often with the first hit in the insertable B-layer, is followed by a silicon microstrip tracker (SCT), which usually provides eight measurements per track. These silicon detectors are complemented by a transition radiation tracker (TRT), which provides radially extended track reconstruction up to $|\eta| = 2.0$. The TRT also contributes to the electron identification based on the fraction of hits, typically 30 in total, above a higher energy-deposit threshold corresponding to transition radiation.

The calorimeter system covers the pseudorapidity range $|\eta| < 4.9$. Within the region $|\eta| < 3.2$, electromagnetic calorimetry is provided by barrel and endcap high-granularity lead/liquid-argon (LAr) calorimeters, with an additional thin LAr presampler covering $|\eta| < 1.8$ to correct for energy loss in material upstream of the calorimeters. For hadron calorimetry, ATLAS uses a steel/scintillator-tile calorimeter in $|\eta| < 1.7$, sectioned into three barrel structures, and two copper/LAr hadron endcap calorimeters. The solid angle coverage is completed with forward copper/LAr and tungsten/LAr calorimeter modules optimised for electromagnetic and hadronic energy measurements respectively.

The MS uses a combination of separate trigger and high-precision tracking chambers measuring the deflection of muons in a magnetic field generated by the superconducting air-core toroidal magnets. The field integral of the toroids ranges between 2.0 and 6 T m. The region $|\eta| < 2.7$ is covered by three layers of precision chambers, each consisting of layers of monitored drift tubes complemented by cathode-strip chambers in the forward region, where the background is highest. The muon trigger system covers the range $|\eta| < 2.4$ with resistive-plate chambers in the barrel, and thin-gap chambers in the endcap regions.
Potentially interesting collision events are recorded based on a two-level trigger system. The first level, implemented in hardware, uses a subset of detector information and accepts events at a rate below 100 kHz. A subsequent software-based trigger further reduces the accepted event rate to an average of 1 kHz depending on data-taking conditions. This second-level trigger uses reconstruction and calibration algorithms similar to those used offline. An extensive software suite [12] is used for real and simulated data reconstruction and analysis, for operation and in the trigger and data acquisition systems of the experiment.

[1] ATLAS uses a right-handed coordinate system with its origin at the nominal interaction point (IP) in the centre of the detector and the z-axis along the beam pipe. The x-axis points from the IP to the centre of the LHC ring, and the y-axis points upwards. Cylindrical coordinates (r, ϕ) are used in the transverse plane, ϕ being the azimuthal angle around the z-axis. The pseudorapidity is defined in terms of the polar angle θ as $\eta = -\ln\tan(\theta/2)$. Angular distance is measured in units of $\Delta R \equiv \sqrt{(\Delta\eta)^2 + (\Delta\phi)^2}$ [5].

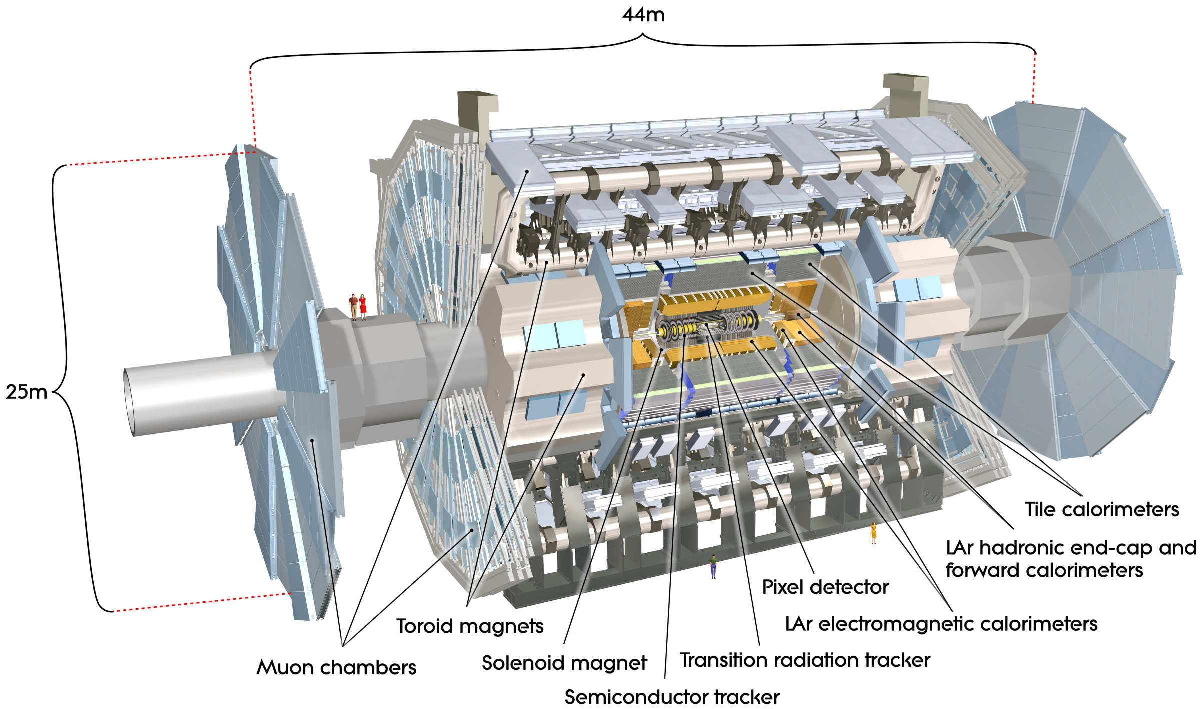

Figure 2: Computer-generated image of the entire ATLAS detector [11].

The studies presented in this document are based on data recorded with the ATLAS detector between 2015 and 2018 in pp collisions at a center-of-mass energy of $\sqrt{s} = 13$ TeV and bunch spacing of 25 ns. The data are required to satisfy criteria that ensure that the detector was in good operating condition [13]. Figure 3 shows the distributions of the cumulative luminosity versus time recorded by ATLAS during the LHC Run 2 as well as the mean number of interactions per bunch crossing for the 2015 – 2018 pp collision data taking periods.

2.3 Particle detection and identification

2.3.1 Tracks, vertices and clusters

Charged particle tracks are reconstruction in the ID by combining space-point measurements in the pixel, microstrip and TRT detectors [15]. Track candidates with $p_T > 400$ MeV are fitted, according to the pion or electron hypothesis depending on various quality requirements [16] using the ATLAS Global χ^2 Track Fitter [17].

Collision vertices are reconstructed from at least two ID tracks, each with a transverse momentum $p_{\mathrm{T}} >$ 500 MeV. The reconstruction procedure is based on two stages: vertex finding and vertex fitting [18, 19]. The vertex finding procedure first associates reconstructed tracks to the vertex candidates. The vertex fitting procedure then determines the actual vertex position and its covariance matrix, estimates the quality of the fit, and performs a refit of the incident tracks. Among all reconstructed vertices, the one with the highest p_{T}^2 sum of all associated tracks is chosen to be the primary vertex (PV) of the event.

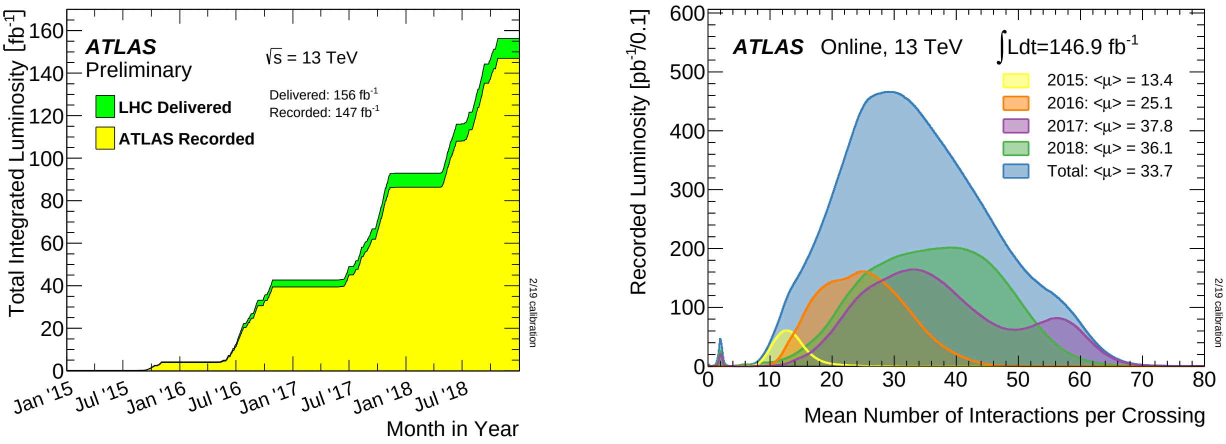

(a) (b)

Figure 3: Distributions of (a) the cumulative luminosity versus time delivered to ATLAS (green) and recorded by ATLAS (yellow) during stable beams for *pp* collisions at 13 TeV centre-of-mass energy in LHC Run 2, and (b) the luminosity-weighted distribution of the mean number of interactions per bunch crossing for the 2015 – 2018 *pp* collision data at 13 TeV centre-of-mass energy [14].

Three-dimensional topo-clusters are massless objects built via a nearest-neighbour algorithm using calorimeter cells as input [20]. Cells are added to a topo-cluster if their energy content is significantly larger than the expected noise contribution. Such topo-clusters are used in the reconstruction of electrons, photons, jets, and hadronically decaying τ-leptons. The nearest-neighbour algorithm attempts to detrmine the energy and directions of incoming particles by exploring the spatial distribution of the cell signals.

For the electron and photon reconstruction, variable-sized superclusters [21] are formed from topo-clusters using a two-staged approach: in the first stage, a seed cluster is selected from a list of EM topo-clusters; in the second stage, EM topo-clusters near the seed are identified as satellite clusters, which may arise from bremsstrahlung radiation or splitting of topo-clusters. The final superclusters are obtained by adding the satellite clusters to the seed cluster if they satisfy the necessary selection criteria [21].

2.3.2 Leptons, photons and jets

Electrons are reconstructed from ID tracks matched to variable-sized superclusters in the electromagnetic calorimeter. The Electron candidate tracks are re-fitted based on a gaussian-sum filter[2] (GSF) [16, 23] to account for non-linear effects related to the energy loss of charged particles via bremsstrahlung. The electron candidates are required to satisfy selection requirements on the transverse impact parameter significance, $|d_0|/\sigma(d_0) < 5.0$, and on the longitudinal impact parameter, $|z_0 \sin(\theta)| < 0.5$ mm. These requirements ensure that the electrons originate from the PV. Prompt electrons entering the tracking volume of the detector ($|\eta| < 2.47$) are identified using a likelihood-based (LH) algorithm [24]. The inputs to this algorithm are based on measurements from the tracking system, the calorimeter system, and observables that combine both tracking and calorimeter information. Furthermore, electrons also have to be isolated from hadronic activity in the event. Both, calorimeter- and track-based isolation criteria [21] are used to reduce the number of hadrons and soft electrons that arise from heavy-flavour decays and that are misidentified as prompt electrons.

[2] The GSF method is based on a generalisation of the Kalman filter [22].

The electron energy resolution is improved using a multivariate regression algorithm that is based on the properties of the shower development in the electromagnetic calorimeter. The absolute energy scale and energy resolution of reconstructed electrons are then adjusted to achieve agreement between data and simulation for the invariant di-electron mass distribution. These corrections are measured as a function of the transverse electron energy and the electron pseudorapidity in data using $Z \to e^+e^-$ decays. The uncertainties on these measurements are dominated by pile-up and material effects, and range up to a few per-mille [25]. The $Z \to e^+e^-$ decays are also used to calibrate the electron reconstruction, identification, isolation, and trigger efficiencies. The measurements of these quantities are based on a tag-and-probe method: One electron, i.e. the *tag*, is required to satisfy strict identification criteria and to have passed the trigger. The second electron candidate in the pair, i.e. the *probe*, is used to test the efficiency of the reconstruction procedure, trigger, and selection requirements [16, 26]. The uncertainties in the measured efficiencies are at the per-cent level for electrons with an E_T of around 20 GeV and reach the per-mille level for electrons with an E_T around 50 GeV.

Muons are reconstructed by matching ID tracks to either full tracks (*combined muons*) or track segments (*segment-tagged muons*) in the MS, and performing a combined track fit using hits from both subdetectors as well as the energy loss in the calorimeters[3]. Objects passing the reconstruction procedure are identified as high-quality muon candidates using specific requirements on the number of hits in the different ID subdetectors and different MS stations, on the track fit properties, and on variables testing the consistency of the individual measurements in the two detectors [27]. In addition, the muon candidates have to fulfil impact-parameter requirements: $|d_0|/\sigma(d_0) < 3.0$ and $|z_0 \sin(\theta)| < 0.5$ mm to ensure that they originate from the PV. Like electrons, muon candidates must pass dedicated isolation requirements [27].

The muon reconstruction, identification, isolation, and trigger efficiencies are measured in data exploiting events containing pairs of muons such as $Z \to \mu^\pm\mu^\mp$ or $J/\psi \to \mu^\pm\mu^\mp$. The measurements of these properties are done using a tag-and-probe method [27], which yields muon reconstruction and identification efficiencies with a precision that is better than the per-mille level for muons with p_T above 10 GeV in most of the detector regions. Measurements of the muon momentum resolution and momentum scale are also performed in samples of $J/\psi \to \mu^\pm\mu^\mp$ and $Z \to \mu^\pm\mu^\mp$ events. The simulations are corrected to match the data. The calibration results are then validated using an independent sample of $Y \to \mu^\pm\mu^\mp$ events. The momentum scale is measured with an uncertainty of around 0.05% (0.1%) at the Z (J/ψ) pole, and the resolution is measured with an uncertainty of around 1.5% (2%) [28].

Photons are reconstructed from variable-sized superclusters in the electromagnetic calorimeter system [21]. Different approaches are used to reconstruct *converted* and *unconverted* photons. Converted photons are reconstructed as superclusters matched to either two tracks forming a conversion vertex or a single track without hit in the innermost pixel layer. Unconverted photons are reconstructed as superclusters matched to neither a single track nor a conversion vertex. Prompt photons and backgrounds from hadronic objects are separated within $|\eta| < 2.37$ using dedicated identification requirements placed on observables describing the lateral electromagnetic shower development, and the leakage into the hadronic calorimeter system. The identification efficiency for unconverted (converted) photons ranges from around 84% (85%) at $p_\mathrm{T} = 25$ GeV to 94% (98%) for $p_\mathrm{T} > 100$ GeV [29]. Like charged leptons, photons have to pass both calorimeter- and track-based isolation requirements to further suppress jets misidentified as photons [21].

[3] As muons are minimum-ionising particles, they deposit only a small fraction of their energy in the calorimeters, leading to a characteristic signature in the detector.

Three complementary techniques are used to measure the photon identification efficiency in intervals of the p_{T} and $|\eta|$ using data [30]. The first technique probes photons from events with inclusive photon production. The second technique selects events with photons radiated from leptons in $Z \to e^+e^-\gamma$ decays. The third technique selected events with electrons from $Z \to e^+e^-$ decays, and then transforms the electron shower shapes to resemble the photon shower shapes. The results of each measurement are compared with Monte Carlo simulations in order to obtain scale factors. These scale factors are then combined to produce a single scale factor, using a weighted average[4]. The uncertainty on the combined identification scale factors ranges from 7% to about 0.5% for unconverted photons, and from 12% to 1% for converted photons. The uncertainties decrease as a function of the photon p_{T}. The measurements in data are performed up to a transverse energy of 1.5 TeV. The photon energy scale and resolution are corrected using the same techniques as for the electron energy calibration. This approach is verified using radiative Z boson decays, $Z \to \ell^+\ell^-\gamma$, to a precision of 0.5% at worst [21, 25].

Jets are collimated bunches of hadrons that are created when highly energetic quarks or gluons are produced within the hard scatter process. Several different jet clustering algorithms have been developed over the past decades. At ATLAS and CMS, jets are mainly clustered using the anti-k_{t} [31] algorithm as implemented in the FastJet package [32]. The anti-k_{t} algorithm iteratively combines reconstructed low-level objects such as tracks of charged particles or topological-clusters in the calorimeter sytem until a final jet is formed. The jet clustering algorithm starts by calculating the distances d_{ij} for each pair of objects in the event and the distances d_{iB} for each particle and the beam. These distances are defined via:

$$d_{iB} = k_{t\,i}^{-2}\,,$$
$$d_{ij} = \min\left(k_{t\,i}^{-2}, k_{t\,j}^{-2}\right)\frac{\Delta_{ij}^2}{R^2}\,,$$

where $k_{t\,i}$ and $k_{t\,j}$ are the transverse momenta of the two objects i and j, R is the radius parameter of the final jet, and $\Delta_{ij}^2 = (y_i - y_j)^2 + (\phi_i - \phi_j)^2$ is the angular distance between the two objects, with y and ϕ as the rapidity and azimuthal angle of the particles. The clustering algorithm proceeds by identifying the smallest distance between any two objects. If this distance is a d_{ij}, then the objects are combined forming a proto-jet. If the smallest distance is a d_{iB}, then the object i is called a jet and is removed from the list of the objects. All distances are then recalculated, and the procedure is repeated until non of the objects is left. The anti-k_{t} algorithm preferentially clusters low-k_t objects to high-k_t objects. As a result, objects with high k_t will accumulate all low k_t objects within a circle of radius R, forming a perfectly conical jet. However, if a second high-k_t object is within $2R$ of the first high-k_t object, the highest-k_t object will form a conical jet, while the other object will form a partly conical jet, missing the part overlapping with the other jet.

Over the past years, the ATLAS collaboration has used a large number of jet definitions [33, 34, 35]. Most analyses based on Run 2 data use small-R jets (with $R = 0.4$) built from noise-suppressed topological clusters of energy deposits in the calorimeter system. Recently, ATLAS analyses have begun to use small-R jets built from particle-flow objects as inputs [34]. Particle-flow objects are a combination of calorimeter clusters and charged-particle tracks, which allows for a more precise measurement of jet properties. Charged particle flow objects are ID tracks matched to the primary vertex, while neutral particle flow objects are modified topo-clusters in the calorimeter system. The jet four-momentum is corrected using p_{T}- and η-dependent scale factors, accounting for the calorimeter's non-compensating response, signal losses due to noise threshold effects, energy lost in passive materials, and contributions from pile-up interaction [36, 37].

[4] The statistical and systematic uncertainties are assumed to be uncorrelated between the three methods.

To reduce the contamination from jets originating from pile-up vertices, selection requirements on dedicated multivariate classifiers are applied to the jets [38, 39, 40]. These classifiers are based on calorimeter and tracking information for jets in the central regions as well as jet shapes and topological jet correlations in pile-up interactions for jets in the forward regions.

Large-R jets (with $R = 1.0$) are used to reconstruct strongly Lorentz-boosted hadronically decaying objects, including W and Z bosons as well as Higgs bosons and top quarks. The inputs to the jet clustering algorithm are either calibrated clusters of energy deposits in calorimeter cells, or a combination of ID tracks and calorimeter clusters [41]. A jet trimming technique [42] is used to remove the contributions that originate from initial-state radiation, pile-up interactions, or the underlying event. This is done by reclustering the constituents of the initial jet, using the k_t algorithm, into subjets with $R = 0.2$. Any subjet with a p_{T} less than 5% of the parent jet p_{T} is removed.

Another type of jets are clustered from ID tracks using a variable radius (VR) that shrinks with increasing p_{T} of the studied proto-jet [43]. VR track-jets are typically used to identify b-hadrons produced in the decay of strongly Lorentz-boosted Higgs bosons, Z bosons or top quarks. These track-jets must have at least two ID tracks compatible with the primary vertex, $p_{\mathrm{T}} > 10$ GeV and $|\eta| < 2.5$.

Tau leptons decay approximately 65% of the time into a final state with hadrons. The reconstruction of hadronically decaying τ leptons, τ_{had}, is seeded by jets formed using the anti-k_t algorithm with a distance parameter of 0.4, and calibrated topo-clusters as inputs. These jets are required to have a transverse momentum $p_{\mathrm{T}} > 5$ GeV and a pseudorapidity $|\eta| < 2.5$. Selected tracks within a cone of $\Delta R = 0.25$ around the jet axis are associated with the τ_{had} candidate. A recurrent neural network (RNN) [44] is then used to classify these tracks as either originating from a true tau decay or from one of several potential background sources. The RNN exploits the information of multiple input quantities that describe the kinematics, geometric distribution, and hit pattern of the tracks. The number of tracks that are considered to have likely originated from a true tau decay is used to classify the τ_{had} candidates into either of two categories: one-prong, i.e. candidates with one asssociated track[5], and three-prong, i.e. candidates with three asssociated tracks[6].

Another RNN-based algorithm has been trained to identify hadronically decaying τ leptons and to reject quark- and gluon-initiated jets that may resemble decays of the τ_{had} [44]. This algorithm exploits the long lifetime of about $2.9 \cdot 10^{-13}$s of the τ lepton, which leads to a significant displacement in the ID. It also uses the multiplicity of decay products and their kinematic properties. The second RNN exploits both charged-particle tracks as well as clusters of energy in the calorimeter system. Given the distinct signatures of one-prong and three-prong τ_{had} decays, the training is performed separately for both tpologies. Four operating points are defined based on the output score of the RNN. The identification efficiencies for these operating points are 95% (95%), 85% (85%), 75% (60%), and 60% (45%) for 1-prong (3-prong) τ_{had} decays.

2.3.3 Jet tagging

Flavour-tagging algorithms are used to distinguish between jets containing b- and c-hadrons, referred to as b-jets and c-jets respectively, and jets containing only light-flavour hadrons, referred to as light-flavour

[5]This category targets decays such as $\tau^- \to \pi^- \nu_\tau$.
[6]This category targets decays such as $\tau^- \to \pi^- \pi^+ \pi^- \nu_\tau$.

jets. The main distingushing features of b- and c-jets are related to their relatively long lifetime, which leads to secondary and tertiary vertices with macroskopic displacement in the detector, their relatively large mass, and their relatively high decay multiplicity. The ATLAS collaboration uses different types of flavour-tagging algorithms for the analysis of pp collision data. These algorithms are based on sophisticated machine learning approaches that combine information from track impact parameters[7] and displaced verticies to distinguish between b-, c- and light-flavour jets.

Dedicated tools are used to either learn track impact-parameter correlations for the different jet-flavours or to reconstruct displaced vertices. These tools are referred to as low-level b-tagging algorithms. The impact parameter based tagging algorithms predict the b-jet, c-jet, and light-flavour jet probabilities. The vertex-based algorithms provide a set of properties, such as the invariant mass of the vertex, its displacement, and the number of associated tracks, which are used to distinguish between the various jet flavours.

During Run 2 of the LHC, most ATLAS analyses used either the *MV2c10* or *DL1r* flavor-tagging algorithms [45]. *MV2c10* is based on boosted decision trees, while *DL1r* is based on a deep neural network. Both algorithms take the outputs of the low-level taggers and the jet kinematics as input to build a single discriminant. Figure 4 shows the distribution of the DL1r score for b-jets, c-jets, and light-flavour jets. The clear separation between the different jet flavors demonstrates the strong performance of the b-tagging algorithm.

The performance of these flavour-tagging algorithms are quantified by the b-tagging efficiency as well as the mis-tagging efficiencies for c- and light-flavour jets:

$$\varepsilon_f = \frac{N_f^{\text{passed}}}{N_f^{\text{all}}}$$

where f refers to the jet flavour with $f \in \{b, c, \text{light}\}$, N_f^{passed} refers to the number of jets with flavour f that pass the b-tagging requirement, and N_f^{all} refers to the number of all jets of flavour f. Four so-called single-cut operating points (OPs) are widely used in ATLAS. These OPs are obtained by placing lower bounds on the output score distribution of the b-tagging algorithm. The four OPs correspond to b-tagging efficiencies of 60%, 70%, 77%, and 85%, respectively. Furthermore, pseudo-continuous OPs are defined by dividing the output score distribution of the b-tagging algorithm in five intervals. These intervals correspond to efficiencies of 100% - 85%, 85% - 77%, 77% - 70%, 70% - 60%, and 60% - 0%.

For Run 3, the ATLAS collaboration has changed their strategy for developing flavor-tagging algorithms. Instead of using the outputs of low-level b-tagging algorithms to train multivariate analysis techniques, a single algorithm based on a graph neural network (GNN) architecture is used [46]. The GNN exploits information from all ID tracks within a jet to predict the jet flavour. It also predicts which physics process produced the different tracks in the jet, and groups the tracks into vertices. These additional training objectives improve the overall flavor-tagging performance significantly.

The ATLAS b-tagging algorithms are trained using simulated jets and therefore require calibration to correct for discrepancies between data and simulation that arise from imperfect detector response and physics modelling effects, such as parton shower and fragmentation modelling in the Monte Carlo simulations.

[7] Impact parameter measure the distance of closest approach of a track to the primary vertex in the transverse or longitudinal plane.

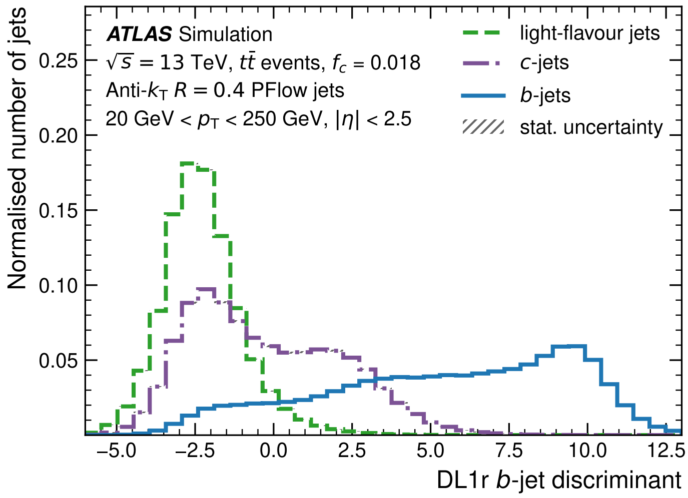

Figure 4: Distributions of the DL1r score for b-jets, c-jets, and light-flavour jets from simulated top-quark pair events [45].

Dedicated calibration scale factors

$$\mathrm{SF}_f = \frac{\varepsilon_f^{\mathrm{data}}}{\varepsilon_f^{\mathrm{MC}}}$$

are determined for each jet flavour by comparing the flavour-tagging efficiency in data, $\varepsilon_f^{\mathrm{data}}$, to the efficiency in MC simulation, $\varepsilon_f^{\mathrm{MC}}$.

The tagging efficiencies for b-jets are calibrated using a sample of events containing top-quark pairs decaying into a final state with two charged leptons and two b-jets. The calibration scale factors are measured in nine different jet p_T intervals, ranging from $20\,\mathrm{GeV}$ to $400\,\mathrm{GeV}$, and tend to be consistent with unity. The uncertainties in the scale factors vary between 1% to 8% depending on the jet p_T interval [47].

The c-jet mis-tagging efficiencies are calibrated using a sample of events containing top-quark pairs decaying into a final state with exactly one charged lepton and several jets, including those from hadronically decaying W bosons. The W boson is a natural source for c-jets due to its relatively large branching fraction for $W \to cs$ decays. The scale factors are measured in four different jet p_T intervals, ranging from $20\,\mathrm{GeV}$ to $250\,\mathrm{GeV}$. The measured scale factors generally agree with those in simulation except for the 60% efficient operation point, where variations in the order of 1.0-1.5 standard deviations are observed. The total uncertainties range from 3%–17%, depending on the considered operating point and jet p_T interval [48].

The mis-tagging efficiencies for light-flavour jets are calibrated using a sample of events containing Z+jets production. A fit to the jet-flavour-sensitive secondary-vertex mass is performed to extract the scale factors from data. The scale factors are measured in four different jet p_T intervals, ranging from $20\,\mathrm{GeV}$ to $300\,\mathrm{GeV}$. These scale factors tend to exceed unity by about 10% to 20%, with the total uncertainties ranging from 11% to 23%, depending on the considered operating point [49].

Since many physics analyses investigate jets with a p_T beyond the reach of these calibration methods, an additional MC-based calibration technique is employed [50]. This calibration procedure is based on variying quantities affecting the flavour-tagging performance, such as the impact parameter resolution, percentage of tracks from random combinations of measurements in the ID, description of the detector material, and the track multiplicity per jet. The additional uncertainties in the flavour-tagging calibration scale factors increase monotonically with increasing jet p_T. The uncertainties range from around 20% for the loosest operation point to around 37% for the tightest operation point at a jet p_T of 3 TeV.

Flavour-tagging calibration scale factors are derived for small-R calorimeter jets and VR track-jets, for both the single-cut operation points and the pseudo-continuous b-tagging intervals.

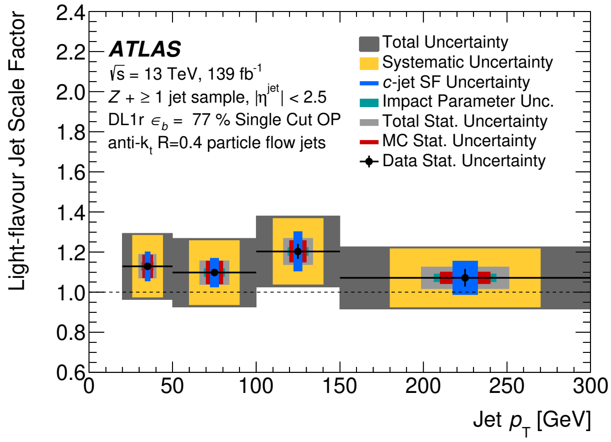

Figure 5: The calibration scale factors and their uncertainties for $\varepsilon_\mathrm{light}$ of the single-cut OP that corresponds to a 70% b-tagging efficiency [49].

Boosted boson tagging refers to the identification of hadronically decaying $W^\pm$, Z, or Higgs bosons that are strongly Lorentz-boosted. The identification of such decays is a crucial component to many searches for new heavy particles with masses at the TeV scale.

A crucial feature of highly Lorentz-boosted massive particles is that their decay products are strongly collimated. The angular separation ΔR in the $\eta\Phi$-plane between the decay products of a particle X with the mass m_X and the transverse momentum p_T^X can be approximated in case of a 2-body decay by

$$\Delta R \approx \frac{2m_X}{p_\mathrm{T}^X} \tag{1}$$

For example, the decay products of a Higgs boson with a transverse momentum of around 250 GeV tend to have an angular separation of $\Delta R \approx 1.0$ [51, 52]. As the Higgs boson p_T increases, the expected angular separation decreases further, until at some point the collimation becomes so strong that the standard reconstruction techniques are no longer capable of resolving the decay products individually. This problem can be mitigated by reconstructing highly Lorentz-boosted hadronically decaying objects via a single large-R jet, instead of using multiple small-R jets. The situation is illustrated in Fugure 6.

Over the past few years, the ATLAS collaboration has developed several algorithms to reconstruct and identify hadronically decaying top quarks, W and Z bosons, as well as Higgs bosons. Large-R jets are used to reconstruct the objects, and multivariate analysis techniques are used to distinguish them from each other

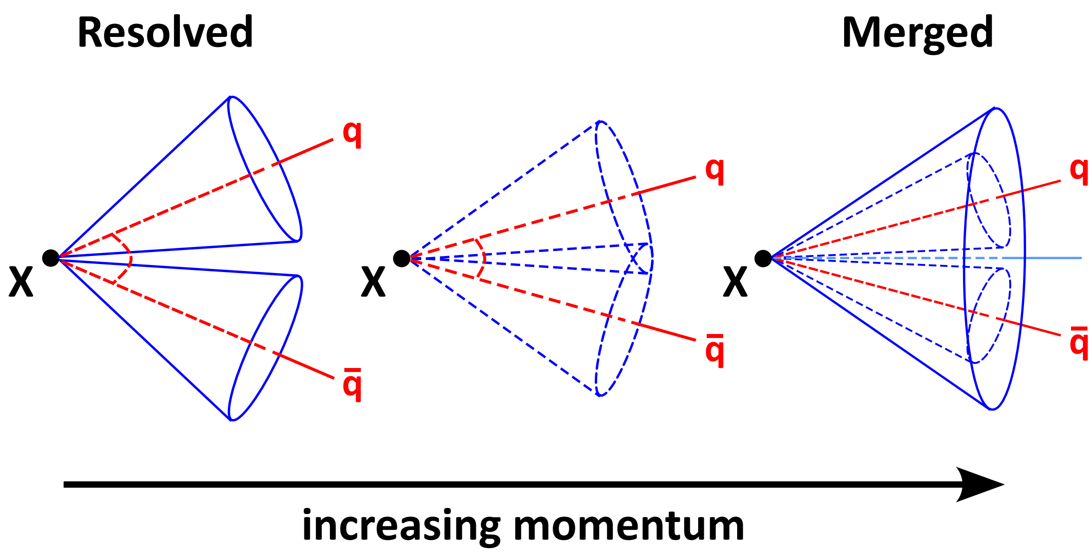

Figure 6: Schematic representation of a Lorentz-boosted particle X decaying into a hadronic final state. For low transverse momenta, the decay products can be reconstructed as two individual small-R jets. For sufficiently large transverse momenta, the decay products are reconstructed as a single large-R jet.

and from jets originating from a single parton. The multivariate analysis techniques are trained with information from the tracking detectors and/or the calorimeter system.

Boosted $W \to q\bar{q}$ and $Z \to q\bar{q}$ decays are identified by imposing p_{T}-dependent selection requirements on the jet mass and jet substructur observables. The mass of the jets must be within a window around the W or Z boson pole, where the window increases as a function of the jet p_{T}. For example, the window is approximately 30 GeV wide at $p_{\mathrm{T}} = 500$ GeV, and it increases to about 60 GeV at $p_{\mathrm{T}} = 2.5$ TeV. In addition, the jet substructure observable $D_2^{(\beta=1)}$ is used. It is defined as the ratio of three-point to two-point energy correlation functions [53], which are based on the energies and pairwise angular distances of the constituents of the large-R jet. The $D_2^{(\beta=1)}$ observable (see Figure 7) is optimised to distinguish between jets stemming from a single parton and those originating from a two-body decay (i.e. $X \to q\bar{q}$). The selection requirement on $D_2^{(\beta=1)}$ becomes looser with increasing jet p_{T}. I.e. for a p_{T} around 250 GeV, the jet is required to pass $D_2^{(\beta=1)} < 1.0$, while for a p_{T} around 2.5 TeV, the jet is required to pass $D_2^{(\beta=1)} < 1.9$. After applying these two selection requirements, the $W \to q\bar{q}$ and $Z \to q\bar{q}$ tagging efficiencies are around 40% for a jet p_{T} of around 250 GeV and rise to around 70% for $p_{\mathrm{T}} = 2.5$ TeV.

Dedicated calibration scale factors for the vector boson tagging algorithm are determined from data. The tagging efficiencies for boosted W boson jets and the rejection rates for boosted top-quark jets are measured in events with top-quark pairs, while the rejection rates of jets stemming from a single parton are measured using multi-jet and γ+jets events. The measured W boson tagging efficiencies and the background rejection rates in data are consistent with the Monte Carlo simulations within the evaluated systematic uncertainties [54].

Boosted $h \to b\bar{b}$ decays are identified exploiting the kinematics of the large-R jet as well as the flavour-tagging information of up to three variable-radius track-jets that are matched via ghost-association [55]. to the reconstructed large-R jet [56]. The identification algorithm is based on a feed-forward neural network which is trained using the probabilities of the b-, c- and light-flavour hypotheses of the three leading variable-

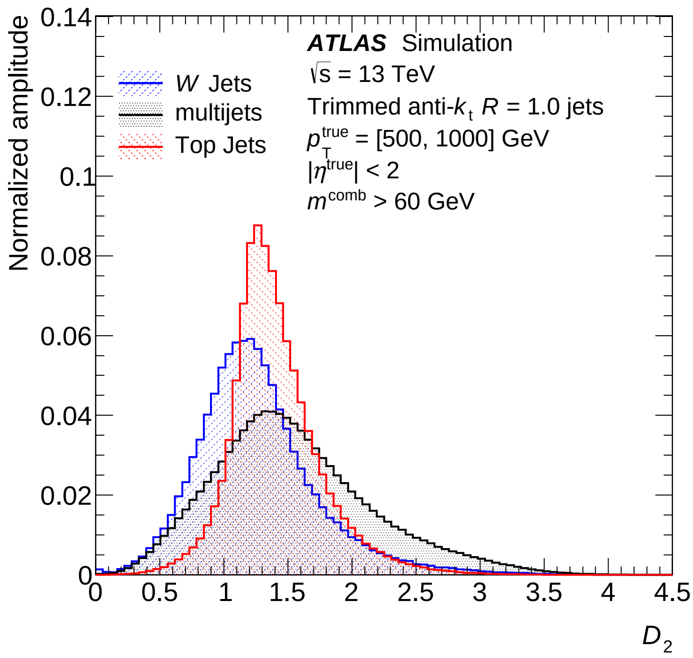

Figure 7: Distribution of the D_2 observable presented for simulated large-R jets from boosted W boson and top-quark decays as well as from large-R jets stemming from single partons extracted from multi-jet production [53].

radius track-jets[8] and the p_T and η of the large-R jet. The neural network is trained to separate boosted $h \to b\bar{b}$ jets from boosted top quark jets and jets arising from multi-jet processes. The network maps the input vector to a three-dimensional output layer. The three output nodes quantify the probabilities for a large-R jet to correspond to the signal class, and to either of the two background classes. The outputs of the neural network are combined into one single discriminant function for the signal-jet hypothesis:

$$D_{\text{Xbb}} = \ln \frac{p_{\text{Higgs}}}{f_{\text{top}} \cdot p_{\text{top}} + (1 - f_{\text{top}}) \cdot p_{\text{multi-jet}}},$$

where f_{top} quantifies the fraction of top-quark jets, which is set to $f_{\text{top}} = 0.25$. Furthermore, p_{Higgs}, p_{top}, and $p_{\text{multi-jet}}$ are the probabilities for the Higgs boson, top quark, and multi-jet hypotheses, respectively. The distribution of the D_{Xbb} score is depicted in Figure 8 for large-R jets from boosted $h \to b\bar{b}$ and top-quark decays as well as for jets from mulijet production. For an operation point that has a $X \to b\bar{b}$ tagging efficiency of 60%, the rejection rates vary between 30 and 80 for large-R jets from multi-jet production and between 10 and 30 for large-R jets from boosted top-quark decays. Compared to the tagging of individual VR track-jets, the performance of the $X \to b\bar{b}$ tagging algorithm is significantly enhanced.

The predicted efficiencies of the $X \to b\bar{b}$ tagging algorithm are corrected to those seen in data. The signal efficiency is calibrated using $Z(\to b\bar{b})$+jets and $Z(\to b\bar{b})\gamma$ events, while the mis-tagging efficiency is calibrated using top-quark pair events [57]. The signal efficiency scale factors vary between $1.45^{+0.47}_{-0.45}$ for large-R jet p_T values of 200 GeV and $0.55^{+0.23}_{-0.22}$ for large-R jet p_T values of 1 TeV. The mis-tag efficiency scale factors vary from 1.1 ± 0.12 at low p_T to 1.0 ± 0.16 at high p_T.

[8] If there are fewer than three associated track-jets with $p_T > 7$ GeV, the inputs corresponding to any missing subjets are replaced with the mean input values.

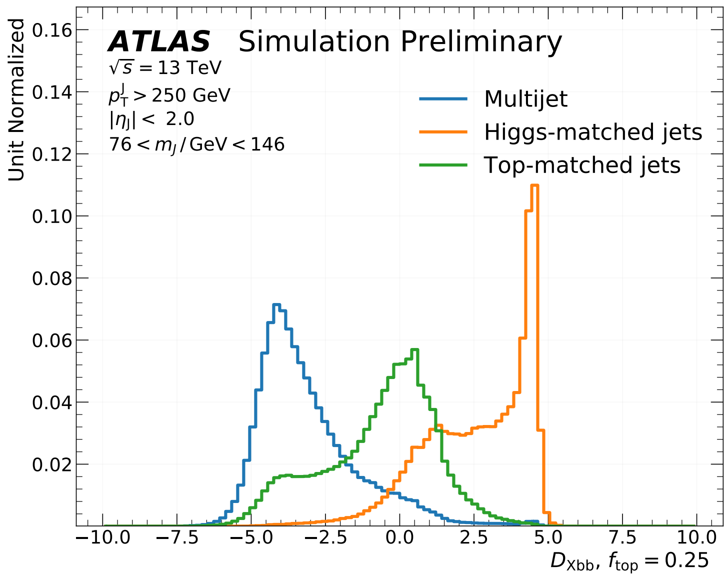

Figure 8: Distributions of the D_{Xbb} score (with $f_{\text{top}} = 0.25$) for large-R jets from boosted $h \to b\bar{b}$ and top-quark decays as well as for jets from mulijet production. All distributions are normalised to unit area. [56].

2.3.4 Missing transverse momenta

Missing transverse momentum, with magnitude $E_{\text{T}}^{\text{miss}}$, serves as an experimental proxy for the transverse momentum carried by undetected particles passing the ATLAS detector. The $E_{\text{T}}^{\text{miss}}$ is reconstructed from the signals of all the detected particles in the final state. A value incompatible with zero may indicate that a neutrino was produced in the particle collisions and subsequently traversed the detector. At the same time, the missing transverse momentum plays also an essential role in searches for so far undiscovered particles suggested in models for physics beyond the SM that escape the detector without being detected. A precise reconstruction of the $E_{\text{T}}^{\text{miss}}$ is a challenging task as it involves measurements from all detector subsystems and requires an unambiguous representation of all visible final state particles.

The reconstructed $E_{\text{T}}^{\text{miss}}$ [58] in ATLAS is characterised by two contributions. The first contribution, referred to as "hard term", is from fully reconstructed and calibrated high-p_{T} objects such as electrons, photons, τ-leptons, muons and jets. The second contribution, referred to as "soft term", is from charged-particle tracks compatible with the primary vertex but not associated to any object from the hard term. The missing transverse momentum is calculated as the negative vector sum of the transverse momenta of all selected leptons, jets and the additional tracks:

$$E_{\text{T}}^{\text{miss}} = \underbrace{- \sum_{\substack{\text{selected}\\ \text{electrons}}} \mathbf{p}_{\text{T}}^{e} - \sum_{\substack{\text{selected}\\ \text{photons}}} \mathbf{p}_{\text{T}}^{\gamma} - \sum_{\substack{\text{selected}\\ \tau-\text{leptons}}} \mathbf{p}_{\text{T}}^{\tau_{\text{had}}} - \sum_{\substack{\text{selected}\\ \text{muons}}} \mathbf{p}_{\text{T}}^{\mu} - \sum_{\substack{\text{selected}\\ \text{jets}}} \mathbf{p}_{\text{T}}^{\text{jet}}}_{\text{hard term}} \underbrace{- \sum_{\substack{\text{additional}\\ \text{tracks}}} \mathbf{p}_{\text{T}}^{\text{track}}}_{\text{soft term}} \tag{2}$$

Analogously, a track-based missing transverse momentum estimator $\vec{p}_{\text{T}}^{\text{miss}}$ is built as the negative vector sum of the transverse momenta of all tracks from the primary vertex. In addition, several ATLAS analyses use an object-based $E_{\text{T}}^{\text{miss}}$ significance $\mathcal{S}$ [59] to separate events in which the reconstructed $E_{\text{T}}^{\text{miss}}$ originates from weakly interacting particles, from those in which the $E_{\text{T}}^{\text{miss}}$ is consistent with contributions coming from detector inefficiencies or resolution effects. The $\mathcal{S}$ observable is calculated on an event-by-event basis considering the expected resolutions and likelihood of mismeasurement of all the objects that enter the $E_{\mathrm{T}}^{\mathrm{miss}}$ reconstruction and also takes directional correlations between the various measurements into account.

2.4 Generation and simulation of Monte Carlo events

A central challenge for the LHC experiments is to accurately predict the properties of particles produced in high-energy proton–proton (pp) collisions and the subsequent detector response to particles interacting with the detector material. To overcome these challenges, the LHC experiments typically use elaborate Monte Carlo (MC) simulations, where samples of simulated signal and background events are generated in several sequential stages.

In the first step, the pp collisions are simulated as a hard scattering process between the constituents (i.e. quarks and gluons) of the two incoming protons, using a dedicated set of parton distribution functions (PDFs) and following the Feynman formalism. Programmes such as MadGraph5 [60] or Powheg-Box [61, 62] are used by the ATLAS collaboration to calculate matrix elements at next-to-leading order (NLO) precision in QCD. The Powheg-Box generator is typically used to simulate matrix elements for the production of top-quark pairs, single top-qaurks, or Higgs bosons. While fixed order calculations are usually sufficient to model such processes, they are insufficient to model multi-jet, W/Z+jet or di-boson plus jets events. Instead, specialised generators such as SHERPA [63] are used to simulate diagrams with several additional parton emissions with NLO precision in QCD. The MadGraph5 generator is commonly used to simulate BSM processes such as BSM Higgs bosons and heavy vector bosons, or alternative samples for SM processes.

In a second step, the parton shower is simulated, which includes gluon emissions, fragmentation, hadronisation, secondary decays and the underlying event (i.e. particles originating from interactions of the beam remnants). This tasks is typically performed by programmes such as Pythia [64], HERWIG [65], or SHERPA, which are based on either the Lund string-model or the cluster-model.

The simulated samples are afterwards processed using either the Geant4-based simulation of the ATLAS detector geometry and response [66, 67] or fast simulation [68], where the Geant4 simulation of the calorimeter response is replaced by a detailed parameterisation of shower shapes. After the detector simulation, the generated signal and background events are overlayed with minimum-bias events from additional pp interactions (pile-up) in the same and neighboring bunch crossings. These minimum-bias events are simulated using the single-, double-, and non-diffractive pp processes of the Pythia generator [69].

Finally, the simulated events are reconstructed using the same algorithms employed for data events.

3 Indirect searches for new physics in the Higgs sector

The Higgs boson properties have been extensively studied in the last 10 years using LHC data. Following its discovery, the spin, parity, mass and width of the Higgs boson have been measured with unprecedented precision [70, 71, 72, 73, 74], as have its coupling properties to gauge bosons and fermions [75, 76]. Owing to the high precision of these measurements, the Higgs boson has become an excellent tool to test the validity of the SM. Thus, measurements of the Higgs boson properties will remain of high interest in the coming years. Many studies will be performed to establish whether the Higgs boson properties are consistent with the predictions of the SM at the percent level, or whether deviations from the SM exist.

As the data sample delivered by the LHC grows larger, the Higgs boson properties can be studied in increasingly "extreme" phase space regions, which are considered to be particularly sensitive to new physics effects. Such studies are ideal to constrain theories of BSM physics, as new (heavy) particles can contribute to the Higgs boson production processes or to its decay via loop-corrections. Such off-shell contributions would lead to an enhancement of the Higgs boson production rates and/or modulations of the (angular) distributions of particles produced either in association to the Higgs boson or in its decay [77, 78, 79].

In the Higgs sector, indirect searches for new physics effects are typically performed using generic approaches such as the κ-framework[9] [80, 81], pseudo-observables (PO)[10] [82, 83] or simplified template cross sections (STXS)[11] [83, 84, 85]. The κ-framework was widely used by the community for studies of the Higgs boson properties during Run 1 of the LHC. However, the κ-framework has several serious shortcomings [86]: (a) it does not enable a straightforward comparison of Higgs boson measurements performed for different production modes, (b) it is blind to new physics effects that would manifest only via modulations of angular-dependent observables, which could happen if the Higgs boson couplings were CP-violating or polarisation-dependent, and (c) it has only low sensitivity to new physics effects appearing in tails of kinematical distributions.

Pseudo-observables and simplified template cross sections are complementary approaches[12] that address

[9] The κ-framework introduces specific coupling modifiers meant to parameterise potential deviations from the SM predictions of the Higgs boson couplings to SM bosons and fermions. For a given production process or decay mode, denoted by "j", the coupling modifiers are defined via $\kappa_j^2 = \sigma_j/\sigma_j^{\mathrm{SM}}$ or $\kappa_j^2 = \Gamma_j/\Gamma_j^{\mathrm{SM}}$, where the measured cross section and partial decay width of the Higgs boson are compared to their respective SM predictions. All κ_j values are equal to unity in the SM.

[10] Pseudo-observables are meant to describe potential deviations from the SM expectations in Higgs boson production and decay processes. They are quantities that are experimentally accessible, theoretically well-defined (i.e. independent of the perturbative accuracy at which New Physics effects are computed), and capture all relevant New Physics effects in a kinematic range where BSM particles do not contribute via on-shell production. The concept of pseudo-observables was already introduced at LEP, where the partial decay rates of the Z boson around the Z pole $\Gamma\left(Z \to f\bar{f}\right)$ is a good example of an intensively studied pseudo-observable.

[11] Simplified template cross sections are defined in mutually exclusive fiducial regions of phase space (refreed to as "bins"). They are designed with the aim to maximise the sensitivity of a measurement while at the same time to minimise any theory dependence. Hence, individual bins are defined for each production mode exploiting the specific characteristica of the given process such as the kinematics of the Higgs boson or the number of particles produced in association to it, while the measurements are meant to be inclusive in the Higgs boson decay. In addition, measurements of simplified template cross sections allow for the use of multivariate analysis techniques and provide a common framework for combining measurements in different decay channels and eventually between the ATLAS and CMS collaborations.

[12] Following two different approaches can be motivated by the fact that at the LHC the Higgs boson interactions with SM particles are probed at multiple energy scales. For example, the decays of Higgs bosons to two vector bosons can be used to probe the same amplitudes as present in the associated production of a Higgs boson with a Z or W boson. However, while the momentum transfer in Higgs decays is kinematically bounded by the Higgs mass, the momentum transfer in the Zh and Wh production can reach scales of a few TeV.

the shortcomings of the κ-framework while retaining its advantages. Their measurements can be used as inputs for subsequent interpretations in the context of any BSM theory. Alternatively, both types of measurements can also be interpreted in the context of Effective Field Theories (EFTs) [83], which allows to probe for new phsics effects in a model independent way. The underlying principle of EFTs is based on supplementing the SM Lagrangian by additional higher-dimension operators and so-called Wilson coefficients that govern the strength of new interactions, such that in the gauge eigenbasis the Lagrangian is specified by

$$\mathcal{L} = \mathcal{L}_{SM} + \sum_i \frac{c_i^{(5)}}{\lambda}\mathcal{O}_i^{(5)} + \sum_i \frac{c_i^{(6)}}{\lambda^2}\mathcal{O}_i^{(6)} + \sum_i \frac{c_i^{(7)}}{\lambda^3}\mathcal{O}_i^{(7)} + \sum_i \frac{c_i^{(8)}}{\lambda^4}\mathcal{O}_i^{(8)} + \ldots$$

where each $\mathcal{O}_i^D$ is an $SU(3) \times SU(2) \times U(1)$ invariant operator of dimension D and the parameters $c_i^{(D)}$ are the Wilson coefficients. Some of the operators encode new structures for the interaction between the Higgs boson and the SM particles. The new interactions modify rates and/or kinematic distributions. The new interaction terms in the Lagrangian can be understood as the low-energy manifestation of new physics that exists at an energy scale λ that is much larger than the partonic centre-of-mass energy being probed at the LHC.

3.1 The main production and decay modes of the Higgs boson at the LHC

Representative lowest order Feynman diagrams of relevant production processes of the Higgs boson are shown in Figure 9. At the LHC, the gluon–gluon fusion (ggF) process is the dominant production mode of the Higgs boson. It is highly enhanced by the dominance of gluon densities, despite being a loop-induced process, and it accounts for about 87% of the inclusive Higgs boson production cross section. The second most frequent production mode is the vector-boson fusion (VBF) process, where either two Z or two W bosons fuse to produce a Higgs boson (7%). The VBF process is characterised by two highly energetic jets emitted in the forward region of the detector, with relatively low hadronic activity between them[13]. Higgs-Strahlung (Vh), i.e. the associated production of a Higgs boson with a Z or a W boson, contributes with around 4%, while the production of a Higgs boson in association with a pair of top quarks ($t\bar{t}h$) or a pair of b-quarks ($b\bar{b}h$) account each for approximately 1% of the total production cross section. These processes have additional leptons and/or jets in the final state, which makes it more challenging to reconstruct the Higgs boson decay but also makes them easy to trigger and helps to suppress relevant backgrounds.

Contributions of other production modes are significantly smaller, i.e. the associated production of a Higgs boson with a single top quark (th) or Higgs boson pair production (hh) only contribute with a few per-mille. Despite their small cross sections, these two processes are expected to be observed during the high-luminosity (HL) phase [10] of the LHC, where particular focus will be given to the study of the Higgs boson self-coupling strenght (accessible via Higgs boson pair production processes), which allows to probe the expected shape of the Higgs boson potential.

The ggF production mode allows to probe the Higgs boson couplings to heavy quarks (running in the loop), while studies of the VBF and Higgs-Strahlung processes allow to directly probe the Higgs boson couplings to vector bosons. Finally, the $t\bar{t}h$ production mode is best suited to directly probe the properties of the top quark Yukawa coupling.

[13] The low hadronic activity in these processes is due to the absence of color exchange.

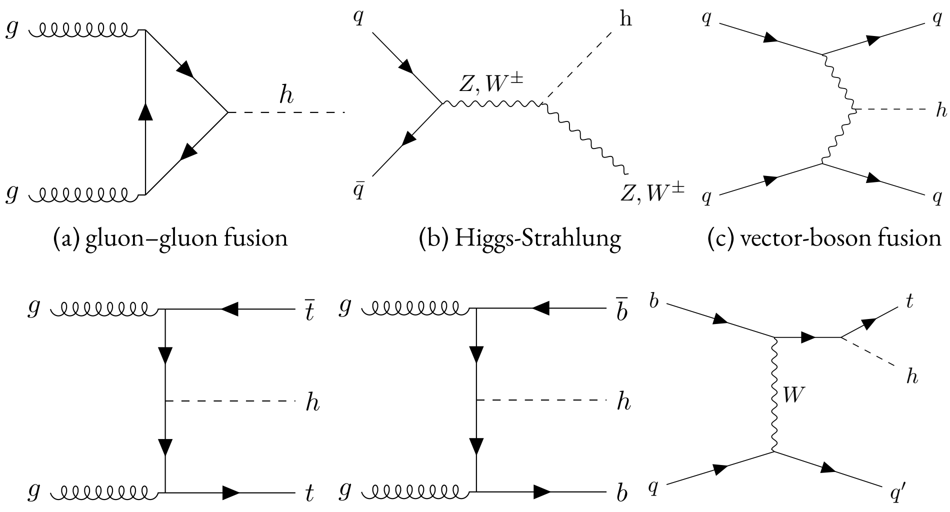

(a) gluon–gluon fusion (b) Higgs-Strahlung (c) vector-boson fusion

(d) $t\bar{t}h$ (e) $b\bar{b}h$ (f) th

Figure 9: Dominant production modes of the Higgs boson at the LHC.

The SM is tested by comparing the observed Higgs boson coupling properties to theory predictions based on the state-of-the-art calculations of Higgs boson production cross sections and branching fractions. Figure 10 shows the cross sections for the most dominant Higgs boson production modes at the LHC as a function of the center-of-mass energy. In physics analyses of the ATLAS and CMS collaborations, simulated event samples containing Higgs boson production are scaled to match these reference cross section values.

The inclusive production cross section for the ggF process is known at next-to-next-to-next-to leading order (NNNLO) precision in QCD with next-to leading order (NLO) electroweak (EW) corrections [87]. For the VBF process, cross-section predictions are available at next-to-next-to leading order (NNLO) precision in QCD with NLO EW corrections, which are obtained by the VBF@NNLO [88] and HAWK [89] programmes, respectively. The production cross sections for the Higgs-Strahlungs processes, Zh and Wh, are calculated at NNLO precision in QCD and NLO precision in EW using the programmes VH@NNLO [90] and HAWK.

The cross sections for the $t\bar{t}h$ and th processes are known at NLO precision in QCD and NLO precision in EW and are calculated with the programme MadGraph5_aMC@NLO [91]. Furthermore, Santander-matched [92] cross sections are used for the $b\bar{b}h$ process based on calculations with NNLO precision in QCD in the five flavour scheme (5FS) and NLO precision in QCD for calculations in the four flavour scheme (4FS). These calculations are based on the programmes SusHi [93] for the 5FS and MadGraph5_aMC@NLO for the 4FS. All cross sections are evaluated for a Higgs boson mass of 125.09 GeV. The calculations are based on the *PDF4LHC15* NNLO PDF sets for the ggF, VBF and Higgs-Strahlung production modes, and the *PDF4LHC15* NLO PDF sets for the other processes.

After its production, the Higgs boson decays almost instantly with a predicted average lifetime of 1.6×10^{-22} seconds. Diagrams of the main decay modes of the Higgs boson are depicted in Figure 11, while Table 1 lists their corresponding branching fractions. Decays into a pair of b-quarks corresponds with around

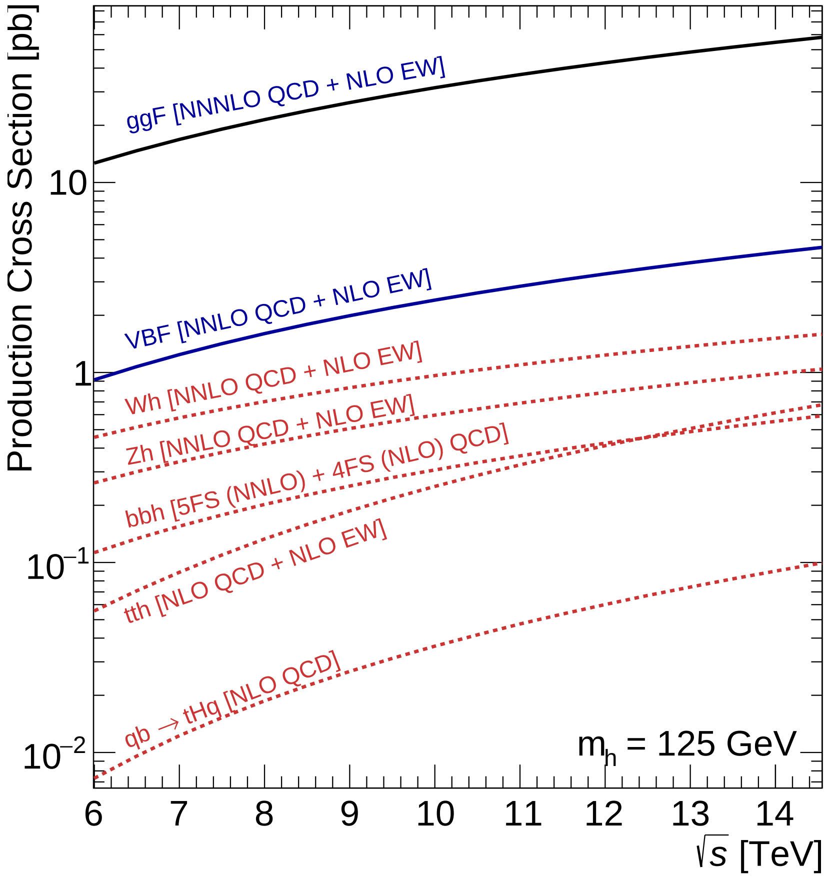

Figure 10: Cross sections for the most dominant Higgs boson production modes at the LHC presented as a function of the center-of-mass energy [83].

58% to the most frequent decay mode, followed by decays into a pair of W bosons[14] with around 21%. Other Higgs boson decays into a pair of bosons contribute with around 8% for $h \to gg$, 3% for $h \to ZZ^*$ and around 0.2% for $h \to \gamma\gamma$.

Invisible Higgs boson decays are expected to contribute with only around 0.1%. Though, significantly enhanced branching fractions for such decays are hypothesised by e.g. models predicting the existence of dark-matter particles [94]. Higgs boson decays are generally very sensitive to contributions from new physics, given the narrow total Higgs boson width of around 4.1 MeV, which is three orders of magnitude smaller than that of the W and Z bosons as well as the top quark. Hence searches for rare or exotic decays of the Higgs boson are another important endeavour of the LHC experiments.

By now, almost all major decay modes of the Higgs boson have been experimentally verified by the ATLAS and CMS collaborations. Only the decays $h \to gg$ and $h \to c\bar{c}$ are so far not yet accessible in data given the large amount of backgrounds. More straight forward are searches for the rare $h \to Z\gamma$ and $h \to \mu^+\mu^-$ decay modes. Despite their small branching fractions, their discoveries are just a matter of time owing to their relative clear experimental signatures.

[14] In Higgs boson decays to vector bosons, one of the decay products must be off-shell, since the mass of the Higgs boson is smaller than twice the mass of the W or Z boson.

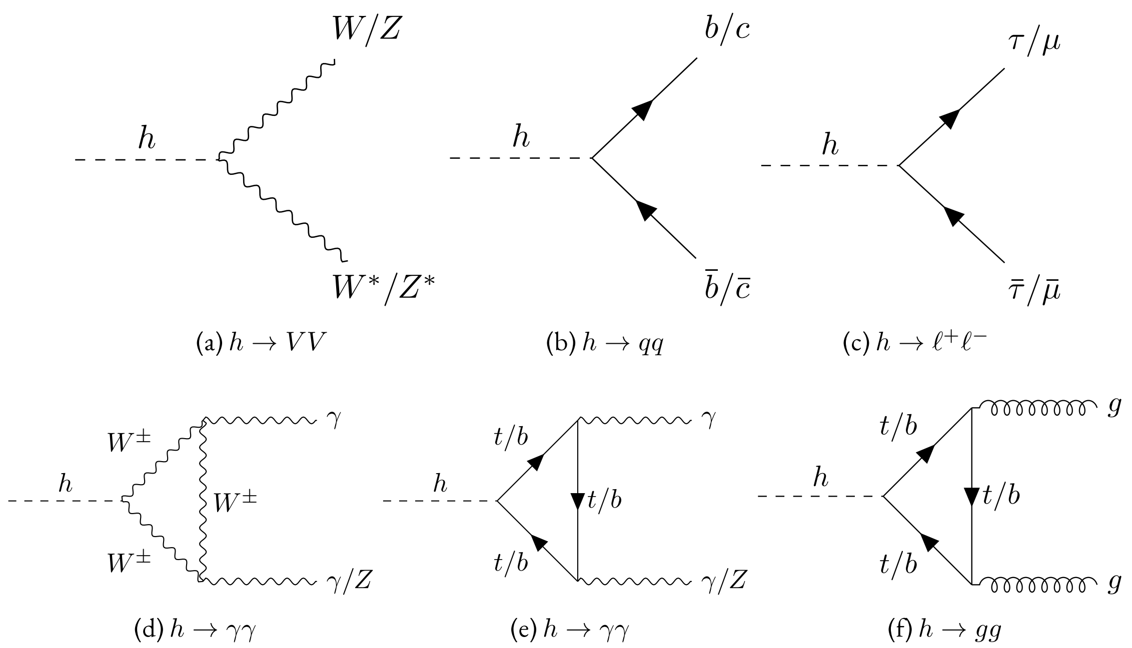

Figure 11: Examples of Feynman diagrams for the Higgs boson decay

Furthermore, rare decays of the Higgs boson, such as decays into a meson and a photon, are also searched for. These decays are well-suited probes for modifications of the Higgs boson's couplings to first- and second-generation fermions. Examples of searches for such decays include $h \to \omega\gamma$ and $h \to K^*\gamma$ decays [95] as well as $h \to J/\psi\,\gamma$ and $h \to \psi(2S)\gamma$ [96]. Probing these decays is attractive because several BSM theories predict enhanced Yukawa couplings between the Higgs boson and light quarks.

Table 1: Higgs boson branching fractions calculated at a mass of 125 GeV [83], using the HDECAY [97] and PROPHECY4F [98] programmes.

Decay Channel	[%]
$h \to b\bar{b}$	58.24
$h \to WW^*$	21.37
$h \to gg$	8.187
$h \to \tau^+\tau^-$	6.272
$h \to c\bar{c}$	2.891
$h \to ZZ^*$	2.619
$h \to \gamma\gamma$	0.2270
$h \to Z\gamma$	0.1533
$h \to \mu^+\mu^-$	0.02176

3.2 Higgs boson property measurements in $h \to WW^*$ decays

The $h \to WW^* \to \ell\nu\ell\nu$ decay channel is one of the most sensitive channels for measuring the Higgs boson couplings to other particles and for determining its spin and parity quantum numbers. Studies in this decay channel profit in particular from the large branching fraction (about 2.4%), and the cleaner signature in the detector compared to the more common $h \to b\bar{b}$ decay. Due to these features, the $h \to WW^* \to \ell\nu\ell\nu$ decay mode was one of the channels in which the Higgs boson was discovered at the LHC in 2012 [99, 100].

The $h \to WW^* \to \ell\nu\ell\nu$ decay is characterised by two charged leptons and two undetected neutrinos in the final state. Additional leptons or jets may be present in the event, depending on the production mode. Kinematic observables built from the leptons (ℓ), jets (j), and $E_{\mathrm{T}}^{\mathrm{miss}}$ in the selected candidate event are used to reduce contributions from relevant backgrounds. The charged leptons ensure high trigger efficiencies. Due to the spin-0 nature of the Higgs boson and the chiral structure of the weak force in the decay of the two W bosons [101], the opening angle between the two charged leptons $\Delta\Phi_{\ell\ell}$ and correspondingly the invariant di-lepton mass $m_{\ell\ell}$ tend to be relatively small (see Figure 12). These two characteristic observables are most crucial to separate the $h \to WW^* \to \ell\nu\ell\nu$ signal process from background contributions originating from the non-resonant WW, the Z/γ^*+jets and top-quark pair production.

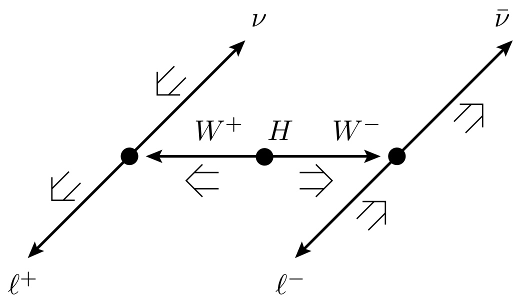

Figure 12: Illustration of the decay of a Higgs boson into two W bosons, $h \to WW^*$, which subsequently decay into a $\ell^\pm\nu\ell^\mp\nu$ final state. The small arrows indicate the direction of motion of the intermediate state and final state particles, while the large double arrows indicate their spin projections. The decays of the Higgs boson and W bosons are shown in the decaying particle's rest frame [102].

Due to the presence of two undetected neutrinos in the final state, the invariant mass of the Higgs boson can not be determined. Instead, the transverse mass is used, which is defined as follows:

$$m_{\mathrm{T}} = \sqrt{\left(E_{\ell\ell} + E_{\mathrm{T}}^{\mathrm{miss}}\right)^2 - \left|\vec{p}_{\mathrm{T},\ell\ell} + \vec{E}_{\mathrm{T}}^{\mathrm{miss}}\right|^2}$$

with $E_{\ell\ell} = \sqrt{|\vec{p}_{\mathrm{T},\ell\ell}|^2 + m_{\ell\ell}^2}$ and $\vec{p}_{\mathrm{T},\ell\ell}$ the combined dilepton momentum vector in the transverse plane. The m_{T} distribution has a kinematic upper bound at the Higgs boson mass, providing a strong separation between the signal process from Higgs boson production and the backgrounds.

Numerous studies of the Higgs boson properties have been performed in the $h \to WW^* \to \ell\nu\ell\nu$ decay channel in recent years[15], such as simple measurements of the signal strength [103, 104], measurements of STXSs or differential cross sections [105, 106], and studies of anomalous Higgs boson couplings [107]. The

[15] Since Run 2, ATLAS analyses have mainly focused on the $h \to WW^* \to e\nu\mu\nu$ decay mode, because it has significantly lower contributions from the Z/γ^*+jets background than the $h \to WW^* \to e\nu e\nu$ and $h \to WW^* \to \mu\nu\mu\nu$ decay modes.

studies have been performed separately for the ggF, VBF, and Higgs-Strahlungs production modes. Furthermore, based on the Run 1 dataset, constraints were placed on the spin and CP quantum numbers of the Higgs boson [108], as well as on the off-shell Higgs boson signal strength [109].

This section highlights a few recent results from studies of the Higgs boson coupling properties in $h \to WW^* \to e\nu\mu\nu$ events based on $\sqrt{s} = 13$ TeV pp collision data collected by the ATLAS detector. Section 3.2.1 summarise the measurements of the Higgs boson production cross sections of the ggF and VBF production modes. In addition, searches for CP violating effects in the effective Higgs-gluon coupling and searches for polarisation-dependent couplings are detailed in the Sections 3.2.2 and 3.2.3. The latter two efforts were under my leadership.

3.2.1 Measurements of Higgs boson production

Recently, the ATLAS collaboration published measurements of the total Higgs boson production cross sections for the ggF and VBF processes[16] using $h \to WW^* \to e\nu\mu\nu$ decays in pp collisions at a center-of-mass energy of 13 TeV [104]. These measurements are based on data that was recorded by the ATLAS detector during Run 2 (2015–2018) of the LHC and that correspond to an integrated luminosity of 139 fb^{-1}. In the context of these studies, measurements of cross sections in kinematic fiducial regions defined in the STXS framework have been provided as well.

The measurements of the cross sections are performed in events consistent with the signature of a $h \to WW^* \to e\nu\mu\nu$ decay. Selected candidate events are further classified based on the number of jets N^{jet} in the event. In total, four categories are used: one for each the $N^{\text{jet}} = 0$ and $N^{\text{jet}} = 1$ channels, which solely target the ggF production mode of the Higgs boson, and two categories for the $N^{\text{jet}} \geq 2$ channel, which has significant contributions from both the ggF and VBF production modes. The event topology of the signal process[17] and the composition of the relevant backgrounds (as depicted in Figure 13) changes significantly depending on the number of jets in the event. Hence, a set of specific selection requirements are applied to each of the four event categories in order to optimise the sensitivity to the signal.

In the $N^{\text{jet}} = 0$ category, the most dominant background contributions stem from $Z/\gamma^* \to \tau\bar{\tau}$ decays, where one of the two τ-leptons decays into an electron and a neutrino and the other τ-lepton decays into a muon and a neutrino. The next largest contributions are from the non-resonant WW production and from processes containing top quarks. The $Z \to \tau\tau$ background is reduced by requiring $E_{\text{T}}^{\text{miss}}$ to point away from the combined dilepton four-momentum (as shown in Figure 12) and by placing selection requirements on the azimuthal angular difference between the two charged leptons, the transverse di-lepton momentum, and the invariant di-lepton mass. The two latter selection requirements also significantly reduce contributions from the non-resonant WW background. In the $N^{\text{jet}} = 1$ and $N^{\text{jet}} \geq 2$ categories, the by far most dominant background contributions are from the top-quark pair production. Thus, events containing a b-tagged jet are vetoed to reduce this type of background. Contributions from $Z(\to \tau\tau)$+jets events are reduced by introducing a selection requirement on $m_{\tau\tau}$. The observable $m_{\tau\tau}$ is calculated from the four-vectors of the two charged leptons and the $E_{\text{T}}^{\text{miss}}$ vector using the collinear approximation [110].

[16] Studies of other production modes are published separately: e.g. the most recent measurement of the production cross section for Higgs-Strahlung in the $h \to WW^* \to e\nu\mu\nu$ decay channel are based on a partial Run 2 dataset [103].

[17] For example in $N^{\text{jet}} = 0$ events, the Higgs boson is typically produced at rest, while the Higgs boson can receive significant Lorentz boost when it recoils against one or several jets.

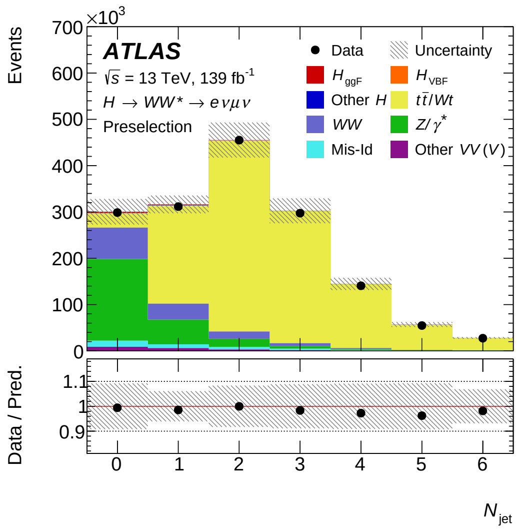

Figure 13: Distribution of the jet multiplicity in $h \to WW^* \to e\nu\mu\nu$ candidate events [104], where jets with $p_\mathrm{T} > 30$ GeV and $|\eta| < 4.5$ are considered. The hatched band corresponds to the normalisation component of the total uncertainty prior to performing any fit to the data.

The $N^\mathrm{jet} \geq 2$ category is divided into two subcategories. One enriched in ggF production of the Higgs boson and the other enriched in VBF production. In order to obtain a sample enriched in VBF production, the characteristic kinematics of the two leading jets in the event are exploited: the candidate events are required to have two jets in the forward region of the detector (moving in opposite hemispheres) and a relatively low amount of hadronic activity between these two jets (referred to as "central jet veto"). In addition, neither of the two charged leptons may lie outside the pseudorapidity gap between the two VBF jets (which is referred to as "outside lepton veto"). The ggF-enriched region contains all events failing either the central jet veto or the outside lepton veto. In the VBF-enriched $N^\mathrm{jet} \geq 2$ category, a deep neural network (DNN) is trained to further separate the VBF signal from the remaining backgrounds (including also Higgs boson production via ggF). The DNN is based on observables that exploit either the kinematics and characteristics of the VBF topology or the features of the $h \to WW^*$ decay. In total, 15 kinematic observables are used. Among them are quantities such as the invariant di-jet and di-lepton masses, the transverse Higgs boson mass, the rapidity difference between the two leading jets, the lepton centralities, the p_T of up to three jets (where priority is given to the leading jets) or the azimuthal angle difference between the two charged leptons.

The signal regions in the $N^\mathrm{jet} = 0$ and $N^\mathrm{jet} = 1$ categories are further split into four subregions to increase the sensitivity to the signal process. The subregions are defined based on the invariant di-lepton mass and the p_T of the subleading lepton in the event. In a similar fashion, the signal regions of the ggF-enriched $N^\mathrm{jet} \geq 2$ category are split into two subregions based on the invariant di-lepton mass.

Background contributions from W+jets and multi-jet production with misidentified leptons, either from nonprompt decays of heavy-flavor hadrons or misidentified jets, are estimated using a data-driven technique. Additionally, dedicated control regions are used to normalise the predictions of the WW, top-quark, and $Z/\gamma^* \to \tau\tau$ backgrounds. These control regions are defined by modifying some of the event selection requirements used to define the signal regions. Different control regions are used for different jet multiplicities.

The cross sections times $h \to WW^*$ branching ratio for the ggF and VBF production modes are determined in a simultaneous[18] profile likelihood fit to all signal and control regions in the $N_{\text{jet}} = 0$, $N_{\text{jet}} = 1$, and $N_{\text{jet}} \geq 2$ categories. The m_{T} distribution is used as the final fit discriminant in the $N^{\text{jet}} = 0$, $N^{\text{jet}} = 1$ and the ggF-enriched $N^{\text{jet}} \geq 2$ categories, while the DNN response score is used in the VBF-enriched $N^{\text{jet}} \geq 2$ category. The post-fit distributions of both observables are depicted in Figure 14. In total, around 4000 signal events are counted in all categories combined. The m_{T} and DNN response score distribution of the observed signal processes agree in both shape and normalisation with their respective SM predictions.

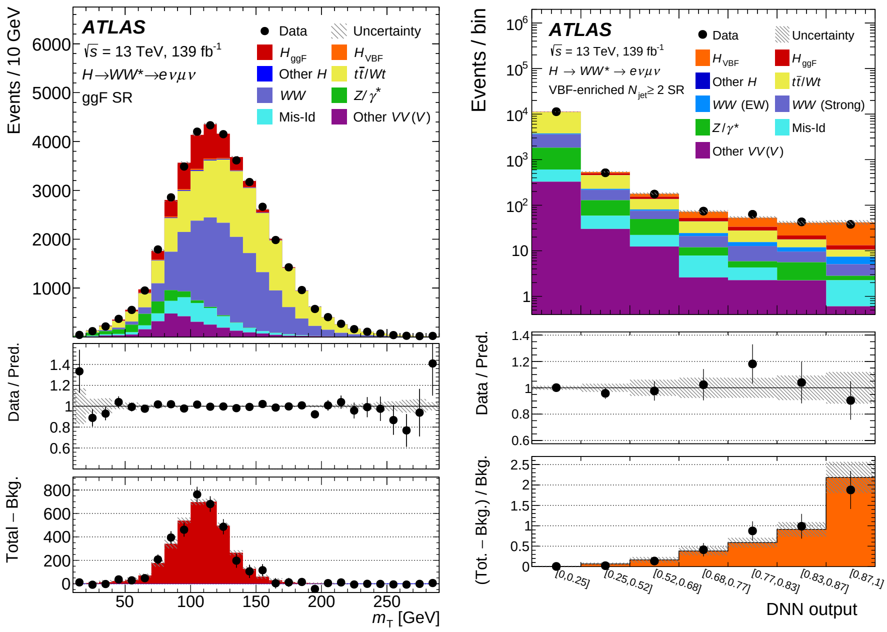

(a) (b)

Figure 14: Post-fit distributions of (a) the transverse mass m_{T} for the combined ggF signal regions and (b) the DNN response score in the VBF signal region. The middle panel depicts the ratio of the data to the sum of the fitted signal and backgrounds, while the bottom panel shows the difference between the data and the estimated background compared to the predicted signal contribution. The hatched band shows the combined statistical and systematic uncertainty for the fitted signal and background processes [103].

The cross sections times $h \to WW^*$ branching ratio for the ggF and VBF production modes for a Higgs boson with mass $m_H = 125.09$ GeV are simultaneously measured to be

$$\sigma_{\text{ggF}} \cdot \mathcal{B}_{h\to WW^*} = 12.0 \pm 0.6(\text{stat.})\, ^{+0.9}_{-0.8}(\text{exp. syst.})\, ^{+0.6}_{-0.5}(\text{sig. theo.}) \pm 0.8(\text{bkg. theo.})\,\text{pb}$$

$$\sigma_{\text{VBF}} \cdot \mathcal{B}_{h\to WW^*} = 0.75 \pm 0.11(\text{stat.})\, ^{+0.07}_{-0.06}(\text{exp. syst.})\, ^{+0.12}_{-0.08}(\text{sig. theo.})\, ^{+0.07}_{-0.06}(\text{bkg. theo.})\,\text{pb}\,,$$

which is consistent to the SM predicted values of 10.4 ± 0.5 pb and 0.81 ± 0.02 pb for the ggF and VBF production modes, respectively. The corresponding signal strength scale factors are $\mu_{\text{ggF}} = 1.15^{+0.14}_{-0.13}$ and $\mu_{\text{VBF}} = 0.93^{+0.23}_{-0.20}$. These results are significantly more precise than the results from previous Higgs boson cross section times $h \to WW^*$ branching ratio measurements from ATLAS. In comparison to the

[18] Two independent and unconstrained parameter of interests are used in the fit to determine the ggF and VBF cross sections.

previous measurements, which are based on $36\,\text{fb}^{-1}$, the total uncertainties in the ggF and VBF production cross section times branching ratio values have been decreased by 38% and 59%, respectively [111]. Improvements are coming in particular from the larger dataset. Due to the larger dataset, the statistical uncertainties are reduced by 50% for the ggF production mode and by 68% for the VBF production mode. Other improvements include a dedicated signal region for ggF production in association with two or more jets and a more refined machine learning approach for separating the VBF signal process from backgrounds. As a result, the experimental uncertainties have been decreased by 40% for the ggF production mode and 65% for the VBF production mode. Furthermore, the uncertainties originating from the modelling of the signal and backgrounds are reduced by around 20% for both production modes following the refined recommendations from the LHC Higgs Working Group [83] and improved Monte Carlo models for several background processes.

The CMS collaboration has also recently measured the cross section times $h \to WW^*$ branching ratio for the most dominant production modes of the Higgs boson using 138 fb^{-1} of pp collision data [112]. For the ggF production mode, the signal strength scale factor has been determined to be $\mu_{\text{ggF}} = 0.92^{+0.11}_{-0.10}$, while a signal strength of $\mu_{\text{VBF}} = 0.71^{+0.28}_{-0.25}$ has been found for the VBF production mode. Thus, CMS has a slightly more precise measurement of μ_{ggF}, while ATLAS has an approximately 20% more precise measurement of μ_{VBF}. The CMS results benefit in particular from additional event categories targeting the $h \to WW^* \to e\nu e\nu$ and $h \to WW^* \to \mu\nu\mu\nu$ decays. The events in these categories are analysed together with those from the $h \to WW^* \to e\nu\mu\nu$ decay channel. At the same time, the ATLAS results on μ_{VBF} profit in particular from the DNN used to separate the VBF signal process from the relevant backgrounds. The algorithm trained by ATLAS proved to be more performant than the DNN used by CMS.

The measurements of μ_{ggF} and μ_{VBF} in $h \to WW^*$ events are compared in Figure 15 to the results of similar measurements performed by the ATLAS collaboration in $h \to ZZ^*$, $h \to \gamma\gamma$, and $h \to \tau^+\tau^-$ candidate events [29, 113, 114]. The signal strength μ_{ggF} is measured with a significantly higher precision in $h \to ZZ^*$ and $h \to \gamma\gamma$ events, while μ_{VBF} (which is still statistically dominated in most channels) is measured with a higher precision in $h \to WW^*$ and $h \to \tau\tau$ events owing to their relatively high event rates in these decay channels.

The reduced Stage-1.2 STXS category scheme is used to measure cross sections in kinematic fiducial regions. This scheme has a finer granularity for regions targeting Higgs bosons with a high transverse momentum than the previously used Stage-1.1 STXS scheme [115]. The fiducial regions, as presented in Figure 16, are defined based on the expected kinematic properties of the Higgs boson, such as its transverse momentum p_{T}^{H} and its rapidity, but also on the number of hadronic jets[19] and the invariant di-jet mass for events with two or more jets. The STXS template definition for the ggF signal process includes the Born-level $gg \to h$ process plus higher-order QCD and EW corrections, such as the $gg \to Z(\to q\bar{q})h$ process. Similarly, the STXS template definition for the VBF process includes both the usual VBF topology and the $q\bar{q} \to V(\to q\bar{q})h$ topology. Overall, the cross sections are measured in 11 disjoint fiducial regions, of which 6 target the ggF production and the other 5 target the VBF production.

For the STXS measurements, the definitions of the signal regions are modified with respect to what is used for the measurements of the inclusive production cross sections times $h \to WW^*$ branching ratio. The

[19] At generator level, jets are build from all stable particles with a lifetime greater than 10 ps, excluding the decay products of the Higgs boson and leptons from W and Z boson decays, using the anti-k_{t} algorithm with a jet radius parameter of $R = 0.4$. These jets must have a transverse momentum larger than 30 GeV.

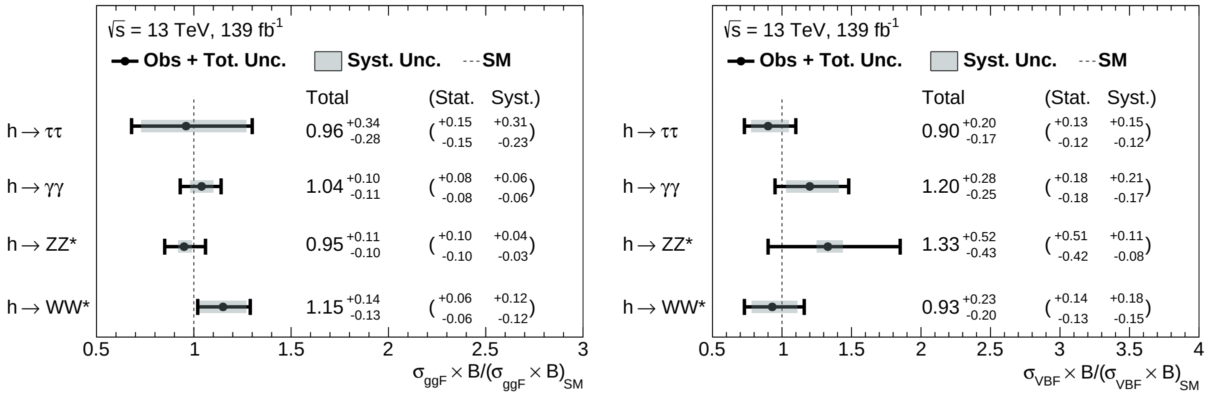

(a) (b)

Figure 15: Cross-sections times branching ratio for $h \to WW^*$, $h \to ZZ^*$, $h \to \gamma\gamma$, and $h \to \tau^+\tau^-$ decays measured by the ATLAS collaboration for ggF (a) and VBF (b) production, normalised to their SM predictions [29, 104, 113, 114]. The black bars show the total uncertainties in the measurements, while the gray bands represent the systematic uncertainties.

aim is to optimise the alignment of the STXS categories and the kinematic regions in which the measurements are performed. The signal regions used for the STXS measurements are detailed in Figure 16.

A simultaneous fit to all signal regions is performed to measure the 11 STXS values, where each cross section is determined via an independent and unconstrained parameter of interest. A summary of the measured cross section values normalised to the corresponding SM predictions is presented in Figure 17. The individual measurements agree within one standard deviation to the SM expectations. Overall, the results are compatible with the SM predictions, with a p-value of 53%.

Personal contributions

The work on this analysis was carried out by a team of 61 researchers from 25 different institutions, including myself. My personal contributions to these efforts included the simulation of the ggF+jets production process using matrix elements at next-to-leading order precision in QCD for diagrams with up to two additional parton emissions. Furthermore, I optimised the configuration of the FxFx merging procedure [116], which eliminates redundancies between identical partonic final states generated at the matrix element and the parton shower stage. These simulations were used for measurements of the inclusive Higgs boson production cross section, STXS values, and differential cross section measurements of Higgs boson properties [106], to calculate the uncertainties in matching the matrix element and parton shower.

Furthermore, I guided a Ph.D. student from Shandong University in designing validation regions for the $W\gamma$ and $Z\gamma$ backgrounds, specifically focusing on events that include non-prompt leptons from photon conversions (i.e. $\gamma \to e^+e^-$), following the studies that I initially carried out for a previous iteration of this analysis [111].

Challenges

Finalising the analysis involved overcoming several significant challenges. One of the most crucial aspects was modelling the background processes. The complex composition of backgrounds, which significantly

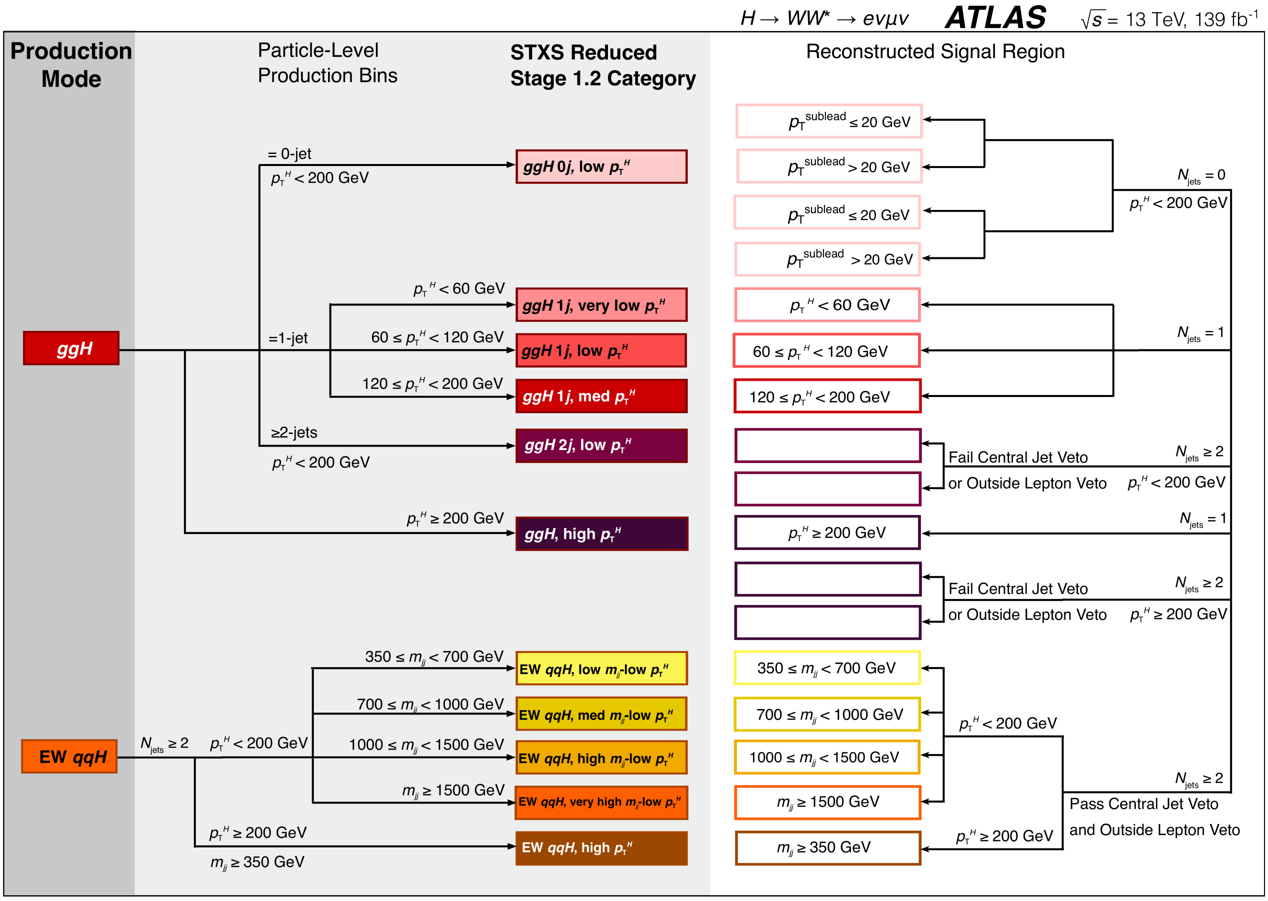

Figure 16: Two sets (Production Mode Stage and Reduced Stage 1.2) of exclusive phase-space regions (production bins) defined at parton level for the measurement of the Higgs boson production cross sections (left and middle-left shaded panels), and the corresponding modified signal regions (right panel) at reconstruction level. The colors of each reconstructed signal region box indicate the STXS bin which provides the largest relative contribution [103].

contribute to the various analysis regions, required a careful consideration when designing the analysis strategy. To address these challenges, dedicated control or validation regions are necessary for essentially all contributing background processes. These regions enable a thorough investigation of potential mismodelling in background normalisation or event kinematics and allow to derive corrections to these effects if necessary.

Disagreements to data were initially seen in the modelling of kinematic observables in the production of top-quark pairs, such as the transverse momenta of the two selected leptons or the jet multiplicity. The mismodelling of these distributions were identified with missing higher-order corrections. Therefore, a NNLO reweighting procedure [117], applied to the simulated sample of top-quark pair events, was used to mitigate these mismodelling effects.

The estimation of the misidentified lepton background proved particularly challenging due to its diverse origins. Misidentified electrons can originate from hadrons mimicking the electron signature, photon conversions, or heavy-flavor hadron decays. Misidentified muons, on the other hand, stem primarily from heavy-flavor hadron decays, in-flight meson decays, or hadrons punching through the calorimeter system. The misidentification rates for these processes as well as their correct relative proportions are not at all de-

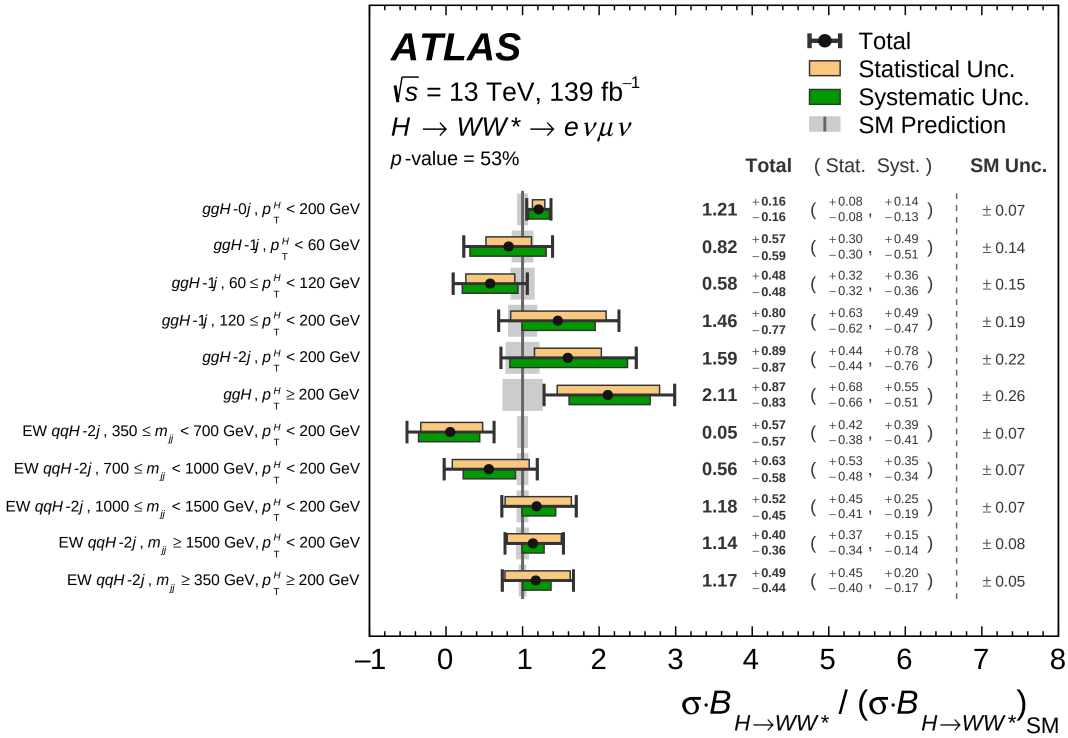

Figure 17: Best-fit value and uncertainties for the $h \to WW^*$ cross section measured in different kinematic regions (i.e. STXS bins), normalised to the corresponding SM prediction. The black error bars, green boxes and tan boxes show the total, systematic, and statistical uncertainties per measurement, respectively. The grey bands show the theory uncertainties in the predictions [103].

scribed well by the Monte Carlo simulations. Hence, both the normalisation and the event kinematics of these backgrounds have to be determined from data.

The data-driven estimation of the misidentified lepton background relies on the use of control samples. These samples are obtained from events that pass all the nominal selection requirements, except that some of the identification criteria of one of the two lepton candidates, referred to as anti-identified lepton, has been inverted. The expected yields and event kinematics of the misidentified lepton background in the signal and control regions are then extrapolated from these control samples, after subtracting the expected contribution from processes with two prompt leptons.

The most crucial part of the estimation procedure is to derive appropriate extrapolation factors. This is achieved in a sample of three-lepton events enriched with Z+jets production, where a misidentified lepton candidate recoils against the leptonically decaying Z boson. The extrapolation factor is defined as the ratio of the number of events where the misidentified lepton candidate passes the full identification requirements to the number of events where it is anti-identified. The extrapolation factors are determined separately for misidentified electrons and muons. They are measured in intervals of p_{T} (and $|\eta|$) in the case of electrons (muons). The precision of the extrapolation factors is limited by several effects. These include: the fact that the sources of misidentified leptons may be different in the Z+jets-enriched events and the signal regions, the precision of the normalisation of processes with two prompt leptons subtracted from the control sample, and biases from the trigger requirements.

Outlook

The inclusive Higgs boson production cross section measurements in $h \to WW^*$ events are by now limited by systematic uncertainties, which means that future measurements will not be improved necessarily by using larger datasets. Instead, future work needs to focus on decreasing systematic uncertainties. Particular important are the parton shower uncertainties associated with both the ggF and VBF production modes of the signal process, as they are currently the single largest sources of uncertainty in the Higgs boson property measurements. These uncertainties are evaluated by comparing the predictions of two sets of Monte Carlo generators: nominally Powheg + Pythia 8 are used to modell the signal processes, whereas Powheg + HERWIG 7 are used as an alternative configuration. Future iterations of Higgs property measurements in $h \to WW^*$ events should therefore attempt to mitigate the dependency on parton shower uncertainties. One promising approach involves training a set of Adversarial Neural Networks to reduce the dependence following the strategy worked out in Reference [118]. Another way could be to derive dedicated sets of tuned parameters for the Pythia 8 and HERWIG 7 parton shower generators based on extensive comparisons to data. Such studies could be done in the context of differential cross section measurements of Higgs boson properties [106].

Further improvements could be obtained by re-introducing signal regions targeting decays where both final state leptons are of the same flavour, such as $h \to WW^* \to e\nu e\nu$ and $h \to WW^* \to \mu\nu\mu\nu$. These additional signal regions are expected to be particularly beneficial for measurements of the Higgs boson properties at high p_T, which are still statistically limited.

The measurements of Higgs boson properties at high p_T will be generally of great interest in the near future, due to their enhanced sensitivity to BSM physics. However, dedicated reconstruction techniques and event selection optimisations are required in this kinematic regime, given the strong collimation of the Higgs boson's decay products. As a consequence, lepton isolation requirements may have to be adjusted or removed entirely to select strongly boosted $h \to WW^* \to \ell\nu\ell\nu$ decays. Furthermore, the $h \to WW \to lvqq$ decay channel may emerge as a potentially viable option at high Higgs boson p_T. In these cases, the entire Higgs boson decay could be reconstructed via a single large-R jet.

3.2.2 Search for CP violation in the Higgs plus two jets production

The origin of the observed matter-antimatter asymmetry in the universe is one of the most important open questions in particle physics. This asymmetry may be explained by the process of baryogenesis, which is suggested to have taken place during the early universe. Three Sakharov conditions [119] must be met for baryogenesis to have occurred. One of these conditions is CP violation. (i.e. the violation of invariance of fundamental interactions under charge conjugation and parity transformation).

In the SM, a source for CP violation is introduced via a complex phase in the Cabibbo–Kobayashi–Maskawa (CKM) matrix [120, 121] for quark mixing. The complex phase in the CKM matrix describes the observations of CP violation in the decays of K-, B-, and D-mesons [122, 123, 124, 125, 126]. However, the measured size of the complex phase and the derived magnitude of CP violation are not sufficient to explain the surplus of matter over anti-matter observed in our Universe, which suggests that further sources of CP violation must exist[20].

[20] Other sources of CP violation may exist in the neutrino sector or the strong interaction.

An extended scalar sector can naturally introduce new sources of CP violation that are sufficient to realise the process of baryogenesis [127]. Simple examples of such extensions are CP-violating 2HDMs, in which the CP-violating effects arise via the mixing of the three neutral Higgs states [128]. Such models motivate to search for additional heavy Higgs-like particles decaying into pairs of weak gauge bosons, and to probe for CP-violating effects in the production and decay of the 125 GeV Higgs boson. As the LHC data does not show any signs of additional Higgs-like particles as of now, direct searches for CP violating effects in the Higgs sector focus on studies of the Higgs boson coupling properties.

During Run I of the LHC, the ATLAS and CMS collaborations extensively studied the CP properties of the Higgs boson using the $h \to WW^*$ and $h \to ZZ^*$ decay modes. By probing the kinematics of final state particles in these decays, a pure CP-odd Higgs boson has been successfully excluded at the 99% confidence level. In addition, a potential mixing of CP even and CP odd contributions in the hWW and hZZ couplings has been significantly constrained [70, 71]. Since the beginning of Run II, the LHC experiments are focusing on searches for CP-violating effects in the various Higgs boson production processes. Studies have been performed in the gluon-gluon fusion + 2 jets signature [107, 129], the vector boson fusion [129, 130, 131, 132] and tth [133, 134, 135, 136] production modes. These studies were carried out in events with Higgs boson decays to WW^*, $\gamma\gamma$, ZZ^*, and $\tau\tau$. In addition, searches for CP violation in the interaction between the Higgs boson and τ-leptons were performed by probing the τ-lepton decay plane [137, 138].

Studies of the gluon–gluon fusion production process are particular interesting as they are sensitive to CP-violating effects (and other new pyhsics effects) in the top-quark and bottom-quark Yukawa couplings, and to contributions of new particles running in the loop. Furthermore, the gluon–gluon fusion process probes the top-quark Yukawa coupling in a different kinematic regime than tth production and therefore complements results obtained in that production mode.

In the large top-quark-mass limit, $m_{\text{top}} \to \infty$, the heavy-quark loop of the gluon–gluon fusion production process can be described by an effective Higgs–gluon interaction. In this approach, the CP structure of the top-quark Yukawa coupling is inherited by the effective Higgs–gluon interaction [139]. This means that contributions from new physics effects can be parametrised by EFT frameworks, such as the Higgs Characterisation (HC) model [140], and that BSM contributions can be directly set on the CP-even and CP-odd coupling strength modifiers of the effective Higgs–gluon interaction. In the HC model, the effective Lagrangian that describes the Higgs–gluon interaction is expressed as

$$\mathcal{L}_0^{\text{loop}} = -\frac{g_{Hgg}}{4} \left(\kappa_{gg} \cos(\alpha) G^a_{\mu\nu} G^{a,\mu\nu} + \kappa_{gg} \sin(\alpha) G^a_{\mu\nu} \tilde{G}^{a,\mu\nu} \right) h \,, \tag{3}$$

where $G^a_{\mu\nu}$ is the gluon field strength tensor, $\tilde{G}^{a,\mu\nu} = G^a_{\rho\sigma}\, \varepsilon^{\mu\nu\rho\sigma}/2$ is the dual tensor, g_{Hgg} is the effective coupling for the SM CP-even ggH interaction, κ_{gg} is the coupling-strength scale factor for the effective Higgs–gluon interaction, and α is the CP-mixing angle. A pure CP-even state is obtained for $\cos(\alpha) = 1$, while a pure CP-odd state is obtained for $\cos(\alpha) = 0$.

The CP nature of the Higgs boson couplings have an impact on the production rates, which are proportional to the sum of squares of CP-even and CP-odd terms (i.e. $|\text{CP}^{\text{even}}|^2 + |\text{CP}^{\text{odd}}|^2$). By comparing the Higgs boson production rates to the SM expectation, one cannot distinguish CP-odd contributions from other new physics effects to the total production rate. In contrast, a study of CP-sensitive observables can provide a direct evidence of CP-violating effects. To construct CP-sensitive observables, at least two additional jets are needed in the final state of the Higgs boson production process. Relevant Feynman diagrams of the lowest-order ggF + 2 jets Higgs boson production process are depicted in Figure 18. Diagrams corresponding to the $qq \to hqq$ subprocess possess gluon exchange in the t-channel and lead to a VBF-like topology in the detector with the two tagging jets going into opposite hemispheres in the forward regions. Moreover, this subprocess is the most sensitive to the CP properties of the Higgs couplings [141].

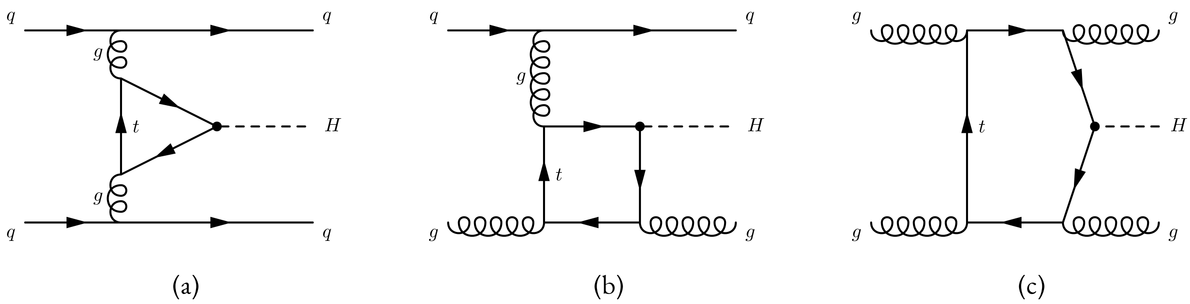

Figure 18: Examples of Feynman diagrams contributing to the production of a Higgs boson in association with two jets via the fusion of two gluons at leading order in QCD. The presented diagrams show examples for the subprocesses (a) $qq \to hqq$, (b) $qg \to hqg$ and (c) $gg \to hgg$.

An example of a CP-sensitive observable is the signed azimuthal angular difference between jets produced in association with a Higgs boson [139, 142]. The angular difference is defined as $\Delta\Phi_{jj} = \phi_{j_1} - \phi_{j_2}$ if $\eta_{j_1} > \eta_{j_2}$, and $\Delta\Phi_{jj} = \phi_{j_2} - \phi_{j_1}$ otherwise, where j_1 is the highest-p_{T} jet and j_2 is the next-highest-p_{T} jet in the event[21]. The distribution of the signed $\Delta\Phi_{jj}$ observable is presented in Figure 19 for different CP hypotheses.

In a recent study, the ATLAS collaboration has set constraints on the CP-mixing angle α by probing the shape of the signed azimuthal angle difference $\Delta\Phi_{jj}$ between the two leading hadronic jets in selected $h \to WW^*(\to e\nu\mu\nu)jj$ events. The study is based on $36.1\,\mathrm{fb}^{-1}$ of $\sqrt{s} = 13\,\mathrm{TeV}$ pp collisions [107], and exploits new analysis techniques for enhancing the sensitivity to interference effects between the CP-even and CP-odd contributions to the effective Higgs–gluon coupling. These new techniques offer the potential to improve the results from previous studies on the CP nature of the effective Higgs–gluon interaction [144, 145, 146].

The analysis is performed on events consistent with the $h\,(\to WW^* \to e\nu\mu\nu)$ + 2 jets final state. Thus, events that contain exactly two charged leptons of different flavors and at least two jets are considered. Further selection requirements are placed on the candidate events to reduce background contributions. To reduce backgrounds from top-quark production, events are vetoed if they contain a b-tagged jet with a p_{T} larger than 20 GeV. The $Z(\to \tau\tau)$ + jets background is reduced by requiring $m_{\tau\tau} < 66$ GeV. In addition, loose selection requirements are placed on the transverse dilepton momentum, the invariant dilepton mass, and the transverse mass of the Higgs boson candidate. The purpose of these requirements is to simply remove regions of phase space without significant contributions from the signal process, while retaining as much statistics as possible for the training and optimisation of boosted decision trees (BDTs). These BDTs aim to distinguish between the signal process and the most dominant backgrounds based on six different input observables: the invariant di-lepton mass, the transverse mass, the transverse di-lepton momentum,

[21] Ordering the jets according to their pseudorapidity values (i.e. the "signing" of the $\Delta\Phi_{jj}$ observable) enhances the sensitive to CP-mixed states as it prevents cancellations of quantum interference effects between the CP-even and CP-odd components. As a consequence, the $\Delta\Phi_{jj}$ distribution of a CP-mixed state is asymmetrically shifted [139] with respect to the distribution of a pure CP-even or CP-odd state.

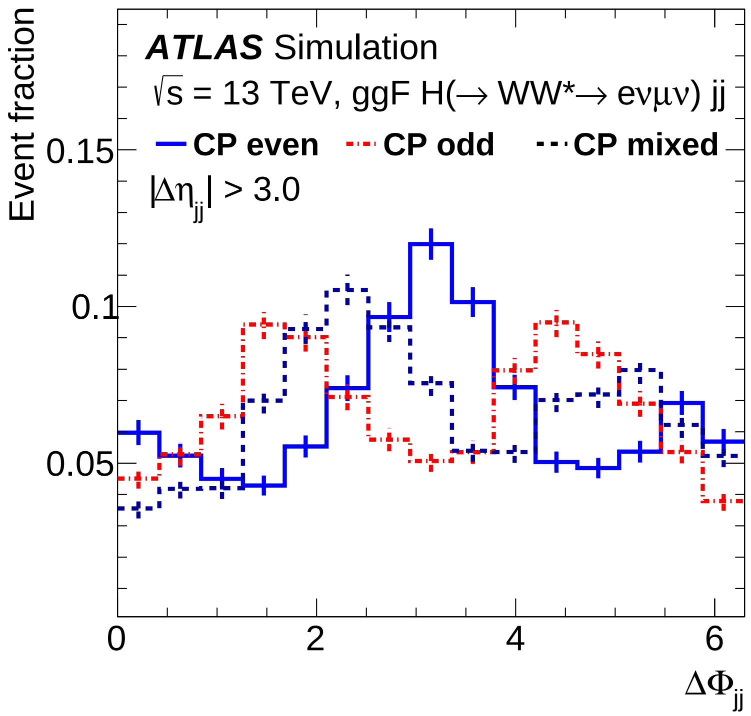

Figure 19: Distributions of the signed $\Delta\Phi_{jj}$ observable shown for CP-even (with $\kappa_{gg} = 1$ and $\cos(\alpha) = 1$), CP-odd (with $\kappa_{gg} = 1$ and $\cos(\alpha) = 0$) and CP-mixed (with $\kappa_{gg} = 1$ and $\cos(\alpha) = \frac{1}{\sqrt{2}}$) benchmark models of the ggF + 2 jets production mode. These comparisons are performed at the generator level using the predictions of the MadGraph5_aMC@NLO 2.4.2 + Pythia 8.212 [143] generators. The $\Delta\Phi_{jj}$ observable is asymmetric due to the interference effects between CP-even and CP-odd contributions.

the azimuthal angle between the two leptons, and the minimum distance between the leading lepton and the two tagging jets as well as the minimum distance between the subleading lepton and the two tagging jets. The training sample consists of simulated ggF + 2 jets events used as signal and the sum of the top quark, di-boson and Z+jets processes as background. The BDT score distribution, presented in Figure 20, provides a significant separation between the signal and the backgrounds. The BDT-score distribution is divided into four intervals: $[-1, 0.1)$, $(0.1, 0.4)$, $(0.4, 0.7)$, and $(0.7, 1.0]$. Background events are most likely to have BDT-score values in the first interval, while signal events are more likely to have BDT-score values in the last three intervals.

The most dominant background contributions stem from the production of top-quark pairs and single top quarks (Wt), non-resonant di-boson production (WW, WZ, ZZ), and Drell-Yan Z/γ^* (primarily from $Z \to \tau\tau$ decays). Other significant background contributions arise from W+jets and multi-jet production with misidentified leptons, which originate either from decays of heavy-flavour hadrons or from jets mimicking prompt-lepton signatures in the detector. This misidentified lepton background is estimated with a data-driven technique [111]. All other backgrounds are estimated using Monte Carlo simulations, where the normalisation of the combined $t\bar{t}$ and Wt backgrounds, WW+jets production and the $Z(\to \tau\tau)$+jets production process are determine via data exploiting dedicated control regions. The control regions are obtained by inverting specific selection requirements to ensure that they do not overlap with the signal regions. In this context, a top quark control region is obtained by requiring exactly one b-tagged jet with a p_{T} large

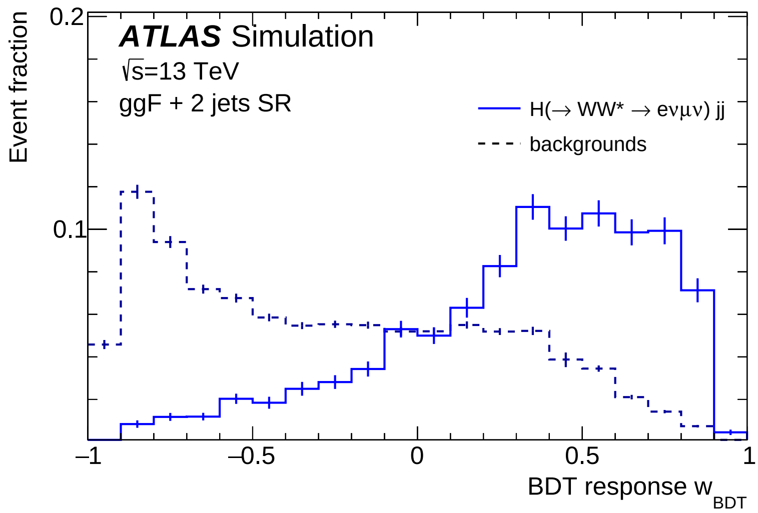

Figure 20: Shape comparison of the BDT response w_{BDT} distribution between $h(\to WW^* \to e\nu\mu\nu)$ + 2 jets events and the sum of backgrounds. The distribution for H + 2 jets represents the sum of events produced via the ggF +2 jets and VBF production modes. Both distributions are normalised to unit area.

than 30 GeV. A $Z \to \tau\tau$ control region is obtained by requiring events to have a $m_{\tau\tau}$ value in a window of 25 GeV around the Z boson pole mass, and a WW enriched control region is obtained by inverting the selection requirements on the invariant dilepton mass.

The final results are obtained by performing maximum likelihood fits based on the signed $\Delta\Phi_{jj}$ observable, which is presented in Figure 21. To optimise the sensitivity of the analysis, the distribution of the signed $\Delta\Phi_{jj}$ is probed separately in 12 disjoint kinematic regions. These regions are obtained by splitting the signal region into three BDT score intervals times four $|\Delta\eta_{jj}|$ intervals. The split into BDT score regions aims to maximise the signal to background ratio, while the split into $|\Delta\eta_{jj}|$ regions is motivated by the fact that signal contributions from diagrams with gluon exchange in the t-channel (i.e. the subprocess that is particularly sensitive to the CP properties of the Higgs boson) are enhanced at large $|\Delta\eta_{jj}|$ values. The bin boundaries for the BDT score and $|\Delta\eta_{jj}|$ intervals are $[0.1, 0.4, 0.7, 1.0]$ and $[0.0, 1.0, 2.0, 3.0, \infty]$, respectively. In addition, the event yields from the top, $Z \to \tau\tau$ and WW control regions, as well as the low-BDT-score intervals (i.e. $w_{BDT} \in [-1.0, -0.3]$ and $w_{BDT} \in [-0.3, 0.1]$) per $|\Delta\eta_{jj}|$ region are included in the maximum likelihood fit. The use of control regions and the low-BDT-score intervals in the fit are crucial, as they provide constraints on the normalisations of the dominant top quark, Z+jets and WW+jets backgrounds. Furthermore, the top and WW control regions help to reduce the impact of the b-tagging uncertainties.

Different types of fit configurations are used to constrain the CP mixing angle α. In one of the fit configurations, the normalisation of the signal process is unconstrained, i.e. freely floating, such that only shape information of the signed $\Delta\Phi_{jj}$ distribution is used to distinguish between different CP scenarios. In another fit configuration, the signal normalisation is constrained to the predictions of the Higgs Characterisation model. Thus, both the shape and rate information are used by the fit to distinguish between different CP scenarios. The results are presented as negative log-likelihood (NLL) curves, which are functions of the CP mixing angle. Each point on the likelihood curve corresponds to a separate fit to data. For each fit, the signal templates of the signed $\Delta\Phi_{jj}$ distributions are varied based on the tested α value, while the background prediction is only affected by changes to nuisance parameters in the minimisation procedure. The best estimate of α is obtained at the point where the NLL curve reaches its minimum. In addition, central confidence intervals at 68% (1σ) and 95% (2σ) are determined with respect to the minimum at the position where the likelihood curves reach values corresponding to 2ΔNLL equal 1 and 3.84, respectively. The values of the NLL are evaluated in steps of $\Delta\alpha = 4°$, and the minima of all fits are consistent with zero, i.e. the SM hypothesis.

If only the shape information is used, the 36.1 fb^{-1} of data are not sufficient to reach likelihood values corresponding to the 68% confidence level interval. If both shape and rate information are used, a best-fit value of $\alpha = 0° \pm 28°$ is obtained for both the fits to data and to the Asimov dataset as presented in Figure 22. The observed sensitivity is slightly worse than the expected sensitivity as the signal strength is found to be $\mu^{\text{ggF+2jets}} = 0.5^{+0.8}_{-0.7}$ (i.e. the rate of ggF+2jets events is smaller than expected). Hence, the fit to this dataset does not provide a 95% CL interval. The results are strongly limited by the statistical uncertainties, which are about a factor of 2 larger than each the experimental and the theoretical uncertainties. The largest experimental uncertainties are in the flavour-tagging, while the largest theoretical uncertainty is in the modelling of the top-quark backgrounds.

The CP properties of the top-quark Yukawa coupling have also been studied in $t\bar{t}h$ and th events. In events with $h \to \gamma\gamma$ decays, the CP mixing angle α has been measured to be $3°\,^{+25°}_{-21°}$ [133], while in events with $h \to b\bar{b}$ decays, α has been measured to be $11°\,^{+52°}_{-73°}$ [134]. All measurements are consistent with the SM predictions. While the precision of the measurements in $t\bar{t}h$ and th events is higher than the precision reached in ggF + 2 jets Higgs boson events[22], studying both channels is crucial given the fact that they are complementary as they probe different kinematic regimes. In addition, the properties of the effective ggH interaction itself may differ from SM predictions if there is a loop contribution from previously unobserved particles.

Further constraints on the CP properties of Higgs-fermion couplings, complementary to those obtained from $t\bar{t}h$, th, and ggF + 2 jets events, can be obtained from high-precision measurements of the electric dipole moment (EDM) [147]. Combined analyses of EDM measurements and direct measurements of the Higgs boson CP properties promise to further strengthen the existing constraints.

Personal contributions

The work on this analysis has been done in close collaboration with researches from the Dutch National Institute for Subatomic Physics (NIKHEF) in Amsterdam (where I was previously employed), Freiburg and DESY Hamburg. While the majority of studies leading to the publication in Reference [107] was done by our small analysis team, we also benefited greatly from the software developments, including work on the analysis framework and statistics tools, as well as the estimation of the misidentified lepton background, both of which were established for the measurements presented in Reference [111]. As this analysis was performed for the first time by any of the LHC experiments, the entire analysis strategy had to be developed from the ground up.

[22] It should be noted that with the current dataset size each of the three analyses still relies on using rate information to constrain the CP-mixing angle. As a consequence, the obtained results are strongly model dependent. A precise measurement of the mixing angle based only on shape information will only be feasible at the high-luminosity LHC.

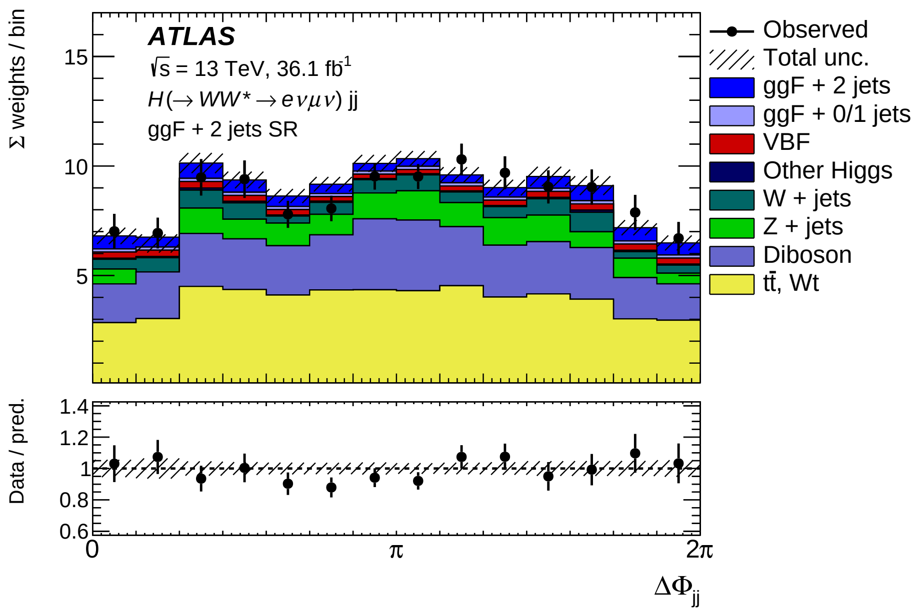

Figure 21: The weighted $\Delta\Phi_{jj}$ post-fit distribution in the ggF + 2 jets signal region, with signal and background yields fixed from the fit to the mixing angle α using shape and rate information. Data-to-simulation ratios are shown at the bottom of the plot. The shaded areas depict the total uncertainty. Events are weighted by $\ln(1 + N_S/N_B)$, where N_S (N_B) is the post-fit signal (background) event yield for each of the 12 kinematic regions, where the shape of the $\Delta\Phi_{jj}$ distribution is probed.

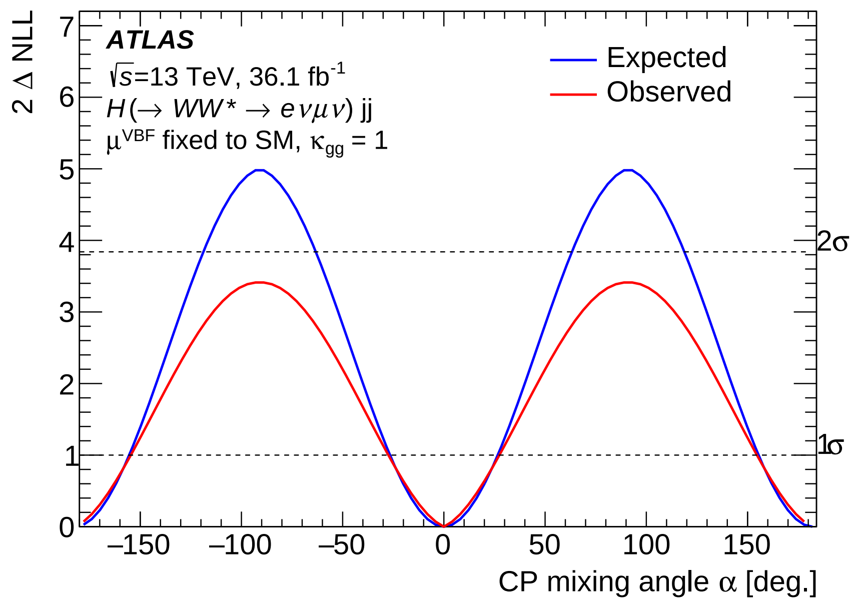

Figure 22: Expected and observed likelihood curves for scans over the CP mixing angle α from fits exploiting both shape and rate information.

My personal contributions to these efforts included the optimisation of the event selection and the design of the signal and control regions, training of the BDTs, modelling studies of the major backgrounds, calculation of experimental and theory uncertainties and the supervision of two PhD students from the NIKHEF group, who were mainly working on the likelihood fits and the optimisation of the binning of the fit input distributions. In addition, I was also the coordinator of the analysis efforts, responsible for assigning tasks, chairing meetings, and discussing the needs of our analysis with the coordinators of the $h \to WW^*$ group. Furthermore, I was the leading editor of the internal documentation and the manuscript submitted for journal publication.

Challenges

To finalise the analysis, we had to overcome several challenges. One particularly difficult task was to distinguish the $h(\to WW^* \to e\nu\mu\nu)jj$ signal process from contributions by the $t\bar{t} \to W^+bW^+\bar{b} \to e\nu\mu\nu bb$ and non-resonant $WW(\to e\nu\mu\nu)jj$ backgrounds, given their similar signatures in the detector. One obvious difference between the signal process and the $t\bar{t}$ background is the expected flavour content of their jets. While top quarks almost exclusively decay into a W boson and a bottom quark, the production of heavy-flavour quarks in association with a Higgs boson is strongly suppressed. Vetoing events containing b-tagged jets reduced the contributions from the $t\bar{t}$ background by around 94%, while having little impact on the signal process. However, the remaining number of $t\bar{t}$ events passing the b-tagging veto due to inefficiencies of the flavour-tagging algorithm were still about two orders of magnitues larger than the number of expected signal events. Hence, a sophisticated machine learning algorithm, i.e. BDTs, had to be developed to further reduce contributions from the $t\bar{t}$ background and from other background sources. To find the optimal setup for these BDTs, a variety of different observables and hyperparameter configurations were tested. The input observables to the training of the BDTs were not only chosen based on their potential to distinguish between the signal and the background processes, but were also required to have no significant correlation with the $\Delta\Phi_{jj}$ observable in order to prevent the BDTs from preferring one CP hypothesis over another. After testing dozens of different kinematic observables, a final set of six input quantities was chosen for the training of the BDTs. Applying these BDTs to the events that were passing the signal region requirements allowed us to define kinematic regions that had a significantly enhanced contribution of the signal process. E.g. in the BDT-score interval $(0.7, 1.0]$, the signal contribution was about 11%.

Given the large contributions from the $t\bar{t}$ background, a precise knowledge of its normalisation was most crucial to the measurements of the CP-mixing angle α. Therefore, it was important to define an appropriate top control region. Various control region definitions were compared, and the final choice was based on two requirements: (a) only few contributions from other background processes should pass the selection requirements, and (b) the control regions should be kinematically similar to the signal regions to ensure that extrapolation uncertainties between these regions are small. In this context, the requirements on the b-tag multiplicity and the jet p_{T} threshold of the b-tagged jet were changed with respect to the signal region definitions. The tested b-tag multiplicity requirements were: (a) exactly one b-tagged jet, (b) at least one b-tagged jet, and (c) at least two b-tagged jets. The possible p_{T} thresholds of these jets were either 20 GeV, 25 GeV or 30 GeV. These studies indicated that the smallest extrapolation uncertainties were obtained for a top control region defined with exactly one b-tagged jet having a p_{T} above 30 GeV.

Another challenge to overcome was the large amount of required Monte Carlo events related to the large number of different signal hypotheses that had to be tested. Each point on the likelihood curve in Figure 22 corresponds to a different signal hypothesis. To guarantee an appropriately fine scan over α, $\mathcal{O}(100)$ different signal samples were required corresponding to around 100 million simulated signal events (passing the full detector simulation). This large number of Monte Carlo simulations would have exceeded by far the computing resources available to our team. Instead of producing so many different Monte Carlo simulations, alternative methods had to be pursued. Hence, parameter morphing [148] was introduced into the workflow of the analysis, and used to interpolate from three distinct benchmark scenarios ($\cos(\alpha) = 1$, $\cos(\alpha) = 0$, and $\cos(\alpha) = \frac{1}{\sqrt{2}}$) to a large variety of signal hypotheses. The parameter morphing had to be carefully validated [149] before it was officially supported by the ATLAS collaboration.

Outlook

The reduction of contributions from the $t\bar{t}$ backgrounds will remain crucial for future measurements of the CP mixing angle (and other properties of the Higgs boson) in ggF+jets events. Given that the modelling uncertainties in the $t\bar{t}$ background are the leading systematic uncertainties in the measurement of the CP mixing angle, further reducing contributions from the $t\bar{t}$ backgrounds will be particularly important once the measurements are no longer statistically limited.

Improving the ATLAS flavour-tagging techniques appears to be a promising approach towards obtaining more precise measurements in the future. As indicated by the studies of a student, who I superviced in the context of a B.Sc. project, the background contributions from top quark pair production could be decreased by around 20%, if the p_{T} threshold of jets used for b-tagging could be lowered from 20 GeV to 15 GeV. Though, in order to implement such a change to the Higgs property measurements, the current ATLAS b-tagging calibration techniques would have to be extended to such low jet p_{T} values. Alternatively, newley developed tagging techniques for b-hadrons with transverse momenta too low to yield a calorimeter jet [150] could be used to reduce contributions of the $t\bar{t}$ background in which the heavy-flavour objects are below threshold. Furthermore, the studies of the B.Sc. student also pointed out that a significant fraction of $t\bar{t}$ events, currently passing the selection requirements of the ggF + 2 jets signal regions, posses at least one high-energy b-jet within the forward regions of the ATLAS detector. Thus, a further reduction of the $t\bar{t}$ background by about 60% could be obtained once the ATLAS inner tracker layout will be upgraded for the high-luminosity LHC operation [151]. This upgrade of the ATLAS ID will extend the current tracking and vertexing capabilities to the range $2.5 < |\eta| < 4.0$, and thus will enable the identification of heavy-flavour jets in the forward regions.

3.2.3 Study of the Higgs boson couplings to longitudinally and transversely polarised vector bosons

The Higgs boson couplings to vector bosons hVV (with $V = W, Z$) are sensitive to a variety of new physics effects. This has motivated numerous searches for anomalous contributions to the hVV vertex. In Run 1, these searches mainly focused on probing the $h \to WW^*$ and $h \to ZZ^*$ decays for BSM CP-even or CP-odd contributions to the hVV coupling [70]. Based on a dataset corresponding to 20 fb^{-1} of pp collisions at a center-of-mass energy of $\sqrt{s} = 8$ TeV, the spin and parity J^P of the Higgs boson was strongly indicated to be 0^+, while a pure BSM CP-even or CP-odd Higgs boson have been excluded at a confidence level above 99.9%.

Since the beginning of Run 2, searches for BSM contributions to the hVV coupling mainly focus on probing the VBF production process of the Higgs boson [131, 152, 130, 132]. Most of these studies aim to constrain CP-violating effects in the HVV coupling. In addition, the Higgs boson coupling properties to longitudinally and transversely polarised W and Z bosons can be probed in the VBF production mode. Such studies are of particular interest as they can help to further our understanding of the mechanism of electroweak symmetry breaking. According to the SM, the Higgs boson couples equally strong to longitudinally and transversely polarised vector bosons. However, if the Higgs boson were not a fundamental particle but a bound state, as predicted in e.g. Higgs compositeness models [153, 154], significant deviations with respect to the SM expectations may occur.

A first study of polarisation-dependent Higgs boson couplings to the massive electroweak gauge bosons were published by the ATLAS collaboration via [107]. These studies are based on data from pp collisions at a center-of-mass energy of 13 TeV and correspond to the data taking periods in 2015 and 2016 yielding an integrated luminosity of 36.1 fb^{-1}.

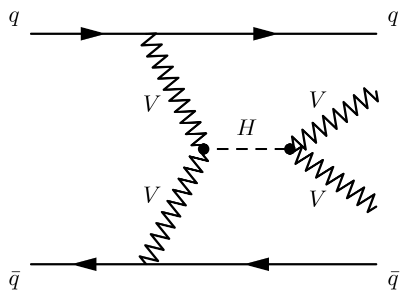

Figure 23: Example of a Feynman diagram contributing to the production of a Higgs boson in association with two jets via the fusion of two vector bosons (V) at leading order in QCD and subsequent decay of the Higgs boson into two vector bosons.

Signs for polarisation-dependent couplings between the Higgs boson and the W and Z bosons are searched for by setting constraints on polarisation-dependent coupling-strength scale factors, which are defined in Ref. [155] as

$$a_{\mathrm{L}} = \frac{g_{HV_{\mathrm{L}}V_{\mathrm{L}}}}{g_{HVV}}\,, \; a_{\mathrm{T}} = \frac{g_{HV_{\mathrm{T}}V_{\mathrm{T}}}}{g_{HVV}}\,, \tag{4}$$

with g_{HVV} being the SM HVV coupling strength, while $g_{HV_{\mathrm{L}}V_{\mathrm{L}}}$ and $g_{HV_{\mathrm{T}}V_{\mathrm{T}}}$ are the measured polarisation-dependent couplings. According to the SM, a_{L} and a_{T} are equal to unity. Since the polarisations depend on the measurement frame, the above description is not Lorentz invariant and as such cannot be described in the Lagrangian framework. Instead, the parameters a_{L} and a_{T} can be mapped to pseudo-observables (POs), following the arguments in Reference [156]:

$$\kappa_{VV} \simeq a_{\mathrm{L}}\,, \quad \varepsilon_{VV} \simeq 0.5 \cdot (a_{\mathrm{T}} - a_{\mathrm{L}})\,.$$

The kinematic distributions of the two jets produced in association to the Higgs boson are related to the intrinsic structure of the Higgs boson production vertex and carry information about the polarisation of the fusing gauge bosons. Hence, variations in a_{L} and a_{T} (and by construction also κ_{VV} and ε_{VV}) with respect to the SM expectations will lead to a shape modulation of distributions such as the $\Delta\Phi_{jj}$, as shown in Figure 24. In addition, the total production cross section of the Higgs boson is particularly sensetive to variations in the parameters a_{L} and κ_{VV} given that longitudinal polarisation vectors of the massive gauge bosons are proportional to the energy transfer. The polarisation-dependent Higgs boson couplings to the massive vector bosons are therefore constrained by exploiting both the rates of the VBF Higgs boson production process as well as the distribution of the signed $\Delta\Phi_{jj}$ observable, where the SM expectations are compared and tested against a large variety of different a_{L}, a_{T}, κ_{VV} and ε_{VV} parameter choices.

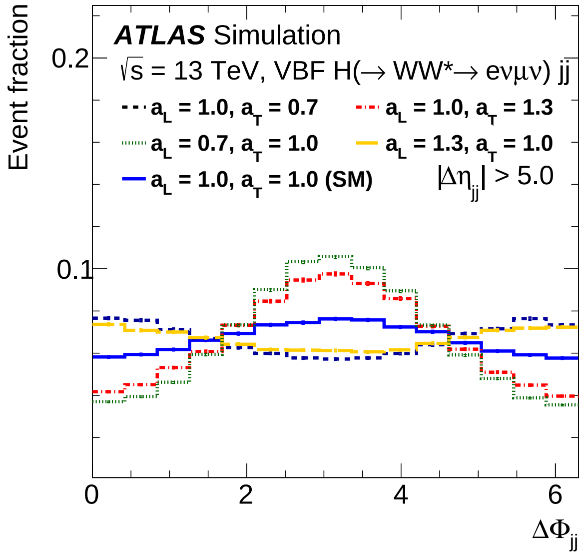

Figure 24: Distributions of the signed $\Delta\Phi_{jj}$ observable shown for various configurations of the $a_{\rm L}$ and $a_{\rm T}$ parameters in VBF events. These comparisons are performed at the generator level using the predictions of the MadGraph5_aMC@NLO 2.4.2 + Pythia 8.212 [143] generators.

The analysis is performed on events that resemble the $h\,(\rightarrow WW^* \rightarrow e\nu\mu\nu)$ + 2 jets final state [111, 107]. Events are retained for further analysis if they contain exactly two charged leptons of different flavour and at least two jets being emitted in opposite hemispheres. To suppress contributions from ggF + 2 jets production, candidate events are not allowed to have hadronic activity in the central region of the detector (i.e. a central jet veto is applied). Contributions from top-quark pairs are reduced by vetoing events containing any b-tagged jet. In addition, boosted decision trees (BDTs) are used to further distinguish between the signal and the various background processes. These boosted decision trees are trained exploiting information from observables such as the invariant di-jet and di-lepton masses, the transverse Higgs boson mass, the rapidity difference between the two jets, and the lepton centralities, which quantify the position of the charged leptons relative to the two VBF jets. The BDT-score distribution is divided into four disjoint categories defined by the intervals $[-1, 0.26, 0.61, 0.86, 1]$. The intervals corresponding to low values of the BDT score are strongly dominated by the backgrounds, while intervales corresponding to higher values of the BDT score have significant contributions from the signal process and relative low contributions from the backgrounds (as shown in Figure 25).

The most dominant background contributions stem from the production of top-quark pairs and single top quarks (Wt), non-resonant di-boson production (WW, WZ, ZZ), and Drell-Yan Z/γ^* (primarily from $Z \rightarrow \tau\tau$ decays). Other significant background contributions arise from W+jets and multi-jet production with misidentified leptons, which originate either from decays of heavy-flavour hadrons or from jets mimicking prompt-lepton signatures in the detector. This misidentified lepton background is estimated with a data-driven technique [111]. All other backgrounds are estimated using Monte Carlo simulations, where the normalisation of the combined $t\bar{t}$ and Wt backgrounds, and the $Z(\rightarrow \tau\tau)$+jets production process are determine via data exploiting dedicated control regions.

The final results are obtained by performing maximum likelihood fits based on the signed $\Delta\Phi_{jj}$ observable (see Figure 26), which is probed separately in each of the four BDT-score intervals within the VBF signal

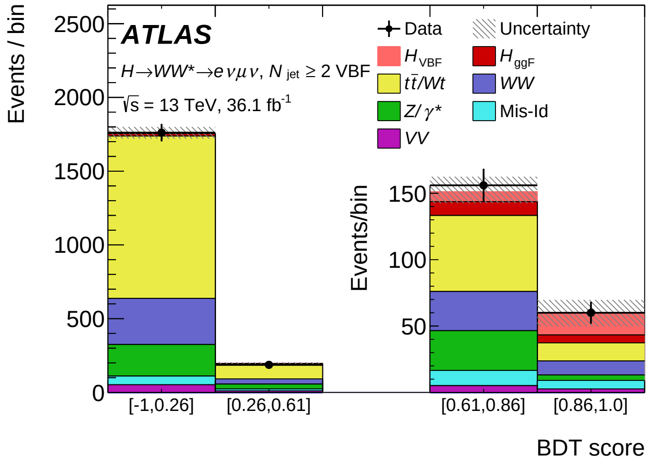

Figure 25: Post-fit distribution of the BDT score showing the signal and background contributions in the VBF signal region. The hatched band shows the total uncertainty of the signal and background processes [111].

region, as well as the signal and background yields in the top quark and $Z \to \tau\tau$ control regions. Different types of fit configurations are used to constrain the parameters of interest, i.e. the $(a_{\mathrm{L}}, a_{\mathrm{T}})$ and $(\kappa_{VV}, \varepsilon_{VV})$. In each fit, a wide range of coupling parameter (or pseudo-observable) hypothesis are probed aiming to find the value that fits the data best. In one configuration, one-dimensional fits are carried out scanning over one of the two parameters, while fixing the other parameter to its SM value. In the other configuration, fits to one parameter are performed with the other being profiled, i.e.the other parameter is allowed to vary independently. These fits are performed exploiting either only the dependence of the input distribution's shape on the selected parameter of interest or both shape and rate information.

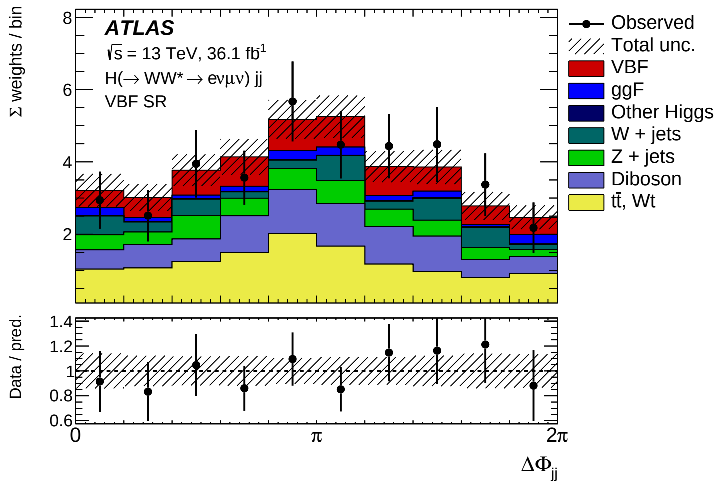

Figure 26: The weighted $\Delta\Phi_{jj}$ distribution in the VBF signal region, with signal and background yields fixed from the fit for ε_{VV} using shape and rate information. Data-to-simulation ratios are shown at the bottom of the plot. The shaded areas depict the total uncertainty.

The results are presented as negative log-likelihood (NLL) curves, which are functions of the relevant coupling parameters (or pseudo-observables). These curves are presented in Figures 27 and 28. The best estimate for the parameter of interest is obtained at the point where the NLL curve reaches its minimum.

In addition, central confidence intervals at 68% (1σ) and 95% (2σ) at the positions where the likelihood curves reach values corresponding to 2ΔNLL = 1 and 3.84, respectively.

In the one-dimensional likelihood fits, where the other parameter was set to its SM value, shape information is sufficient to constrain the coupling to transversely polarised vector bosons as shown in Figure 27 (a). With this fit configuration $a_{\mathrm{T}} = 1.3^{+0.8}_{-0.4}$(stat.)$^{+0.3}_{-0.2}$(syst.) is obtained. In all other fit configurations, informations from both shape and rate are required to constrain the parameters of interest[23]. When using both shape and rate information, $a_{\mathrm{T}} = 1.19^{+0.27}_{-0.32}$(stat.)$^{+0.12}_{-0.14}$(syst.) and $a_{\mathrm{L}} = 0.90^{+0.09}_{-0.13}$(stat.)$^{+0.08}_{-0.18}$(syst.) are obtained. With an approximate mapping to pseudo-observables the following constraints are obtained in a fit where one parameter is scanned and the other parameter is profiled: $\kappa_{VV} = 0.91^{+0.10}_{-0.18}$(stat.)$^{+0.09}_{-0.17}$(syst.) and $\varepsilon_{VV} = 0.13^{+0.28}_{-0.20}$(stat.)$^{+0.08}_{-0.10}$(syst.). All measurements are consistent with the expectations for the SM Higgs boson. The dominant sources of uncertainty are related to the limited data statistics and to the uncertainties in modelling of backgrounds from the top-quark pair and non-resonant WW production. The impact of other systematic uncertainties is significantly smaller.

Further results from this study are presented in Reference [107].

Personal contributions

The studies of the Higgs boson couplings to longitudinally and transversely polarised vector bosons were conducted by a team of researchers from NIKHEF, the University of Freiburg, DESY Hamburg, the Institute of Nuclear Physics in Cracow (IFJ PAN), and myself. The analysis team was almost identical to the one that performed the CP studies of the effective Higgs-gluon interaction. Since both analyses were performed in the same final state, many tasks and challenges were common to both analysis efforts, so personnel and resources were shared.

I made significant contributions to these efforts. As the coordinator of this analysis, I assigned tasks, chaired meetings, and discussed the needs of our analysis with the coordinators of the physics group for Higgs boson property measurements. I also supported and guided a Ph.D. student from the NIKHEF group who produced and validated signal samples, validated the modelling of the dominant background processes, and worked on the statistical interpretation of the analysis results. Additionally, I helped to evaluate the modelling uncertainties of the major backgrounds.

Challenges

Similar to the CP studies, these measurements were the first of their kind at the LHC. However, unlike the CP studies, the analysis strategy did not need to be developed from scratch. This is because the VBF signal and control region definitions and the BDT training could be reused from an existing measurement of the Higgs boson production cross section in the VBF production mode [111]. However, modeifications to the background model were required since we studied the $\Delta\Phi_{jj}$ observable in all four categories of the BDT score distribution, while the cross section measurement only used the signal and background yields to these regions.

Understanding the modelling of the $\Delta\Phi_{jj}$ distribution in the four BDT score intervals was one of the most challenging tasks of this analysis. A particular challenge was the known mismodelling of the Z+jets back-

[23] Using rate information adds a certain degree of model dependence, as the rate can be affected by BSM effects beyond the scope of this analysis. Thus, performing fits based only on the shape of the the input distribution are generally preferred.

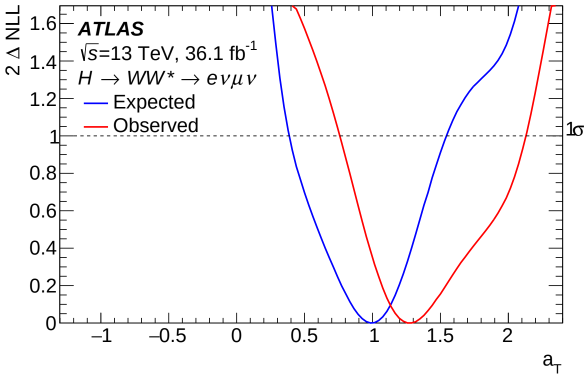

(a) a_{T} shape only fit with $a_{\mathrm{L}} = 1$

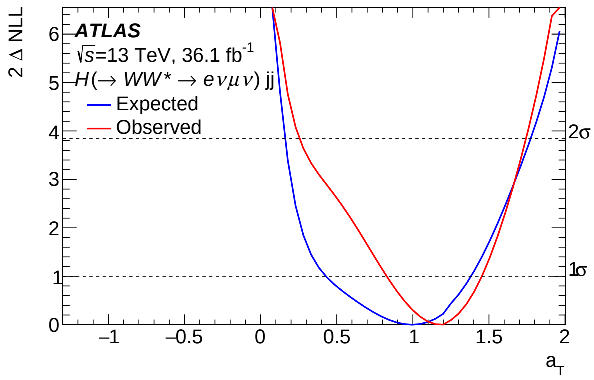

(b) a_{T} shape+rate fit with $a_{\mathrm{L}} = 1$

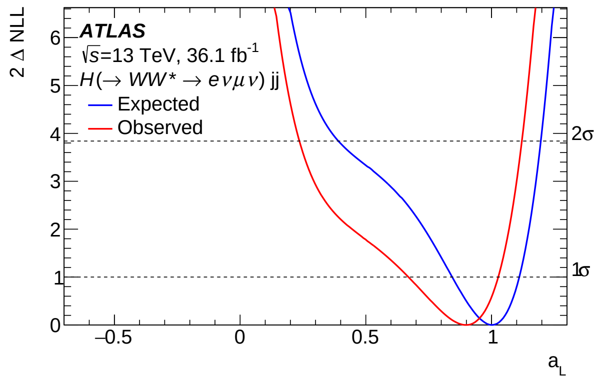

(c) a_{L} shape+rate fit with $a_{\mathrm{T}} = 1$

Figure 27: Likelihood scans over the transversely (a) and longitudinally (b) polarised couplings. Fits using shape+rate information are shown. All relevant experimental and theoretical systematic uncertainties are considered in the fits.

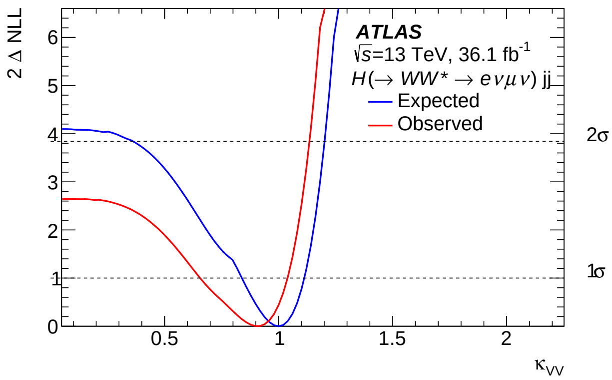

(a) κ_{VV} shape+rate fit with profiled ε_{VV}

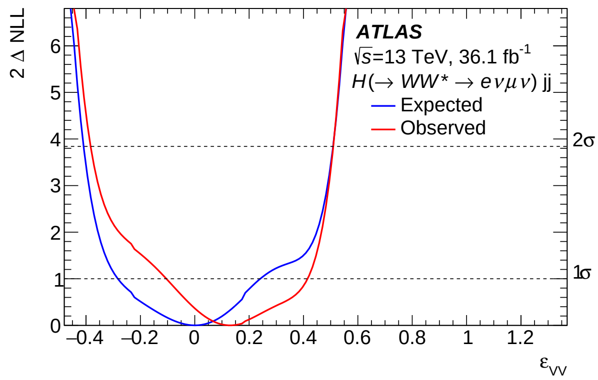

(b) ε_{VV} shape+rate fit with profiled κ_{VV}

Figure 28: Likelihood scans over (a) κ_{VV} and (b) ε_{VV}, with the other parameter profiled. The fits are performed using both shape and rate information. All relevant experimental and theoretical systematic uncertainties are considered in the fits.

ground for large $\Delta\eta_{jj}$ values, where the default Monte Carlo generator for Z+jets backgrounds, SHERPA 2.2.1, severely overshoots the data [157]. To mitigate this mismodelling, we introduced additional nuisance parameters to the likelihood fit to modulate the shapes of the $\Delta\Phi_{jj}$ and BDT response distributions of all backgrounds. We obtained these shapes uncertainties by reweighting the di-jet invariant mass spectrum such that the data and simulations agreed[24]. We then compared the $\Delta\Phi_{jj}$ and BDT response distributions before and after the reweighting was applied, and took their difference as an uncertainty.

3.3 Combination of Higgs boson coupling property measurements

Ten years after its discovery, the Higgs boson's properties have been measured with unprecedented precision in almost all dominant production modes and decay channels. Its couplings to vector bosons and third-generation leptons and quarks agree well with the predictions of the Standard Model. In the next few years, the ATLAS and CMS collaborations expect to measure the Higgs boson's couplings to second-generation leptons, as they have recently achieved significances ranging from 2.0σ to 3.0σ in their searches for the $h \to \mu^{\pm}\mu^{\mp}$ decay mode [158, 159]. Furthermore, ATLAS and CMS have set strong upper limits at 95% confidence level on the product of the cross section and branching ratio for the $pp \to h \to Z\gamma$ production mode. Observed (expected) upper limits by ATLAS are 3.6 (2.4) times larger than the Standard Model predictions, while the observed (expected) upper limits by CMS are 4.1 (1.8) times larger. Thus, the discovery of the $pp \to h \to Z\gamma$ decay channel is also just a matter of a few more years of data taking.

The ATLAS and CMS collaborations recently published a detailed map of the measured Higgs boson properties [75, 76]. These publications focused on the statistical combinations of individual Higgs boson property measurements. The combination procedure is based on simultaneous fits to all relevant production and decay modes to maximise the use of the available data. Because the individual analyses are complementary, the statistical combinations significantly strengthen the constraints on the Higgs boson properties.

The combined cross section measurements are based on results from studies of $h \to b\bar{b}$ [160, 161, 162, 163], $h \to WW^* \to \ell^{\pm}\nu\ell^{\mp}\nu$ [103, 104], $h \to \tau^+\tau^-$ [114], $h \to \gamma\gamma$ [29], $h \to ZZ^* \to \ell^+\ell^-\ell^+\ell^-$ [113], $h \to Z\gamma \to \ell^+\ell^-\gamma$ [164] and $h \to \mu^+\mu^-$ [158] decays[25], which are based on the full set of Run 2 data. For these studies the ggF, VBF, Wh, Zh, $t\bar{t}h$, and th production modes of the Higgs boson are taken into account[26].

Assuming that all production and decay modes scale with the same global signal strength[27], the inclusive Higgs boson production rate relative to the SM prediction is measured to be

$$\mu = 1.05 \pm 0.06 = 1.05 \pm 0.03(\text{stat.}) \pm 0.03(\text{exp. syst.}) \pm 0.04(\text{sig. theo.}) \pm 0.02(\text{bkg. theo.})$$

The total uncertainty of this measurement are decomposed into components for statistical uncertainties, experimental uncertainties, and theory uncertainties in the modelling of the signal and background pro-

[24] The non-closure between data and simulations is on the order of a few percent at low m_{jj} values, and ranges up to 15% for m_{jj} values above 1 TeV.

[25] The relative weight of each measurement depends on its precision. I.e. the more precise a measurement is, the stronger it contributes to the combined result.

[26] The $b\bar{b}h$ process is experimentally indistinguishable from ggF production as the associated b-jets are emitted into the forward region of the detector, where the b-tagging efficiencies are low. Thus, the $b\bar{b}h$ and ggF processes are grouped together, with $b\bar{b}h$ contributing by about 1%.

[27] The Higgs boson production is also studied separately for each production mode. The results are presented in Reference [75].

cesses. A similar combination of the inclusive Higgs boson production cross sections has recently been performed by the CMS collaboration [76] yielding a global signal strength of

$$\mu = 1.00 \pm 0.06 = 1.00 \pm 0.03(\text{stat.}) \pm 0.03(\text{exp. syst.}) \pm 0.04(\text{sig. theo.}),$$

which is compatible to the ATLAS results within the uncertainties. For the combined measurements from both ATLAS and CMS, the experimental and theoretical uncertainties are decreased by almost a factor of 2.0 with respect to those in the Run 1 result [80], while the statistical uncertainties are decreased by a factor of 2.3. Overall, the total uncertainties in the new combined measurements are decreased by a factor of around 4.5 compared to the Run 1 results. By now, the measurements of inclusive Higgs boson production cross sections are no longer statistically limited. Hence, future measurements require a more precise description of the signal processes and the relevant backgrounds in order to significantly improve the latest results.

Figure 29 shows the results of the combined production cross section measurements and the combined branching ratio measurements. For the gluon-gluon fusion (ggF) and vector boson fusion (VBF) production modes, which were already observed during Run 1 of the LHC, the cross sections are measured with a precision of 7% and 12%, respectively. In addition, the newest combined measurements now also lead to observations of the Wh, Zh, and the $t\bar{t}h + th$ production modes, which are observed (expected) with significances of 5.8σ (5.1σ), 5.0σ (5.5σ), and 6.4σ (6.6σ), respectively.

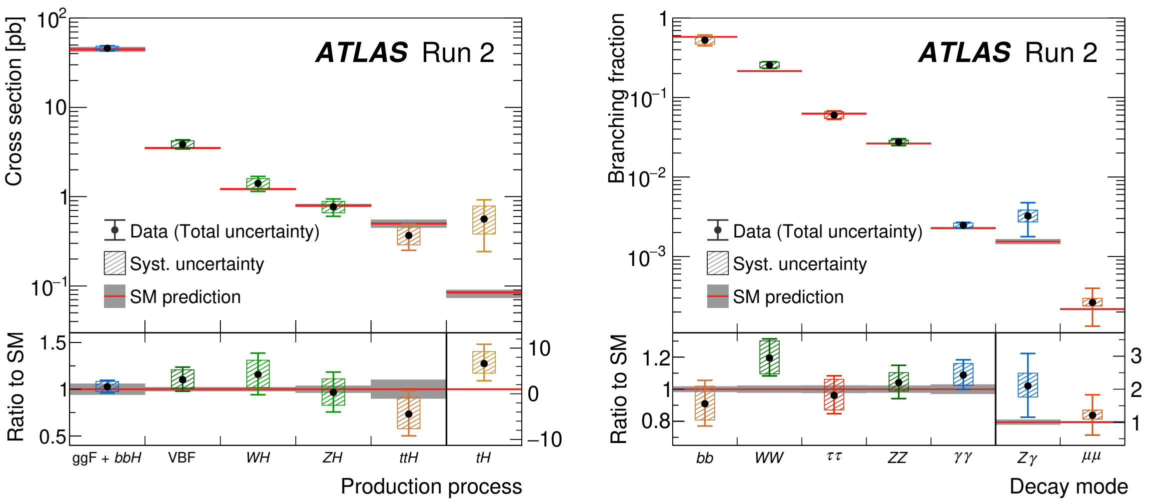

(a) (b)

Figure 29: Observed and predicted Higgs boson production cross-sections and branching fractions. (a) the cross sections for the different Higgs boson production modes are measured assuming SM values for the branching ratios. (b) the branching ratios for different Higgs boson decay modes are measured assuming SM values for the production cross sections. The lower panels show the ratios of the measured values to their SM predictions. The combined p-value indicating the compatibility of the measurement and the SM prediction is 65% for the cross section measurements and 56% for the branching ratio measurements [75].

The latest combined measurement of kinematic properties of the Higgs boson production is based on individual measurements for all relevant production processes using the STXS framework. Depending on the available statistics, the cross sections are probed for disjoint kinematic regions, which are defined separately for each production process based on the jet multiplicity, the transverse momentum of the Higgs boson (p_{T}), the momentum of vector bosons (p_{T}^{W} and p_{T}^{Z}) and the invariant di-jet mass (m_{jj}). In total, 36 independent measurements are performed (see Figure 30), which are all consistent with the SM predictions.

Compared to previous results based on a partial Run 2 dataset [165], a significantly larger number of kinematic regions are probed. In particular, the granularity of regions targeting Higgs bosons with a high transverse momentum was increased. Events containing such highly boosted Higgs bosons are considered to be particularly important given their enhanced sensitivity to BSM effects [166]. As a consequence, it can be expected that more effort will be made in the near future to develop dedicated reconstruction algorithms for identifying highly Lorentz-boosted Higgs boson decays.

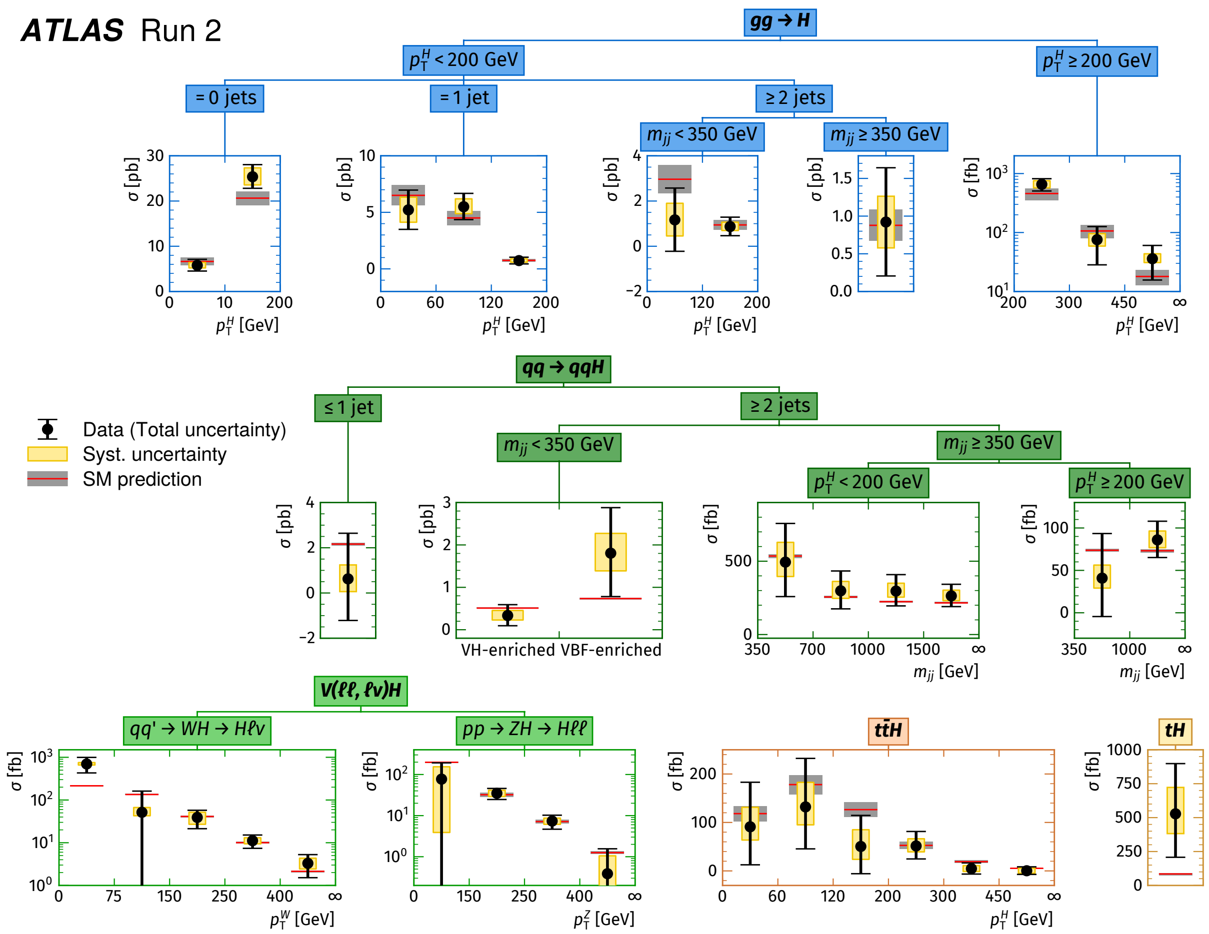

Figure 30: Observed and predicted Higgs boson production cross sections presented in different kinematic regions [75]. The vertical bar on each point represents the 68% confidence interval [75].

The combined measurements of Higgs boson production cross-sections, simplified template cross-sections, fiducial differential cross-sections, and decay rate measurements are commonly used to constrain Wilson coefficients in effective field theories and UV-complete extensions such as the two-Higgs-doublet model and the Minimal Supersymmetric Standard Model. The most recent results of such interpretations are reported in Reference [167].

4 Recent searches for new heavy di-boson resonances

Direct searches for new particles and phenomena beyond the Standard Model have been a major focus of particle physics experiments in recent years. One particularly active area is the search for di-boson resonances, i.e. new heavy particles decaying into a pair of bosons such as WW, WZ, ZZ, Wh, Zh, or $\gamma\gamma$. Examples of BSM theories that predict di-boson resonances are composite Higgs models [168, 169], technicolour models [170, 171], or warped extra dimensions [172, 173]. These models are theoretically well motivated as they offer solutions to the naturalness problem. Di-boson resonances are also predicted in models with an extended scalar sector [127, 174].

By now, a diverse set of characteristic final states including di-photon, multi-lepton, lepton + jets, and multi-jet signatures is used to search for di-boson resonances [175] and to constrain theories predicting BSM physics.

Depending on the specific BSM scenario that is investigated, a di-boson resonance can be produced through various mechanisms: gluon–gluon fusion (ggF), quark-antiquark annihilation (qqA), bottom-quark and/or top-quark associated production ($b\bar{b}X$, $t\bar{t}X$, or $b\bar{t}H^+$), vector-boson associated production, or vector-boson fusion (VBF). Figure 31 presents representative lowest order Feynman diagrams for these production processes.

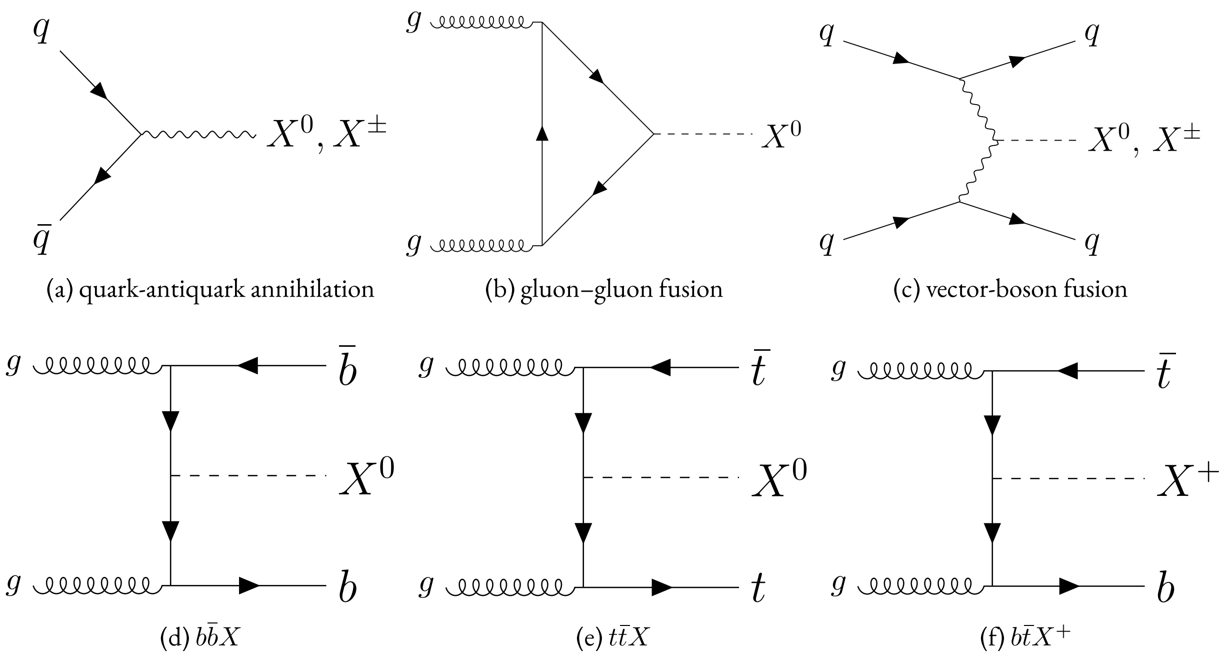

(a) quark-antiquark annihilation (b) gluon–gluon fusion (c) vector-boson fusion

(d) $b\bar{b}X$ (e) $t\bar{t}X$ (f) $b\bar{t}X^+$

Figure 31: Representative lowest order Feynman diagrams for possible production modes of BSM particles at the LHC.

An extensive overview of recent searches for di-boson resonances at the LHC is given in Table 2. These searches cover relevant production modes and a diverse set of different final states. The table also highlights which spin hypotheses are covered by each analysis.

Table 2: Recent di-boson resonance searches performed by the ATLAS and CMS experiments.

Production mode	Decay channel	Spin-0	Spin-1	Spin-2	Reference
ggF, VBF	$ZZ \to \ell^\pm\ell^\mp\ell^\pm\ell^\mp$	✓	–	✓	[176, 177]
ggF, VBF	$ZZ \to \nu\nu\ell^\pm\ell^\mp$	✓	–	✓	[176, 177]
ggF, qqA, VBF	$W^\pm W^\mp \to \ell^\pm\nu\ell^\mp\nu$	✓	✓	✓	[178, 179]
VBF	$W^\pm W^\pm \to \ell^\pm\nu\ell^\pm\nu$	✓	–	–	[180]
qqA, VBF	$W^\pm Z \to \ell^\pm\nu\ell^\pm\ell^\mp$	✓	✓	–	[181]
ggF, qqA	$W^\pm W^\pm/W^\mp Z/ZZ \to q\bar{q}q\bar{q}$	✓	✓	✓	[182, 183, 184]
ggF, qqA, VBF	$W^\pm Z/ZZ \to \nu\nu q\bar{q}$	✓	✓	✓	[185, 186]
ggF, qqA, VBF	$W^\pm W^\mp/W^\pm Z \to \ell^\pm\nu q\bar{q}$	✓	✓	✓	[185, 187, 188, 179]
ggF, qqA, VBF	$WZ/ZZ \to \ell^\pm\ell^\mp q\bar{q}$	✓	✓	✓	[185, 177]
qqA	$Wh/Zh \to q\bar{q}b\bar{b}$	–	✓	–	[189, 184]
ggF, qqA, $b\bar{b}X$, VBF	$Zh \to \nu\nu b\bar{b}$	✓	✓	–	[190, 191]
qqA, VBF	$Wh \to \ell^\pm\nu b\bar{b}$	–	✓	–	[190, 188]
ggF, qqA, $b\bar{b}X$, VBF	$Zh \to \ell^\pm\ell^\mp b\bar{b}$	✓	✓	–	[190, 191]
ggF, $b\bar{b}X$	$Zh \to \ell^\pm\ell^\mp\tau^\pm\tau^\mp$	✓	–	–	[192]
ggF, VBF	$\gamma\gamma$	✓	–	✓	[193, 194, 195]
ggF, qqA	$Z\gamma \to \ell^\pm\ell^\mp\gamma$	✓	–	✓	[196]
ggF, qqA	$Z\gamma/W\gamma \to q\bar{q}\gamma$	✓	✓	✓	[197, 198]
qqA	$h\gamma \to b\bar{b}\gamma$	–	✓	–	[199, 200]

These searches are typically designed to be as model independent as possible. This is achieved by probing for a localised excess in a characteristic distribution such as the invariant or transverse mass of the relevant final state particles (see Figure 32). In the absence of strong indications for contributions by a signal process, upper limits on the production cross section and/or branching ratio are set at the 95% confidence level (CL). The upper limits are typically evaluated using a modified frequentist method known as CL_S [201] and a profile-likelihood-ratio test statistic using either an asymptotic approximation approach [202] or pseudo-experiments if necessary. The results are derived independently for different production modes, spin and CP hypotheses, and are subsequently interpreted in the context of simplified theories. Some of the most commonly used BSM theories are briefly introduced in Section 4.1.

The following sections present a representative selection of recent results on searches for new heavy di-boson resonances based on proton–proton collision data at $\sqrt{s} = 13$ TeV, with the full Run 2 dataset collected by the ATLAS detector. Sections 4.2 and 4.3 describe searches performed by the ATLAS collaboration that I have been leading recently. These searches probe for new heavy particles that decay into a Higgs boson and a vector boson V (with $V = W$ or Z). Further prominent di-boson resonance searches are briefly discussed in Section 4.4. Most of these efforts were carried out, while I was the coordinator of the ATLAS di-boson resonance searches. A statistical combination of di-boson, di-lepton and di-quark searches is described in Section 4.5, while Section 4.6 gives a brief outlook into future developments within the field.

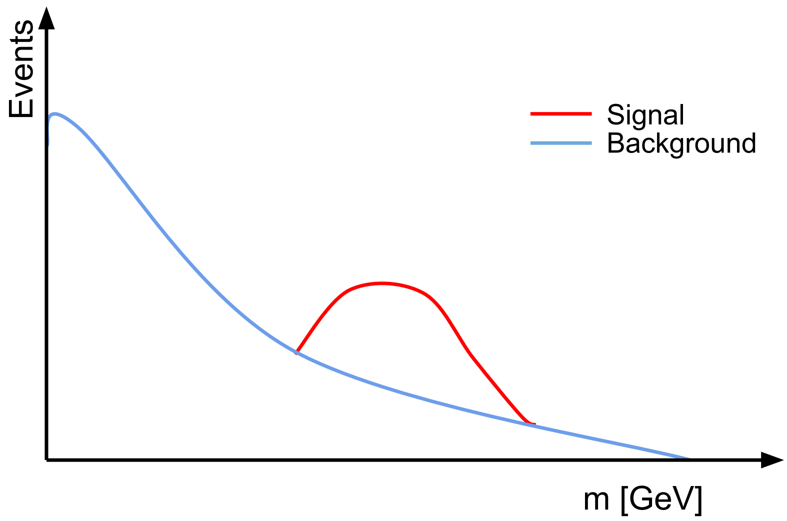

Figure 32: A schematic representation of a resonant signal over the smoothly falling mass spectrum of a background process.

4.1 Simplified Models

Resonance searches are typically not sensitive to all of the free parameters of an underlying theory. Instead, they are only sensitive to those parameters or combination of parameters that control the mass and width of the resonance, as well as the interactions involved in its production and decay mode. This allows for the use of simplified models, which are described by phenomenological Lagrangians containing only the essential couplings and mass parameters. This approach makes resonance searches relatively model-independent. Some common examples of simplified models are discussed below.

4.1.1 Extended Higgs Sector

A common denominator in a large fraction of BSM theories is an extended scalar sector as opposed to the minimalistic approach that was initially proposed by Peter Higgs, François Englert, Robert Brout and others [203, 204]. In fact, simple extensions to the Higgs mechanism of the SM can facilitate baryogenesis and thus explain the large asymmetry between matter and antimatter [205], enhance vacuum stability [127], provide dark matter candidates [94], or provide a solution to the strong CP problem, i.e. predict axions [206]. In short, extending the scalar sector provides solutions to some of the questions the Standard Model fails to answer. Furthermore, extending the scalar sector, inevitably leads to the existence of additional neutral and/or charged Higgs-like particles which may be accessible at current collider experiments.

Extensions of the scalar sector may appear ad hoc at first glance. Yet, many such scenarios are intrinsically important for theories attempting to solve the shortcomings of the SM. For instance, two Higgs doublets are necessary in models with a supersymmetric extension of the Standard Model [207, 208], while Higgs triplets are required in models generating neutrino masses, such as those employing the seesaw mechanism [209, 210, 211].

Two extended scalar sector models are discussed below. These models are commonly used to interpret the results of di-boson resonance searches conducted by the ATLAS and CMS collaborations.

Two-Higgs-Doublet Model

One of the simplest possible extension of the Higgs sector is obtained by adding an additional complex $SU(2)_L$ doublet to the theory. This extension is referred to as the two-Higgs-doublet model (2HDM). Following the arguments in Reference [127], the Higgs potential of the most general 2HDM is conventionally parametrised as

$$V(\Phi_1,\Phi_2) = m_{11}^2\Phi_1^\dagger\Phi_1 + m_{22}^2\Phi_2^\dagger\Phi_2 - m_{12}^2(\Phi_1^\dagger\Phi_2 + \Phi_2^\dagger\Phi_1) + \frac{\lambda_1}{2}(\Phi_1^\dagger\Phi_1)^2 + \frac{\lambda_2}{2}(\Phi_2^\dagger\Phi_2)^2 \\ + \lambda_3(\Phi_1^\dagger\Phi_1)(\Phi_2^\dagger\Phi_2) + \lambda_4(\Phi_1^\dagger\Phi_2)(\Phi_2^\dagger\Phi_1) + \frac{\lambda_5}{2}\left[(\Phi_1^\dagger\Phi_2)^2 + (\Phi_2^\dagger\Phi_1)^2\right],$$

where all the parameters are real. The minimisation of this potential gives:

$$\langle\Phi_1\rangle_0 = \begin{pmatrix} 0 \\ \frac{v_1}{\sqrt{2}} \end{pmatrix}, \quad \langle\Phi_2\rangle_0 = \begin{pmatrix} 0 \\ \frac{v_2}{\sqrt{2}} \end{pmatrix}$$

with v_1 and v_2 being the vacuum expectation values of the two fields. By convention, one sets $v \equiv \sqrt{v_1^2 + v_2^2} = 246$ GeV. Having two complex scalar $SU(2)$ doublets, there are eight fields:

$$\Phi_{1,2} = \begin{pmatrix} \Phi_{1,2}^+ \\ (v_{1,2} + h_{1,2} + i\eta_{1,2})/\sqrt{2} \end{pmatrix}$$

Three of those get absorbed to give mass to the $W^\pm$ and Z gauge bosons. The remaining five fields correspond to physical states. Assuming that the Higgs potential is CP-conserving, two of these physical states are charged scalars ($H^\pm$), two are neutral scalars (H and h), and one is a pseudoscalar (A).

The most important parameters of the 2HDM are $\tan\beta = \frac{v_2}{v_1}$, i.e. the ratio of vacuum expectation values, and α, which is the mixing angle of the two CP-even neutral scalars. The parameters α and β govern the interactions of the Higgs fields with both vector bosons and fermions, thus determining the phenomenology of the extended Higgs model. For $\cos(\beta-\alpha) \to 0$, the couplings of the lighter neutral scalars (h) become identical to those predicted by the SM. This behavior is referred to as the alignment limit.

Typically, four prominent versions of the 2HDM are considered, distinguished by how the SM particles couple to the two Higgs doublets:

- **Type I:** one Higgs doublet couples to vector bosons, while the other doublet couples to fermions.
- **Type II:** one Higgs doublet couples to up-type quarks and the other one to down-type quarks and charged leptons.
- **Lepton-specific:** the Higgs bosons have the same couplings to quarks as in the Type I model and to charged leptons as in the Type II model.
- **Flipped:** the Higgs bosons have the same couplings to quarks as in the Type II model and to charged leptons as in the Type I model.

Each of these four scenarios has seven free parameters: m_A, m_H, $m_{H^\pm}$, m_h, $\tan\beta$, $\cos(\beta-\alpha)$, and m_{12}^2.

Further versions of the 2HDM are obtained by relaxing some restrictions, such as CP conservation or the absence of flavor-changing neutral currents. CP-violating 2HDMs are discussed in References [212, 213], while flavor-violating versions of the 2HDM are discussed in References [214, 215].

Higgs Triplet Models

Another approach to extending the scalar sector involves Higgs Triplets, which are a popular solution for the generation of neutrino masses [209, 210, 211]. However, these and other models with high-dimensional Higgs multiplets are generally severely constrained. To fulfill these constraints, fine-tuning of the theory is required, with the simplest allowed options being models that contain Higgs multiplets without neutral states or representations with a very small vacuum expectation value [216].

The Georgi-Machacek (GM) model [174, 217, 218] is a specific example of a Higgs triplet model, where the Higgs sector includes two electroweak triplets (one real, one complex) alongside the standard doublet. This model preserves the custodial $SU(2)$ symmetry and allows for larger values of the triplet's vacuum expectation value. These large values can lead to significant mixing between the GM and the SM sector leading to a wide range of interesting new signatures that can be probed at the LHC.

The scalar sector of the GM model consists of a complex doublet (ϕ^+, ϕ^0) with hypercharge $Y = 1$, which is responsible for the fermion masses as in the SM, one real $SU(2)_L$ triplet (ξ^+, ξ^0, ξ^-) with hypercharge $Y = 0$, and one complex $SU(2)_L$ triplet $(\chi^{++}, \chi^+, \chi^0)$ with hypercharge $Y = 2$. In order to make the global $SU(2)_L \times SU(2)_R$ symmetry explicit, the doublet is written in the form of a bi-doublet Φ, and the triplets are combined to form a bi-triplet X:

$$\Phi = \begin{pmatrix} \Phi^{0*} & \Phi^+ \\ -\Phi^- & \Phi^0 \end{pmatrix}, \quad X = \begin{pmatrix} \chi^{0*} & \xi^+ & \chi^{++} \\ -\chi^- & \xi^0 & \chi^+ \\ \chi^{--} & -\xi^- & \chi^0 \end{pmatrix} \tag{5}$$

The most general gauge-invariant scalar potential of the GM model can be written as:

$$\begin{aligned} V(\Phi, \chi) = {} & \frac{\mu_\Phi^2}{2} \operatorname{Tr}\left(\Phi^\dagger \Phi\right) + \frac{\mu_X^2}{2} \operatorname{Tr}\left(X^\dagger X\right) + \lambda_1 \left[\operatorname{Tr}\left(\Phi^\dagger \Phi\right)\right]^2 + \lambda_2 \operatorname{Tr}\left(\Phi^\dagger \Phi\right) \operatorname{Tr}\left(X^\dagger X\right) \\ & + \lambda_3 \operatorname{Tr}\left(X^\dagger X X^\dagger X\right) + \lambda_4 \left[\operatorname{Tr}\left(X^\dagger X\right)\right]^2 - \lambda_5 \operatorname{Tr}\left(\Phi^\dagger \tau_a \Phi \tau_b\right) \operatorname{Tr}\left(X^\dagger t_a X t_b\right) \\ & - M_1 \operatorname{Tr}\left(\Phi^\dagger \tau_a \Phi \tau_b\right) (U X U^\dagger)_{ab} - M_2 \operatorname{Tr}\left(X^\dagger t_a X t_b\right) (U X U^\dagger)_{ab} , \end{aligned}$$

where the τ_i are the generators for the doublet representation of the $SU(2)$, the t_i are the generators of the triplet representation of the $SU(2)$, and the matrix U, which rotates X into the Cartesian basis [219].

After electroweak symmetry breaking, ten physical states remain. These Higgs bosons are organised in custodial symmetry multiplets: one fermiophobic quintuplet (H_5^{++}, H_5^+, H_5^0, H_5^-, H_5^{--}) of common mass m_5, one triplet (H_3^+, H_3^0, H_3^-) of common mass m_3, and two CP-even singlets (h and H) with masses m_h and m_H, respectively. One of the singlet states, h or H, is identified with the already discovered 125 GeV Higgs boson. The phenomenology of the GM model is strongly dependent on the parameters $\cos\theta_H = \frac{v_\phi}{v}$ and $\sin\theta_H = \frac{2\sqrt{2}v_\chi}{v}$, where v_ϕ and v_χ are the vacuum expectation values of the doublet and triplets, which follow $v \equiv \sqrt{v_\phi^2 + 8v_\chi^2} \approx 246$ GeV.

Given that the quintuplet scalars do not couple to fermions, their phenomenology differs significantly from additional Higgs bosons found in singlet extensions of the SM [220] or 2HDMs. Instead of gluon-gluon fusion or top-quark associated production, their dominant production modes are via vector-boson fusion or Higgs-Strahlung. Furthermore, their decay modes also differ with respect to other extended scalar sector models: the singly-charged scalars primarily decay via $H^{\pm} \to W^{\pm}Z$, a process strongly suppressed in 2HDMs, while the neutral Higgs bosons predominantly decay into $W^{\pm}W^{\mp}$ or ZZ, and the doubly-charged Higgs bosons exclusively decay via $H^{\pm\pm} \to W^{\pm}W^{\pm}$. These unique characteristics make quintuplet scalars attractive targets for di-boson resonance searches, which are typically used to probe the m_5–$\sin\theta_H$ plane of the so-called *H5plane* benchmark scenario [83].

4.1.2 Heavy Vector Triplets

Searches for new heavy spin-1 particle are commonly interpreted in the context of the Heavy Vector Triplet (HVT) model [221]. The HVT model comprises an iso-triplet of additional colourless vector bosons with zero hypercharge: an electrically charged W' boson and an electrically neutral Z' boson, with masses that are nearly identical. A small number of new coupling parameters are introduced to govern the strength of the W' and Z' bosons' interactions with the SM particles. The Lagrangian is then defined via:

$$\begin{aligned}\mathcal{L}_V = &-\frac{1}{4}D_{[\mu}V^a_{\nu]}D^{[\mu}V^{\nu]\,a} + \frac{m_V^2}{2}V^a_\mu V^{\mu\,a}\\ &+ i g_H V^a_\mu H^\dagger \tau^a \overset{\leftrightarrow}{D}{}^{\mu} H + g_f V^a_\mu J^{\mu\,a}_F\\ &+ \frac{g_V}{2}c_{VVV}\epsilon_{abc}V^a_\mu V^b_\nu D^{[\mu}V^{\nu]} + g_V^2 c_{VVHH}V^a_\mu V^{\mu\,a}H^\dagger H - \frac{g}{2}c_{VVW}\epsilon_{abc}W^{\mu\nu a}V^b_\mu V^c_\nu\,,\end{aligned}$$

where the first line describes the kinetic and mass terms of the new fields, the second line incorporates their direct interactions with the Higgs current and left-handed fermionic current, and finally the third line includes higher-dimension operators, which are however not accesible at the LHC. The parameters g_H and g_f correspond to the coupling strengths between the triplet field and the Higgs and fermion fields, respectively. The triplet field interacts with the Higgs field and consequently with the longitudinally polarised W and Z bosons according to the equivalence theorem [222]. Therefore, g_H governs the interactions of the W' and Z' bosons with the SM vectors and with the Higgs boson, and in particular its decays into bosonic channels. The other free parameters of the theory are the masses of the W' and Z' resonances, which are degenerate.

For the interpretations of their results, the ATLAS and CMS collaboration focus on three representative scenarios:

- Benchmark model A corresponds to the parameter choice $g_F = -0.55$ and $g_H = -0.56$, which reproduces the phenomenology of weakly coupled extended gauge theories [223].
- Benchmark model B corresponds to $g_F = 0.14$ and $g_H = -2.9$, which implements a strongly coupled scenario as in composite Higgs models [168].
- Benchmark model C corresponds to $g_F = 0$ and $g_H = -0.56$, which results in the W' and Z' bosons being fermiophobic.

In the benchmark model A, W' and Z' resonances have larger couplings to fermions than bosons, with branching fractions to quarks enhanced by QCD colour factors. Conversely, model B features large branching fractions to boson pairs ($W^{\pm}W^{\mp}$, ZZ, $W^{\pm}Z$, Zh and $W^{\pm}h$). Benchmark models A and B are typically used to interpret results from di-boson resonance searches in the qqA production mode, while benchmark model C is used for interpreting results from searches for the VBF production mode. The lowest order Feyman diagrams of the qqA and VBF production modes of W' and Z' resonances, indicating the relevant coupling parameters for the production and decay vertex, are presented in Figure 33. Other production modes of the W' and Z' resonances are insignificant and are therefore not considered in the ongoing search efforts.

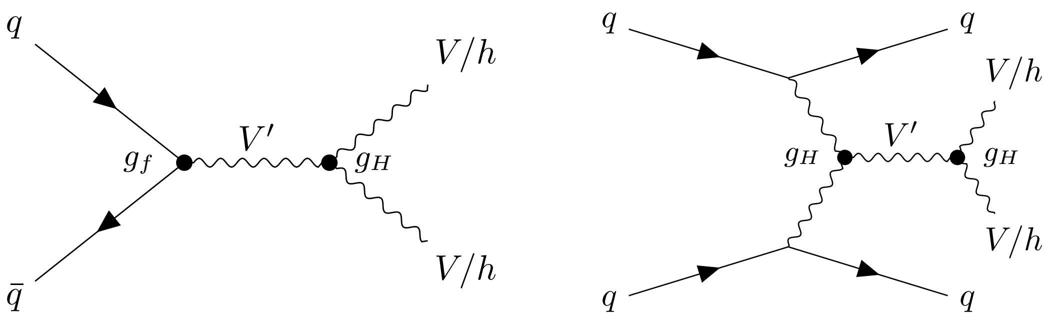

(a) quark-antiquark annihilation (b) vector-boson fusion

Figure 33: Lowest order Feyman diagrams of (a) the quark-antiquark annihilation production mode and (b) the vector-boson fusion production mode of a V' boson (with $V' = W', Z'$) from the Heavy Vector Triplet model. The V' boson decays into a pair of SM bosons. The relevant coupling parameters are indicated at the production and decay vertices.

4.1.3 Warped Extra Dimensions

Warped extra dimension models [173] propose the existence of an extra spatial dimension that is compactified between two fixed "branes". The region between these branes, known as the bulk, is governed by an exponential metric. The warp factor (k) in this metric, a fundamental component of these models, controls the gap between the Planck scale (M_{Pl}) and the EW scale. This class of models predicts the existence of new particles with significant branching ratios to di-boson systems. Particularly interesting in this context are the spin-0 radion (R) and the spin-2 Kaluza-Klein excitation of the graviton (G_{KK}) [172]. Their branching ratios are illustrated Figure 34.

Two types of warped extra dimension models are commonly used to interpret results from searches for spin-2 particles. In the Randall-Sundrum 1 (RS1) model, only gravity is allowed to propagate in the extra dimension. The couplings between the KK gravitons and matter fields are controlled by the dimensionless parameter $\sqrt{8\pi} \cdot k/M_{\mathrm{Pl}}$. Benchmark scenarios where $\sqrt{8\pi} \cdot k/M_{\mathrm{Pl}}$ is respectively set to 0.01, 0.05, 0.1, 0.5 and 1.0 are typically considered by the ATLAS and CMS collaborations. In contrast, the Randall-Sundrum (RS) bulk model allows the SM fields to propagate in the extra dimension. This leads to KK graviton couplings that depend on the localisation of SM fields in the bulk.

The scalar radion is introduced to the Randall–Sundrum framework in order to stabilise the radius of the compactified extra dimension, r_c [224, 225]. The coupling of the radion to SM particles scales inversely proportional to the model parameter $\Lambda_R = e^{-k\pi r_c} \cdot \sqrt{6M_5^3/k}$, where M_5 is the five-dimensional Planck mass. The size of the extra dimension is therefore given via $k\pi r_c$. A benchmark scenario with $k\pi r_c = 35$ and $\Lambda_R = 3$ TeV is usually considered.

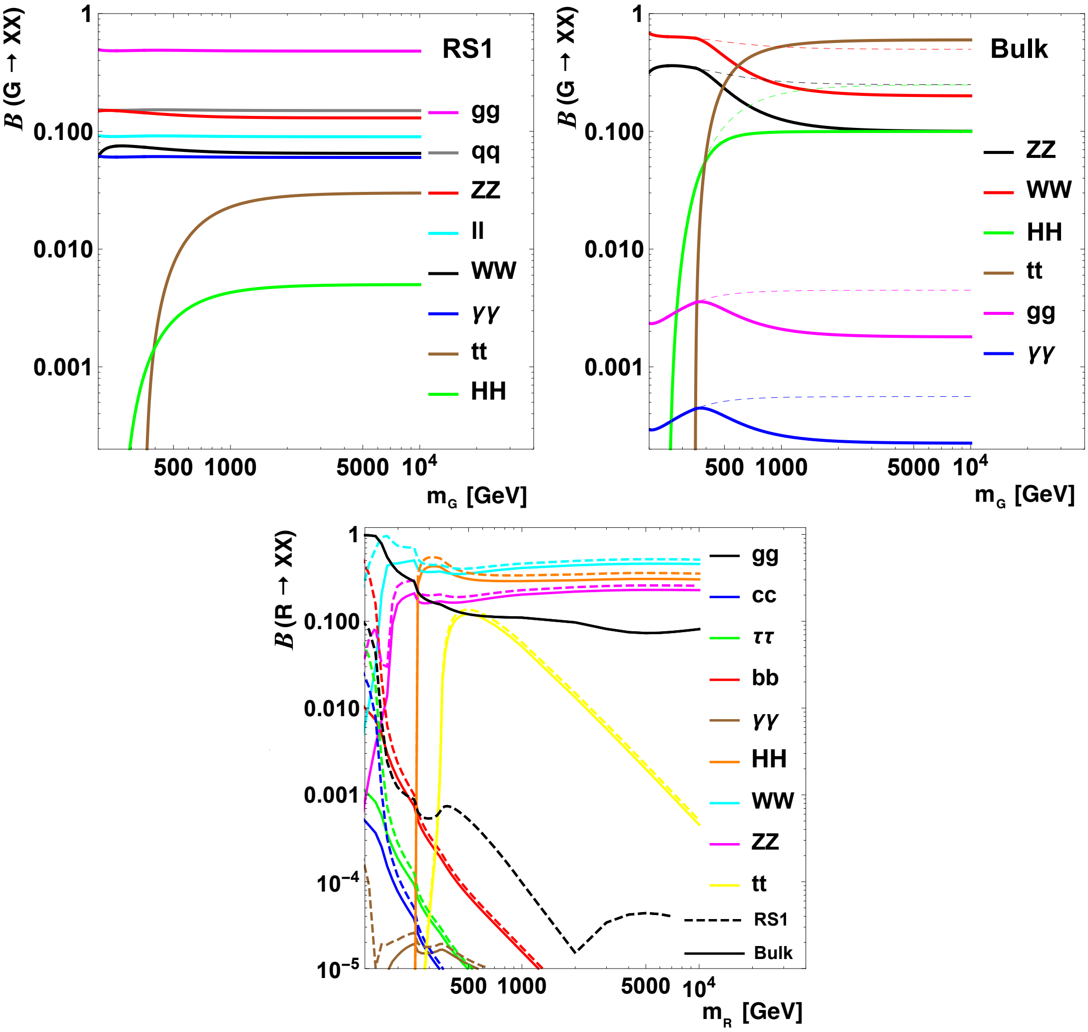

Figure 34: Decay branching ratios of a RS1 graviton (top left), bulk RS graviton (top right), and radion (bottom). Solid lines assume a fully elementary top quark, while the dashed lines ignore the coupling of the graviton to top quarks[226].

4.2 Searches for a heavy resonance decaying to Zh or Wh

Searches for the resonant production of a Higgs boson and a W or Z boson are strongly motivated by the large number of different models that predict these processes. Examples are: Minimal Walking Technicolour [170, 171, 227], Little Higgs [228], composite Higgs [169, 229], and models with extra dimensions [172, 173, 230], which all attempt to solve the electroweak hierarchy problem by introducing new heavy vector bosons that have large branching fractions for decays into a Wh or Zh system. Furthermore, several theories with an extended Higgs sector, such as two-Higgs-doublet models [127, 231], three-Higgs-doublet models [232], or Higgs triplet models [233, 234, 235, 236] predict pseudoscalar resonances decaying via $A \to Zh$.

Semi-leptonic final states comprising b-quark pairs from the Higgs boson decay and leptons (including electrons, muons, or neutrinos) from the vector boson decays are promising candidates for the search for Zh and Wh resonances. The $h \to b\bar{b}$ decay provides the highest sensitivity due to the largest Higgs boson branching fraction, while vector boson decays into pairs of leptons ensure high trigger efficiencies over a large range of resonance masses and overall a much cleaner signatures in the detector compared to fully-hadronic final states. Therefore, searches for Zh and Wh resonances tend to focus on the following three search channels: $Z' \to Zh \to \nu\nu b\bar{b}$, $W' \to W^{\pm}h \to \ell\nu b\bar{b}$, and $Z' \to Zh \to \ell\ell b\bar{b}$.

The searches for Zh and Wh resonances probe for a localised excess in the invariant mass distributions of the $\ell\nu bb$ and $\ell\ell bb$ final states as well as the transverse mass distribution of the $\nu\nu bb$ final state. Because these searches cover a wide range of mass values, from a few hundred GeV to a few TeV, dedicated analysis techniques are used to ensure a high sensitivity to both low- and high-mass resonances. At low resonance masses, when the final state particles have a relatively low Lorentz-boost, the decay products of the Higgs boson are reconstructed as individual jets (such decays are referred to as "resolved"). At high resonance masses, when the final state particles have a relatively large Lorentz-boost, the Higgs boson is reconstructed as a single large-R jet (such decays are referred to as "merged").

The most recent search for Zh and Wh resonances in semi-leptonic final states by the ATLAS collaboration is based on $139\,\text{fb}^{-1}$ of $\sqrt{s} = 13\,\text{TeV}$ pp collision data [190]. This search is performed on events consistent with the $\nu\nu bb$, $\ell\nu bb$ and $\ell\ell bb$ final states, where $\ell = e$ or μ. Consequently, events that contain exactly zero, one, or two charged leptons and at least two small-R jets or one large-R jet are retained for further analysis. Each of these three final states produces a characteristic signature in the detector. Examples are depicted in Figures 35 and 36.

The signal candidate events are triggered using $E_{\text{T}}^{\text{miss}}$ triggers [237] (applied in the 0- and 1-lepton channels) and single-lepton triggers [238, 239] (applied in the 1- and 2-lepton channels). Dedicated selection requirements are applied to the three lepton channels to reduce contributions from relevant background sources.

The 0-lepton channel is dedicated to the search for $Zh \to \nu\nu b\bar{b}$ and $W^{\pm}h \to \tau_{\text{had}}^{\pm}\nu b\bar{b}$ decays. For the Z' and A boson searches, events are vetoed if they contain any electron, muon, or hadronically decaying τ-lepton candidate. For the W' search, the veto on τ-lepton candidates is relaxed such that events with at most one τ-lepton are selected aiming to recover $W' \to Wh \to \tau_{\text{had}}\nu bb$ events. Furthermore, strict selection requirements on the $E_{\text{T}}^{\text{miss}}$, $p_{\text{T}}^{\text{miss}}$, and the $E_{\text{T}}^{\text{miss}}$ significance are placed to suppress backgrounds from multi-jet production. Selection requirements are not only applied on the magnitudes of these three observables, but also on the angular separation between the $E_{\text{T}}^{\text{miss}}$ and $p_{\text{T}}^{\text{miss}}$ vectors, $\Delta\Phi(\vec{E}_{\text{T}}^{\text{miss}}, \vec{p}_{\text{T}}^{\text{miss}})$, and on the angular separation between the $E_{\text{T}}^{\text{miss}}$ vector and the momentum vector of the Higgs boson candidate, $\Delta\Phi(\vec{E}_{\text{T}}^{\text{miss}}, h)$. The selection requirement on $\Delta\Phi(\vec{E}_{\text{T}}^{\text{miss}}, \vec{p}_{\text{T}}^{\text{miss}})$ removes events in which a significant fraction of the $E_{\text{T}}^{\text{miss}}$ originates from pile-up activity. The selection requirement on $\Delta\Phi(\vec{E}_{\text{T}}^{\text{miss}}, h)$ removes events in which a significant fraction of the $E_{\text{T}}^{\text{miss}}$ is caused by incorrect measurements of the jet energies. After applying these requirements, the contributions from the multi-jet background are negligible, while large background contributions originate from the W+jets with around 15%, Z+jets with about 30%, and top-quark pair production with around 50%.

The 1-lepton channel is dedicated to the search for $W' \to W^{\pm}h \to \ell\nu b\bar{b}$ decays. Hence, selected events are required to have exactly one electron or one muon. In these events, the W boson candidate is reconstructed from the sum of the four-momenta of the charged lepton and the neutrino[28]. The multi-jet background is

[28] The momenta of the neutrino in the x- and y-directions are obtained from the corresponding components of the $E_{\text{T}}^{\text{miss}}$ vector. The momentum of the neutrino in the z-direction is calculated by imposing a W boson mass constraint on the lepton–neutrino system, which results in a quadratic equation. The neutrino's momentum in the z-direction is then taken as either the real component of the complex solutions, or the real solution with the smaller absolute magnitude.

reduced by applying a strict selection requirement on $E_{\mathrm{T}}^{\mathrm{miss}}$, while the dominant backgrounds from W+jets and top-quark pair production are reduced by applying a m_{Wh}-dependent requirement on the transverse momentum of the W boson candidate, $p_{\mathrm{T},W}$. This selection requirement exploits the fact that the m_{Wh} and $p_{\mathrm{T},W}$ observables are more strongly correlated for the signal process than for backgrounds. The contribution from top-quark pair events can be further reduced by only selecting events with either two or three jets[29]. After applying these selection requirements, the most dominant background contributions stem from events containing top quarks with almost 80% of all selected events, and W+jets production with about 20%. Other processes give only minor contributions. For example, contributions from multi-jet events are at the level of a few per mille of the total background in the resolved event categories and completely negligible in the merged event categories.

The 2-lepton channel is dedicated to the search for $Z' \to Zh \to \ell\ell b\bar{b}$ decays. Therefore, events containing same-flavour lepton pairs, i.e. e^+e^- and $\mu^+\mu^-$, are selected. Contributions from the dominant background processes, i.e. the production of Z+jets and top-quark pair events, are reduced by applying m_{Zh}-dependent selection requirements on the mass of the dilepton system $m_{\ell\ell}$, the transverse momentum of the di-lepton system $p_{\mathrm{T},\ell\ell}$ and the $E_{\mathrm{T}}^{\mathrm{miss}}/\sqrt{H_{\mathrm{T}}}$, where H_{T} is calculated as the scalar sum of the p_{T} of the leptons and small-R jets in the event. The selection requirements on these observables become looser for larger resonance masses to account for the smaller backgrounds in this kinematic range and the fact that the momentum and energy resolution degrade with increasing boost of the final-state particles. After applying these selection requirements, the most dominant background contributions stem from Z+jets production, yielding up to 90%.

In each of the three lepton channels, minor background contributions arise from the di-boson, SM Vh, $t\bar{t} + h$ and $tt + V$ production.

Events that pass the selection requirements of either of the three lepton channels are placed in the resolved category if the Higgs boson candidate is reconstructed from two small-R jets[30], or the merged category if the Higgs boson candidate is reconstructed from a large-R jet. If an event satisfies the criteria for both the resolved and merged categories, it is assigned to the resolved category because of its better mass resolution. The events are then further classified into signal and control regions based on the mass of the Higgs boson candidate. Events with a mass within a window around the Higgs boson pole enter the signal regions, while events with a mass outside of this window enter the control regions[31]. Additional control regions for processes containing top quarks are used in the 2-lepton channel. These regions are obtained by selecting events with a pair of different-flavour leptons $e^{\pm}\mu^{\mp}$, and without the requirement on $E_{\mathrm{T}}^{\mathrm{miss}}/\sqrt{H_{\mathrm{T}}}$. The events are further split based on the number of b-tagged objects in the event.

Heavy vector bosons, such as Z' and W', are mainly produced via qqA, while pseudoscalars are mainly produced via ggF or associated production with bottom or top-quarks. Representative lowest-order Feynman diagrams for the production of a Z', W', or A boson and their subsequent decays in the targeted final states are depicted in Figure 37.

29 Given that $t\bar{t}$ decays into a single-lepton final state tend to have at least four reconstructed jets.

30 If two b-tagged jets are present in the event, the Higgs boson candidate is reconstructed from the two b-tagged small-R jets. If an event contains more than two b-tagged jets, the Higgs boson candidate is reconstructed from the two leading b-tagged jets. If only one b-tagged jet is present, the Higgs boson candidate is reconstructed from the b-tagged jet and the leading small-R jet in the remaining set.

31 The mass window requirements vary slightly between the three lepton channels and the resolved and merged event categories given that some channels and categories have fewer background contributions than others.

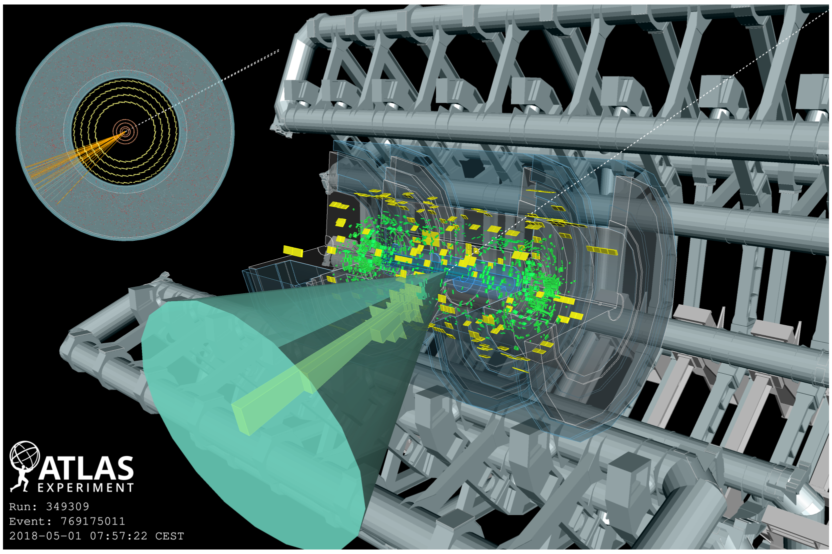

Figure 35: Event display of a $X \to Zh \to \nu\nu bb$ candidate in the merged 2 b-tags signal region. The missing transverse energy has a value of 1.21 TeV and is indicated by the dashed white line. The Higgs-boson candidate is comprised of a large-R jet which contains two b-tagged VR track-jet. The large-R jet is indicated by the turquoise cone and has a transverse momentum of $p_{\mathrm{T}} = 1.15$ TeV. The yellow blocks correspond to energy depositions in the hadronic calorimeter. The transverse mass of the Zh candidate is $m_{\mathrm{T},Zh} = 2.4$ TeV. The event was recorded in 2018 (Run 349309, Event 769175011).

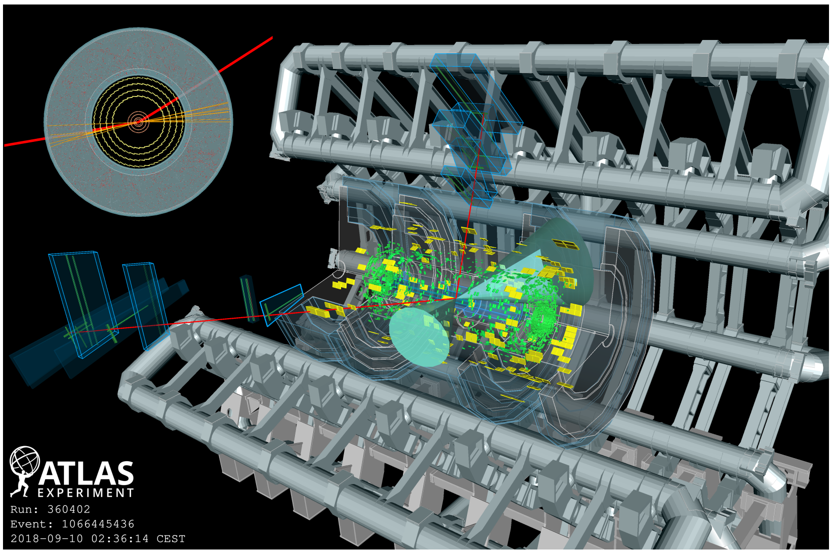

Figure 36: Event display of a $X \to Zh \to \mu\mu bb$ candidate in the resolved 2 b-tag signal region. The leading and second leading muons comprising the Z boson candidate have transverse momenta of 86 GeV and 22 GeV respectively, while the two b-tagged jets comprising the Higgs-boson candidate have transverse momenta of 86 GeV and 31 GeV. The muons are indicated by red solid lines and the two jets are indicated by the turquoise cones. The yellow blocks correspond to energy depositions in the hadronic calorimeter and the blue boxes to muon chambers with hits from the muon. The invariant mass of the four objects is $m_{Zh} = 300$ GeV. The event was recorded in 2018 (Run 360402, Event 1066445436).

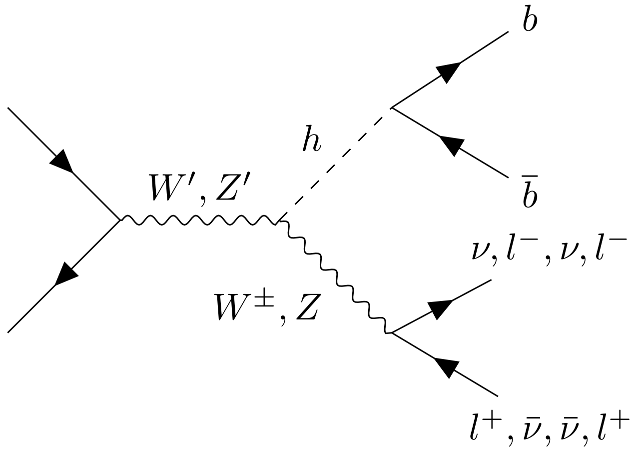

(a) quark–antiquark annihilation

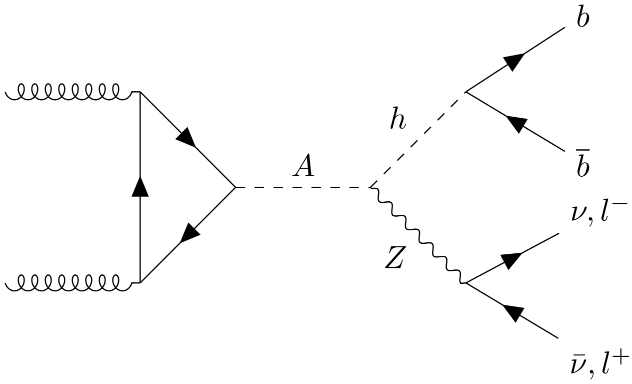

(b) gluon-–gluon fusion

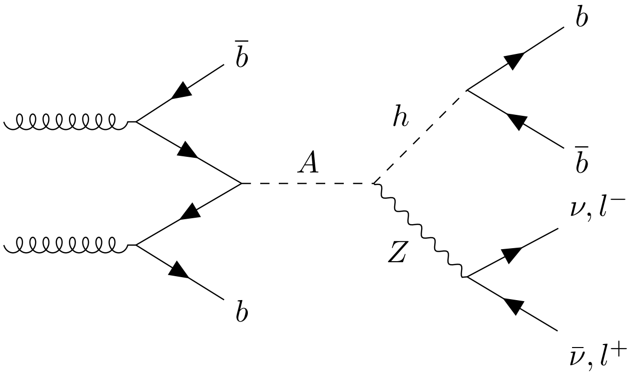

(c) b-associated production

Figure 37: Representative lowest order Feynman diagrams of the resonant production of a W or Z boson and a Higgs boson via (a) quark-antiquark annihilation, (b) gluon–gluon fusion, and (c) b-associated production. The subsequent decays into the $\nu\nu bb$, $\ell\nu bb$ and $\ell\ell bb$ final states are depicted as well.

In case the new heavy particle is produced in association with jets (or other objects), the reconstruction of the final state becomes more challenging due to the additional activity in the event. At the same time, the multiplicity and kinematics of the additional objects in the final state can be exploited to further suppress the backgrounds. As a consequence, the analysis strategies, the background estimation techniques and the configuration of the fit models have been optimised individually for the search for new heavy vector bosons and the search for pseudoscalars to maximise the sensitivity to both types of signals. Further details on the search for heavy vector bosons are given in Section 4.2.1, while the searches for pseudoscalars are discussed in Section 4.2.2.

4.2.1 Search for heavy vector bosons

In the searches for Z' and W' bosons, events that pass the aforementioned selection requirements are further split into two exclusive categories based on the number of b-tagged jets in the event[32]. One category is dedicated to events with exactly one b-tagged jet, while the other is dedicated to events with exactly two b-tagged jets. Events with more than two b-tagged jets are not considered for these searches. Splitting events

[32] In resolved event categories, b-tagging is applied to small-R calorimeter jets and in merged event categories, b-tagging is applied to VR track-jets.

by b-tagging multiplicity significantly improves the sensitivity to the signal process. The categories with two b-tagged jets are the most sensitive, as they have a much larger expected signal purity. However, the categories with one b-tagged jet are still useful, as they help to constrain the background contributions by providing a larger overall statistics in data.

Contributions from multi-jet production are estimated using data-driven techniques. In the 0-lepton channel, the number of multi-jet events has been estimated with an ABCD-method [240]. This method defines three non-overlapping and signal-depleted control regions (B, C, D) to complement the signal region (A). The additional regions are defined by inverting one or both of the selection requirements on two of the observables used in the event selection. A transfer factor T is then calculated from the ratio of events in regions C and D, and is used to extrapolate the observed number of multi-jet events in the control region B into the phase-space of the signal region: $N_A \approx T \cdot N_B := N_C/N_D \cdot N_B$, where the N_i are the event counts in the four regions. The number of multi-jet events in the control regions is obtained by subtracting the simulation-based estimates of all processes except multi-jet production from the corresponding yields in data. Using this ABCD method, the contribution from multi-jet production to all signal regions of the 0-lepton channel is found to be small compared to the uncertainties in the data statistics. As a consequence, background contributions from multi-jet production are neglected for searches in the 0-lepton channel.

In the 1-lepton channel, the template method that was developed for the studies presented in [241] is used: templates for the m_{Vh} and $m_{\mathrm{T},Vh}$ distributions are extracted from a dedicated control region, which is enriched with multi-jet events. The control region is obtained by inverting the lepton isolation requirements. The shape of the templates are obtained by subtracting the contributions from all other backgrounds from data. The normalisation of these templates are derived by performing a two-component fit in the sideband regions of the Higgs boson candidate. In this procedure, the templates for the multi-jet backgrounds and the sum of the other background contributions are fitted to data. The template normalisation is then extrapolated from the sideband regions to the mass window region using information from the simulations.

The other background distributions are estimated from samples of simulated events, with the normalisations of the dominant backgrounds derived from control regions in data. As the production of vector bosons in association with heavy-flavour jets is not well described by the state-of-the art Monte Carlo generators [242], dedicated correction procedures are used. The mismodelling of the event rates is compensated by splitting the W/Z+jets simulated event samples into three components: W/Z + hf (W/Z + bb, W/Z + bc, and W/Z + cc), W/Z + hl (W/Z + bl, and W/Z + cl), and W/Z + lf; where 'h' and 'l' refer to heavy-flavour and light-flavour jets, respectively. The normalisations of these three components are determined individually via a maximum likelihood fit. Furthermore, the mismodelling of event kinematics observed for the simulated W/Z+jets events are corrected to match the data. In this context, the sum of the W/Z+jets background contributions is reweighted as a function of the transverse momentum of the di-jet system, $p_{\mathrm{T},jj}$, based on fits to the data/simulation distribution in the m_{jj} sideband regions. These corrections are derived separately for the three lepton channels.

To simplify the background model, the $t\bar{t}$, single-top-quark, $t\bar{t} + V$, and $t\bar{t} + h$ processes are combined into one single component, which is referred to as the top-quark backgrounds.

The searches for heavy vector bosons are based on combined fits in the 0-lepton and 2-lepton channels (for the Z'), and the 0-lepton and 1-lepton channels (for the W'). The fit model for the Z' search includes the signal cross section and the global normalisations of the top-quark, Z + hf, and Z + hl backgrounds as free parameters. The normalisation of the top-quark background is determined separately for the 0-lepton and 2-lepton event categories, while common normalisation factors for the two lepton channels are used for the Z + hf and Z + hl backgrounds. The fit model for the W' search includes the signal cross section and the global normalisations of the top-quark, Z + hf, Z + hl, W + hf, and W + hl backgrounds as free parameters. These fits are performed in the relevant signal and control regions, probing either the $m_{\mathrm{T},Vh}$ distribution (in the 0-lepton channel) or the m_{Vh} distribution in the (1- and 2-lepton channels). A few examples of the fit input distributions are presented in Figure 38. The combined fits are performed for 19 simulated signal mass hypotheses covering a range from 300 GeV to 5 TeV. In addition, parameter morphing [148] is applied to the shape and normalisation of the $m_{\mathrm{T},Vh}$ and m_{Vh} distributions in order to interpolate between the simulated signal mass points.

The 95% CL upper limits on the production cross section for $Z' \to Zh$ are shown in Figure 39 (a) as a function of the resonance mass. The observed limits range from 0.9 pb for $m_{Z'} = 300$ GeV to 0.3 fb for $m_{Z'} = 5$ TeV. These limits exclude Z' masses below 2.8 TeV for HVT benchmark Model A, and below 3.2 TeV for Model B. The combined limits are dominated by the 0-lepton channel for resonance masses above 800 GeV, and by the 2-lepton channel for resonance masses below 800 GeV. The largest deviation from the Standard Model expectations is found for a resonance mass of 500 GeV and corresponds to a local significance of about 2.1 standard deviations, or a p-value of 0.017. The global significance of this excess is 1.1 standard deviations.

Figure 39 (b) shows the 95% CL upper limits on the production cross section for $W' \to Wh$ as a function of the resonance mass. The limits range from 1.3 pb for $m_{W'} = 400$ GeV to 0.4 fb for $m_{W'} = 5$ TeV. These limits exclude W' masses below 2.95 TeV for HVT benchmark Model A, and below 3.3 TeV for Model B. The combined limits are dominated by the 1-lepton channel across the full range of tested mass hypotheses. The largest deviation from the Standard Model expectations is found for a resonance mass of 400 GeV with a local significance of about 2.0 standard deviations, or a p-value of 0.02, and around 3.0 TeV with a local significance of about 1.7 standard deviations, or a p-value of 0.05.

For resonance masses above 700 GeV, both searches are limited by statistical uncertainties, while the uncertainties in the flavour tagging and in the modelling of the Z+jets, W+jets, and top-quark backgrounds are dominant for the lowest resonance masses.

The upper limits on the production cross section times branching ratio obtained from the Z' and W' searches are converted into 95% CL exclusion contours in the HVT parameter plane $\{g_F, g_H\}$. These exclusion contours are presented in Reference [190] for resonance masses of 2, 3, and 4 TeV.

The cross-section limits of the Z' and W' searches have been significantly improved with respect to the last iteration of the analysis [243], which has been performed by the ATLAS collaboration at $\sqrt{s}$ =13 TeV with an integrated luminosity of 36.1 fb^{-1}. The improvements range from about 50% for a resonance mass of 300 GeV to about 400% for a mass of 5 TeV. The improvements at low resonance masses are mainly due to the larger dataset, while the improvements at high resonance masses are mostly due to refined b-tagging techniques, including the use of variable-radius track-jets instead of track-jets clustered with a fixed radius parameter of $R = 0.2$.

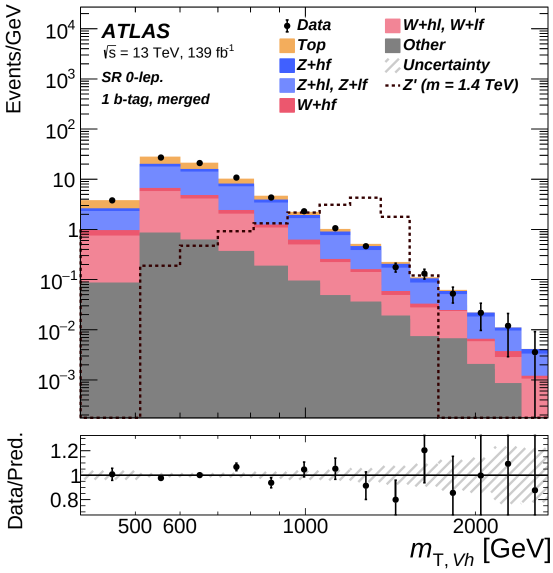

(a)

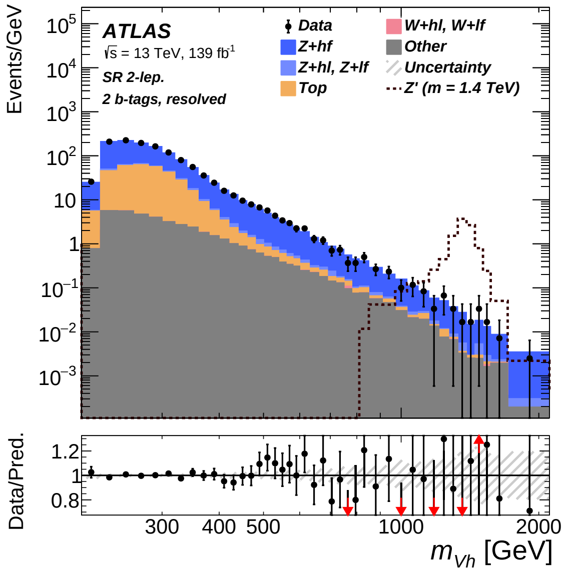

(b)

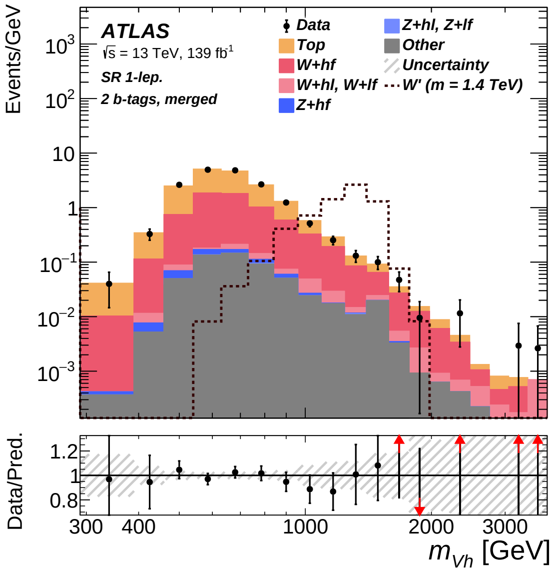

(c)

Figure 38: Post-fit distribution of (a) the transverse mass $m_{\mathrm{T},Vh}$ for the 1 b-tag merged 0-lepton signal region, (b) the invariant Vh mass for the 2 b-tag resolved 2-lepton signal region, and (c) the invariant Vh mass for the 2 b-tag merged 1-lepton signal region. The quantity on the vertical axis is the number of data events divided by the bin width in GeV. The term 'Top' summarises events from $t\bar{t}$, single-top-quark, $t\bar{t}+h$ and $t\bar{t}+V$ contributions. In each plot, the last bin contains the overflow. The background prediction is shown after a background-only maximum-likelihood fit to the data. The lower panels show the ratio of the observed to the estimated SM background. The background uncertainty band shows the post-fit statistical and systematic components added in quadrature. The signal for the benchmark HVT *Model A* with $m_{Z'} = 1.4$ TeV, normalised to $\sigma \times B(Zh) \times B(h \to b\bar{b}) = 0.1$ pb, is shown as a dashed line [190].

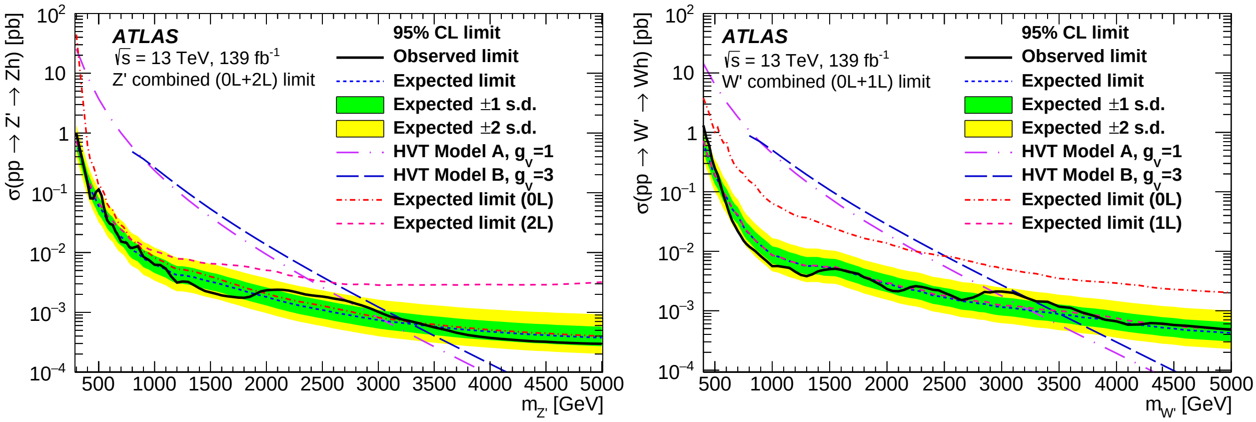

(a) (b)

Figure 39: Upper limits at the 95% CL on the product of the cross section for $pp \to Z'$ and the branching fraction to Zh from the combination of the 0-lepton (0L) and 2-lepton (2L) channels (a) and on the product of the cross section for $pp \to W'$ and the branching fraction to Wh from the combination of the 0-lepton and 1-lepton (1L) channels (b). For the Z' and W' search, the branching fraction of $h \to b\bar{b}, c\bar{c}$ is assumed to be 0.598 [190].

Searches for new heavy vector bosons decaying via $Z' \to Zh \to \nu\nu b\bar{b}$, $Z' \to Zh \to \ell^{\pm}\ell^{\mp}b\bar{b}$ or $W' \to Wh \to \ell^{\pm}\nu b\bar{b}$ have also been performed by the CMS collaboration with an integrated luminosity of 137 fb^{-1} [188, 191]. In addition, results have been published in other final states: ATLAS has performed a search in the fully-hadronic final state [189], based on an integrated luminosity of 139 fb^{-1}, and CMS has published results in the fully-hadronic final state [184] and the $\tau^+\tau^-\ell^+\ell^-$ final state [244], based on integrated luminosities of 138 fb^{-1} and 35.9 fb^{-1}, respectively.

Expected upper limits on the production cross section times branching ratio for the most recent $Z' \to Zh$ and $W' \to Wh$ searches by the ATLAS and CMS collaborations are compared in Figure 40. Limits are shown for the search efforts by ATLAS in the semi-leptonic and fully-hadronic final state, and from the CMS search efforts in semi-leptonic final states[33].

The CMS searches focus exclusively on high-mass spin-1 particles. Their searches for $Z' \to Zh \to \nu\nu b\bar{b}$ and $Z' \to Zh \to \ell^{\pm}\ell^{\mp}b\bar{b}$ decays are optimised for a mass range from 800 GeV to 5 TeV, and their search for $W' \to Wh \to \ell^{\pm}\nu b\bar{b}$ decays is optimised for a mass range from 1 TeV to 4.5 TeV. This is refelected in their analysis strategy, which only consideres merged event topologies. Consequently, ATLAS has stronger limits for the Z' and W' searches in the intermediate mass regions ranging up to 1 TeV for Z' bosons and 1.4 TeV for W' bosons. For higher resonance masses, CMS has significantly stronger expected limits than ATLAS for both searches. For example, CMS has approximately twice as stringent expected upper limits on $\sigma(pp \to Z' \to Zh)$ as ATLAS for a resonance mass of 4 TeV, and approximately 1.6 times as stringent expected upper limits on $\sigma(pp \to W' \to W^{\pm}h)$ at the same resonance mass.

The CMS search for $Z' \to Zh$ decays benefits in particular from aggressive event selection requirements on the ratio of E_T^{miss} to the p_T of the Higgs boson candidate within the 0-lepton channel. After applying these

[33] The searches for heavy resonances in fully-hadronic final state by CMS consider decays to WW, WZ, ZZ, Wh, or Zh boson pairs. The results from these search efforts are expressed as upper limits on the cross section for $pp \to V' \to VV + Vh$ production, with $V = W, Z$, instead of $pp \to V' \to VV$ and $pp \to V' \to Vh$ individually. Thus, these results can not be directly compared to the results by ATLAS nor to the CMS results in the semi-leptonic final states.

requirements, the total background yields in the ≤ 1 b-tag category, which dominates the combined results for high mass resonance searches, are an order of magnitude smaller than the total background yields in the 1 b-tag region of the ATLAS analysis. Despite this, the expected signal yields from CMS are only 25% smaller than those from ATLAS. Overall, the CMS search benefits from a significantly better expected signal-to-background ratio in its search regions. The selection requirements on $E_{\mathrm{T}}^{\mathrm{miss}}/p_{\mathrm{T}}^{H}$ are particularly effective at discriminating against contributions from the $t\bar{t}$ background. After applying these requirements, top quark pair production is no longer a dominant background to the $Z' \to Zh$ search, which significantly simplifies the background model in the maximum likelihood fit.

The CMS search for $W' \to W^{\pm}h$ decays benefits in particular from a newly developed double-b tagging algorithm [245]. This algorithm uses a multivariate discriminant that combines information from displaced tracks and (multiple) secondary vertices within large-R jets to distinguish between $h \to b\bar{b}$ and $Z \to b\bar{b}$ decays, as well as backgrounds that involve light-flavor jets. This approach performs significantly better than the tagging of single VR track-jets, which was the default method in ATLAS until recently.

Comparing the expected upper limits on $\sigma(pp \to Z' \to Zh)$ between the ATLAS searches in the semi-leptonic and fully-hadronic final states, the semi-leptonic results are superior over the entire range of probed Z' masses. However, the expected upper limits on $\sigma(pp \to W' \to W^{\pm}h)$ are relatively similar for masses above 2 TeV.

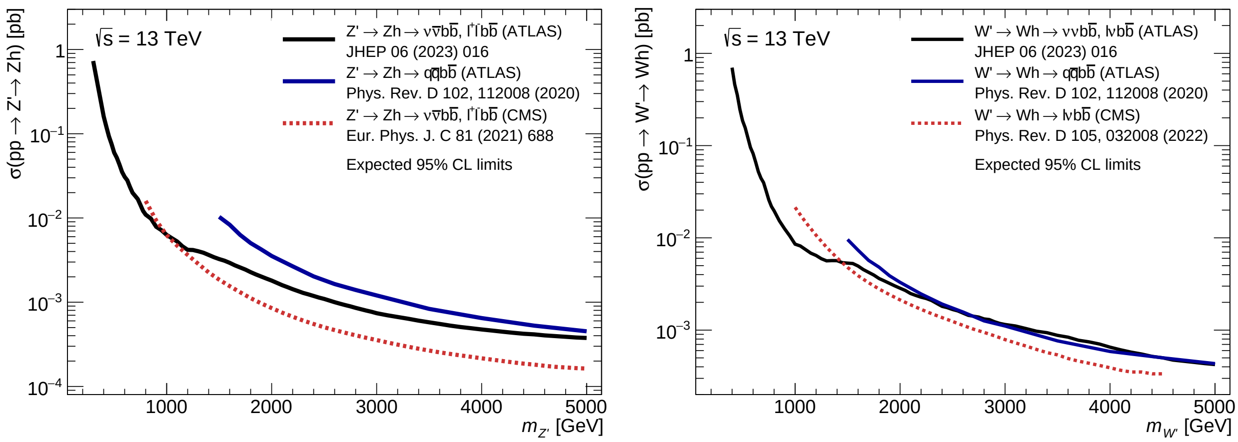

(a) (b)

Figure 40: Expected upper limits at 95% CL on (a) $\sigma(pp \to Z' \to Zh)$ and (b) $\sigma(pp \to W' \to W^{\pm}h)$ as a function of the Z' and W' pole masses, respectively. The upper limits from recent searches for Vh resonances are compared, including results from the CMS collaboration in the semi-leptonic final states [188, 191] and from the ATLAS collaboration in both semi-leptonic [190] and fully-hadronic [189] final states.

Personal contributions

The work on this analysis was carried out with strong contributions from two Ph.D students of the TU Munich and MPI, whom I supervised, as well as myself. In addition, researchers from Michigan State University, the University of Massachusetts, Queen Mary University of London, and Shandong University also gave significant contributions to these efforts. In total, 13 researchers were involved in this project. In my role as the coordinator of this analysis, I was responsible for organising the analysis efforts, assigning tasks, chairing meetings, setting timelines and discussing the needs of our analysis with the coordinators of the physics group for Di-Higgs and Di-Boson searches. Under my supervision, the two Ph.D students developed the software framework that we used for this analysis, optimised the analysis strategy in the 0-lepton channel, performed data-to-simulation comparisons, implemented and vallidated a method to interpolate between simulated signal mass hypothese (i.e. parameter morphing), evaluated the theory uncertainties in the signal and background processes for all three lepton channels, and performed combined fits in the 0-lepton and 2-lepton channels to extract the upper limits on the production cross section times branching fraction. These studies are all detailed in their Ph.D theses [240, 246]. In addition, I derived data-to-simulation correction functions for the 0-lepton and 1-lepton channels to account for the mismodelling of the vector boson p_{T} in W+jets and Z+jets events. Furthermore, I significantly contributed to the writing of the internal documentation, and I was the leading editor of the manuscript submitted for journal publication. Beyond these active contributions, I provided guidance and support to students from other institutes involved in this analysis [247, 248], ensuring that their contributions were integrated into the workflow of our analysis.

Challenges

To finalise the analysis, we had to overcome a number of challenges. One common problem for all three lepton channels was the severe mismodelling of the vector boson p_{T} distribution in events where W or Z bosons are produced in association with heavy-flavour jets. This mismodelling is actually a well known issue of the SHERPA 2.2.1 MC generator [242] which tends to significantly overestimate QCD activity and predicts larger W/Z boson p_T values than seen in the ATLAS data[34]. To counter this mismodelling, we decided to reweight the simulated W+jets and Z+jets samples as a function of the transverse momentum of the dijet system, $p_{\mathrm{T},jj}$, in the resolved event categories, and as a function of the large-R jet p_{T} in the merged event categories. These two quantities were chosen because they are strongly correlated with the vector boson p_{T}[35], which cannot be directly determined in the 0-lepton channel due to the two neutrinos in the final state. The correction functions were derived from fits to the data-to-simulation ratio of the $p_{\mathrm{T},jj}$ and the large-R jet p_{T} distributions in the m_{jj} sideband control regions after accounting for differences in the overall normalisation between data and the simulations. Separate correction functions were derived for the three lepton channels to account for their different kinematic regions. After the correction functions were applied, residual mismodellings, i.e. moderate non-closures in comparisons between data and simulation, were observed in the $p_{\mathrm{T}}^{\mathrm{miss}}$ distribution in the 0-lepton channel, and the p_{T}^{W} distribution in the 1-lepton channel. The magnitude of these mismodellings depends on the m_{Vh} and ranges from 1% to 10%. These residual mismodellings were not corrected, but the data-to-simulation ratios were used to define systematic uncertainties in the shapes of the $m_{\mathrm{T},Vh}$ and m_{Vh} distributions. These uncertainties were applied to all backgrounds as uncorrelated nuisance parameters.

A crucial question in resonance searches is how many mass hypotheses to probe and what step size to use. Choosing a mass spacing that is too small wastes resources (such as CPU and storage space), while choosing a mass spacing that is too coarse may leave the search insensitive to a narrow signal. Ideally, the choice of mass spacing should be guided by the mass resolution of an analysis. We found that the m_{Vh} resolution ranges from 2%–5% (5%–9%) for the resolved (merged) 2-lepton event categories, and from 7%–12% (9%–12%) for the resolved (merged) 1-lepton event categories. Furthermore, we found that the $m_{\mathrm{T},Vh}$ resolution ranges from 8% to about 28% (from 12% to 17%) for the resolved (merged) event categories. The resolution of the m_{Vh} and $m_{\mathrm{T},Vh}$ observables worsens within the resolved (merged) event categories with

[34] Newer versions of the SHERPA generator ($\geq$ 2.2.10) and the MadGraph5_aMC@NLO +Pythia 8 generator [249] perform significantly better. However they were not yet available when we performed the search for Vh resonances.

[35] In W/Z+jets events, the $p_{\mathrm{T},jj}$ and large-R jet p_{T} observables are calculated from jets that recoil against the vector boson.

increasing (decreasing) resonance mass. Due to the good mass resolutions in the 1- and 2-lepton channels, we would have required an immense amount of simulated signal samples to achieve an adequate coverage of the mass range. However, generating such a fine grid of signal mass hypotheses is computationally infeasible for a single analysis, given the large number of different searches for new particles performed by the ATLAS collaboration. To address this problem, I suggested testing the same parameter morphing technique [148] that was also used to study of Higgs boson properties (Sections 3.2.2 and 3.2.3). The morphing technique is used to interpolate between two adjacent simulated mass hypotheses to create a number of signal templates at intermediate mass points. Injection tests demonstrated the importance of using such an interpolation technique to generate additional signal templates. We injected a signal with a mass of 440 GeV into the Asimov data and used this dataset as input to our likelihood procedure. When we fitted mass hypotheses of 420 GeV and 460 GeV to the adjusted Asimov data, the corresponding p_0-values were reduced by 3-4 orders of magnitude compared to when we fitted the 440 GeV signal hypothesis to the adjusted dataset. The validation studies of the morphing technique and injection tests are detailed in the Ph.D thesis of one of my students [240].

One of the biggest challenges in this analysis was developing and validating the fit models used to perform the search for Z' and W' bosons. For example, the search for the Z' boson was based on a combined maximum-likelihood fit in the signal and control regions of the resolved and merged 0-lepton and 2-lepton channels. In total, the proxy for the resonance mass (i.e. the m_{Vh} or $m_{\mathrm{T},Vh}$ distribution) was probed in 13 distinct categories. The modelling of the backgrounds had to be understood in each of these regions, which was a non-trivial task. This is for example because the kinematics of the final state particles vary strongly from one region to another, and thus the normalisation of a certain background may be different between these regions. Hence, dedicated nuisance parameters were introduced into the fit model to account for extrapolation effects between the signal and control regions, the resolved and merged categories, and the different lepton channels. In total, the likelihood function contained around 160 nuisance parameters describing the systematic uncertainties, about 30 nuisance parameters accounting for extrapolation effects between regions, about 250 parameters describing the per-bin uncertainties of the Monte Carlo statistics, 12 nuisance parameters governing the normalisations of minor backgrounds, 4 freely-floating normalisation factors to determine the global normalisation of the dominant backgrounds, and one normalisation factor for the hypothesised signal process. With this configuration, the search for Zh (and Wh) resonances has one of the most complex fit models among all resonance searches performed by the ATLAS collaboration. Studying the behavior of each of the nuisance parameters in the fit was a time-consuming task, as each pulled or constrained nuisance parameter had to be understood.

Nuisance parameters related to modelling uncertainties usually require particular attention. This is because they are estimated by comparing the shapes of the fit input distributions between different Monte Carlo models. However, Monte Carlo samples typically have limited statistics. Therefore, modelling uncertainties are vulnerable to large statistical fluctuations in the tails of the distribution or in extreme regions of the phase space. Large variations in single bins of the uncertainty band can lead to instabilities in the fit or significant overconstraints of the corresponding nuisance parameters. To mitigate these issues, we developed a new method based on Gaussian kernel smoothing [250, 251] to remove statistical fluctuations from the individual uncertainties [246].

Outlook

The results of our searches for Zh and Wh resonances are expected to improve significantly when implementing one of the recently developed $X \to b\bar{b}$ tagging algorithms [56, 252] into the analysis workflow.

Furthermore, migrating to the newest SHERPA versions for the predictions of the Z+jets, W+jets and di-boson backgrounds will significantly improve the modelling of the data and reduced modelling uncertainties. However, the best way forward is to reduce our reliance on Monte Carlo predictions. I.e. future versions of the Zh and Wh resonance searches should attempt to estimate the contributions of the Z+jets and W+jets backgrounds using data-driven methods, similar to those used by CMS [188, 191].

In the future, it will be important to extend the current ATLAS search efforts to cover alternative production modes for Zh and Wh resonances. Vector-boson fusion is the most obvious next promising production mode to consider[36]. The CMS collaboration has already performed searches in this channel. However, their results only cover a mass range above 1 TeV and they are not yet sensitive to any of the commonly considered benchmark models. A study of the prospects for Zh resonance searches in the 2-lepton channel using ATLAS data was conducted by one of my Ph.D. students [246], and the expected limits on the production cross section times branching ratio range from around 0.2 pb for $m_{Z'} = 300$ GeV to 4 fb for $m_{WZ'} = 3$ TeV. For resonance masses below $m_{Z'} = 400$ GeV, the limits are close to the cross section predictions of the HVT benchmark model C.

Interpreting the results with additional signal models, such as models with extra dimensions that predict decays of the Kaluza-Klein excitations of the W and Z bosons via $W_{KK} \to Wh$ and $Z_{KK} \to Zh$, would be another attractive addition to these search efforts [172]. Another possibility are axion-like particles decaying to Zh [253].

Further thoughts on how to improve or extend future searches for Vh and other di-boson resonances are discussed in more detail in Section 4.6.

4.2.2 Search for pseudoscalars

The most recent search for pseudoscalars decaying via $A \to Zh$ by the ATLAS collaboration focuses on the ggF and b-associated production modes. Representative lowest order Feynman diagrams for these processes are depicted in Figure 37. The relative importance of these two production modes depends on the type of model and the choice of model parameters. For example, the ggF production mode is dominant over the full parameter space of Type-I and Lepton-specific 2HDMs, while the b-associated production mode becomes dominant in Type-II and Flipped 2HDMs for $\tan\beta$ values above 7.5. Other production modes are significantly smaller and are therefore not considered for these searches[37].

The searches for pseudoscalars use the same signal regions as the searches for heavy vector bosons plus regions that require additional b-tagged jets to enhance the sensitivity to the b-associated production mode. For events with resolved $h \to b\bar{b}$ decays, an additional category with at least three b-tagged small-R calorimeter jets is exploited. For events with merged $h \to b\bar{b}$ decays, additional categories are used, with b-tagged VR track-jets that are outside of the large-R jet.

[36] ATLAS has already performed searches for heavy di-boson resonances produced via VBF and decaying via $X \to W^+W^-$, $X \to ZZ$, or $X^\pm \to W^\pm Z$ [181, 185].

[37] The production of pseudoscalars in association with top quarks can have sizeable cross sections (up to a few hundred femtobarn for low A boson masses) in the Type-I and Lepton-specific 2HDMs for $\tan\beta << 1$ [254]. However, the contribution to the total production cross section is always below 1% for all common 2HDM types. Nevertheless, it may be beneficial to probe for Zh resonances in $t\bar{t}A$ production in the future. The multiplicity and kinematics of the additional final state particles can be exploited to obtain larger signal-to-background ratios than for other production modes. A first search for the $t\bar{t}A$ production mode was recently performed in $t\bar{t}A(\to t\bar{t})$ events [255].

The event categories with at least three b-tagged jets are sensitive to the production of top-quark pairs in association with additional bottom or charm quarks. However, the state-of-the-art Monte Carlo generators do not model this type of background well. Therefore, fits that include the $b\bar{b}A$ production mode of the pseudoscalar use a different background model than the one used for the searches for heavy vector bosons. Specifically, the top-quark backgrounds are split into two components. This categorisation is based on the flavour of the additional jets in the event, following the same strategy as described in Reference [256]. Events containing at least one b or c-quark jet not originating from a top quark, W, Z or Higgs boson decay are classified as top + hf (with hf denoting 'heavy flavour'), while all other events are classified as top + lf (with lf denoting 'light flavour'). The top + lf component also includes contributions from the single-top-quark, $t\bar{t} + V$, and $t\bar{t} + h$ processes. Another difference from the background model of the Z' search is that the Z + hf background normalisation in regions with at least three b-tagged jets is determined independently from regions with lower b-tagging multiplicity. This is to account for the decreased perturbative accuracy of the background predictions for events with additional heavy-flavour jets in the final state. The background composition in regions with at least three b-tagged jets is indicated in Figure 41. This figure shows the distribution of the transverse Vh mass of the 0-lepton channel and the invariant Vh mass of the 2-lepton channel.

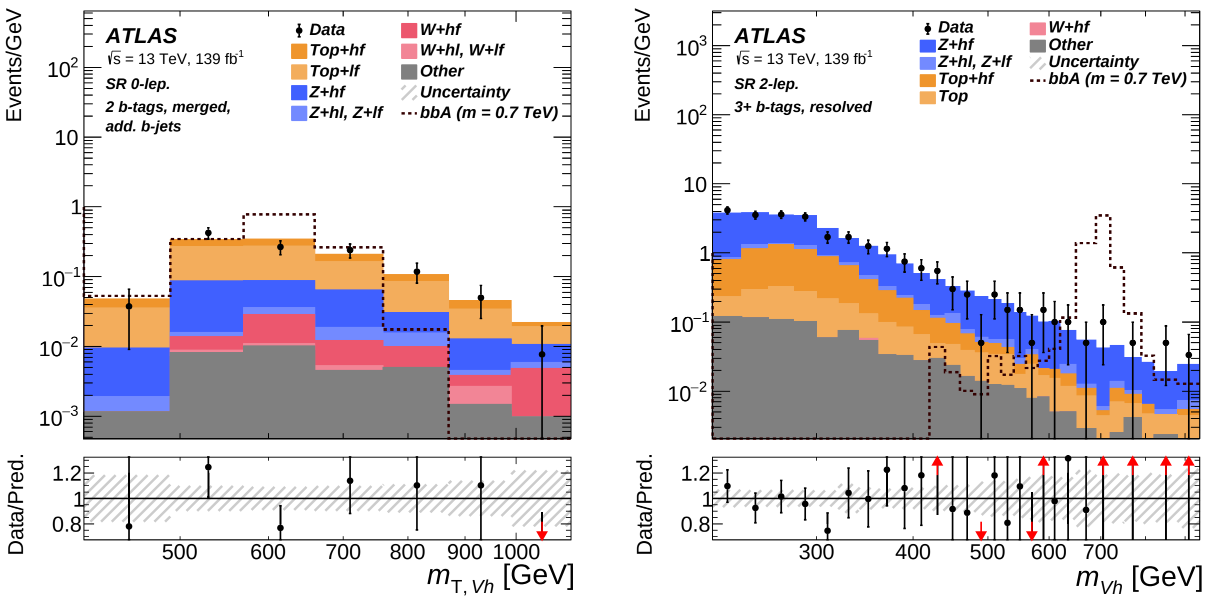

(a) (b)

Figure 41: Post-fit distributions of (a) the transverse Vh mass of the merged 0-lepton signal region and (b) the invariant Vh mass of the resolved 2-lepton channel presented for events with at least three b-tagged jets. The quantity on the vertical axis is the number of data events divided by the bin width in GeV. In each plot, the last bin contains the overflow. The background prediction is shown after a background-only maximum-likelihood fit to the data. The signal for the benchmark 2HDM model with $m_A = 0.7$ TeV, normalised to $\sigma \times B(Zh) \times B(h \to b\bar{b}) = 0.1$ pb, is shown as a dashed line. The lower panels show the ratio of the observed to the estimated SM background. The background uncertainty band shows the post-fit statistical and systematic components added in quadrature [190].

The searches for pseudoscalars are based on combined fits in the 0-lepton and 2-lepton channels. A variety of fit configurations are used to interpret the available data in different contexts.

One dimensional fits are performed to independently set upper limits on the ggF and $b\bar{b}A$ production cross sections times the $A \to Zh$ branching fraction in a mass range from 220 GeV to 2 TeV. The search for the ggF production mode follows the same strategy as the search for the Z' boson. On the other hand, the fit model for the search for the $b\bar{b}A$ production mode includes the signal cross section as a free parameter and the global normalisations of the top + lf, top + hf, Z + hf, and Z + hl backgrounds. In events with three or more b-tagged jets, a different normalisation factor is used for the Z+jets background than in events with fewer b-tagged jets. This is because the deviations between the data and the simulations increase as a function of the b-tagging multiplicity.

Figure 42 shows the 95% CL upper limits on the product of the cross section for the $gg \to A$ and $gg \to b\bar{b}A$ production modes and their respective branching ratio to Zh. The upper limits on the ggF production mode of the pseudo-scalar closely resemble the upper limits on the Z' production. This search also sees mild deviations at a resonance mass of 500 GeV, with the same significance as the Z' search. The $b\bar{b}A$ search also displays a similar excess for this mass value, but with a smaller significance of 1.6σ corresponding to a local p-value of 0.059. The lower local significance in the $b\bar{b}A$ search is due to the lack of excess in data in the additional signal regions used for this search.

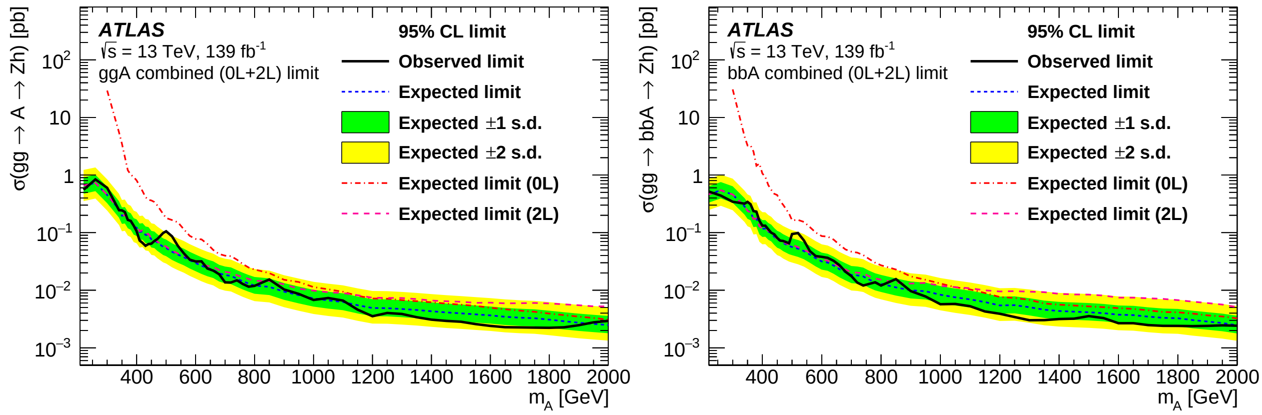

(a) (b)

Figure 42: Observed and expected upper limits at 95% CL on the product of the cross section for (a) $gg \to A$ and (b) $gg \to b\bar{b}A$ and their respective branching fraction to Zh from the combination of the 0-lepton (0L) and 2-lepton (2L) channels. For both searches, a branching fraction of 0.569 for $h \to b\bar{b}$ is assumed [190].

Furthermore, simultaneous fits of the ggF and $b\bar{b}A$ signal hypotheses are performed for a variety of different $\sigma_{b\bar{b}A}$ and σ_{ggA} combinations. For each combination, a negative log-likelihood (NLL) value is calculated, and the best estimate is obtained at the point where the NLL curve reaches its minimum. Contours at 68% and 95% CL are determined relative to the minimum. The background model is the same as that used for the $b\bar{b}A$ search. The expected and observed results for these fits (i.e. the two-dimensional likelihood scans for various pseudoscalar masses m_A) are presented in Figure 43. For each mass hypothesis, the best-fit value is compatible with the absence of a signal. The largest difference between the observed and expected best-fit values is found for a resonance mass of $m_A = 500$ GeV. However, this excess does not exceed beyond the expected 95% CL contour.

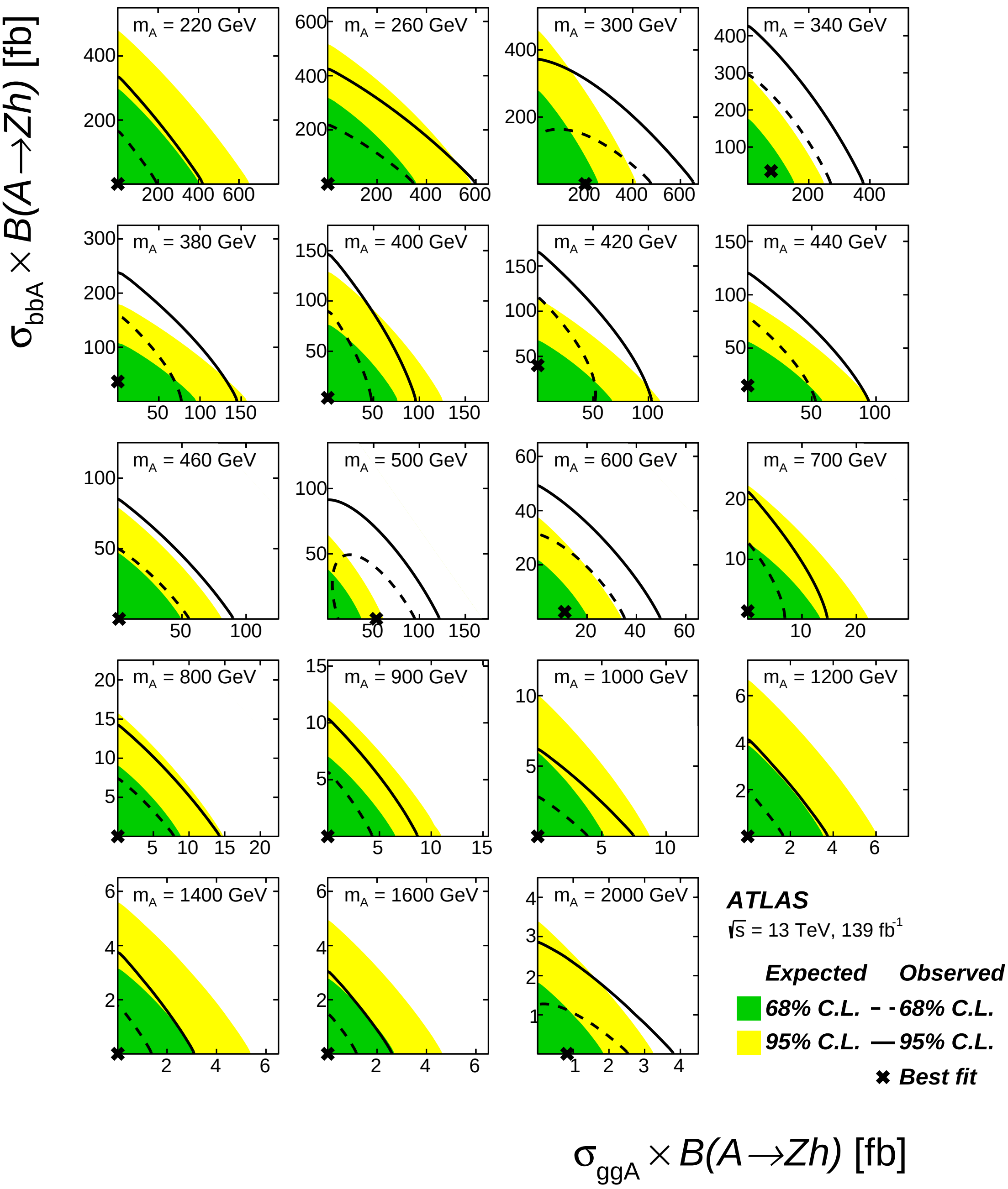

Figure 43: Expected and observed two-dimensional likelihood scans of the b-associated production cross section times branching fraction, $\sigma_{b\bar{b}A} \times \mathcal{B}(A \to Zh)$, vs. the gluon-gluon fusion cross section times branching fraction, $\sigma_{ggA} \times \mathcal{B}(A \to Zh)$, for a given A boson mass (m_A). For each mass, a variety of different cross-section hypotheses are scanned. At each point, $2\Delta(NLL)$ is calculated, defined as the negative-log-likelihood (NLL) of the conditional fit to the Asimov and observed datasets with $b\bar{b}A$ and ggA fixed to their values at that point and with the minimum NLL value at any point subtracted. The best-fit point and the preferred 68% and 95% CL boundaries are found at $2\Delta(NLL)$ values of 0.0, 2.30 and 5.99, respectively [190].

In addition, combined fits of the ggF and $b\bar{b}A$ production modes are performed. In these fits, one free parameter is used to determine the total cross section of the two components. These fits are performed for different admixtures of the ggF and $b\bar{b}A$ contributions, as well as different A boson widths Γ_A. The background model is the same as for the one dimensional fits targeting the $b\bar{b}A$ production mode. The results of these fits are used to constrain the parameter space of the 2HDM. Representative results from these studies are presented in Figure 44. These figures show the constraints on the parameter space of the 2HDM Type-I and Type-II scenarios as a function of the parameters $\tan\beta$ and $\cos(\beta-\alpha)$ for a pseudoscalar mass of 700 GeV and as a function of the parameters $\tan\beta$ and m_A for $\cos(\beta-\alpha) = 0.1$.

The shapes of the expected and observed exclusion contours are determined by the interplay of two factors: the cross-section limits, which decrease as a function of the pseudoscalar mass m_A, and the signal production cross section times the $A \to Zh$ branching fraction at given m_A, $\tan\beta$, and $\cos(\beta-\alpha)$ values. The branching fraction decreases significantly at $m_A = 350$ GeV because the $A \to t\bar{t}$ decay becomes kinematically possible, but increases again at higher m_A values. The parameter $\tan\beta$ controls the admixture of the ggF and b-quark associated production, leading to a varying sensitivity as a function of $\tan\beta$.

The search for $A \to Zh$ resonances generally has low sensitivity around $\cos(\beta-\alpha) \approx 0$, as the branching fraction for $A \to Zh$ decays vanishes in the alignment limit $\cos(\beta-\alpha) \to 0$. However, for model scenarios with a pseudoscalar mass of 700 GeV, $\cos(\beta-\alpha)$ values down to around 0.07 can be excluded at the 95% CL for 2HDM Type-I and Type-II scenarios. Furthermore, $\tan\beta$ values greater than 10 are excluded for Type-I 2HDMs. The sensitivity to high $\tan\beta$ values is enhanced for Type-II 2HDM scenarios, due to the larger cross section for the b-quark associated production process. The narrow inclined regions with no sensitivity for $\tan\beta$ values below 10 are caused by a vanishing $h \to b\bar{b}$ branching fraction.

For a value of $\cos(\beta-\alpha) = 0.1$, the $A \to Zh$ search is sensitive to pseudoscalars from Type-I 2HDMs with masses between 220 GeV and 1200 GeV for low $\tan\beta$ values. For Type-II 2HDMs, the search is sensitive to pseudoscalars with masses between 220 GeV and 1000 GeV for low $\tan\beta$ values, and between 450 GeV and 1500 GeV for large $\tan\beta$ values.

The CMS collaboration has also performed searches for heavy pseudoscalars decaying via $Z' \to Zh \to \nu\nu b\bar{b}, \ell^{\pm}\ell^{\mp}b\bar{b}$ and $Z' \to Zh \to \ell^{\pm}\ell^{\mp}\tau^{\pm}\tau^{\mp}$. These searches have been conducted using an integrated luminosity of 35.9 fb^{-1} collected at $\sqrt{s} = 13$ TeV [257, 258]. However, since these searches are based on a partial Run 2 dataset, their limits are significantly weaker than the most recent limits obtained by ATLAS. Searches for heavy pseudoscalars are also performed in other decay channels. In addition to the $A \to Zh$ search, the ATLAS collaboration has also performed searches for heavy pseudoscalars decaying to $\tau^{\pm}\tau^{\mp}$ and $t\bar{t}$ [255, 259, 260]. A comprehensive comparison of the results from these different searches is given in Section 4.5.2 for a selection of different benchmark models.

Challenges

The searches for heavy pseudoscalars were conducted by the same analysis team that performed the searches for heavy vector bosons. Both analyses are generally very similar, which means that they faced almost the same challenges. The main difference between both searches was the background model. For the A boson search, the top quark backgrounds were split into two components: top + hf and top + lf, following the developments from other ATLAS analyses [256] performed in final states with large b-jet multiplicities.

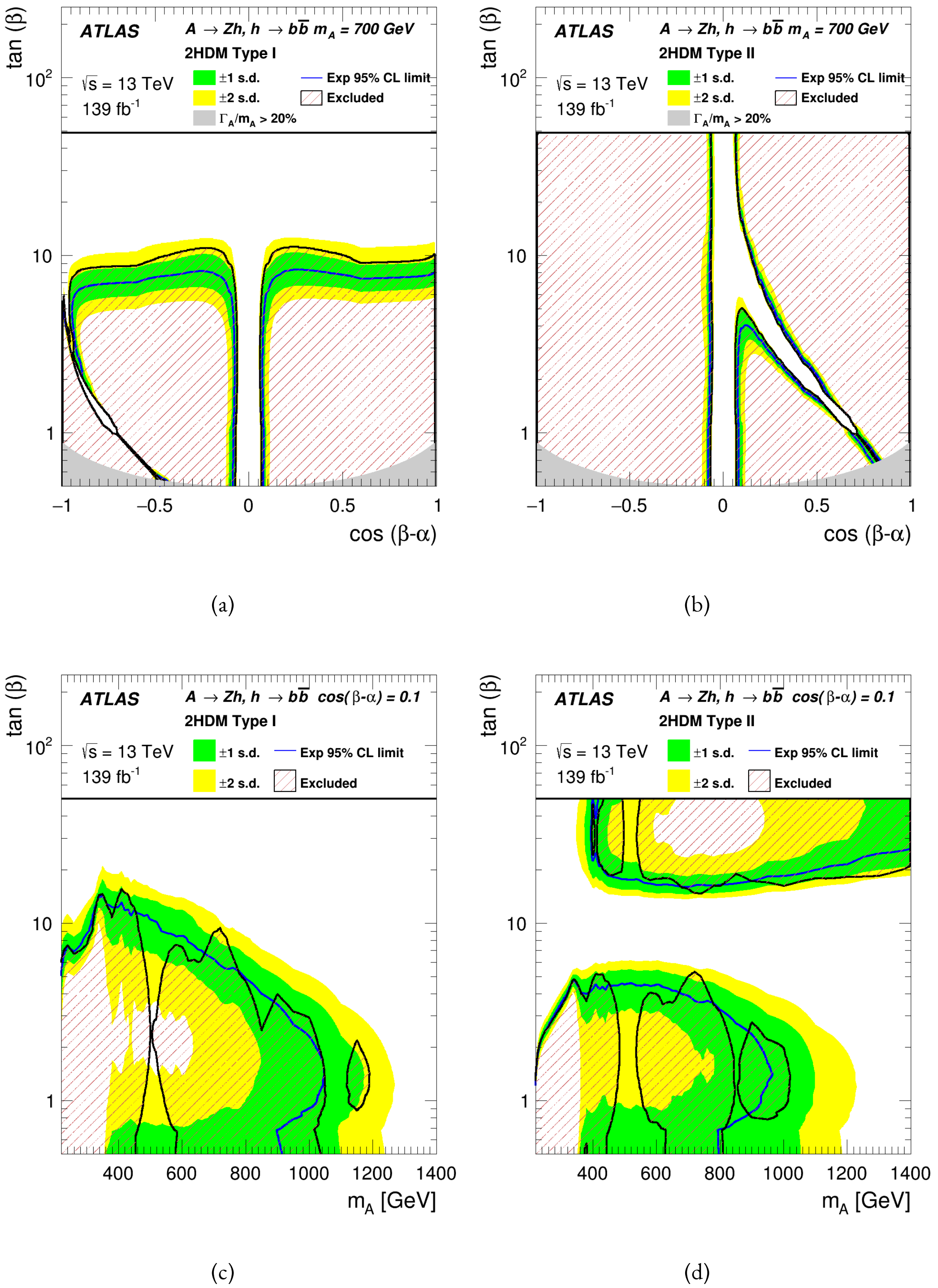

Figure 44: The interpretation of the cross-section limits in the context of the 2HDM Type-I (left column) and Type-II (right column) as a function of the parameters $\tan\beta$ and $\cos(\beta-\alpha)$ for $m_A = 700$ GeV (top row) and as a function of the parameters $\tan\beta$ and m_A for $\cos(\beta-\alpha) = 0.1$ (bottom row). Variations of the natural width up to $\Gamma_A/m_A = 20\%$ have been taken into account. For the interpretation in the Type-II 2HDM, the b-quark associated production is included in addition to the ggF production mode [190].

In the previous iteration of the $A \to Zh$ search [243], the $t\bar{t}$ background was modeled as a single component, with independent normalisation scale factors applied to regions with ≥ 3 b-tagged jets and regions with ≤ 2 b-tagged jets. However, we found that this background model was not capabale of describing the data sufficiently well when using the significantly larger dataset. Therefore, I suggested moving to a more sophisticated background model, which was implemented and vallidated by one of my students. Detailed studies on this topic are documented in his Ph.D thesis [240]. Splitting the top quark backgrounds into two components instead of using only one component significantly improved the fit model by increasing the quality of the likelihood fit. This is evident from the improved overall agreement between the data and the simulation, as well as the reduced tensions in several nuisance parameters.

Outlook

In the future, the $A \to Zh$ search could be improved by exploiting spin- and CP-sensitive observables, such as the $\cos\theta^*$ and other angles in the rest frame of the A boson decay [261], to further separate the signal process from relevant backgrounds. These observables should particularly increase the sensitivity to low-mass pseudoscalars.

It would also be valuable to extend the list of benchmark models used to interpret the $A \to Zh$ search in the near future. The signatures probed by this analysis are relevant for CP-violating 2HDMs [212, 213], models predicting dark matter mediators such as the 2HDM + Z' model [262] or different scenarios of the N2HDM [263], Higgs Triplet models such as the Georgi-Machacek model [218] and 3HDMs [264].

4.3 Search for charged Higgs bosons decaying to Wh

Various theories predicting an extended scalar sector predict also the existence of at least one set of charged Higgs bosons in addition to the discovered neutral one: for example models that add a second doublet [127] or one or more triplets [233, 234, 235, 236, 265] to the scalar sector. The main production and decay modes of these new particles depend strongly on the studied model. In the alignment limit of the 2HDM, the dominant production mode for charged Higgs bosons heavier than the sum of the top and bottom quark masses is expected to be in association with a top quark and a bottom quark (tbH^+), while the dominant charged Higgs boson decay modes are $H^\pm \to tb$ or $H^\pm \to \tau\nu$ depending on the choice of model parameters. Other production and decay modes are less relevant in these scenarios. However, less commonly probed extended scalar sector models, such as N2HDMs, 3HDMs, or Higgs triplet models, predict that other decay and production modes can be significant. One example is the charged Higgs boson decay into a SM-like Higgs boson, h, (with $m_h = 125$ GeV) and a W boson: $H^\pm \to W^\pm h$. This decay mode has not yet been searched for by neither ATLAS nor CMS, although various models predict significant branching ratios for this decay channel [128, 264, 266, 267].

The ATLAS collaboration is currently finalising a first search for a charged Higgs boson produced in association with a top quark and a bottom quark, followed by decays via $H^\pm \to W^\pm h \to \ell\nu bb$ or $H^\pm \to W^\pm h \to qqbb$. This search is based on 140 fb^{-1} of pp collision data and probes events consistent with the final state $\ell\nu b\bar{b}b\bar{b}q\bar{q}$, where $\ell = e$ or μ. The charged lepton can originate either from the decay chain of the charged Higgs boson or from the decay chain of the associated top quark. Representative lowest-order Feynman diagrams for this process, including the two possible decay chains, are depicted in Figure 45. The event kinematics of the $\ell\nu b\bar{b}$ and $q\bar{q}b\bar{b}$ decay channels can differ significantly depending on the considered H^+ mass hypothesis. Therefore, dedicated signal regions are defined for each decay mode based on selection requirements on kinematical observables.

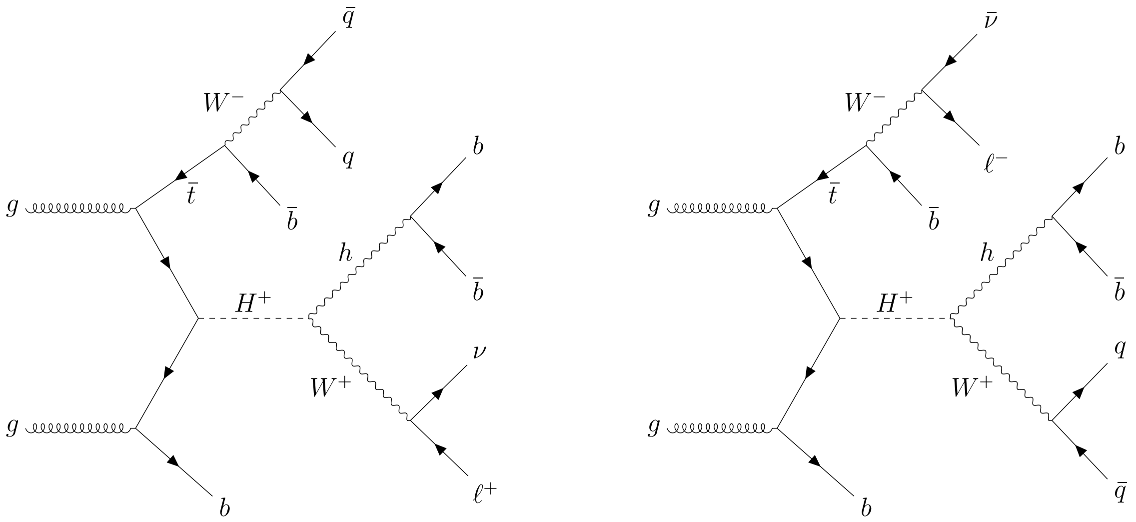

(a) (b)

Figure 45: Representative lowest order Feynman diagrams of $pp \to tH^+b$ production and subsequent decays via $H^+ \to W^+h \to \ell^+\nu bb$ (a) and $H^+ \to W^+h \to qqbb$ (b).

To ensure high sensitivity to both low- and high-mass charged Higgs bosons, two different analysis techniques are used, similar to other di-boson resonance searches. At low charged Higgs boson masses, when the final state particles have a relatively low Lorentz-boost, the decay products of the Higgs boson and the hadronically decaying W boson are reconstructed as individual jets (such decays are referred to as "resolved"). At high charged Higgs boson masses, when the final state particles have a relatively large Lorentz-boost, the Higgs boson and the hadronically decaying W boson are reconstructed as single large-R jets (such decays are referred to as "merged"). Consequently, this search for charged Higgs bosons targets events that contain exactly one prompt electron or muon, a significant amount of missing transverse momentum, and either at least five small-R jets of which at least three must be b-tagged for resolved event topologies or at least one large-R jet for merged event topologies. Furthermore, in the merged event topologies, the recently developed $X \to b\bar{b}$ tagging algorithm [56] is used to identify boosted Higgs boson decays to a collimated bottom-quark pair.

For low charged Higgs boson masses, the $\ell\nu b\bar{b}$ and $q\bar{q}b\bar{b}$ decay channels produce identical detector signatures. To distinguish between them, events are classified based on the reconstructed leptonic top-quark mass, $m_{\text{top}}^{\text{lep}}$. This observable is calculated from the four-vector sum of a selected b-tagged jet, the charged lepton, and the neutrino[38]. Given that several jets in the event are b-tagged, the b-tagged jet that minimises $|m_{\ell\nu j} - 172.5\,\text{GeV}|\,/m_{\ell\nu j}$ is chosen. Here, $m_{\ell\nu j}$ corresponds to the invariant mass of the combined b-tagged jet, charged lepton, and neutrino four-vector. The $m_{\text{top}}^{\text{lep}}$ observable peaks around the top-quark pole mass for events containing a leptonically decaying top quark (as in the $q\bar{q}b\bar{b}$ decay channel), while it exhibits broader distributions at higher values for events from the $\ell^{\pm}\nu b\bar{b}$ decay channel. Hence, events distributed around the top-quark pole mass enter the resolved $q\bar{q}b\bar{b}$ analysis categories, while events with larger $m_{\text{top}}^{\text{lep}}$ values enter the resolved $\ell^{\pm}\nu b\bar{b}$ analysis categories.

[38] As for the studies presented in Section 4.2, the momenta of the neutrino in the x- and y-directions are obtained from the corresponding components of the $E_{\text{T}}^{\text{miss}}$ vector, while the neutrino momentum in z-direction is calculated by imposing a W boson mass constraint on the lepton–neutrino system.

For sufficiently high charged Higgs boson masses, the ambiguities between the $\ell\nu b\bar{b}$ and $q\bar{q}b\bar{b}$ decay channels are largely reduced due to their distinct detector signatures. Hence, the events in the merged analysis are classified based on the number and properties of selected large-R jets. Events enter the merged $q\bar{q}b\bar{b}$ analysis categories if they have exactly one $X \rightarrow b\bar{b}$-tagged large-R jet and another large-R jet with a mass m_J within the W boson mass window, $50\,\text{GeV} < m_J < 110\,\text{GeV}$. Events with exactly one $X \rightarrow b\bar{b}$-tagged large-R jet but without a second large-R jet with mass around the W boson pole mass enter the merged $\ell\nu b\bar{b}$ analysis categories. Consequently, the charged Higgs boson four-vector is reconstructed using a charged lepton, a neutrino, and one large-R jet (for the $\ell\nu b\bar{b}$ channel) or two large-R jets (for the $q\bar{q}b\bar{b}$ channel).

Machine learning techniques are employed to process the selected events and enhance the separation between the hypothesised signal process and relevant backgrounds. In the resolved analysis categories, two sets of boosted decision trees are used to reconstruct the charged Higgs boson decay. These boosted decision trees are trained to identify the correct pairing of final state particles that correspond to the decay chain of the charged Higgs boson. Separate boosted decision trees are trained for the events in the $q\bar{q}b\bar{b}$ and $\ell^{\pm}\nu b\bar{b}$ analysis categories, where the kinematics of the lepton and jets as well as their invariant masses are used as input features for the training. The boosted decision trees are then iteratively applied to all possible pairings of final state objects[39]. The pairing with the largest output score of the boosted decision tree, $w_{\text{BDT}}^{\text{max}}$, is used to construct the four-momentum vector (and hence the invariant mass) of the charged Higgs boson candidate. Both sets of boosted decision trees are found to perform well in reconstructing the targeted final states. At a charged Higgs boson pole mass of 500 GeV, the final state is reconstructed correctly in about 70% (60%) of the time for the $H^{\pm} \rightarrow W^{\pm}h \rightarrow \ell\nu b\bar{b}$ ($H^{\pm} \rightarrow W^{\pm}h \rightarrow q\bar{q}b\bar{b}$) decay mode. The success rates increase with increasing pole mass values, reaching around 90% for both decay modes at masses above 1 TeV. With this approach, the charged Higgs boson masses are determined with a resolution below 10% for both decay chains.

In the merged analysis categories, two sets of neural networks are used to further separate between the selected signal and background events within the merged $q\bar{q}b\bar{b}$ and $\ell^{\pm}\nu b\bar{b}$ analysis categories. Kinematic observables such as the azimuthal angular difference and the pseudorapidity difference between the reconstructed final state objects are exploited for the training of the networks. The invariant mass of the charged Higgs boson candidates in the merged analysis categories is reconstructed with a resolution below 9% for the $\ell\nu b\bar{b}$ decays and below 6% for $q\bar{q}b\bar{b}$ decays.

The final signal and control regions are defined by applying additional selection criteria on top of the preselection and event classification requirements. The signal and control regions of the resolved analysis are obtained based on selection requirements on the w_{BDT}^{max} observable. Events with low w_{BDT}^{max} values enter control regions, while events with high w_{BDT}^{max} values enter the signal regions. Events enter the signal regions of the merged analysis, if the mass of the $X \rightarrow b\bar{b}$ tagged large-R jet is in a window around the Higgs boson pole, $95\,\text{GeV} < m_h < 140\,\text{GeV}$. The analysis regions are further split into low-NN-score, medium-NN-score and high-NN-score signal regions based on the output score of the neural network. In addition, two sets of sideband control regions are defined in the merged analysis by inverting the selection requirement on m_h. Low-mass sidebands ($50\,\text{GeV} < m_h < 95\,\text{GeV}$) are defined to constrain the W+jets background, while high-mass sidebands ($140\,\text{GeV} < m_h < 250\,\text{GeV}$) are defined to target backgrounds containing boosted top-quarks.

[39] To be precise, the boosted decision trees trained in the $\ell\nu b\bar{b}$ categories. are applied to all possible lepton, neutrino, and di-jet pairings, while the boosted decision trees trained in the $q\bar{q}b\bar{b}$ categories are applied to all possible four-jet pairings in the event.

The various signal and control regions of the resolved analysis categories are further split according to the overall number of jets (j), and the number of b-tagged jets (b) in the event. In this context, four exclusive categories are defined: $5j3b$, $5j \geq 4b$, $\geq 6j3b$, and $\geq 6j \geq 4b$. The signal and control regions of the merged analysis categories are also further split based on the number of additional b-tagged jets (b), considering only small-R jets that are spatially separated from either of the two large-R jets. Two exclusive categories are defined this way: $0b$ and $\geq 1b$.

The background composition in the signal and control regions depends on the event categories and b-jet multiplicities. In the resolved categories, the by far most dominant background source is the $t\bar{t}$+jets production. Other backgrounds such as W/Z+jets or Wt production are significantly smaller. In the merged categories, the most significant background contributions originate from $t\bar{t}$+jets and W+jets production. Contributions from diboson, SM Vh, $t\bar{t}+h$ and $t\bar{t}+V$ are small in all channels. Background contributions from events containing non-prompt leptons are found to be negligible.

All backgrounds are estimated from samples of simulated events, with the normalisation of the dominant backgrounds obtained from data. In addition, shape corrections are derived for the $t\bar{t}$+jets production process using a data-driven approach. To describe the $t\bar{t}$ backgrounds sufficiently well at high jet multiplicities, events containing top-quark pairs are categorised according to the flavour of jets produced in association with the $t\bar{t}$ system. The same procedure as described in Section 4.2.2 is used for this purpose, yielding a $t\bar{t}$ + HF and $t\bar{t}$ + LF component. Other background processes are grouped into four components: single-top-quark production includes (s- and t-channels, Wt production, tZq, and tWZ), VV&V+jets (includes W/Z+jets, WW, ZZ, and WZ), $t\bar{t}+X$ (includes $t\bar{t}+h$, $t\bar{t}+W$, and $t\bar{t}+Z$), and the remaining backgrounds referred to as "Others" (includes $tHjb$, tWh, $t\bar{t}t\bar{t}$, and SM Vh).

In order to test for the presence of a massive charged Higgs boson in data, the invariant mass distribution of the reconstructed $\ell\nu b\bar{b}$ and $q\bar{q}b\bar{b}$ systems are probed for a localised excess using a binned maximum-likelihood approach. Two separate fits are performed in this search: one for the resolved analysis and the other for the merged analysis. Each fit includes the dedicated signal and control regions for the $qqbb$ and $\ell\nu bb$ analysis categories. The fit models differ between the two analyses. The resolved fit has the signal cross section and the global normalisation factor of the $t\bar{t}$+HF background as free parameters, while the merged fit has the signal cross section and the global normalisation factors of the $t\bar{t}$ + HF, $t\bar{t}$ + LF, and VV & V+jets backgrounds as free parameters.

The results from this search will be made public by the ATLAS collaboration within the next few months.

Personal contributions

The work on this analysis has been conducted with strong contributions from a Ph.D student of the TU Munich and MPI, whom I supervised, as well as myself. In addition, researchers from the University of Bonn, the Queen Mary University of London, the institute for High Energy Physics in Barcelona (IFAE), and the McGill University in Montreal gave significant contributions to these efforts. In total, 12 researchers were involved in this project.

These efforts built upon the initial studies carried out by two B.Sc. and one M.Sc. student from the TU Munich, whom I supervised. Their work provided a valuable foundation for the development of the final analysis strategies for both the resolved and merged event categories. Preliminary results from an early stage of the analysis were presented in a master's thesis [268]. Beyond initiating this project, I significantly contributed as the analysis contact and lead editor of the manuscript soon to be submitted for journal publication. In my role as the coordinator of this analysis, I was responsible for organising the analysis efforts, assigning tasks, chairing meetings, setting timelines and discussing the needs of our analysis with the coordinators of the physics group for Di-Higgs and Di-Boson searches. Under my supervision, the Ph.D student designed the analysis techniques used to search for the resolved $H^{\pm} \to W^{\pm}h \to \ell\nu b\bar{b}$ decays, defined the corresponding signal and control regions, performed data-to-simulation comparisons, evaluated the theory uncertainties in the signal and background processes, developed the fit model for the search for merged $H^{\pm} \to W^{\pm}h$ decays and derived upper limits on the production cross section times branching fraction. In addition to these active contributions, I provided guidance and support to students and postdocs from other institutes involved in this analysis, ensuring their contributions to be integrated into the workflow of our analysis.

Challenges

To finalise the analysis, we had to overcome a number of challenges. A key hurdle was distinguishing the correct decay products of the charged Higgs boson from the complex final state of leptons and up to six jets. At low charged Higgs boson masses, jets from the associated top quark could be easily misidentified as those from the charged Higgs boson decay. To address this, we developed sets of boosted decision trees that effectively identified the true decay products of the charged Higgs boson, enabling us to accurately reconstruct its invariant mass.

Another significant challenge in this analysis was accurately modelling the $t\bar{t}$+jets production process, particularly in the high jet and b-jet multiplicity signal regions of the resolved analysis. Given that the additional jets in the $t\bar{t}$+jets events are simulated in the parton shower, high jet multiplicities and the hardness of additional jet emissions were found to be mis-modelled. To overcome the mismodelling, we had to develope a dedicated correction procedure to correct the simulated samples. The correction procedure is based on reweighting the $t\bar{t}$+jets events as a function of the $H_{\mathrm{T}}^{\mathrm{all}}$ observable[40] obtained from fits to the data-to-simulation ratio in a validation regions, which includes events with at least five jets of which exactly two have to be b-tagged. The reweighting procedure is performed separately for different jet multiplicity intervals, distinguishing events with five, six, seven, or at least eight jets. The reweighting factors are described as a function of the $H_{\mathrm{T}}^{\mathrm{all}}$ observable:

$$r_i\left(H_{\mathrm{T}}^{\mathrm{all}}\right) = \frac{N_i^{\mathrm{Data}}\left(H_{\mathrm{T}}^{\mathrm{all}}\right) - N_i^{\mathrm{MC,non}-t\bar{t}}\left(H_{\mathrm{T}}^{\mathrm{all}}\right)}{N_i^{\mathrm{MC},t\bar{t}}\left(H_{\mathrm{T}}^{\mathrm{all}}\right)},$$

where N_i is the number of events in a $H_{\mathrm{T}}^{\mathrm{all}}$ interval and the i-th jet bin. The ensemble of $r_i\left(H_{\mathrm{T}}^{\mathrm{all}}\right)$ is fitted per jet bin with a parametric functional form. The choice of the functional form was crucial in this context. We tested an exponential-plus-sigmoid function, a hyperbola-plus-sigmoid function, and a 2nd-order-polynomial-plus-first-order-exponential function. Based on the results of this comparison, the exponential-plus-sigmoid function fitted the data best. Therefore, we applied this function to correct the $t\bar{t}$+jets background within the $5j3b$, $5j \geq 4b$, $\geq 6j3b$ and $\geq 6j \geq 4b$ regions of the resolved analysis. Since the merged analysis channels are more inclusive with respect to jet multiplicity, they are less sensitive to the modelling of additional jet activity, and thus, no such correction was necessary.

[40] The $H_{\mathrm{T}}^{\mathrm{all}}$ observable is defined as the scalar sum of the transverse momenta of all jets and the charged lepton in the event.

Similar to the Z' and W' searches (presented in Secion 4.2), developing the fit models for the $H^{\pm} \to W^{\pm}h$ search was a major challenge due to its high complexity. With up to 20 analysis regions contributing to the fit, the final fit model is even more intricate than those used in the Z' and W' searches. Consequently, a substantial amount of time was dedicated to designing and validating this model.

Outlook

Future search efforts for charged Higgs bosons could benefit from exploring additional decay channels. Intriguing candidates, according to theorists, are the $H^{\pm} \to W^{\pm}H(\to b\bar{b})$ and $H^{\pm} \to W^{\pm}H(\to t\bar{t})$ channels (with $m_H \neq 125$ GeV) [269]. These decay modes are predicted to be dominant across a significant portion of the 2HDM's parameter space and other extended Higgs sector models, and they are both not yet studied at the LHC.

Furthermore, charged Higgs bosons can also be indirectly probed through high-precision measurements of the Higgs boson's properties. In particular, the $h \to \gamma\gamma$ decay is sensitive to the presence of charged Higgs bosons due to their contributions at the one-loop level (see Figure 46). The studies presented in Reference [269] show that for charged Higgs boson masses of $m_{H^+} \lesssim 200$ GeV, the $h \to \gamma\gamma$ decay rate can deviate from the SM prediction by up to $\pm 17\%$. For charged Higgs boson masses of $m_{H^+} \gtrsim 300$ GeV, positive deviations from the SM of up to 5% and negative deviations of up to 15% are possible. Constraints from Higgs boson property measurements are expected to become competetive with direct search efforts during the HL-LHC era.

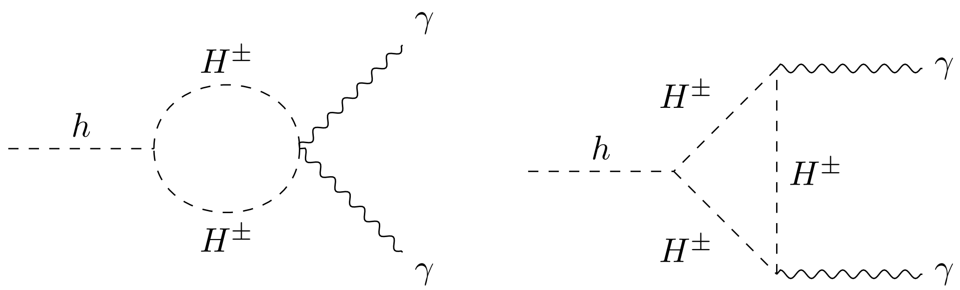

Figure 46: Contribution of a charged Higgs boson to the $h \to \gamma\gamma$ decay at one-loop level [269].

4.4 Summary of di-boson resonance searches

The ATLAS collaborations has published a large variety of di-boson resonance searcbes (see Table 2), in addition to the searches for Zh and Wh resonances. The following section highlights a few recently published results, most of which were derived while I was the coordinator of the ATLAS di-boson resonance search efforts.

Searches for ZZ, WZ, and WW Resonances

The searches for ZZ, WZ, and WW resonances are performed in fully-leptonic final states ($\ell^{\pm}\ell^{\mp}\ell^{\pm}\ell^{\mp}$, $\nu\nu\ell^{\pm}\ell^{\mp}$, $\ell^{\pm}\nu\ell^{\pm}\ell^{\mp}$, and $\ell^{\pm}\nu\ell^{\mp}\nu$), in semi-leptonic final states ($\ell^{\pm}\ell^{\mp}qq$, $\ell^{\pm}\nu qq$, and $\nu\nu qq$), and in fully-hadronic final states ($q\bar{q}q\bar{q}$). Searches in the fully-leptonic final states provide the highest sensitivity at resonance masses of a few hundred GeV, while searches in the semi-leptonic final state are superior to searches in the other final states for masses at the TeV scale.

Recently updated results on searches for heavy di-boson resonances in the $ZW^{\pm}/ZZ \rightarrow \nu\nu q\bar{q}$ (0-lepton), $W^{\pm}W^{\mp} \rightarrow \ell^{\pm}\nu q\bar{q}$ (1-lepton), and $ZW^{\pm}/ZZ \rightarrow \ell^{\pm}\ell^{\mp}q\bar{q}$ (2-lepton) final states have been published via [185]. These searches are optimised to provide high sensitivity to new heavy particles produced via either of the ggF, qqA, or VBF production modes. Dedicated analysis techniques are used to ensure a high sensitivity to both low- and high-mass resonances. In this sense, the hadronic $V \rightarrow q\bar{q}$ decays are reconstructed either as two separate small-R jets (such decays are referred to as "resolved") or as one single large-R jet (such decays are referred to as "merged") depending on the transverse momentum of the vector boson. For events in the merged event categories, novel jet substructure techniques (see Section 2.3.3) are used to reject backgrounds originating from multi-jet and W/Z+jet production. Furthermore, contributions from top-quark pair events are reduced by vetoing events with b-tagged jets.

The selected candidate events are classified as either VBF-like or qqA/ggF-like using a recurrent neural network (RNN). The RNN exploits the kinematics of additional jets in the final state to enhance the sensitivity to the VBF production mode. The RNN uses the four-momenta of up to two small-R jets that are not considered in the reconstruction of the hadronically decaying vector boson to distinguish between the different production modes. Events with no additional small-R jets are automatically classified as qqA/ggF-like. The distribution of the RNN score is presented in Figure 47 for a variety of signal hypotheses.

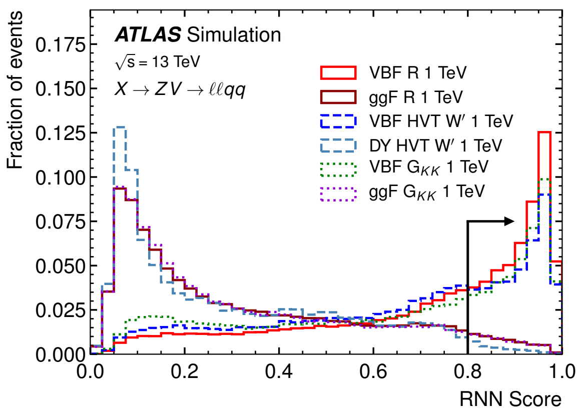

Figure 47: RNN score distributions for the production of a 1 TeV resonance presented for different production modes and spin hypotheses. Events with a RNN score larger (smaller) than 0.8 are classified into a VBF-like (qqA/ggF-like) signal region [185].

The searches for heavy resonances are performed using a combination of fits to the various signal regions of the 0-lepton, 1-lepton, and 2-lepton channels. Separate fits are performed for the $X \rightarrow W^{\pm}W^{\mp}, ZZ$ and $X^{\pm} \rightarrow W^{\pm}Z$ decay chains, which include 21 and 19 different signal regions respectively as well as a selection of dedicated control regions. The fits are performed to the transverse mass m_T spectrum (in the 0-lepton channel) and the invariant mass m_{VV} spectrum (in the 1-lepton and 2-lepton channels) of the reconstructed di-boson system.

Upper limits are set on the production of heavy resonances in the mass range from 300 GeV to 5 TeV through the ggF, qqA, and VBF processes. None of these searches found a statistically significant deviation from the Standard Model expectations. The limits on the production cross section are interpreted in the context of the heavy vector triplet model and models with warped extra dimensions. The cross section limits are then converted into lower mass limits for the considered benchmark scenarios. Based on the results, the ggF production mode for RS radions is excluded at the 95% CL for radion masses below 3.2 TeV. KK gravitions are excluded below masses of 2.0 (0.76) TeV for the ggF (VBF) production modes. Furthermore, the qqA production mode is excluded for Z' bosons with masses below 3.5 (3.9) TeV in the HVT Model A (Model B). For W' bosons, the qqA production mode is excluded for masses below 3.9 (4.3) TeV. Two representative results from these efforts are presented in Figure 48. This figure shows the observed and expected upper limits on the production cross section times branching fractions for searches for radions produced via ggF and KK gravitons produced via VBF.

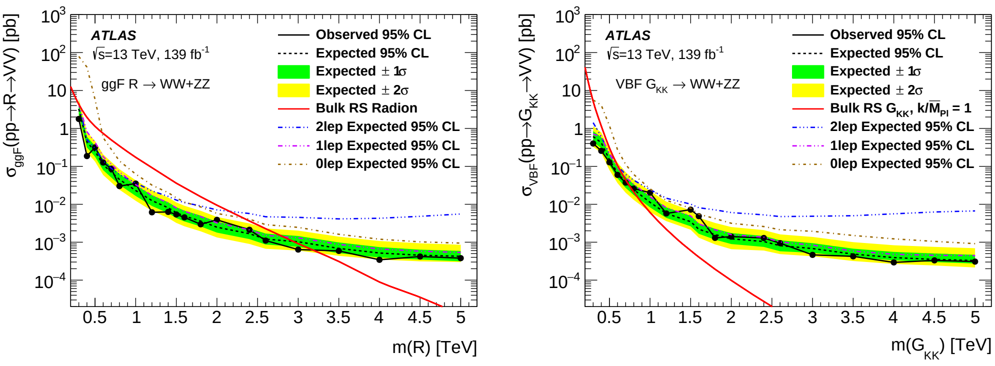

(a) (b)

Figure 48: Observed and expected upper limits at 95% CL on (a) the product of the ggF production cross section times branching fraction for $pp \rightarrow R \rightarrow VV$ and (b) the product of the VBF production cross section times branching fraction for $pp \rightarrow G_{KK} \rightarrow VV$ presented as a function of the resonance mass. The theory predictions (red solid curves) for the Bulk RS radion and KK graviton are overlaid [185].

Searches for WZ resonances are also performed in final states with three charged leptons and missing transverse energy (i.e. $\ell^{\pm}\nu\ell^{\pm}\ell^{\mp}$ where $\ell = e$ or μ). These searches are carried out using two different signal regions. One signal region is targeting the qqA and the other the VBF production mode.

Events with exactly three charged leptons are retained for further analysis. In addition, one of the lepton pairs is required to have an invariant mass that is consistent with the Z boson pole mass. The third lepton and the missing transverse momentum are used to reconstruct the W boson candidate, where the longitudinal component of the neutrino momentum is obtained by constraining the invariant mass of the lepton + $E_{\mathrm{T}}^{\mathrm{miss}}$ system to the pole mass of the W boson.

The signal region that targets the qqA production mode is obtained by placing a selection requirement on the ratio $p_{\mathrm{T}}^{V}/m_{WZ}$ of the boson transverse momentum to the invariant mass of the reconstructed WZ system[41]. Events failing this requirement enter a dedicated control region. The signal region that targets the VBF production mode is populated by events that contain at least two jets in the forward regions of the detector, emitted in opposite hemispheres. An artificial neural network (ANN) is then trained to distinguish the signal process from the relevant backgrounds based on a variety of different input observables such as the invariant mass of the two VBF jets, the azimuthal angular difference between these two jets, the rapidity of the reconstructed W and Z bosons, the missing transverse momentum, and the sum of the transverse momenta of all reconstructed objects in the event. The output score of the ANN is then used to define the

[41] This selection requirement exploits that heavy resonances tend to be produced at rest in the s-channel. Hence, the W and Z bosons should have transverse momenta close to 50% of the resonance mass. At the same time, most backgrounds tend to have $p_{\mathrm{T}}^{V}/m_{WZ}$ values that are relatively low.

VBF signal region and relevant control regions, where events with a relatively large score enter the signal region and events with lower score enter a control region.

The search for WZ resonances is performed by fitting the invariant mass spectrum of the reconstructed WZ system. Separate fits are performed to probe for the qqA and VBF production modes of heavy di-boson resonances individually. The qqA signal and control regions are used to search for new heavy vector bosons, W', while the VBF signal and control regions are used to search for both new heavy vector bosons and heavy charged scalars. The HVT model is used to interpret the results of the heavy vector boson search, while the Georgi–Machacek model is used to interpret the results of the heavy charged scalar search.

Upper limits are set on the production of WZ resonances in the mass range from 200 GeV to 5 TeV for the qqA production mode and in the mass range from 200 GeV to 2 TeV for the VBF production mode. The largest deviation with respect to the Standard Model expectations is found in the search for the VBF production mode at a resonance mass of 375 GeV. This excess corresponds to a local (global) significances of 2.8 (1.6) standard deviations for the spin-0 signal hypothesis and 2.5 (1.7) for the spin-1 hypothesis. No significant excess is found in the search for the qqA production mode.

Based on these results, the production of W' bosons via qqA can be excluded at 95% CL for masses below 2.4 TeV for the HVT model A and below 2.5 TeV for the HVT model B. For the VBF production mode, several benchmark points corresponding to different coupling parameter values can be excluded. For example, masses below 340 GeV, 700 GeV, 945 GeV, and 1145 GeV can be excluded for $c_F = 0$ and $g_V c_H$ values of 1.0, 2.0, 3.0, and 4.0, respectively. Furthermore, heavy charged scalars from the Georgi–Machacek model can be excluded at the 95% CL for $\sin\theta_H > 0.3$ and resonance masses between 200 GeV and 1 TeV.

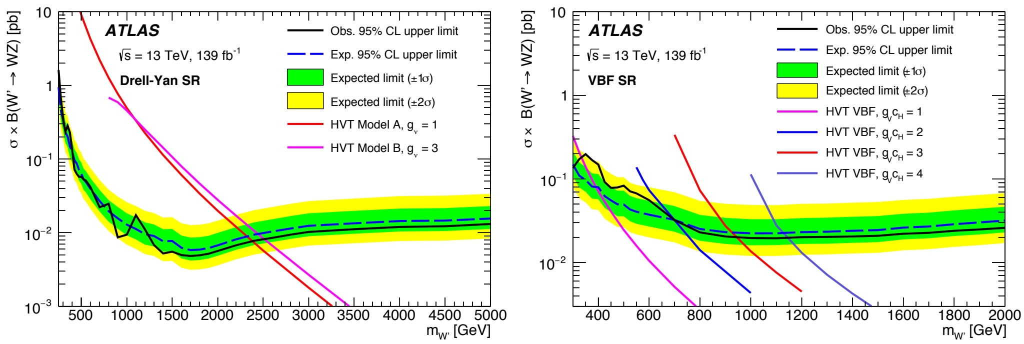

(a) (b)

Figure 49: Observed and expected upper limits at 95% CL on the product of the cross section for $pp \to W'$ and the branching fraction to WZ for (a) the quark-antiquark annihilation and (b) the vector-boson fusion production modes presented as a function of the resonance mass. The LO theory predictions for HVT benchmarks with different values of the coupling parameters g_V and c_H are also shown.

Searches for $\gamma\gamma$, $V\gamma$, and $h\gamma$ Resonances

Searches for heavy di-boson resonances are also performed in final states containing photons. Recent examples are searches for new particles in $\gamma\gamma$ [193, 194, 270], $Z\gamma$ [197, 271], $W^{\pm}\gamma$ [197], and $h\gamma$ [199] events. The search for heavy $h\gamma$ resonances probes for a narrow spin-1 particle, Z', in events consistent with the $Z' \to h\gamma \to b\bar{b}\gamma$ final state, where the two b quarks from the Higgs boson decay are reconstructed as a single large-R jet. An alternative approach to the standard ATLAS $X \to b\bar{b}$ tagging techniques is used to identify the strongly Lorentz-boosted $h \to b\bar{b}$ decays[42] [273].

Events are classified into signal regions if the mass of the large-R jet is within a window around the Higgs boson pole mass, and in control regions if the jet mass is outside of the mass window. The event sample is further split into a single- or double-b-tagged category depending on the number of b-tagged subjets of the large-R jet. Further selection requirements are applied on the photon p_{T} and the large-R jet p_{T} in order to enhance the search sensitivity. The selection requirements are optimised individually for events in the single- and double-b-tagged categories.

The invariant mass of the photon and large-R jet, $m_{J\gamma}$, is used as the final discriminant between the hypothetical signal and background processes, the latter mainly being γ+jets production. The signal is modelled as the sum of a Crystal Ball function [274] and a Gaussian component that describes tail effects. The background model is described via the parametric function $B\left(m_{J\gamma}\right) = (1-x)^{p_1}\, x^{p_2+p_3\log(x)}$, where $x = m_{J\gamma}/\sqrt{s}$ and the three dimensionless shape parameters p_1, p_2, and p_3 are allowed to float freely in the fit to data. The results are obtained as upper limits on the production of heavy resonances in the mass range from 700 GeV to 4 TeV by performing a combined fit of the signal and background functions to data. The distribution of the reconstructed $m_{J\gamma}$ and the upper limits on the production cross section as a function of the resonance mass are presented in Figure 50. No significant excess of events is observed.

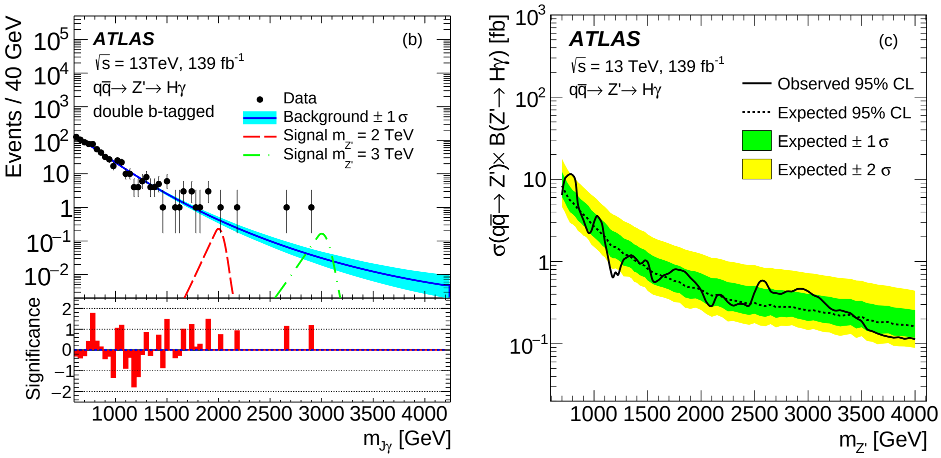

(a) (b)

Figure 50: (a) Distributions of the reconstructed $m_{J\gamma}$ in the double-b-tagged event category presented for two signal hypotheses and the background-only hypothesis, and (b) the observed and expected 95% CL limits on the cross section times branching fraction as a function of the resonance mass [199].

[42] In this technique, the topo-clusters and tracks associated with the large-R jet are boosted to the jet's rest frame, where the decay products resulting from the Higgs boson decay can be more easily separated into a back-to-back topology. The algorithm works by first using the EEkT algorithm [272] to reconstruct exactly two subjets from the topo-clusters. Afterwards, tracks are spatially matched to these subjets. Subsequently, both the subjets and tracks are boosted back to the laboratory frame. Finally, standard ATLAS b-tagging algorithms are applied to each subjet to identify those containing heavy-flavor hadrons.

Di-Higgs resonances

Searches for resonant production of Higgs boson pairs are strongly motivated by almost all extensions of the Higgs sector, including models with additional weak isospin singlets, doublets or triplets [275] as well as by models with extra dimensions [276]. Searches for such new particles are performed at the LHC in the $b\bar{b}b\bar{b}$, $b\bar{b}\tau^+\tau^-$, and $b\bar{b}\gamma\gamma$ final states. Recently, the ATLAS collaboration published a combined search for hh resonances considering these three channels [277].

The combined results as well as the results from the individual three analyses, are presented in Figure 51. The upper limits are set on the production of hh resonances in the mass range from 250 GeV to 5 TeV. The largest deviation with respect to the SM expectations is found around a mass of 1.1 TeV and corresponds to a local (global) signicances of 3.3 (2.1) standard deviations. The combined limits are dominated by the $b\bar{b}\gamma\gamma$ channel for masses below 400 GeV, by the $b\bar{b}\tau^+\tau^-$ channel for masses between 400 GeV and 800 GeV, and by the $b\bar{b}b\bar{b}$ channel for masses above 800 GeV.

The results are also interpreted in the context of the Type-I 2HDM and hMSSM benchmark models, excluding parameter space that was previously allowed by the most sensitive searches for these models [277].

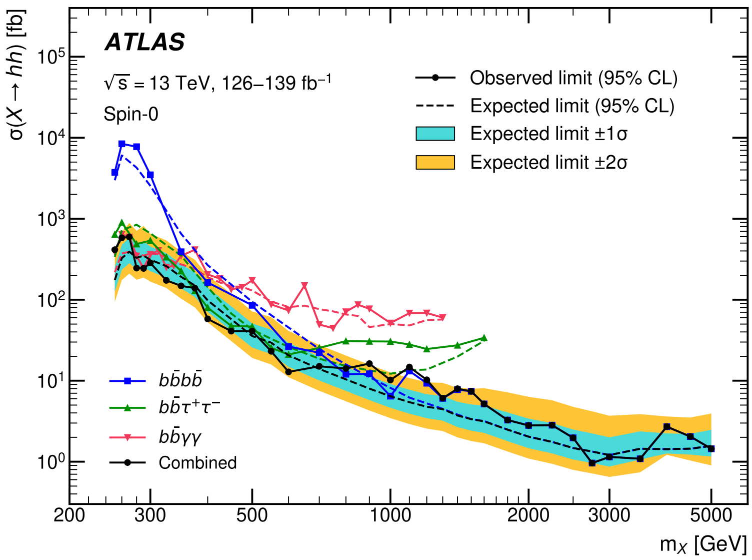

Figure 51: Observed and expected upper limits at the 95% CL on the production cross section for resonant Higgs boson pairs presented as a function of the resonance mass m_X [277].

Di-boson resonance searches via anomaly detection

The increasing popularity of machine learning has led to a surge in new analysis techniques being explored and tested within the particle physics community. Among these, anomaly detection has emerged as a particularly promising approach, attracting growing interest in recent years. Unlike traditional supervised learning, which relies on labeled data from Monte Carlo simulations, anomaly detection can train classifiers directly on collision data, without relying on a predefined physics model. This enables the development of model-agnostic resonance searches, which are not constrained by specific BSM assumptions. Such generic approaches are well-suited to complement the existing model-driven programme of searches for new heavy particles.

The ATLAS collaboration has recently published two searches for heavy di-boson resonances using either weakly- or fully-unsupervised machine learning techniques [278, 279]. Both analyses probe all-hadronic final states using the full LHC Run 2 pp dataset collected by the ATLAS experiment.

The studies presented in Reference [278] describe the search for a new heavy particle Y decaying into another new particle X and a 125 GeV Higgs boson ($Y \to Xh$). The efforts focus on events in which the particle X and the Higgs boson decay via $X \to q\bar{q}$ and $h \to b\bar{b}$, respectively. These hadronic decays are reconstructed via two small-R jets ("resolved") or one large-R jet ("merged"). A variational recurrent neural network [280] (VRNN), which consists of a variational autoencoder whose latent space is updated at each time step of a recurrent neural network is trained on large-R jets in data exploiting jet substructure information. The VRNN's anomaly score defines a signal region selecting X candidates based on their incompatibility with background jets. Two additional signal regions are defined for merged and resolved decays of a nominal two-prong X benchmark signal, used for validation. All three signal regions also impose stringent requirements on the Higgs boson candidate's mass and $X \to b\bar{b}$ tagging score [56].

Separate neural networks are used to estimate the normalisation and shape of the dominant multi-jet background within these signal regions, extrapolating from dedicated control regions which are obtained by modifying the selection requirements on the h boson candidate. The distribution of the invariant mass of the X and h candidates, m_Y, is then probed for bumps within different windows around m_X in the three signal regions. The largest excess in the anomaly score signal region is found in the m_X interval $[75.5, 95.5]$ GeV and reaches a global significance of 1.43σ. The m_Y distribution corresponding to this m_X window is shown in Figure 52, along with the post-fit background distribution. These results are also interpreted as 95% CL upper limits on the cross section $\sigma(pp \to Y \to Xh \to q\bar{q}b\bar{b})$ spanning the two-dimensional space defined by m_Y and m_X. Examples of such upper cross section limits are presented in Figure 52 (b) for seven benchmark signal processes.

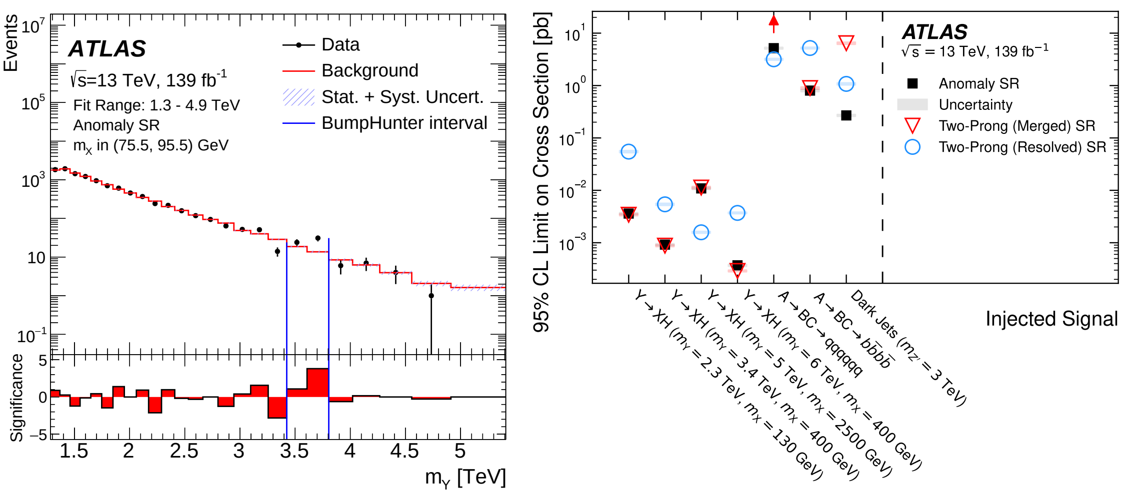

(a) (b)

Figure 52: (a) the m_Y distribution associated with the m_X interval $[75.5, 95.5]$ GeV in the anomaly signal region, where the background estimation is fully data-driven. Both the statistical and systematic uncertainties are included. (b) the 95% CL upper limit on the cross section for seven benchmark signal processes, comparing the anomaly, two-prong merged, and two-prong resolved signal region selections [278]. All signals are labeled by the masses of the BSM particles except the $A \to BC$ signals, where $m_A = 3$ TeV, $m_B = 200$ GeV, and $m_C = 400$ GeV.

Comparison of mass exclusion limits

Figure 53 shows a set of mass exclusion limits at 95% CL on a selection of HVT, bulk RS, and RS1 benchmark scenarios from recent ATLAS di-boson searches. The mass exclusion limits are obtained from 11 individual searches that target a variety of different final states. Depending on the benchmark model, production mode, and decay channel, heavy resonances are excluded in their respective simplified theories in a mass range spanning from a few hundred GeV up to several TeV. This comparison also highlights the complementary nature of the individual search channels: i.e. searches in fully-leptonic final states tend to provide the strongest constraints on new heavy resonances at low masses, while searches in semi-leptonic and fully-hadronic final states tend to provide the strongest constraints at medium and high masses.

Most of these efforts were carried out, while I was the coordinator for the ATLAS di-boson resonance searches. As a group coordinator, I was responsible for steering all aspects of the data analysis and publication process. This included ensuring that all steps of the analyses and papers met the quality standards of the collaboration.

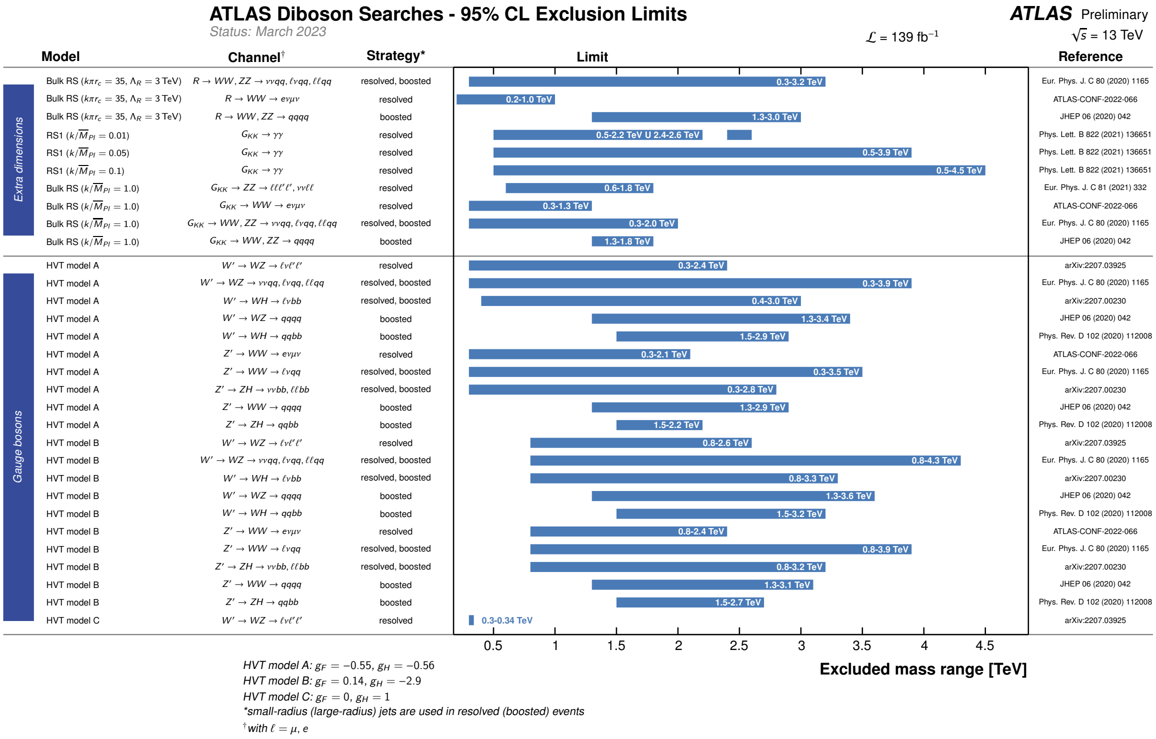

Figure 53: A set of mass exclusion limits at 95% confidence level from ATLAS di-boson searches for new phenomena. The results are based on the full 13 TeV pp collision dataset [175].

4.5 Combination of searches for heavy resonances

The ATLAS and CMS collaborations conduct searches for new heavy resonancess in a wide range of final states. In addition to the aformentioned searches for di-boson resonances, the search programme of the LHC experiments is complemented by searches for heavy resoannce decaying into pairs of leptons or pairs of (heavy) quarks. To exploit the full potential of the available data, statistical combinations of the individual analysis channels are performed within selected theoretical frameworks or benchmark models[43]. By combining individual searches, which typically constrain only a subset of the coupling parameters, significantly stronger constraints on relevant model parameters can be obtained.

Dedicated combination efforts are performed for different classes of models. Prominent examples are combinations of searches for heavy vector bosons, which have a long-standing tradition in both ATLAS and CMS [281, 282]. Similar efforts are done to combine searches for dark matter mediators [283, 284] and searches for supersymmetric partners of SM particles [285, 286, 287, 288].

The most recent efforts to combine the searches for heavy Z' and W' bosons performed by the ATLAS collaboration [289] are summarised in Section 4.5.1. These efforts combine recent searches for di-boson resonances with searches for di-lepton and di-quark resonances. Searches for di-boson resonances also play a major role in models with BSM Higgs bosons. However, the ATLAS collaboration has not yet performed a dedicated combination of results from its various BSM Higgs boson search efforts. Therefore, Section 4.5.2 provides a brief overview of recent BSM Higgs boson searches, summarises their interpretation in a selection of general benchmark models, and compares the exclusion contours from relevant analyses.

4.5.1 Combination of searches for new heavy vector bosons

The most recent efforts to combine searches for new heavy vector bosons use a total of 21 individual analyses of independent final states, all of which use proton-proton collision data collected during 2015-2018 with the ATLAS detector. Table 3 lists the individual searches entering the statistical combination, details their final states, and specifies the discriminating variable used for each search.

The searches for heavy particles decaying to pairs of quarks ($q\bar{q}$, $b\bar{b}$, $t\bar{t}$, and $t\bar{b}$) and third-generation leptons ($\tau^{\pm}\nu$ and $\tau^{\pm}\tau^{\mp}$) are included for the first time in a heavy resonance combinations of ATLAS.

The individual analysis channels are optimised independently aiming to reach maximal sensitivity to search for new heavy resonances. However, for the statistical combination of these channels, minimal additional selection requirements are introduced to ensure that collision events are not used in more than one analysis channel. These additional selection requirements are chosen to maximise the sensitivity of the combined result. Additionally, the design of the combination's statistical model is carefully considered, and the correlations of the uncertainties between individual analysis channels are extensively studied.

The combined results are obtained by a simultaneous maximum likelihood fit to the signal discriminants (i.e. invariant or transverse masses) across all of the analysis channels. Each analysis contributes to the fit with dedicated signal and control regions, where the background normalisations and their uncertainties are not correlated across the various analysis channels to maximise the flexibility of the background modelling. The results are presented as either one-dimensional upper limits at the 95% CL on the signal production cross section times branching fraction or as two-dimensional constraints on the coupling strengths parameters (i.e. g_H, g_q, and g_ℓ) of the HVT model. The masses of the Z' and W' bosons are assumed to be degenerated for both types of fits, which is a well-motivated approximation in the studied parameter space. Hence, a common mass term $m_{V'}$ is used to parametrise the model predictions.

[43] The model dependency is inevitable in the context of statistical combinations as the relevance of a given production or decay mode (and therefore its contribution to a combined search) depends strongly on the properties (such as mass, couplings and spin) of the hypothesised new particle.

Table 3: Summary of the individual analysis channels (and their respective final states) entering the statistical combination of heavy resonance searches. Entries which are separated by a comma denote an "OR" of different selection requirements. For jets, "j" corresponds to small-R jets, while "J" corresponds to large-R jets. The symbol, $\subset$, denotes any combination of at least one of the objects inside the bracket up to the number shown. Entries denoted with a "–" indicate that no explicite requirement for that object is used. The VBF column indicates whether an analysis has an additional category targeting the VBF production mode. Another column states the discriminating variable used in a given search [289].

Analysis channel	Charged leptons	$E_{\mathrm{T}}^{\mathrm{miss}}$	jets	b-tags	VBF	Discriminating variable	Reference
$WW/WZ \to q\bar{q}q\bar{q}$	0	Veto	$\geq 2J$	–	–	m_{JJ}	[182]
$WZ \to \nu\nu q\bar{q}$	0	Yes	$\geq 1J$	0,1,2	Yes	m_{T}	[185]
$WW/WZ \to \ell^{\pm}\nu q\bar{q}$	$1e, 1\mu$	Yes	$\geq 2j, \geq 1J$	0	Yes	$m_{\ell\nu jj}, m_{\ell\nu J}$	[185]
$WZ \to \ell^{\pm}\ell^{\mp}q\bar{q}$	$2e, 2\mu$	No	$\geq 2j, \geq 1J$	0	Yes	$m_{\ell\ell jj}, m_{\ell\ell J}$	[185]
$WZ \to \ell^{\pm}\nu\ell^{\pm}\ell^{\mp}$	$3 \subset (e, \mu)$	Yes	–	0	Yes	$m_{\ell\nu\ell\ell}$	[181]
$Wh/Zh \to q\bar{q}b\bar{b}$	0	Veto	$\geq 2J$	1,2	–	m_{JJ}	[189]
$Zh \to \nu\nu b\bar{b}$	0	Yes	$\geq 2j, \geq 2J$	1,2	–	m_{T}	[190]
$Wh \to \ell^{\pm}\nu b\bar{b}$	$1e, 1\mu$	Yes	$\geq 2j, \geq 2J$	1,2	–	$m_{\ell\nu jj}, m_{\ell\nu J}$	[190]
$Zh \to \ell^{\pm}\ell^{\mp}b\bar{b}$	$2e, 2\mu$	Veto	$\geq 2j, \geq 2J$	1,2	–	$m_{\ell\ell jj}, m_{\ell\ell J}$	[190]
$\ell^{\pm}\nu$	$1e, 1\mu$	Yes	–	–	–	m_{T}	[290]
$\tau^{\pm}\nu$	1τ	Yes	–	–	–	m_{T}	[291]
$\ell^{\pm}\ell^{\mp}$	$2e, 2\mu$	No	–	–	–	$m_{\ell\ell}$	[292]
$\tau^{\pm}\tau^{\mp}$	0, $1e, 1\mu$	Yes	–	0, ≥ 1	–	$m_{\tau\tau}$	[259]
$t\bar{t}$	0	–	2J	1,2	–	m_{tt}	[293]
$t\bar{b}$	0	–	$\geq (1j, 1J)$	≥ 1	–	m_{tb}	[294]
$t\bar{b}$	1e,1μ	Yes	2j, 3j	1,2	–	m_{tb}	[294]
$q\bar{q}$	0	–	2j	0	–	m_{jj}	[295]
$b\bar{b}$	0	–	2j	1,2	–	m_{bb}	[295]

When calculating one-dimensional upper limits on the production cross section and two-dimensional constraints on the coupling strengths parameters, the signal contributions to each analysis channel are weighted appropriately following the cross section and branching ratio predictions of the HVT benchmark model [221]. As both, the signal cross sections $\sigma\,(pp \to W')$ and $\sigma\,(pp \to Z')$ as well as the branching fractions vary as a function of the coupling strengths parameters, the fits have to be repeated for each set of coupling strengths parameter values. Given the model-dependent assumptions on the cross sections and branching ratios, the obtained results cannot be interpreted as general constraints on the production of new heavy particles.

The local p-values for the individual search channels, subcombinations, and their subsequent full combination are evaluated over the full range of considered pole masses spanning from 400 GeV to 6 TeV. The corresponding scans for the HVT models A, B, and C are depicted in Figure 54. Combining the individual search channels offers the advantage that small local excesses from a true signal present in multiple channels gets reinforced, while larger excesses due to a fluctuation in a single channel do not get corroborated. In fact, a number of 1σ and 2σ fluctuations are observed in the individual search channels targeting the qqA production mode, while their subcombination and full combination scans generally do not exhibit any sizeable excess. For the VBF channels, a modest increase in significance is observed for the combination at a pole mass of 1.5 TeV with a local significance of 2.6σ, where the $qq\nu\nu$, $qq\ell\nu$, and $qq\ell\ell$ channels each show some minor excess over the background expectations.

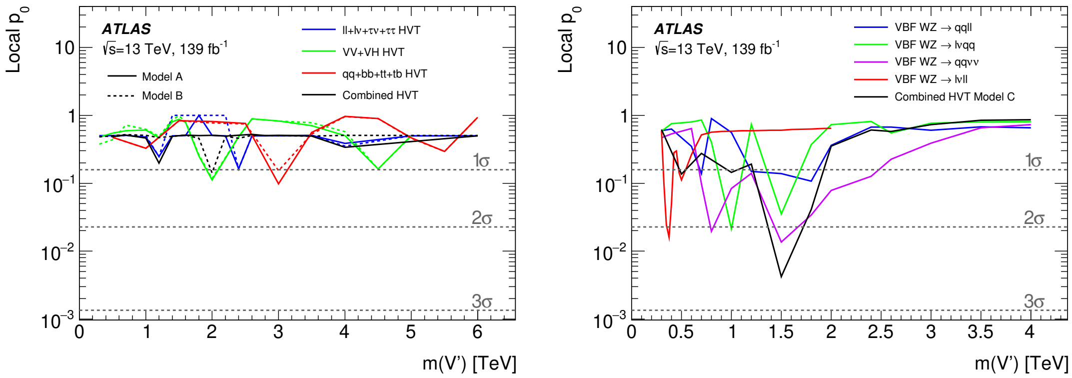

(a) (b)

Figure 54: Local p-values presented for the subcombinations and the full combination at a selection of pole mass hypotheses. Scans are shown for (a) the HVT model A and model B, and (b) the HVT model C [289].

Figure 55 shows the observed and expected 95% CL upper limits on the V' cross section of the qqA and the VBF production modes for the individual analyses and their respective combination, assuming the coupling of the HVT models A, B or C. For the HVT model A, the combined observed upper limits on the production cross section range from around 50 fb for a pole mass of 400 GeV to around 0.2 fb for a mass of 6 TeV. For the HVT model B, the combined observed upper limits on the production cross section range from about 20 fb for a mass of 1 TeV to about 0.3 fb for a pole mass of 5 TeV. As expected, the $VV + Vh$ channels dominate the combined limits under the HVT model B assumption, while the leptonic channels dominate the combined limits for the HVT benchmark model A. The resulting observed (expected) 95% CL exclusion limits on the resonance mass are presented in Table 4. For HVT model A, the observed (expected) lower limit on the mass of V' is 5.8 (5.6) TeV and the corresponding limit in the HVT model B is 4.4 (4.4) TeV. For the HVT model C, the combined observed upper limits on the production cross section range from around 400 fb for a pole mass of 300 GeV to around 0.9 fb for a mass of 4 TeV. The upper limits on the cross section are compared to three different versions of the HVT model C corresponding to bosonic coupling strengths of $g_H = 1$, $g_H = 3$, and $g_H = 6$. For the HVT model C (with $g_H = 1$), the observed (expected) lower limit on the mass of V' is 0.4 (0.5) TeV, for $g_H = 3$ the lower mass limit is 1.0 (1.1) TeV, and for $g_H = 6$ the lower mass limit is 1.5 (1.8) TeV.

Figure 56 presents the exclusion contours at 95% CL on the coupling strengths parameters of the HVT model. The first coupling scenario makes the assumption of common fermionic couplings ($g_f = g_\ell = g_q$), and probes the $\{g_H, g_f\}$ plane. The second coupling scenario assumes independent fermionic couplings, and probes the $\{g_q, g_\ell\}$ plane with $g_H = -0.56$, which takes the value predicted in the HVT benchmark model A. The results are presented here for a resonance mass of 4TeV, while further scans are shown in Reference [289] (contained in the attachment). The scan over the $\{g_H, g_f\}$ plane highlight the complementarity of the bosonic channels compared to the other channels. The bosonic channels can more tightly constrain the region where g_f tends to zero, while the leptonic and quarkonic channels remain strong where g_H is close to zero. Combining all channels results in narrow horizontal bands that cannot be excluded, given that the $q\bar{q}$ production cross section vanishes for $g_f \to 0$. Only searches in the VBF production mode have a chance to constrain this regions, but their sensitivity is currently still too low.

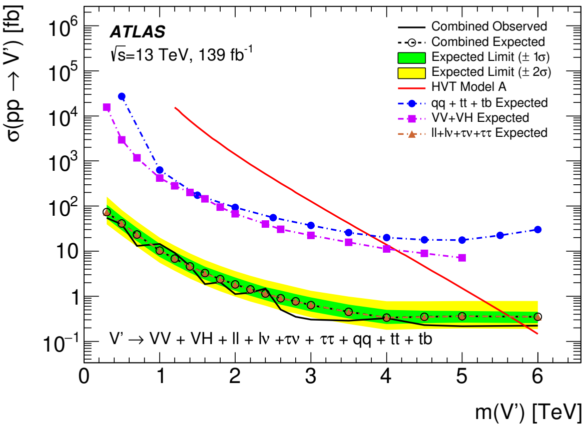

(a)

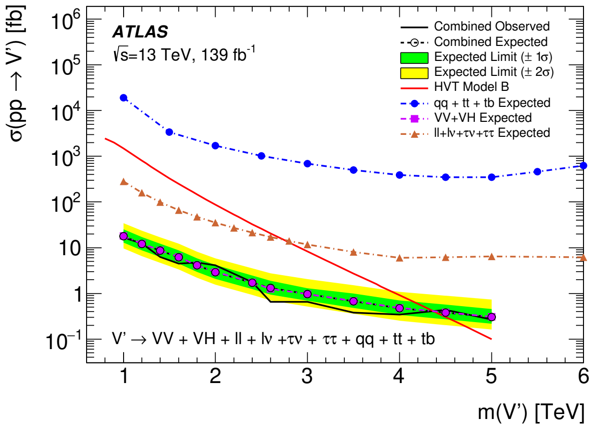

(b)

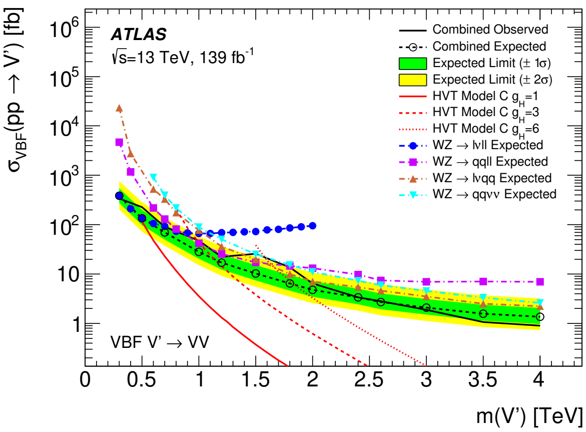

(c)

Figure 55: Observed and expected upper limits at 95% CL on the V' cross section shown as a function of the V' pole mass for the subcombinations and full combination, assuming a) the HVT benchmark model A, b) the HVT benchmark model B, and c) the HVT benchmark model C [289]. For the HVT model A and B, searches targeting the qqA production mode are exploited. For HVT model C interpretations, searches targeting the VBF production mode are used. Furthermore, only the valid range of theory cross-sections is displayed; i.e. regions of parameter space where the corresponding HVT model versions fail to reproduce the SM predictions at lower V' pole masses are omitted.

Comparison to previous results

The constraints at low masses are so strong that the combination of channels does not bring significant improvements. However, at the high masses, such as $m_{V'} = 5$ TeV, the combination of the various analysis channels improves the limits by up to 40%. Compared to the previous combination of resonance searches [281], which used 36.1 fb^{-1} of $\sqrt{s} = 13$ TeV data, the constraints on the HVT model parameters improved siginificantly. For resonance masses of 3 TeV and 4 TeV the expected limit on g_f has improved by 10% to 50% depending on the value of g_H. For a resonance mass of 5 TeV, the improvements are between 40% and 60%.

Table 4: Observed and expected 95% CL mass exclusion limits on the HVT benchmark model A and B for the $q\bar{q}$ production mode [289].

Channel	HVT model A Exclusion Limit		HVT model B Exclusion Limit	
	Observed [TeV]	Expected [TeV]	Observed [TeV]	Expected [TeV]
VV	4.1	4.0	4.3	4.2
Vh	3.6	3.5	3.9	3.9
VV + Vh	4.3	4.1	4.4	4.4
$\ell^{\pm}\nu + \tau^{\pm}\nu + \ell^{\pm}\ell^{\mp} + \tau^{\pm}\tau^{\mp}$	5.8	5.6	3.2	2.7
$t\bar{t} + t\bar{b} + b\bar{b} + q\bar{q}$	4.1	3.8	–	–
Full combination	5.8	5.6	4.4	4.4

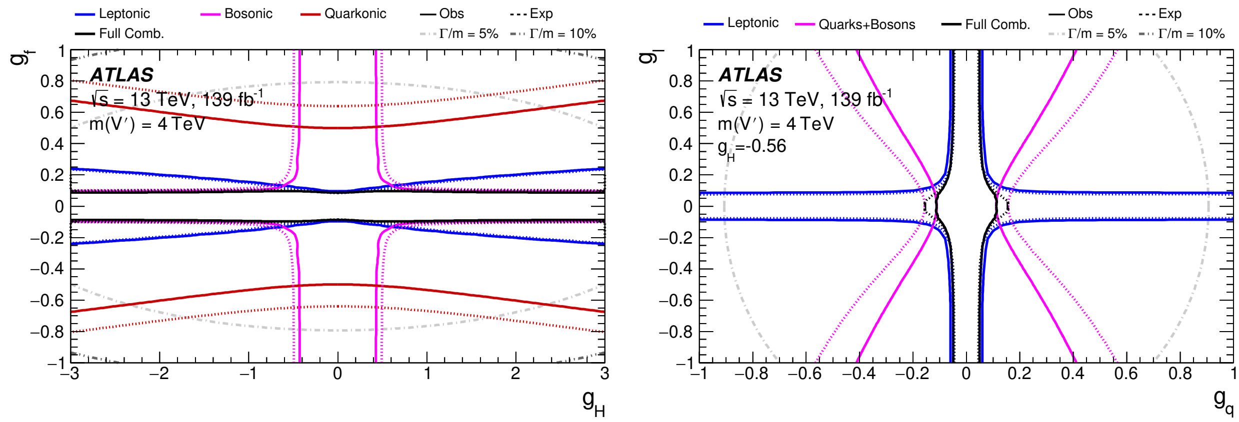

(a) (b)

Figure 56: Observed and expected 95% CL mass exclusion contours for the full combination in the 2D coupling plane for (a) $\{g_H, g_f\}$ and (b) $\{g_q, g_\ell\}$ presented at a V' pole mass of 4 TeV, for the qqA production mode. The dashed grey lines shows the region where the resonance width is 5% and 10% of the resonance mass [289].

Personal contributions

The work on this analysis was carried out by a team of 37 researchers, including myself and a Ph.D. student from TU Munich and MPI under my supervision. This student performed studies to assess the overlap between our Vh resonance search and other searches contributing to the combined analysis, and developed a strategy to remove the identified overlap. Additionally, in my role as the coordinator of the ATLAS diboson resonance searches, I ensured that the combined analysis efforts were set up following the ATLAS quality requirements from the beginning.

Challenges

The combination of multiple resonance searches presented several challenges. A critical one was to ensure orthogonality between the search regions of the various analyses. Initially, significant overlaps were identified between the signal regions of several searches. To assess these overlaps, all analyses were applied to a common set of simulated HVT signal events, covering a range of pole masses from 500 GeV to 3 TeV. This sample was then used to determine the fraction of events shared by each pair of analyses.

The most significant overlap occurred between the $W^{\pm}W^{\mp} \to q\bar{q}q\bar{q}$ search and the $q\bar{q}$ search, with around 90% of events selected by the former also being selected by the latter. Additionally, a substantial overlap of around 70% was observed between the $W^{\pm}h/Zh \to q\bar{q}b\bar{b}$ search and the $q\bar{q}$ search. Significant overlaps were also identified between several of the semi-leptonic di-boson resonance searches: $Zh \to \nu\nu bb$ and $ZW \to \nu\nu qq$, $Zh \to \ell\ell bb$ and $ZW \to \ell\ell qq$, and $Wh \to \ell\nu bb$ and $WW/WZ \to \ell\nu qq$. Their overlaps ranged up to around 20%.

To address the identified overlaps and prevent data events to be counted more than one time, additional selection criteria were implemented. For instance, to achieve orthogonality between the semi-leptonic Vh and VV di-boson searches, the invariant di-jet mass window for events in the resolved Vh category and the invariant mass requirement for large-R jets in the merged Vh category were tightened. These modifications resulted in a slight reduction in the sensitivity of the individual Vh resonance search channels. However, the overall sensitivity to search for new heavy vector bosons was largely maintained because events excluded from one analysis were likely selected by another.

Outlook

The latest version of the combined search for heavy resonances has achieved significant milestones, including surpassing constraints on the HVT coupling parameters set by LEP electroweak precision measurements for resonance masses extending to several TeV.

Future iterations of the combined search for heavy resonances will aim to push the existing mass exclusion limits even higher and further strengthen constraints on the coupling parameters g_H and g_ℓ, when g_q is close to zero. In such scenarios, the VBF production mode will be dominant. However, significant improvements on either front will require a substantially larger dataset, which will take several years of data collection at the HL-LHC.

Future combined searches would also benefit from considering a broader range of signal hypotheses. The current version focuses solely on Spin-1 particles, but interpretations involving heavy Spin-0 and Spin-2 particles are also of considerable interest to the community. Expanding the scope of the combination to include additional spin hypotheses would naturally motivate the inclusion of further search channels, such as $X \to hh \to b\bar{b}b\bar{b}$, $X \to hh \to b\bar{b}\tau\bar{\tau}$, $X \to hh \to \gamma\gamma b\bar{b}$, and $X \to \gamma\gamma$. These channels, while irrelevant for Spin-1 particles, become crucial when searching for Spin-2 particles. Furthermore, combining the results from existing searches for Spin-0 and Spin-2 particles has the potential to significantly strengthen current constraints on extended Higgs sector models and extradimensional models, respectively.

4.5.2 Interpretation of BSM Higgs boson searches

By now, the ATLAS and CMS collaborations have performed a wide range of searches for extra Higgs bosons covering a large variety of different production and decay modes. The most recent searches for additional neutral, singly and doubly charged Higgs bosons based on data from pp collisions at 13 TeVare summarised in Table 5. Lowest order diagrams for the considered production modes are also presented.

The upper limits of the individual heavy Higgs searches are interpreted in the context of specific benchmark models to set exclusion limits on relevant model parameters.

Examples are presented in Figure 57, Figure 58, and Figure 59, which show overlays of observed and expected exclusion limits at 95% CL on parameters of the hMSSM[44], the Type-I 2HDM[45], and the Georgi-Machacek model, respectively.

Figure 57 shows the overlay of exclusion contours from nine different direct searches for BSM Higgs bosons, as well as the exclusion contours obtained from the constraints from combined fits on the coupling parameters of the 125 GeV Higgs boson, which are derived in Reference [167]. The combined fits provide strong constraints on the hMSSM, excluding heavy Higgs bosons for masses below 500 GeV. A large fraction of the hMSSM parameter space is excluded by a search for $H/A \to \tau^{\pm}\tau^{\mp}$ decays, which excludes heavy Higgs bosons with masses up to 2 TeV for large $\tan\beta$ values. Searches for $H^{+} \to t\bar{b}$ decays exclude low $\tan\beta$ regions for masses up to 800 GeV, while searches for $H \to hh \to b\bar{b}b\bar{b}, b\bar{b}\tau^{\pm}\tau^{\mp}, b\bar{b}\gamma\gamma$ decays exclude intermediate $\tan\beta$ regions for heavy Higgs boson masses up to 700 GeV. The search for $A \to Zh$ decays, introduced in Section 4.2.2, excludes heavy Higgs bosons with masses from 220 GeV to 450 GeV and $\tan\beta$ values up to 4.5. However, other direct searches and the constraints from combined coupling parameter measurements exclude the same parameter space.

The results from the $A \to Zh$ search are more relevant in Type-I 2HDMs for scenarios with $\cos(\beta-\alpha) \geq 0.1$. As shown in Figure 58, the $A \to Zh$ search provides significantly stronger constraints on $\tan\beta$ as a function of the BSM Higgs boson mass than the searches for $A/H \to \tau^{\pm}\tau^{\mp}$ and $H \to hh$. Furthermore, the $A \to Zh$ search provides exclusion limits in regions of the paraneter space in which the $H \to hh$ search results are invalid due to a large H boson width[46]. Other BSM Higgs boson searches are not yet sensitive to this parameter space.

Further comparisons are presented in Figure 59 which shows an overlay of observed and expected exclusion limits at 95% CL on the *H5plane* benchmark of the Georgi-Machacek model presented as a function of the mass m_5 of the heavy Higgs bosons and the ratio of vacuum expectation values $sin(\theta_H)$. The exclusion contours are obtained from searches for various di-boson resonances.

Despite the large number of ongoing search efforts, a large fraction of the parameter space of the hMSSM, the Type-I 2HDM and the Georgi-Machacek model remain unconstrained. Searches for so far uncovered signal production or decay modes, and a larger dataser are required to close these gaps.

[44] The hMSSM scenario corresponds to a CP-conserving Two Higgs Doublet model and describes the Higgs sector of the Minimal Supersymmetric Standard Model. It contains five Higgs bosons (h, H, A, $H^{\pm}$), where h has the mass m_h = 125 GeV, and is effectively described by only two free parameters: the ratio of vacuum expectation values ($\tan\beta$) and the mass of the A boson (m_A) [296].

[45] The considered benchmark scenario is CP-conserving with the relevant parameters set to $m_h = 125$ GeV, $m_H = mA = m_{H^{\pm}}$, and $m_{12}^2 = m_A^2 \sin\beta\cos\beta$. This leaves the three parameters m_H, $\tan\beta$, and $\cos(\beta-\alpha)$ free.

[46] For widths beyond 5%, interference effects between the resonant $H \to hh$ production and the SM continuum become substantial. These interference effects are currently not account for in searches for resonant hh production, which is why the limits are not valid for H boson widths above 5%.

Table 5: Summary of recent direct searches for additional Higgs bosons by the ATLAS collaboration based on data from pp collisions at $\sqrt{s} = 13$ TeV [297].

	Production modes	References	Diagrams
Neutral Higgs bosons	gluon–gluon fusion	[194, 193, 298, 259, 299, 190, 300, 178, 301]	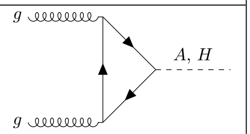
	b/t associated	[259, 299, 190, 255, 302, 303]	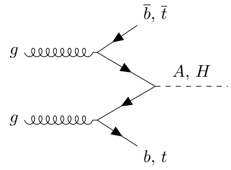
	vector-boson fusion	[298, 178]	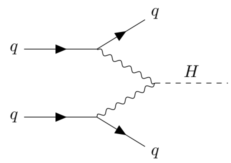
	Higgs Strahlung	[187, 300]	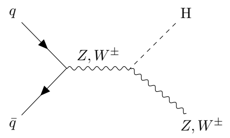
Singly-charged Higgs bosons	via top-quark decays	[304, 305]	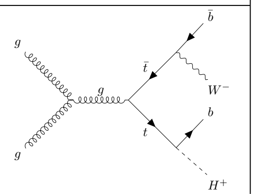
	tb associated	[305, 306]	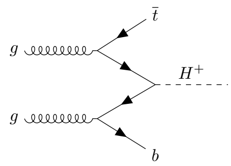
	vector-boson fusion	[181]	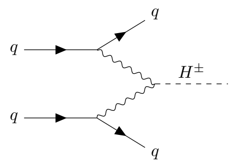
Doubly-charged Higgs bosons	pair production	[307, 308]	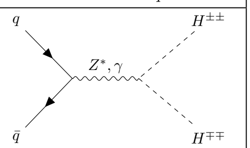
	Higgs boson associated	[308]	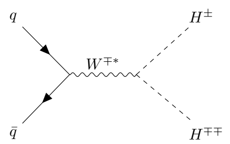

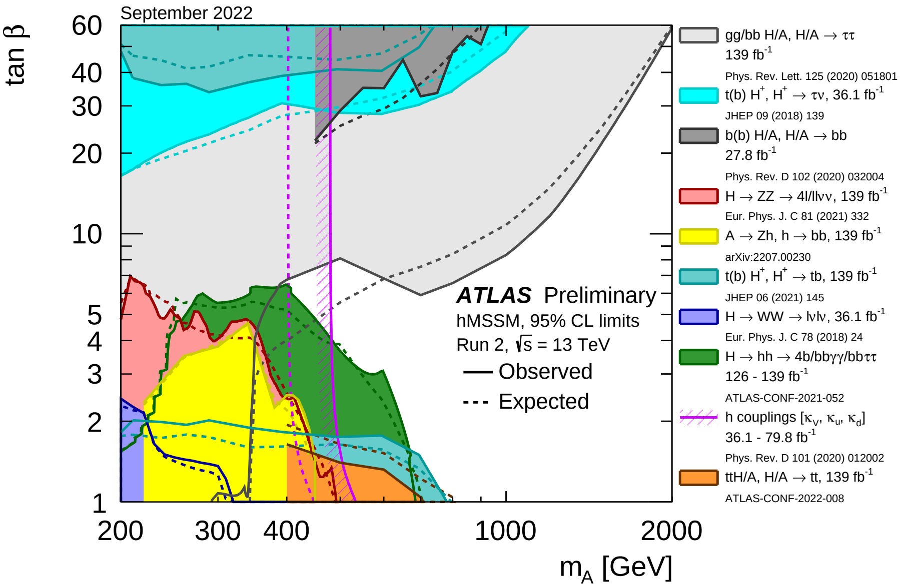

Figure 57: Overlay of observed (indicated as solid lines) and expected (indicated as dashed lines) exclusion limits at 95% CL on the hMSSM scenario presented as a function of the heavy Higgs boson mass m_A and the ratio of vacuum expectation values $\tan\beta$. The limits are obtained via direct searches for heavy Higgs bosons and via fits to the measured rates of the observed Higgs boson production and decays [309].

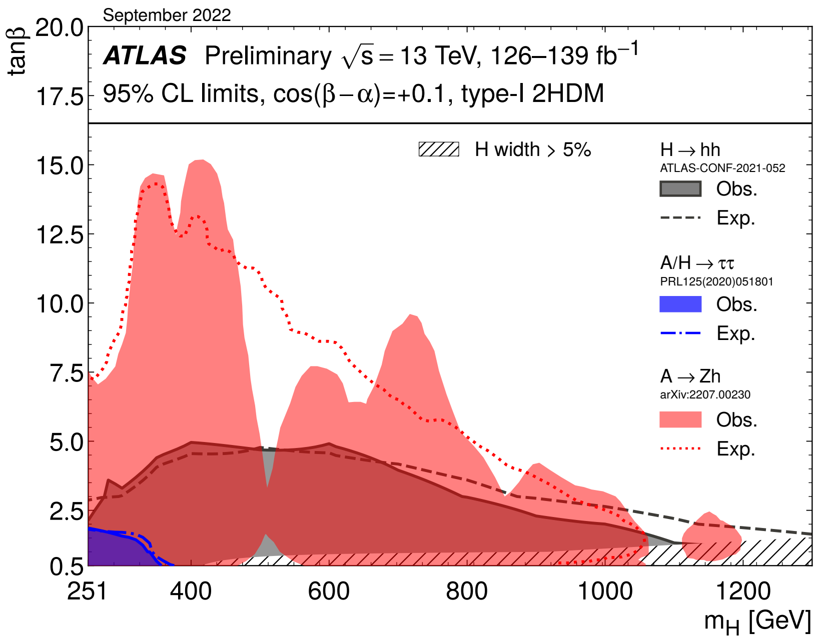

Figure 58: Regions of the $[m_H, \tan\beta]$ plane that are excluded in the type-I 2HDM via direct searches for heavy Higgs bosons for $\cos(\beta-\alpha) = +0.1$. The observed (colour filled areas) and expected (lines) limits are quoted at 95% CL. The hatched region indicates H boson widths larger than 5%, for which the experimental limits for the H boson searches are not valid [309].

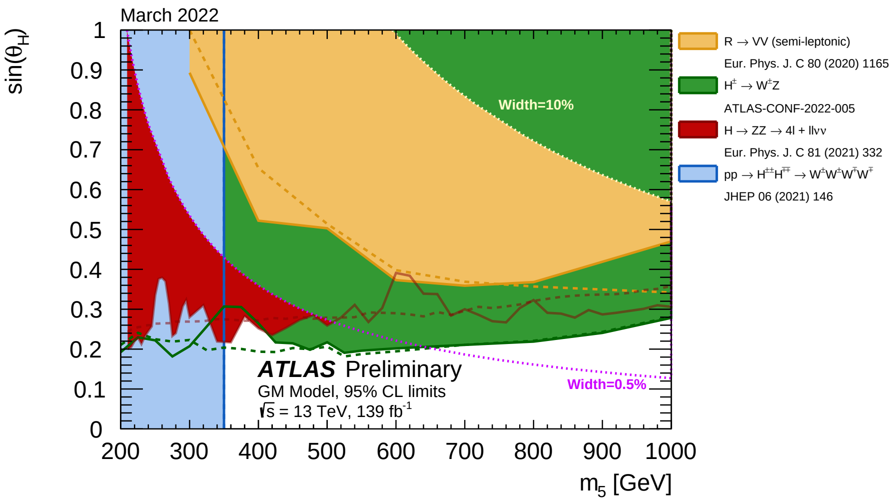

Figure 59: Overlay of observed (indicated as solid lines) and expected (indicated as dashed lines) exclusion limits at 95% CL on the H5plane benchmark of the Georgi-Machacek model presented as a function of the mass m_5 of the heavy Higgs bosons and the ratio of vacuum expectation values $sin(\theta_H)$. The limits are obtained via direct searches for new, heavy, neutral or charged Higgs bosons [310].

4.6 Outlook to future resonance searches

Despite extensive searches for new fundamental particles at the LHC, no convincing evidence for BSM physics has been found so far. The absence of any new signal has placed strong constraints on many BSM theories, and some have even been ruled out completely. However, large regions of parameter space remain experimentally unconstrained for some of the most natural extensions of the Standard Model [311].

While some regions of the open parameter space will become accessible over time as more data is collected, other regions will remain inaccessible with conventional searches. Therefore, new and more complicated signal signatures need to be explored. At the same time, new and improved algorithms are required to reconstruct and identify the decays of strongly Lorentz-boosted SM particles, in order to maximise the sensitivity to search for new physics effects.

Sections 4.6.1 and 4.6.2 discuss limitations of recent di-boson resonance searches and missing interpretations of the search results, respectively. Furthermore, Section 4.6.3 provides an outlook for future searches for unexplored signal signatures in multi-boson events[47] with the ATLAS detector, and Section 4.6.4 details the development of novel reconstruction and identification algorithms.

4.6.1 Limitations of recent di-boson resonance searches

Most resonance searches performed by ATLAS (but also CMS) assume that new heavy particles are narrow, with a width that is negligible compared to the detector resolution. While these assumptions are justified for some BSM scenarios, they are not generally true and can even be inadequate for certain types of models.

[47] The recent observations of the $W\gamma\gamma$, $WZ\gamma$, $Z\gamma\gamma$, and WWW processes [312, 313, 314, 315] strongly motivate searches for new physics effects in such multi-boson events.

Large width effects play an important role in Two-Higgs-Doublet models and other models with a non-minimal Higgs sector. Depending on the mass and coupling properties, the widths of Higgs bosons can become substantial, as shown in Figure 60(a). The importance of considering such large width effects is demonstrated in Figure 60(b), which shows that the upper limits on the production of a heavy resonance obtained for a narrow resonance can differ significantly from those obtained for a wide resonance.

Wide resonances pose additional challenges to our search efforts because they typically exhibit significant interference effects with the SM backgrounds. Such interference effects can significantly distort the shape of the signal mass spectrum. For example, in Type-II 2HDMs, destructive interference effects between the $gg \to t\bar{t}$ and $gg \to A \to t\bar{t}$ processes can become substantial at large $\tan\beta$ values [260]. Figure 61 shows the invariant mass distribution of top-quark pairs from the decay of a heavy pseudo-scalar before and after accounting for interference effects with the SM $t\bar{t}$ production process. Due to the interference effects, the signal shape is distorted from a Breit–Wigner peak to a peak-dip structure. These studies clearly demonstrate that ignoring interference effects has a dramatic impact on our search results.

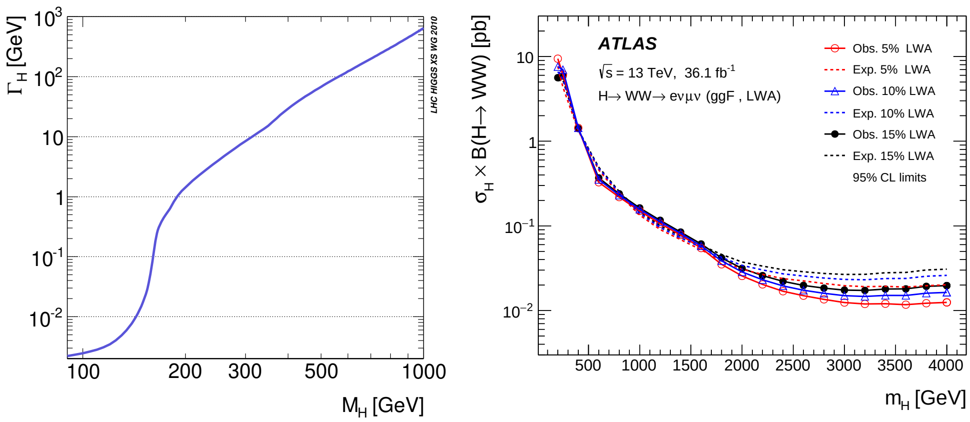

(a) (b)

Figure 60: (a) total width of the SM Higgs boson shown as a function of its mass and (b) observed and expected upper limits at 95% CL on the product of the $gg \to H$ production cross section times the $H \to W^{\pm}W^{\mp}$ branching ratio, as a function of the resonance mass and for three different signal widths [83, 316].

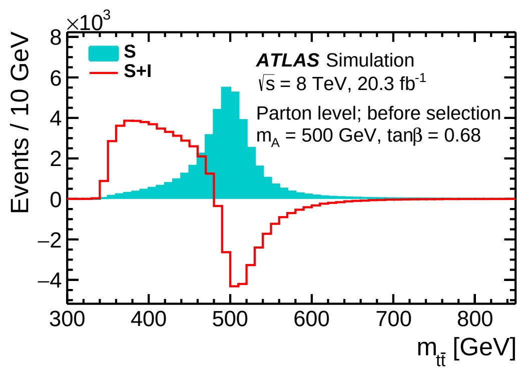

Figure 61: Distributions of the invariant mass of top-quark pairs from the decay of a pseudoscalar A with mass $m_A =$ 500 GeV for the pure resonance S (filled) and signal+interference contribution S + I (unfilled) [260].

4.6.2 Missing interpretations

Axion-like particles (ALPs), and more generally pseudo-Goldstone bosons, appear in several extensions of the Standard Model. They may be related to the solution to the strong CP problem [317], and/or to the existence of new spontaneously-broken global symmetries in Nature. Furthermore, ALPs are promising dark matter candidates [318, 319].

The existing constraints on ALPs are dominated by astrophysics and cosmological experiments for ALP masses $m_a < 1$ GeV, while collider experiments are particularly important for $m_a > 1$ GeV. The LHC experiments have conducted numerous searches for ALPs, mainly focusing on long-lived particles or prompt decays into pairs of photons and leptons. However, the couplings of ALPs to gg, ZZ, WW, $Z\gamma$, and Zh remain largely unconstrained. This is why recent phenomenological studies have proposed to conduct searches for ALPs in di-boson events. For masses $m_a \sim 200$ GeV, on-shell production of $a \to ZZ$ or $a \to W^\pm W^\mp$ can become dominant [320], while for masses $m_a << 100$ GeV, gluon-initiated di-boson scattering processes such as $gg \to ZZ, W^\pm W^\mp, Z\gamma$, and Zh, mediated by a virtual ALP, may have sizable cross sections [253]. Diagrams for di-boson production mediated via off-shell ALPs are shown in Figure 62.

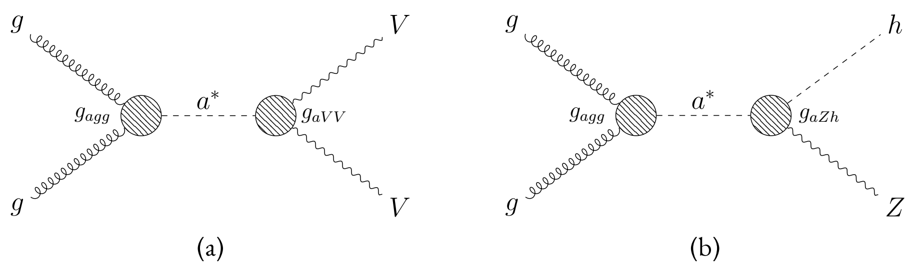

Figure 62: Feynman diagrams for the processes (a) $gg \to ZZ$, $gg \to W^\pm W^\mp$ and (b) $gg \to Zh$ mediated via an off-shell axion-like particle in the s-channel. The blobs represent an effective couplings between the axion-like particles and the SM bosons.

Constraints on the resonant production of di-boson systems via $a \to ZZ$ or $a \to W^\pm W^\mp$ can be easily inferred from existing searches for radions decaying via $R \to ZZ$ or $R \to W^\pm W^\mp$ [178, 185]. However, dedicated search efforts are required to probe for di-boson production mediated by an off-shell ALP via the $gg \to a^* \to ZZ$, $gg \to a^* \to W^\pm W^\mp$, $gg \to a^* \to Z\gamma$, or $gg \to a^* \to Zh$ prcesses. Such searches would need to probe for enhancements in the tails of the invariant mass distributions of relevant final state particles, rather than for a narrow peak.

The upper limits on the cross sections for on-shell and off-shell ALP production can be converted to constraints on the effective coupling parameters between ALPs and SM particles. Such constraints would be complementary to those from any other ongoing ALP searches.

4.6.3 Unexplored signal signatures

Good candidates for new physics searches are cascade decays of new massive particles such as the Kaluza-Klein excitations of the SM gauge bosons [321, 322], which are predicted in models with extra dimensions, or heavy Higgs bosons [311, 323] predicted in models with an extended scalar sector. These cascade decays can lead to exotic final states with multiple SM bosons in the event. Although they could occur at significant rates at the LHC, their non-standard signatures make them easily missed by conventional searches.

Figure 63 presents a few examples of cascade decays of new heavy particles that can result in tri-boson events. These diagrams depict the production and decay of Kaluza-Klein (KK) excitations of the W boson, the photon, and the gluon, followed by their subsequent decays into a radion, R, and a SM boson. These types of decays would lead to distinctive final states such as $\gamma\gamma\gamma$, $\gamma\gamma q\bar{q}$, $\ell^{\pm}\nu\gamma\gamma$, $\ell^{\pm}\ell^{\mp}\ell^{\pm}\ell^{\mp}\gamma$, $\ell^{\pm}\nu q\bar{q}q\bar{q}$, or $\ell^{\pm}\ell^{\mp}q\bar{q}q\bar{q}$ [321, 322]. If the mass difference between the radion and the particle in the s-channel is sufficiently large, the decay products of the radion will be strongly collimated. This can lead to challenging signatures, such as four-prong large-R jets from boosted $R \to W^{\pm}W^{\mp} \to q\bar{q}q\bar{q}$ or $R \to Z^{\pm}Z^{\mp} \to q\bar{q}q\bar{q}$ decays, or overlapping di-photon signatures from boosted $R \to \gamma\gamma$ decays. The current ATLAS reconstruction and identification algorithms are not well-suited to these signatures, so that new algorithms would need to be developed to probe these decays.

Multi-boson events are also predicted in models with an extended Higgs sector. A few examples are presented in Figure 64. As discussed in Reference [269], a large portion of the phenomenologically viable parameter space of type-I 2HDMs feature multi-boson signatures from events containing a charged Higgs boson. In these scenarios, the charged Higgs boson decays predominantly into a W boson and a non-SM like neutral Higgs boson h_{BSM} (or A), which then decays with significant branching fractions into pairs of bosons (WW, ZZ, or $\gamma\gamma$). Additional vector bosons can arise from the production process of the charged Higgs boson[48]. Depending on the production mode, candidate events can contain up to five vector bosons, resulting in final states with multiple charged leptons, multiple photons, and/or multiple jets. Analogously, multi-boson cascades initiated by the decay of a heavy neutral Higgs boson are predicted in CP violating 2HDMs, N2HDMs [263], three-Higgs-doublet models [128, 264, 311, 323] or models with massive ALPs [320].

Multi-boson signatures from cascade decays are predicted in many other BSM theories [324], beyond the few examples given above. Most of these signatures have not yet been directly searched for by ATLAS or CMS, while many theorists and phenomenologists have been urging the experimental community for years to initiate dedicated searches for them.

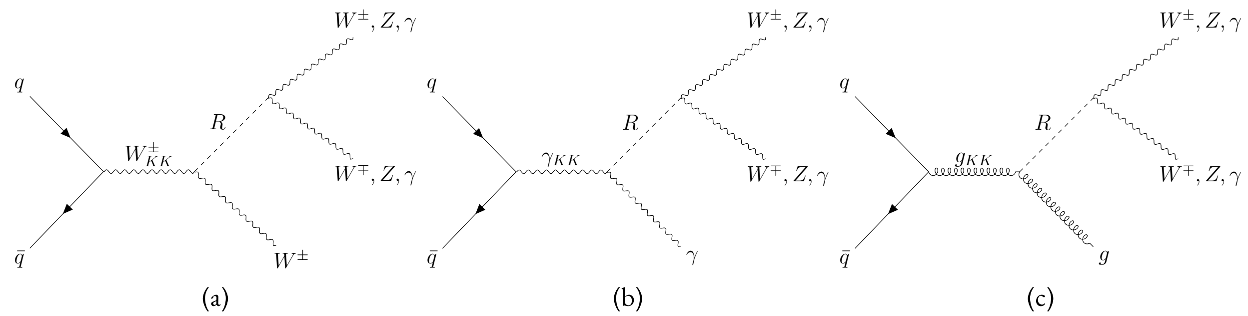

Figure 63: Representative lowest-order diagrams for the production and decay of Kaluza-Klein excitations of the W boson, the photon, and the gluon, followed by their subsequent decays into a radion, R, and a SM boson. The radion then decays into a pair of SM bosons.

[48] At the LHC, the three main channels for direct charged Higgs boson production are: associated production of a charged Higgs boson with a top and a bottom quark, associated production with a neutral Higgs boson, and associated production of a charged Higgs boson and a W boson.

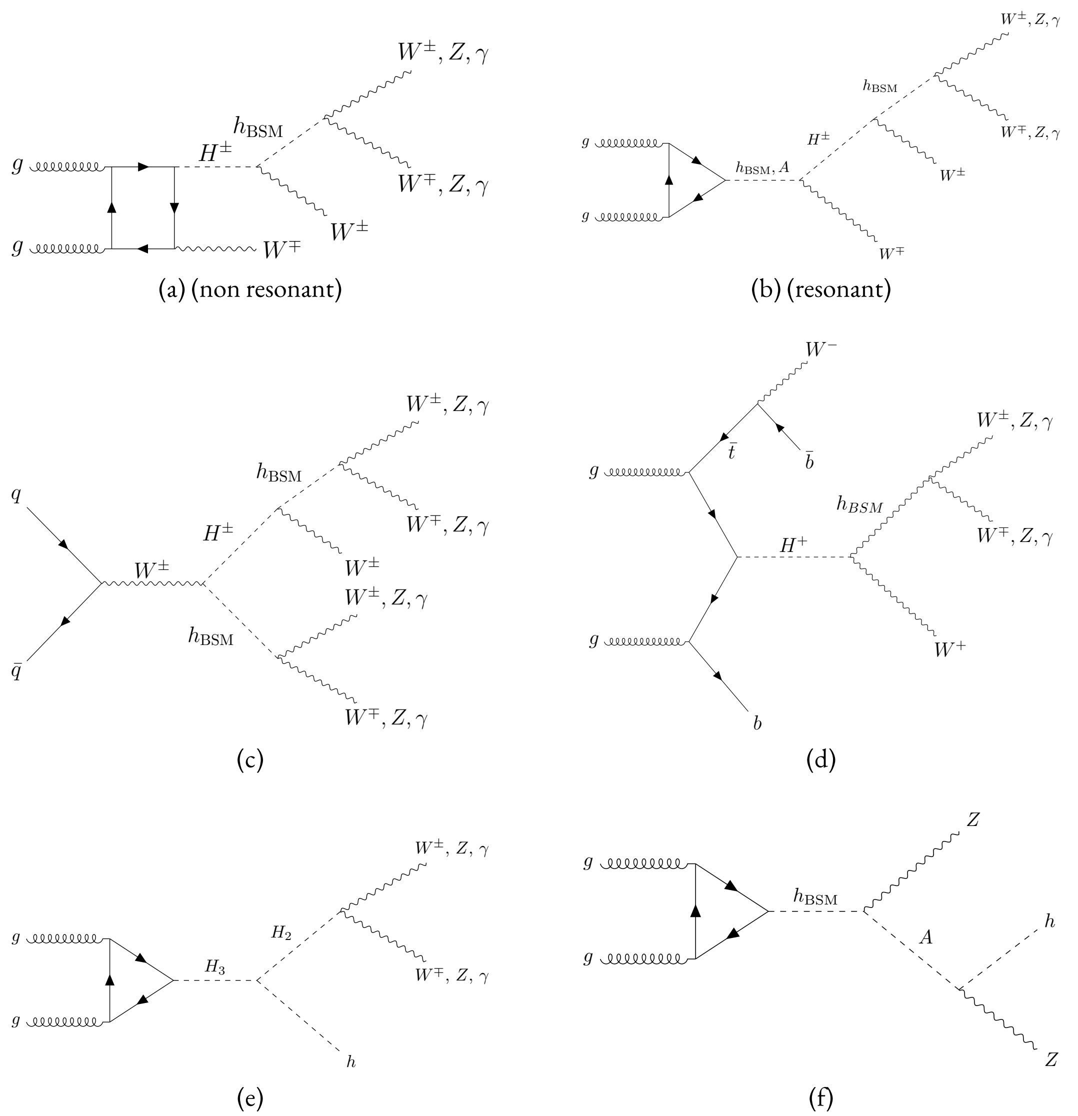

Figure 64: Representative lowest-order diagrams for the production of Higgs-like bosons and their cascade decays, where $H^\pm$ is a charged Higgs boson and h_{BSM} is an additional neutral Higgs-like particle, which may be lighter or heavier than 125 GeV.

4.6.4 Development of new reconstruction techniques

Numerous efforts are ongoing in the ATLAS and CMS collaborations to develop new machine learning-based algorithms to improve the reconstruction and identification of collimated decays of strongly Lorentz-boosted massive particles. These algorithms are essential to probe for signs of new physics at a mass scale extending to several TeV. To date, the development of boosted boson tagging algorithms has mainly focused on the reconstruction and identification of hadronic boson decays (such as $W \to q\bar{q}$, $Z \to q\bar{q}$, or $h \to b\bar{b}, c\bar{c}$) [55, 56, 325, 326] or boosted decays of $\tau^\pm\tau^\mp$ systems [327]. However, little effort has been spent on the identification of highly boosted $Z \to e^+e^-$ decays.

Several recent di-boson resonance searches based on channels targeting leptonic Z boson decays, were found to be limited by the inefficiency to reconstruct and identify highly Lorentz-boosted $Z \to e^+e^-$ decays [181, 185, 190]. Figure 65 depicts the products of kinematic acceptance and reconstruction efficiency[49] for $Z' \rightarrow Zh \rightarrow \ell^+\ell^- b\bar{b}/c\bar{c}$, $W' \rightarrow ZW^\pm \rightarrow \ell^\pm\ell^\mp q\bar{q}$ and $W' \rightarrow W^\pm Z \rightarrow \ell^\pm\nu\ell^\pm\ell^\mp$ decays as a function of the resonance mass. The acceptance times efficiency declines dramatically in all three searches for masses around 2 TeV.

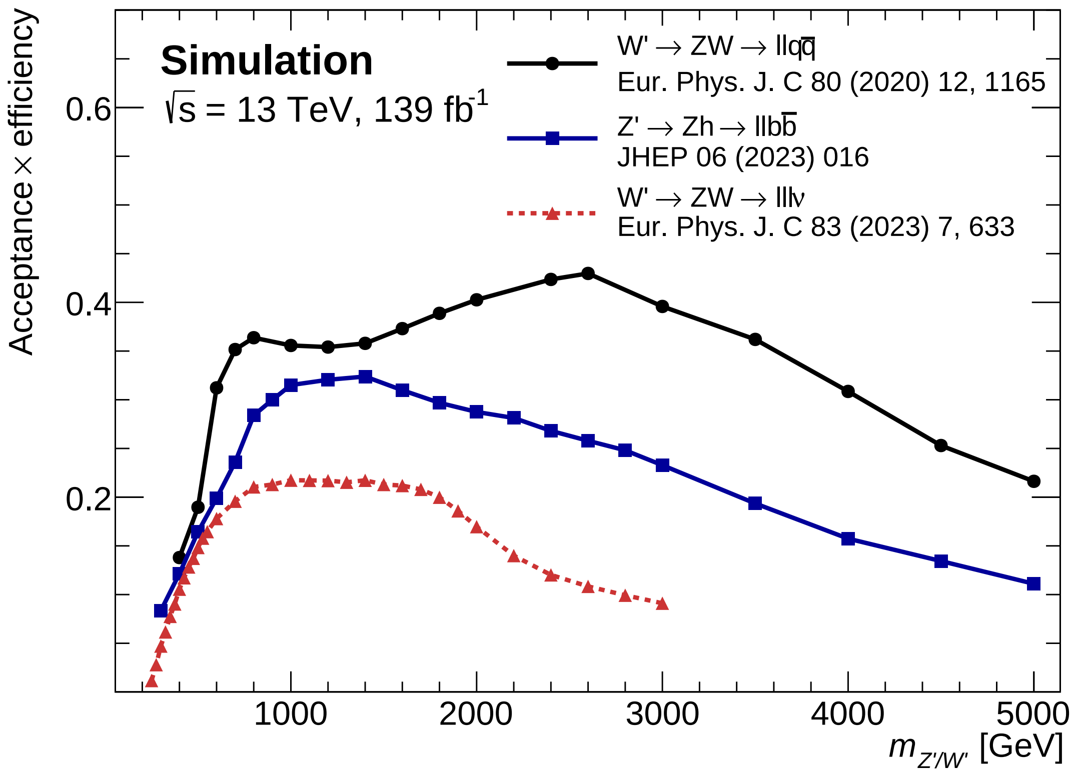

Figure 65: Product of acceptance and efficiency for selecting events of hypothetical heavy vector boson (Z' or W') decays presented as a function of the resonance mass. The curves are obtained from recent di-boson resonance searches by the ATLAS collaboration, including $Z' \rightarrow Zh \rightarrow \ell^+\ell^- b\bar{b}/c\bar{c}$, $W' \rightarrow ZW^\pm \rightarrow \ell^\pm\ell^\mp q\bar{q}$, and $W' \rightarrow W^\pm Z \rightarrow \ell^\pm\nu\ell^\pm\ell^\mp$ [181, 185, 190].

The standard electron reconstruction and identification procedures of the ATLAS collaboration perform well over a wide kinematic range, but their performance is significantly limited in highly Lorentz-boosted $Z \rightarrow e^+e^-$ decays, as shown in Figure 66. As the Lorentz boost of the Z boson increases, the decay products become more collimated, and the efficiency of reconstructing both final state particles decreases dramatically. The degradation effects for large Z boson momenta (i.e. for strongly collimated e^+e^- systems) are driven by e.g. the merging of energy clusters and a distortion of shower shapes and track quality observables used in the electron identification procedure.

To mitigate the efficiency losses of the ATLAS standard electron reconstruction and identification techniques, a new algorithm dedicated to identifying highly boosted $Z \rightarrow e^+e^-$ decays has been developed [328]. Jets, clustered via the anti-k_t algorithm using a radius parameter of 0.4 and particle-flow objects as inputs, are used to reconstruct the $Z \rightarrow e^+e^-$ candidates (as illustrated in Figure 67). Afterwards, a deep neural

[49] In this context, the acceptance is defined as the fraction of simulated signal events for which the expected final state particles pass all relevant object definition requirements, and the reconstruction efficiency is defined as the fraction of simulated signal events passing the various selection criteria of the signal regions.

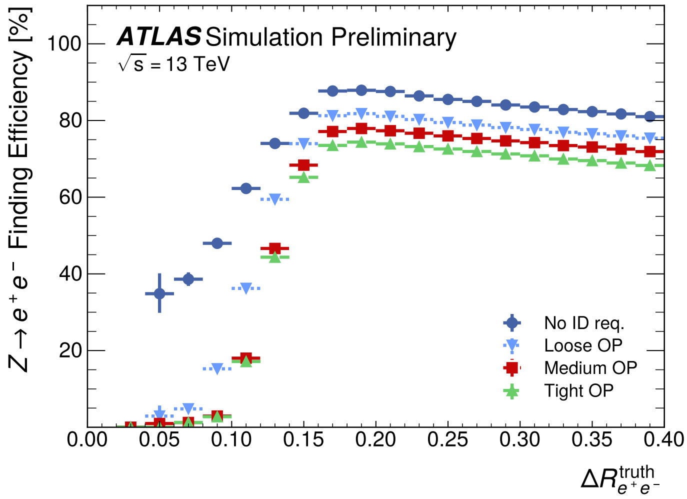

Figure 66: Efficiency to reconstruct and identify $Z \to e^+e^-$ decays using standard ATLAS electron reconstruction and identification algorithms as a function of the angular separation $\Delta R^{\text{truth}}_{e^+e^-}$ between the generator-level objects. The efficiencies are presented for different operating points (OP) of electron identification and without applying any identification requirements [328].

network (DNN) trained on 29 different jet properties (such as the mass, width, fraction of electromagnetic energy, number of constituents, and substructure information) is used to reduce backgrounds from single electrons or single photons, τ leptons as well as quarks and gluons.

The DNN maps the input vector to a four-dimensional output layer through four hidden layers, each with 200 nodes. The four output nodes quantify the probabilities of a jet being classified as signal, or as one of the three background classes. The training with multiple output nodes allows for high flexibility in constructing the final discriminant of the identification algorithm. Combining the probabilities of the signal and background classes can further optimise the algorithm's performance. Following the arguments of Reference [329], the outputs of the DNN are combined into a single discriminant function for the signal-jet hypothesis:

$$D_{\text{Zee}} = \ln\left(\frac{f_{Z\to ee} \cdot p_{Z\to ee}}{f_{q/g} \cdot p_{q/g} + f_{e/\gamma} \cdot p_{e/\gamma} + f_{(\tau)\tau} \cdot p_{(\tau)\tau}}\right), \tag{6}$$

where the p_i are the probabilities for the various signal and background hypotheses as predicted by the DNN, while the f_i are the jet fractions[50].

Figure 68 (a) shows the distribution of the D_{Zee} score for the signal and the three background classes. The signal is clearly separated from the backgrounds. Operating points corresponding to signal identification efficiencies of 97%, 95%, 93%, and 88% are defined based on selection requirements on the D_{Zee} score distribution. The selection requirements on D_{Zee} are chosen to be p_{T} dependent, in order to stabilise the identification efficiency as a function of the jet p_{T}.

[50] The relative importance of the q/g-, e/γ- and $(\tau)\tau$-jet rejection can be adjusted by varying the f_i parameters. In the initial studies, the f_i were set to match the jet fractions of the testing sample: $f_{Z\to ee} = 0.217$, $f_{q/g} = 0.488$, $f_{e/\gamma} = 0.230$, and $f_{(\tau)\tau} = 0.065$. However, the optimal choice of the f_i may vary significantly between different physics analyses, depending on the expected event kinematics and background composition.

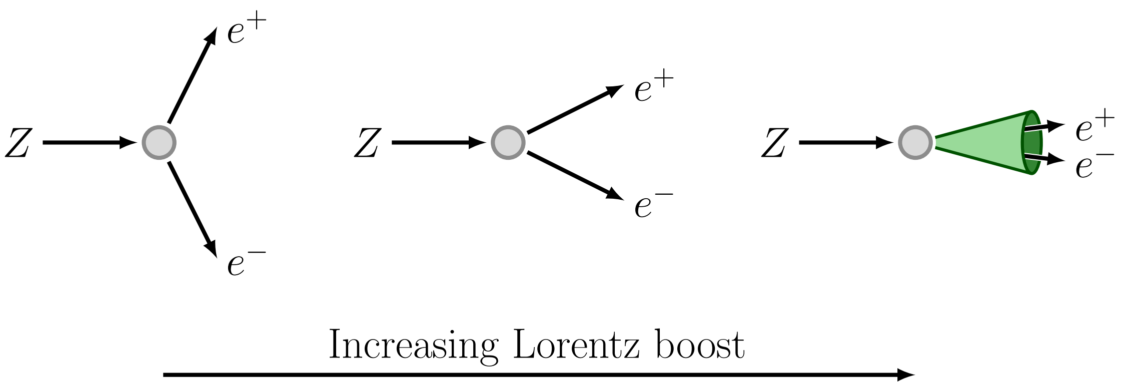

Figure 67: Schematic representation of a strongly Lorentz-boosted $Z \to e^+e^-$ decay. The angular separation between the decay products of the Z boson decreases as a function of the Z boson p_{T} [330].

The efficiency of the newly developed DNN to reconstruct and identify boosted $Z \to e^+e^-$ decays via a single anti-k_t jet is shown in Figure 68 (b) as a function of the angular separation between the generator-level electron-positron pair, $\Delta R^{\mathrm{truth}}_{e^+e^-}$, for different operating points. Both the reconstruction efficiency and the identification efficiencies decline with decreasing $\Delta R^{\mathrm{truth}}_{e^+e^-}$ values. However, the new $Z \to e^+e^-$ tagging algorithm is significantly more stable than the standard ATLAS electron reconstruction and identification techniques (see Figure 66). For example, the new algorithm is around 15 to 40 times more efficient at reconstructing and identifying $Z \to e^+e^-$ decays with angular distances between 0.06 and 0.08 than the standard techniques, depending on the operating point. Therefore, this new tagging algorithm promises to be a useful tool to enhance the sensitivity to searches for di-boson resonances in final states including leptonic decays of highly boosted $Z \to e^+e^-$ bosons (such as $Z' \to Zh \to \ell^\pm\ell^\mp b\bar{b}$, $R \to ZZ \to \ell^\pm\ell^\mp q\bar{q}$, or $W' \to W^\pm Z \to \ell^\pm\nu\ell^\pm\ell^\mp$).

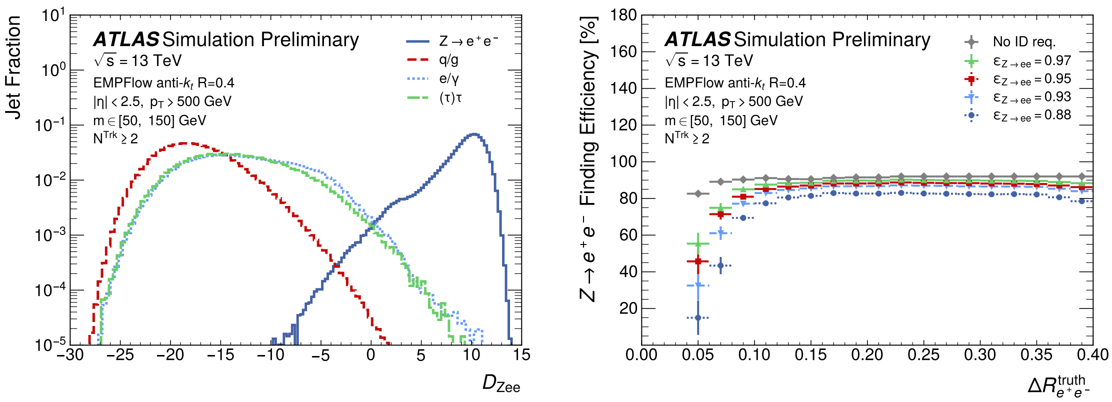

(a)

(b)

Figure 68: (a) distribution of the combined DNN output discriminant presented separately for signal jets and jets from the background classes and (b) the efficiencies to reconstruct and identify boosted $Z \to e^+e^-$ decays via a single anti-k_t jet as a function of the angular separation between the generator-level electron-positron pair, $\Delta R^{\mathrm{truth}}_{e^+e^-}$, presented for different operating points [328].

The work on this algorithm has been made public by the ATLAS collaboration [328] and are the product of long-standing research efforts carried out over several years by myself and various students, including two from the TU Munich. In 2019, a high school student conducted the initial studies on this subject. I supervised the student for two weeks as part of the CERN project weeks organised by the "Netzwerk Teilchenwelt". The work done during this internship was followed up by a B.Sc. project, during which a first mature version of the multi-class identification algorithm was developed. The results from the B.Sc. project were then further improved during a M.Sc.project [330] by adding more features to the DNN and by performing extensive hyperparameter scans to optimise the performance of the network. In addition, detailed studies on the mass and transverse momentum response scale and resolution for $Z \to e^+e^-$ jets were conducted during this M.Sc. project. The new $Z \to e^+e^-$ tagging algorithm was also applied to the search for $Z' \to Zh \to \ell^{\pm}\ell^{\mp}b\bar{b}$ decays, resulting in an improvement by a factor of two in the upper limits on the production cross section times branching ratio, compared to the limits obtained when using the ATLAS standard techniques for electron reconstruction and identification [330].

Most recently, the algorithm has been extended to identify strongly boosted $h \to \gamma\gamma$ decays, which can have a similar signature in the detector as boosted $Z \to e^+e^-$ decays. Additionally, the algorithm now uses a second neural network, called an adversary, which has been trained to infer the jet mass from the output of the classifier network. The goal of this is to minimise the dependence of the classifier's output on the jet mass[51]. This work was done in collaboration with a group from the Edinburgh School of Informatics, which I recently initiated through a joint M.Sc. project [331].

This new algorithm has a wide range of potential applications in the field. For example, it could be used in measurements of the Higgs bosons and Z bosons properties in kinematic regions that are not yet well-explored. It can also be used in searches for heavy new particles that decay into Higgs bosons or Z bosons. Furthermore, since the algorithm's performance is decorrelated from the mass of the jet, it can also be used to search for any highly Lorentz-boosted massive particle that decays into two photons or two electrons. This could improve the sensitivity of searches for a wide range of exotic particles, such as axion-like particles [332], BSM Higgs bosons [269], radions [321], or massive dark photons [333].

[51] The ability to decouple the performance of the identification algorithm from the jet mass makes it more widely usable, as it prevents the algorithm from distorting the background mass spectrum. This is essential for background estimation techniques that rely on fitting data in dedicated sideband regions and extrapolating the background shapes to the signal region.

5 Summary and Concluding Remarks

One of the main goals of the experiments at the LHC is to find and characterise BSM physics. A particularly active area of research are direct searches for new di-boson resonances, which decay into pairs of bosons such as hh, WW, WZ, ZZ, Zh, Wh, or $\gamma\gamma$. Searches for such new particles are well-motivated because they are predicted in models that address some of the most fundamental open questions in particle physics, such as the naturalness problem, baryogenesis, vacuum stability, dark matter, or the strong CP problem.

The discovered Higgs boson is the first example of a massive fundamental particle that decays into pairs of bosons. The measurements of its properties provide another handle to probe for BSM physics. Such indirect searches are an important complement to direct searches for new heavy particles. Therefore, measurements of the Higgs boson properties are a high priority for the recently started Run 3 of the LHC and for the high-luminosity phase of the LHC, as well as for future collider experiments.

In this thesis, a selection of recent results based on data from the ATLAS experiment at the LHC is presented, including both direct searches for new physics probing for resonant production of di-boson events and indirect searches via studies of Higgs boson properties. These are results to which I gave leading contributions, namely: searches for heavy vector bosons and pseudoscalars decaying to a vector boson and a Higgs boson, searches for charged Higgs bosons decaying to a W boson and a Higgs boson, and combinations of such searches, as well as measurements of Higgs boson production by gluon-gluon and vector-boson fusion, and studies of Higgs boson properties in decays to W boson pairs in associated production with a pair of jets. The corresponding journal publications are attached in Appendix B.

The di-boson resonance searches are based on 139 fb^{-1} of pp collision data collected by the ATLAS detector during Run 2 of the LHC. These searches place strong constraints on common benchmark models such as the Two-Higgs-Doublet Model and Heavy Vector Triplets. In the latter case, strongly coupled heavy vector bosons with masses up to 4.4 TeV are excluded at 95% CL. Statistical combinations are used to further strengthen these constrains by performing likelihood fits that include results from di-boson, and di-lepton resonance searches, and from searches for new particles decaying to pairs of quarks.

The Standard Model predictions were found to be consistent with the observations. However, in a few cases small deviations were seen for certain mass values. One example is the search for $W^{\pm}Z \rightarrow \ell^{\pm}\nu\ell^{\pm}\ell^{\mp}$ resonances, where an excess with a local significance of 2.8σ has been found under the spin-0 hypothesis at a resonance mass around 375 GeV. Furthermore, low-mass di-photon resonance searches by ATLAS and CMS have observed small excesses around 95 GeV with local significances of 1.7σ [270] and 2.9σ [334], respectively. These results are currently causing some discussions in the community, as previous searches for $\tau^{\pm}\tau^{\mp}$ (2.6σ by CMS) and $b\bar{b}$ (2σ by LEP) resonances have also seen small excesses around similar mass values [335].

In general, however one has to conclude that after more than a decade of searches at the LHC, no statistically significant signs for new physics have been found. Therefore, new particles must be either too heavy or too weakly coupled to be detected with the currently available datasets, or they decay into non-standard final states that have not been considered in searches up to now.

Multi-boson events from cascade decays of new heavy particles are promising examples of signal signatures that have not yet been sufficiently studied. Such decays are predicted in models with extra dimensions or models with an extended scalar sector. Searching for such decays is a natural extension of the existing di-boson resonance searches, and is supported by the recent observations of tri-boson processes such as $W\gamma\gamma$, $WZ\gamma$, $Z\gamma\gamma$, and WWW.

The development of new and improved identification algorithms for the decays of strongly Lorentz-boosted SM particles is crucial to extend the sensitivity of searches for multi-boson resonances and other new heavy particles. The algorithm introduced in Section 4.6.4 significantly improves the efficiency of reconstructing heavy particle decays into strongly collimated e^+e^- or $\gamma\gamma$ pairs and offers a wide range of potential applications, from searches for exotic particles such as ALPs, BSM Higgs bosons, radions, or massive dark photons as well as for measurements in the Higgs boson and Z boson production at high p_{T}.

The importance of developing such new techniques is highlighted by the recent progress in identifying strongly Loorentz-boosted $h \to c\bar{c}$ decays. This decay mode was long thought to be inaccessible at the LHC due to the overwhelming amount of backgrounds. However, the recent developments in machine learning algorithms may make it possible to find this challenging decay mode after all. In fact, projections from recent results of the CMS collaboration [336] suggest that a discovery could be feasible at the LHC.

Novel machine learning techniques are also becoming increasingly important in the design of analysis strategies. An example is the di-boson resonance search presented in Section 4.3, which use boosted decision trees (BDTs) to identify charged Higgs boson decays in a complicated final state with a charged lepton, missing transverse momentum and several jets. Another example are unsupervised learning techniques that can be trained on data to select events with anomalous properties, as presented in Section 4.4.

The Higgs boson properties are highly sensitive to BSM effects, as new particles can contribute to the Higgs boson production or decay via loop processes. These contributions can lead to an enhancement of the Higgs boson production cross section and to modulations of the angular distributions of particles produced either in association to the Higgs boson or in its decay. Such studies are sensitive to effects of new particles with masses far beyond the LHC energy scale.

The Higgs boson couplings to gauge bosons play a crucial role in several indirect searches for new physics. Examples are searches for CP-violation in Higgs boson production in association with two jets and studies of the Higgs boson couplings to longitudinally and transversely polarised vector bosons. Another example are measurements of differential Higgs boson production cross sections in $h \to WW^*$ decays, where the high-transverse-momentum regions are expected to be particularly sensitive to new physics effects.

The Higgs boson property measurements in the production with at least two associated jets are based on 36.1 fb^{-1} of pp collision data collected by the ATLAS detector during the 2015 and 2016 runs of the LHC. These searches place first constraints on the CP properties of the effective Higgs-gluon coupling and on polarisation-dependent coupling strengths. As the results are limited by statistical uncertainties, significant improvements are expected when the studies are repeated using combined datasets from Run 2 and Run 3 of the LHC.

The measurement of Higgs boson production in $h \to WW^*$ decays is based on 139 fb^{-1} of pp collision data. The cross section times decay branching ratio is determined with a precision of 12% for the ggF production mode and with a precision of 23% for the VBF production mode. All measurements were found to be consistent with the SM predictions. Furthermore, they are no longer statistically limited, which is why future measurements will rely heavily on improvements in the modelling of signals and backgrounds.

The sensitivity to searches for heavy resonances and measurements of Higgs boson properties in extreme phase space regions will increase significantly with the final datasets from the ongoing Run 3 of the LHC and of course from the HL-LHC phase, which will provide around twice and twenty times more statistics, respectively. Also, the upgrade of the ATLAS detector for the upcoming Run 4 of the LHC will allow for improvements of di-boson resonance searches and Higgs boson property measurements. For example, extended tracking acceptance in the forward direction will enhance the sensitivity to the b-associated production mode of heavy scalars, and significantly improve measurements of Higgs boson properties in associated production with a jet pair by helping to reduce background contributions from $t\bar{t}$ events.

Bibliography

[1] X. Fan, T. G. Myers, B. A. D. Sukra, and G. Gabrielse. "Measurement of the Electron Magnetic Moment". In: *Phys. Rev. Lett.* 130.7 (2023), p. 071801. DOI: 10.1103/PhysRevLett.130.071801. arXiv: 2209.13084 [physics.atom-ph].

[2] ATLAS Collaboration. "Observation of a new particle in the search for the Standard Model Higgs boson with the ATLAS detector at the LHC". In: *Phys. Lett. B* 716 (2012), pp. 1–29. DOI: 10.1016/j.physletb.2012.08.020. arXiv: 1207.7214 [hep-ex].

[3] CMS Collaboration. "Observation of a new boson at a mass of 125 GeV with the CMS experiment at the LHC". In: *Phys. Lett. B* 716 (2012), pp. 30–61. DOI: 10.1016/j.physletb.2012.08.021. arXiv: 1207.7235 [hep-ex].

[4] L. Evans and P. Bryant. "LHC Machine". In: *Journal of Instrumentation* 3.08 (2008), S08001. DOI: 10.1088/1748-0221/3/08/S08001. URL: https://dx.doi.org/10.1088/1748-0221/3/08/S08001.

[5] ATLAS Collaboration. "The ATLAS Experiment at the CERN Large Hadron Collider". In: *JINST* 3 (2008), S08003. DOI: 10.1088/1748-0221/3/08/S08003.

[6] CMS Collaboration. "The CMS Experiment at the CERN LHC". In: *JINST* 3 (2008), S08004. DOI: 10.1088/1748-0221/3/08/S08004.

[7] ALICE Collaboration. "The ALICE experiment at the CERN LHC". In: *JINST* 3 (2008), S08002. DOI: 10.1088/1748-0221/3/08/S08002.

[8] LHCb Collaboration. "The LHCb Detector at the LHC". In: *JINST* 3 (2008), S08005. DOI: 10.1088/1748-0221/3/08/S08005. URL: https://dx.doi.org/10.1088/1748-0221/3/08/S08005.

[9] R. van den Broeck. *THE CERN ACCELERATOR COMPLEX. Complexe des accelerateurs du CERN*. 2019. URL: https://cds.cern.ch/record/2693837.

[10] L. Rossi et al. "High-Luminosity Large Hadron Collider (HL-LHC): Technical design report". In: 10/2020 (Dec. 2020). DOI: 10.23731/CYRM-2020-0010.

[11] J. Pequenao. *Computer generated image of the whole ATLAS detector*. 2008. URL: https://cds.cern.ch/record/1095924.

[12] ATLAS Collaboration. *The ATLAS Collaboration Software and Firmware*. ATL-SOFT-PUB-2021-001. 2021. URL: https://cds.cern.ch/record/2767187.

[13] ATLAS Collaboration. "ATLAS data quality operations and performance for 2015–2018 data-taking". In: *JINST* 15.04 (2020), P04003. DOI: 10.1088/1748-0221/15/04/P04003. arXiv: 1911.04632 [physics.ins-det].

[14] ATLAS Collaboration. *Public ATLAS Luminosity Results for Run-2 of the LHC*. https://twiki.cern.ch/twiki/bin/view/AtlasPublic/LuminosityPublicResultsRun2. Accessed: 14-03-2024.

[15] ATLAS Collaboration. "Performance of the ATLAS track reconstruction algorithms in dense environments in LHC Run 2". In: *Eur. Phys. J. C* 77 (2017), p. 673. DOI: 10.1140/epjc/s10052-017-5225-7. arXiv: 1704.07983 [hep-ex].

[16] ATLAS Collaboration. “Electron reconstruction and identification in the ATLAS experiment using the 2015 and 2016 LHC proton–proton collision data at $\sqrt{s} = 13$ TeV”. In: *Eur. Phys. J. C* 79 (2019), p. 639. DOI: 10.1140/epjc/s10052-019-7140-6. arXiv: 1902.04655 [hep-ex].

[17] T. G. Cornelissen et al. “The global χ^2 track fitter in ATLAS”. In: *Journal of Physics: Conference Series* 119.3 (2008), p. 032013. DOI: 10.1088/1742-6596/119/3/032013. URL: https://doi.org/10.1088/1742-6596/119/3/032013.

[18] ATLAS Collaboration. “Reconstruction of primary vertices at the ATLAS experiment in Run 1 proton–proton collisions at the LHC”. In: *Eur. Phys. J. C* 77 (2017), p. 332. DOI: 10.1140/epjc/s10052-017-4887-5. arXiv: 1611.10235 [hep-ex].

[19] G. Piacquadio, Kirill Prokofiev, and A. Wildauer. “Primary vertex reconstruction in the ATLAS experiment at LHC”. In: *J. Phys. Conf. Ser.* 119 (2008). Ed. by Randall Sobie, Reda Tafirout, and Jana Thomson, p. 032033. DOI: 10.1088/1742-6596/119/3/032033.

[20] ATLAS Collaboration. “Topological cell clustering in the ATLAS calorimeters and its performance in LHC Run 1”. In: *Eur. Phys. J. C* 77 (2017), p. 490. DOI: 10.1140/epjc/s10052-017-5004-5. arXiv: 1603.02934 [hep-ex].

[21] ATLAS Collaboration. “Electron and photon performance measurements with the ATLAS detector using the 2015–2017 LHC proton–proton collision data”. In: *JINST* 14 (2019), P12006. DOI: 10.1088/1748-0221/14/12/P12006. arXiv: 1908.00005 [hep-ex].

[22] R. Frühwirth. “Application of Kalman filtering to track and vertex fitting”. In: *Nuclear Instruments and Methods in Physics Research Section A: Accelerators, Spectrometers, Detectors and Associated Equipment* 262.2 (1987), pp. 444–450. ISSN: 0168-9002. DOI: https://doi.org/10.1016/0168-9002(87)90887-4. URL: https://www.sciencedirect.com/science/article/pii/0168900287908874.

[23] ATLAS Collaboration. *Improved electron reconstruction in ATLAS using the Gaussian Sum Filter-based model for bremsstrahlung*. Tech. rep. 2012. URL: https://cds.cern.ch/record/1449796.

[24] ATLAS Collaboration. “Electron and photon efficiencies in LHC Run 2 with the ATLAS experiment”. In: *JHEP* 05 (2024), p. 162. DOI: 10.1007/JHEP05(2024)162. arXiv: 2308.13362 [hep-ex].

[25] ATLAS Collaboration. “Electron and photon energy calibration with the ATLAS detector using 2015–2016 LHC proton-proton collision data”. In: *JINST* 14.03 (2019), P03017. DOI: 10.1088/1748-0221/14/03/P03017. arXiv: 1812.03848 [hep-ex].

[26] ATLAS Collaboration. “Performance of electron and photon triggers in ATLAS during LHC Run 2”. In: *Eur. Phys. J. C* 80.1 (2020), p. 47. DOI: 10.1140/epjc/s10052-019-7500-2. arXiv: 1909.00761 [hep-ex].

[27] ATLAS Collaboration. “Muon reconstruction and identification efficiency in ATLAS using the full Run 2 *pp* collision data set at $\sqrt{s} = 13$ TeV”. In: *Eur. Phys. J. C* 81.7 (2021), p. 578. DOI: 10.1140/epjc/s10052-021-09233-2. arXiv: 2012.00578 [hep-ex].

[28] ATLAS Collaboration. “Studies of the muon momentum calibration and performance of the ATLAS detector with pp collisions at $\sqrt{s} = 13$ TeV”. In: *Eur. Phys. J. C* 83.8 (2023), p. 686. DOI: 10.1140/epjc/s10052-023-11584-x. arXiv: 2212.07338 [hep-ex].

[29] ATLAS Collaboration. "Measurement of the properties of Higgs boson production at $\sqrt{s} = 13$ TeV in the $H \rightarrow \gamma\gamma$ channel using 139 fb^{-1} of pp collision data with the ATLAS experiment". In: *JHEP* 07 (2023), p. 088. DOI: 10.1007/JHEP07(2023)088. arXiv: 2207.00348 [hep-ex].

[30] ATLAS Collaboration. "Measurement of the photon identification efficiencies with the ATLAS detector using LHC Run 2 data collected in 2015 and 2016". In: *Eur. Phys. J. C* 79.3 (2019), p. 205. DOI: 10.1140/epjc/s10052-019-6650-6. arXiv: 1810.05087 [hep-ex].

[31] G. Salam et al. "The anti-k_t jet clustering algorithm". In: *JHEP* 04 (2008), p. 063. DOI: 10.1088/1126-6708/2008/04/063. arXiv: 0802.1189 [hep-ph].

[32] M. Cacciari et al. "FastJet User Manual". In: *Eur. Phys. J. C* 72 (2012), p. 1896. DOI: 10.1140/epjc/s10052-012-1896-2. arXiv: 1111.6097 [hep-ph].

[33] ATLAS Collaboration. "Jet energy scale and resolution measured in proton–proton collisions at $\sqrt{s} = 13$ TeV with the ATLAS detector". In: *Eur. Phys. J. C* 81 (2020), p. 689. DOI: 10.1140/epjc/s10052-021-09402-3. arXiv: 2007.02645 [hep-ex].

[34] ATLAS Collaboration. "Jet reconstruction and performance using particle flow with the ATLAS Detector". In: *Eur. Phys. J. C* 77 (2017), p. 466. DOI: 10.1140/epjc/s10052-017-5031-2. arXiv: 1703.10485 [hep-ex].

[35] ATLAS Collaboration. "Optimisation of large-radius jet reconstruction for the ATLAS detector in 13 TeV proton–proton collisions". In: *Eur. Phys. J. C* 81 (2020), p. 334. DOI: 10.1140/epjc/s10052-021-09054-3. arXiv: 2009.04986 [hep-ex].

[36] ATLAS Collaboration. "Jet energy scale measurements and their systematic uncertainties in proton-proton collisions at $\sqrt{s} = 13$ TeV with the ATLAS detector". In: *Phys. Rev. D* 96.7 (2017), p. 072002. DOI: 10.1103/PhysRevD.96.072002. arXiv: 1703.09665 [hep-ex].

[37] ATLAS Collaboration. "Jet energy resolution in proton-proton collisions at $\sqrt{s} = 7$ TeV recorded in 2010 with the ATLAS detector". In: *Eur. Phys. J. C* 73.3 (2013), p. 2306. DOI: 10.1140/epjc/s10052-013-2306-0. arXiv: 1210.6210 [hep-ex].

[38] ATLAS Collaboration. *Tagging and suppression of pileup jets with the ATLAS detector*. Tech. rep. 2014. URL: https://cds.cern.ch/record/1700870.

[39] ATLAS Collaboration. "Performance of pile-up mitigation techniques for jets in pp collisions at $\sqrt{s} = 8$ TeV using the ATLAS detector". In: *Eur. Phys. J. C* 76.11 (2016), p. 581. DOI: 10.1140/epjc/s10052-016-4395-z. arXiv: 1510.03823 [hep-ex].

[40] ATLAS Collaboration. "Identification and rejection of pile-up jets at high pseudorapidity with the ATLAS detector". In: *Eur. Phys. J. C* 77.9 (2017). [Erratum: Eur.Phys.J.C 77, 712 (2017)], p. 580. DOI: 10.1140/epjc/s10052-017-5081-5. arXiv: 1705.02211 [hep-ex].

[41] ATLAS Collaboration. "Jet reconstruction and performance using particle flow with the ATLAS Detector". In: *Eur. Phys. J. C* 77.7 (2017), p. 466. DOI: 10.1140/epjc/s10052-017-5031-2. arXiv: 1703.10485 [hep-ex].

[42] D. Krohn, J. Thaler, and L. Wang. "Jet Trimming". In: *JHEP* 02 (2010), p. 084. DOI: 10.1007/JHEP02(2010)084. arXiv: 0912.1342 [hep-ph].

[43] ATLAS Collaboration. *Variable Radius, Exclusive-k_T, and Center-of-Mass Subjet Reconstruction for Higgs($\rightarrow b\bar{b}$) Tagging in ATLAS*. Tech. rep. 2017. URL: https://cds.cern.ch/record/2268678.

[44] ATLAS Collaboration. *Reconstruction, Identification, and Calibration of hadronically decaying tau leptons with the ATLAS detector for the LHC Run 3 and reprocessed Run 2 data*. Tech. rep. 2022. URL: https://cds.cern.ch/record/2827111.

[45] ATLAS Collaboration. "ATLAS flavour-tagging algorithms for the LHC Run 2 pp collision dataset". In: *Eur. Phys. J. C* 83.7 (2023), p. 681. DOI: 10.1140/epjc/s10052-023-11699-1. arXiv: 2211.16345 [physics.data-an].

[46] ATLAS Collaboration. *Graph Neural Network Jet Flavour Tagging with the ATLAS Detector*. Tech. rep. URL: https://cds.cern.ch/record/2811135.

[47] ATLAS Collaboration. "ATLAS b-jet identification performance and efficiency measurement with $t\bar{t}$ events in pp collisions at $\sqrt{s} = 13$ TeV". In: *Eur. Phys. J. C* 79.11 (2019), p. 970. DOI: 10.1140/epjc/s10052-019-7450-8. arXiv: 1907.05120 [hep-ex].

[48] ATLAS Collaboration. "Measurement of the c-jet mistagging efficiency in $t\bar{t}$ events using pp collision data at $\sqrt{s} = 13$ TeV collected with the ATLAS detector". In: *Eur. Phys. J. C* 82.1 (2022), p. 95. DOI: 10.1140/epjc/s10052-021-09843-w. arXiv: 2109.10627 [hep-ex].

[49] ATLAS Collaboration. "Calibration of the light-flavour jet mistagging efficiency of the b-tagging algorithms with Z+jets events using 139 fb^{-1} of ATLAS proton-proton collision data at $\sqrt{s} = 13$ TeV". In: *Eur. Phys. J. C* 83 (2023), p. 728. DOI: 10.1140/epjc/s10052-023-11736-z. arXiv: 2301.06319 [hep-ex].

[50] ATLAS Collaboration. *Simulation-based extrapolation of b-tagging calibrations towards high transverse momenta in the ATLAS experiment*. Tech. rep. 2021. URL: https://cds.cern.ch/record/2753444.

[51] ATLAS Collaboration. "Performance of jet substructure techniques for large-R jets in proton-proton collisions at $\sqrt{s}$ = 7 TeV using the ATLAS detector". In: *JHEP* 09 (2013), p. 076. DOI: 10.1007/JHEP09(2013)076. arXiv: 1306.4945 [hep-ex].

[52] ATLAS Collaboration. *b-tagging in dense environments*. Tech. rep. 2014. URL: https://cds.cern.ch/record/1750682.

[53] ATLAS Collaboration. "Performance of top-quark and W-boson tagging with ATLAS in Run 2 of the LHC". In: *Eur. Phys. J. C* 79.5 (2019), p. 375. DOI: 10.1140/epjc/s10052-019-6847-8. arXiv: 1808.07858 [hep-ex].

[54] ATLAS Collaboration. *A W/Z-boson tagger using Track-CaloCluster jets with ATLAS*. Tech. rep. URL: https://cds.cern.ch/record/2718218.

[55] ATLAS Collaboration. "Identification of boosted Higgs bosons decaying into b-quark pairs with the ATLAS detector at 13 TeV". In: *Eur. Phys. J. C* 79.10 (2019), p. 836. DOI: 10.1140/epjc/s10052-019-7335-x. arXiv: 1906.11005 [hep-ex].

[56] ATLAS Collaboration. *Identification of Boosted Higgs Bosons Decaying Into $b\bar{b}$ With Neural Networks and Variable Radius Subjets in ATLAS*. Tech. rep. 2020. URL: https://cds.cern.ch/record/2724739.

[57] ATLAS Collaboration. *Efficiency corrections for a tagger for boosted $H \to b\bar{b}$ decays in pp collisions at $\sqrt{s} = 13$ TeV with the ATLAS detector*. Tech. rep. 2021. URL: https://cds.cern.ch/record/2777811.

[58] ATLAS Collaboration. "Performance of missing transverse momentum reconstruction with the ATLAS detector using proton-proton collisions at $\sqrt{s} = 13$ TeV". In: *Eur. Phys. J. C* 78.11 (2018), p. 903. DOI: 10.1140/epjc/s10052-018-6288-9. arXiv: 1802.08168 [hep-ex].

[59] ATLAS Collaboration. *Object-based missing transverse momentum significance in the ATLAS detector*. Tech. rep. July 2018. URL: https://cds.cern.ch/record/2630948.

[60] R. Frederix et al. "The automated computation of tree-level and next-to-leading order differential cross sections, and their matching to parton shower simulations". In: *JHEP* 07 (2014), p. 079. DOI: 10.1007/JHEP07(2014)079. arXiv: 1405.0301 [hep-ph].

[61] S. Frixione, P. Nason, and C. Oleari. "Matching NLO QCD computations with parton shower simulations: the POWHEG method". In: *JHEP* 11 (2007), p. 070. DOI: 10.1088/1126-6708/2007/11/070. arXiv: 0709.2092 [hep-ph].

[62] S. Alioli, P. Nason, C. Oleari, and E. Re. "A general framework for implementing NLO calculations in shower Monte Carlo programs: the POWHEG BOX". In: *JHEP* 06 (2010), p. 043. DOI: 10.1007/JHEP06(2010)043. arXiv: 1002.2581 [hep-ph].

[63] E. Bothmann et al. "Event generation with Sherpa 2.2". In: *SciPost Phys.* 7.3 (2019), p. 034. DOI: 10.21468/SciPostPhys.7.3.034. arXiv: 1905.09127 [hep-ph].

[64] T. Sjöstrand et al. "An introduction to PYTHIA 8.2". In: *Comput. Phys. Commun.* 191 (2015), p. 159. DOI: 10.1016/j.cpc.2015.01.024. arXiv: 1410.3012 [hep-ph].

[65] J. Bellm et al. "Herwig 7.0/Herwig++ 3.0 release note". In: *Eur. Phys. J. C* 76.4 (2016), p. 196. DOI: 10.1140/epjc/s10052-016-4018-8. arXiv: 1512.01178 [hep-ph].

[66] ATLAS Collaboration. "The ATLAS Simulation Infrastructure". In: *Eur. Phys. J. C* 70 (2010), p. 823. DOI: 10.1140/epjc/s10052-010-1429-9. arXiv: 1005.4568 [physics.ins-det].

[67] GEANT4 Collaboration. "GEANT4 – a simulation toolkit". In: *Nucl. Instrum. Meth. A* 506 (2003), p. 250. DOI: 10.1016/S0168-9002(03)01368-8.

[68] ATLAS Collaboration. *The simulation principle and performance of the ATLAS fast calorimeter simulation FastCaloSim*. Tech. rep. 2010. URL: https://cds.cern.ch/record/1300517.

[69] ATLAS Collaboration. *The Pythia 8 A3 tune description of ATLAS minimum bias and inelastic measurements incorporating the Donnachie–Landshoff diffractive model*. Tech. rep. 2016. URL: https://cds.cern.ch/record/2206965.

[70] ATLAS Collaboration. "Study of the spin and parity of the Higgs boson in diboson decays with the ATLAS detector". In: *Eur. Phys. J. C* 75.10 (2015). [Erratum: Eur.Phys.J.C 76, 152 (2016)], p. 476. DOI: 10.1140/epjc/s10052-015-3685-1. arXiv: 1506.05669 [hep-ex].

[71] CMS Collaboration. "Constraints on the spin-parity and anomalous HVV couplings of the Higgs boson in proton collisions at 7 and 8 TeV". In: *Phys. Rev. D* 92.1 (2015), p. 012004. DOI: 10.1103/PhysRevD.92.012004. arXiv: 1411.3441 [hep-ex].

[72] ATLAS Collaboration. "Evidence of off-shell Higgs boson production from ZZ leptonic decay channels and constraints on its total width with the ATLAS detector". In: (Apr. 2023). arXiv: 2304.01532 [hep-ex].

[73] CMS Collaboration. "Measurement of the Higgs boson width and evidence of its off-shell contributions to ZZ production". In: *Nature Phys.* 18.11 (2022), pp. 1329–1334. DOI: 10.1038/s41567-022-01682-0. arXiv: 2202.06923 [hep-ex].

[74] ATLAS Collaboration. "Measurement of the Higgs boson mass in the $H \to ZZ^* \to 4\ell$ and $H \to \gamma\gamma$ channels with $\sqrt{s} = 13$ TeV pp collisions using the ATLAS detector". In: *Phys. Lett. B* 784 (2018), pp. 345–366. DOI: 10.1016/j.physletb.2018.07.050. arXiv: 1806.00242 [hep-ex].

[75] ATLAS Collaboration. "A detailed map of Higgs boson interactions by the ATLAS experiment ten years after the discovery". In: *Nature* 607.7917 (2022). [Erratum: Nature 612, E24 (2022)], pp. 52–59. DOI: 10.1038/s41586-022-04893-w. arXiv: 2207.00092 [hep-ex].

[76] CMS Collaboration. "A portrait of the Higgs boson by the CMS experiment ten years after the discovery". In: *Nature* 607.7917 (2022), pp. 60–68. DOI: 10.1038/s41586-022-04892-x. arXiv: 2207.00043 [hep-ex].

[77] F. Demartin, F. Maltoni, K. Mawatari, B. Page, and M. Zaro. "Higgs characterisation at NLO in QCD: CP properties of the top-quark Yukawa interaction". In: *Eur. Phys. J. C* 74.9 (2014), p. 3065. DOI: 10.1140/epjc/s10052-014-3065-2. arXiv: 1407.5089 [hep-ph].

[78] P. Artoisenet et al. "A framework for Higgs characterisation". In: *JHEP* 11 (2013), p. 043. DOI: 10.1007/JHEP11(2013)043. arXiv: 1306.6464 [hep-ph].

[79] F. Maltoni, K. Mawatari, and M. Zaro. "Higgs characterisation via vector-boson fusion and associated production: NLO and parton-shower effects". In: *Eur. Phys. J. C* 74.1 (2014), p. 2710. DOI: 10.1140/epjc/s10052-013-2710-5. arXiv: 1311.1829 [hep-ph].

[80] ATLAS & CMS Collaboration. "Measurements of the Higgs boson production and decay rates and constraints on its couplings from a combined ATLAS and CMS analysis of the LHC pp collision data at $\sqrt{s} = 7$ and 8 TeV". In: *JHEP* 08 (2016), p. 045. DOI: 10.1007/JHEP08(2016)045. arXiv: 1606.02266 [hep-ex].

[81] J R Andersen et al. "Handbook of LHC Higgs Cross Sections: 3. Higgs Properties". In: (July 2013). Ed. by S Heinemeyer et al. DOI: 10.5170/CERN-2013-004. arXiv: 1307.1347 [hep-ph].

[82] A. David and G. Passarino. "Through precision straits to next standard model heights". In: *Rev. Phys.* 1 (2016), pp. 13–28. DOI: 10.1016/j.revip.2016.01.001. arXiv: 1510.00414 [hep-ph].

[83] LHC Higgs Cross Section Working Group. "Handbook of LHC Higgs Cross Sections: 4. Deciphering the Nature of the Higgs Sector". In: 2/2017 (Oct. 2016). DOI: 10.23731/CYRM-2017-002. arXiv: 1610.07922 [hep-ph].

[84] N. Berger et al. "Simplified Template Cross Sections - Stage 1.1". In: (June 2019). arXiv: 1906.02754 [hep-ph].

[85] J. R. Andersen et al. "Les Houches 2015: Physics at TeV Colliders Standard Model Working Group Report". In: *9th Les Houches Workshop on Physics at TeV Colliders*. May 2016. arXiv: 1605.04692 [hep-ph].

[86] J. de Blas et al. "Higgs Boson Studies at Future Particle Colliders". In: *JHEP* 01 (2020), p. 139. DOI: 10.1007/JHEP01(2020)139. arXiv: 1905.03764 [hep-ph].

[87] M. Bonvini, S. Marzani, C. Muselli, and L. Rottoli. "On the Higgs cross section at N^{3}LO+N^{3}LL and its uncertainty". In: *JHEP* 08 (2016), p. 105. DOI: 10.1007/JHEP08(2016)105. arXiv: 1603.08000 [hep-ph].

[88] M. Cacciari et al. "Fully Differential Vector-Boson-Fusion Higgs Production at Next-to-Next-to-Leading Order". In: *Phys. Rev. Lett.* 115.8 (2015). [Erratum: Phys. Rev. Lett. 120 (2018) 139901], p. 082002. DOI: 10.1103/PhysRevLett.115.082002. arXiv: 1506.02660 [hep-ph].

[89] A. Denner et al. "HAWK 2.0: A Monte Carlo program for Higgs production in vector-boson fusion and Higgs strahlung at hadron colliders". In: *Comput. Phys. Commun.* 195 (2015), pp. 161–171. DOI: 10.1016/j.cpc.2015.04.021. arXiv: 1412.5390 [hep-ph].

[90] R. V. Harlander, J. Klappert, S. Liebler, and L. Simon. "vh@nnlo-v2: New physics in Higgs Strahlung". In: *JHEP* 05 (2018), p. 089. DOI: 10.1007/JHEP05(2018)089. arXiv: 1802.04817 [hep-ph].

[91] R. Frederix et al. "The automated computation of tree-level and next-to-leading order differential cross sections, and their matching to parton shower simulations". In: *JHEP* 07 (2014), p. 079. DOI: 10.1007/JHEP07(2014)079. arXiv: 1405.0301 [hep-ph].

[92] R. Harlander, M. Kramer, and M. Schumacher. "Bottom-quark associated Higgs-boson production: reconciling the four- and five-flavour scheme approach". In: (Dec. 2011). arXiv: 1112.3478 [hep-ph].

[93] R. Harlander, S. Liebler, and H. Mantler. "SusHi: A program for the calculation of Higgs production in gluon fusion and bottom-quark annihilation in the Standard Model and the MSSM". In: *Comput. Phys. Commun.* 184 (2013), pp. 1605–1617. DOI: 10.1016/j.cpc.2013.02.006. arXiv: 1212.3249 [hep-ph].

[94] J. Abdallah et al. "Simplified Models for Dark Matter Searches at the LHC". In: *Phys. Dark Univ.* 9-10 (2015), pp. 8–23. DOI: 10.1016/j.dark.2015.08.001. arXiv: 1506.03116 [hep-ph].

[95] ATLAS Collaboration. "Search for exclusive Higgs and Z boson decays to $\omega\gamma$ and Higgs boson decays to $K^*\gamma$ with the ATLAS detector". In: (Jan. 2023). arXiv: 2301.09938 [hep-ex].

[96] ATLAS Collaboration. "Searches for exclusive Higgs and Z boson decays into $J/\psi\gamma$, $\psi(2S)\gamma$, and $\Upsilon(nS)\gamma$ at $\sqrt{s} = 13$ TeV with the ATLAS detector". In: *Phys. Lett. B* 786 (2018), pp. 134–155. DOI: 10.1016/j.physletb.2018.09.024. arXiv: 1807.00802 [hep-ex].

[97] A. Djouadi et al. "HDECAY: A program for Higgs boson decays in the Standard Model and its supersymmetric extension". In: *Comput. Phys. Commun.* 108 (1998), p. 56. DOI: 10.1016/S0010-4655(97)00123-9. arXiv: hep-ph/9704448.

[98] A. Bredenstein et al. "Precise predictions for the Higgs-boson decay $H \to WW/ZZ \to 4$ leptons". In: *Phys. Rev. D* 74 (2006), p. 013004. DOI: 10.1103/PhysRevD.74.013004. arXiv: hep-ph/0604011.

[99] ATLAS Collaboration. "Observation of a new particle in the search for the Standard Model Higgs boson with the ATLAS detector at the LHC". In: *Phys. Lett. B* 716 (2012), p. 1. DOI: 10.1016/j.physletb.2012.08.020. arXiv: 1207.7214 [hep-ex].

[100] CMS Collaboration. "Observation of a new boson at a mass of 125 GeV with the CMS experiment at the LHC". In: *Phys. Lett. B* 716 (2012), p. 30. DOI: 10.1016/j.physletb.2012.08.021. arXiv: 1207.7235 [hep-ex].

[101] C. A. Nelson and A. Charles. "Correlation Between Decay Planes in Higgs Boson Decays Into W Pair (Into Z Pair)". In: *Phys. Rev. D* 37 (1988), p. 1220. DOI: 10.1103/PhysRevD.37.1220.

[102] ATLAS Collaboration. "Observation and measurement of Higgs boson decays to WW* with the ATLAS detector". In: *Phys. Rev. D* 92.1 (2015), p. 012006. DOI: 10.1103/PhysRevD.92.012006. arXiv: 1412.2641 [hep-ex].

[103] ATLAS Collaboration. "Measurement of the production cross section for a Higgs boson in association with a vector boson in the $H \to WW^* \to \ell\nu\ell\nu$ channel in pp collisions at $\sqrt{s}$ = 13 TeV with the ATLAS detector". In: *Phys. Lett. B* 798 (2019), p. 134949. DOI: 10.1016/j.physletb.2019.134949. arXiv: 1903.10052 [hep-ex].

[104] ATLAS Collaboration. "Measurements of Higgs boson production by gluon-gluon fusion and vector-boson fusion using $H \to WW^* \to e\nu\mu\nu$ decays in pp collisions at $\sqrt{s} = 13$ TeV with the ATLAS detector". In: *Phys. Rev. D* 108 (2023), p. 032005. DOI: 10.1103/PhysRevD.108.032005. arXiv: 2207.00338 [hep-ex].

[105] ATLAS Collaboration. "Measurements of differential cross sections of Higgs boson production through gluon fusion in the $H \to WW^* \to e\nu\mu\nu$ final state at $\sqrt{s} = 13$ TeV with the ATLAS detector". In: *Eur. Phys. J. C* 83.9 (2023), p. 774. DOI: 10.1140/epjc/s10052-023-11873-5. arXiv: 2301.06822 [hep-ex].

[106] ATLAS Collaboration. "Fiducial and differential cross-section measurements for the vector-boson-fusion production of the Higgs boson in the $H \to WW^* \to e\nu\mu\nu$ decay channel at 13 TeV with the ATLAS detector". In: *Phys. Rev. D* 108.7 (2023), p. 072003. DOI: 10.1103/PhysRevD.108.072003. arXiv: 2304.03053 [hep-ex].

[107] ATLAS Collaboration. "Constraints on Higgs boson properties using $WW^*(\to e\nu\mu\nu)jj$ production in $36.1\,\text{fb}^{-1}$ of $\sqrt{s} = 13$ TeV pp collisions with the ATLAS detector". In: *Eur. Phys. J. C* 82 (2021), p. 622. DOI: 10.1140/epjc/s10052-022-10366-1. arXiv: 2109.13808 [hep-ex].

[108] ATLAS Collaboration. "Determination of spin and parity of the Higgs boson in the $WW^* \to e\nu\mu\nu$ decay channel with the ATLAS detector". In: *Eur. Phys. J. C* 75.5 (2015), p. 231. DOI: 10.1140/epjc/s10052-015-3436-3. arXiv: 1503.03643 [hep-ex].

[109] ATLAS Collaboration. "Constraints on the off-shell Higgs boson signal strength in the high-mass ZZ and WW final states with the ATLAS detector". In: *Eur. Phys. J. C* 75.7 (2015), p. 335. DOI: 10.1140/epjc/s10052-015-3542-2. arXiv: 1503.01060 [hep-ex].

[110] T. Plehn et al. "A Method for identifying $H \to \tau^+\tau^- \to e^\pm\mu^\mp p_T$ at the CERN LHC". In: *Phys. Rev. D* 61 (2000), p. 093005. DOI: 10.1103/PhysRevD.61.093005. arXiv: hep-ph/9911385 [hep-ph].

[111] ATLAS Collaboration. "Measurements of gluon-gluon fusion and vector-boson fusion Higgs boson production cross-sections in the $H \to WW^* \to e\nu\mu\nu$ decay channel in pp collisions at $\sqrt{s} = 13$ TeV with the ATLAS detector". In: *Phys. Lett. B* 789 (2019), p. 508. DOI: 10.1016/j.physletb.2018.11.064. arXiv: 1808.09054 [hep-ex].

[112] CMS Collaboration. "Measurements of the Higgs boson production cross section and couplings in the W boson pair decay channel in proton-proton collisions at $\sqrt{s}$ = 13 TeV". In: (June 2022). arXiv: 2206.09466 [hep-ex].

[113] ATLAS Collaboration. "Higgs boson production cross-section measurements and their EFT interpretation in the 4ℓ decay channel at $\sqrt{s}$ =13 TeV with the ATLAS detector". In: *Eur. Phys. J. C* 80.10 (2020). [Erratum: Eur.Phys.J.C 81, 29 (2021), Erratum: Eur.Phys.J.C 81, 398 (2021)], p. 957. DOI: 10.1140/epjc/s10052-020-8227-9. arXiv: 2004.03447 [hep-ex].

[114] ATLAS Collaboration. "Measurements of Higgs boson production cross-sections in the $H \to \tau^+\tau^-$ decay channel in pp collisions at $\sqrt{s}$ = 13 TeV with the ATLAS detector". In: *JHEP* 08 (2022), p. 175. DOI: 10.1007/JHEP08(2022)175. arXiv: 2201.08269 [hep-ex].

[115] N. Berger et al. *Simplified Template Cross Sections - Stage 1.1*. arXiv: {1906.02754} (hep-ph).

[116] R. Frederix and S. Frixione. "Merging meets matching in MC@NLO". In: *JHEP* 12 (2012), p. 061. DOI: 10.1007/JHEP12(2012)061. arXiv: 1209.6215 [hep-ph].

[117] M. Czakon et al. "Top-pair production at the LHC through NNLO QCD and NLO EW". In: *JHEP* 10 (2017), p. 186. DOI: 10.1007/JHEP10(2017)186. arXiv: 1705.04105 [hep-ph].

[118] G. Louppe, M. Kagan, and K. Cranmer. "Learning to Pivot with Adversarial Networks". In: (Nov. 2016). arXiv: 1611.01046 [stat.ML].

[119] A. D. Sakharov. "Violation of CP invariance, C asymmetry, and baryon asymmetry of the universe". In: *Soviet Physics Uspekhi* 34.5 (), p. 392. DOI: {10.1070/PU1991v034n05ABEH002497}.

[120] Cabibbo, Nicola. "Unitary Symmetry and Leptonic Decays". In: *Phys. Rev. Lett.* 10 (12), 531–533. DOI: {10.1103/PhysRevLett.10.531}.

[121] M. Kobayashi and T. Maskawa. "CP Violation in the Renormalizable Theory of Weak Interaction". In: *Prog. Theor. Phys.* 49 (1973), pp. 652–657. DOI: 10.1143/PTP.49.652.

[122] J. H. Christenson et al. "Evidence for the 2π Decay of the K_2^0 Meson". In: *Phys. Rev. Lett.* 13 (1964), pp. 138–140. DOI: 10.1103/PhysRevLett.13.138.

[123] LHCb Collaboration. "First observation of CP violation in the decays of B_s^0 mesons". In: *Phys. Rev. Lett.* 110.22 (2013), p. 221601. DOI: 10.1103/PhysRevLett.110.221601. arXiv: 1304.6173 [hep-ex].

[124] LHCb Collaboration. "Observation of CP violation in $B^\pm \to DK^\pm$ decays". In: *Phys. Lett. B* 712 (2012). [Erratum: Phys.Lett.B 713, 351 (2012)], pp. 203–212. DOI: 10.1016/j.physletb.2012.04.060. arXiv: 1203.3662 [hep-ex].

[125] BaBar Collaboration. "Observation of direct CP violation in $B^0 \to K^+\pi^-$ decays". In: *Phys. Rev. Lett.* 93 (2004), p. 131801. DOI: 10.1103/PhysRevLett.93.131801. arXiv: hep-ex/0407057.

[126] LHCb Collaboration. "Observation of CP Violation in Charm Decays". In: *Phys. Rev. Lett.* 122.21 (2019), p. 211803. DOI: 10.1103/PhysRevLett.122.211803. arXiv: 1903.08726 [hep-ex].

[127] G. C. Branco et al. "Theory and phenomenology of two-Higgs-doublet models". In: *Phys. Rept.* 516 (2012), pp. 1–102. DOI: 10.1016/j.physrep.2012.02.002. arXiv: 1106.0034 [hep-ph].

[128] V. Keus et al. "CP Violating Two-Higgs-Doublet Model: Constraints and LHC Predictions". In: *JHEP* 04 (2016), p. 048. DOI: 10.1007/JHEP04(2016)048. arXiv: 1510.04028 [hep-ph].

[129] CMS Collaboration. "Constraints on anomalous Higgs boson couplings to vector bosons and fermions from the production of Higgs bosons using the $\tau\tau$ final state". In: (May 2022). arXiv: 2205.05120 [hep-ex].

[130] ATLAS Collaboration. "Test of CP-invariance of the Higgs boson in vector-boson fusion production and its decay into four leptons". In: (Apr. 2023). arXiv: 2304.09612 [hep-ex].

[131] ATLAS Collaboration. "Test of CP Invariance in Higgs Boson Vector-Boson-Fusion Production Using the H$\to\gamma\gamma$ Channel with the ATLAS Detector". In: *Phys. Rev. Lett.* 131.6 (2023), p. 061802. DOI: 10.1103/PhysRevLett.131.061802. arXiv: 2208.02338 [hep-ex].

[132] ATLAS Collaboration. "Test of CP invariance in vector-boson fusion production of the Higgs boson in the $H \to \tau\tau$ channel in proton–proton collisions at $\sqrt{s} = 13$ TeV with the ATLAS detector". In: *Phys. Lett. B* 805 (2020), p. 135426. DOI: 10.1016/j.physletb.2020.135426. arXiv: 2002.05315 [hep-ex].

[133] ATLAS Collaboration. "CP Properties of Higgs Boson Interactions with Top Quarks in the $t\bar{t}H$ and tH Processes Using $H \to \gamma\gamma$ with the ATLAS Detector". In: *Phys. Rev. Lett.* 125.6 (2020), p. 061802. DOI: 10.1103/PhysRevLett.125.061802. arXiv: 2004.04545 [hep-ex].

[134] ATLAS Collaboration. "Probing the CP nature of the top-Higgs Yukawa coupling in $t\bar{t}H$ and tH events with $H \to b\bar{b}$ decays using the ATLAS detector at the LHC". In: (Mar. 2023). arXiv: 2303.05974 [hep-ex].

[135] CMS Collaboration. "Search for CP violation in ttH and tH production in multilepton channels in proton-proton collisions at $\sqrt{s}$ = 13 TeV". In: (Aug. 2022). arXiv: 2208.02686 [hep-ex].

[136] CMS Collaboration. "Measurements of $\mathrm{t\bar{t}}H$ Production and the CP Structure of the Yukawa Interaction between the Higgs Boson and Top Quark in the Diphoton Decay Channel". In: *Phys. Rev. Lett.* 125.6 (2020), p. 061801. DOI: 10.1103/PhysRevLett.125.061801. arXiv: 2003.10866 [hep-ex].

[137] ATLAS Collaboration. "Measurement of the CP properties of Higgs boson interactions with τ-leptons with the ATLAS detector". In: (2022). arXiv: 2212.05833 [hep-ex].

[138] CMS Collaboration. "Analysis of the CP structure of the Yukawa coupling between the Higgs boson and τ leptons in proton-proton collisions at $\sqrt{s}$ = 13 TeV". In: *JHEP* 06 (2022), p. 012. DOI: 10.1007/JHEP06(2022)012. arXiv: 2110.04836 [hep-ex].

[139] F. Maltoni et al. "Higgs characterisation at NLO in QCD: CP properties of the top-quark Yukawa interaction". In: *Eur. Phys. J. C* 74.9 (2014), p. 3065. DOI: 10.1140/epjc/s10052-014-3065-2. arXiv: 1407.5089 [hep-ph].

[140] P. Artoisenet et al. "A framework for Higgs characterisation". In: *JHEP* 11 (2013), p. 043. DOI: 10.1007/JHEP11(2013)043. arXiv: 1306.6464 [hep-ph].

[141] K. Hagiwara, Q. Li, and K. Mawatari. "Jet angular correlation in vector-boson fusion processes at hadron colliders". In: *JHEP* 07 (2009), p. 101. DOI: 10.1088/1126-6708/2009/07/101. arXiv: 0905.4314 [hep-ph].

[142] V. Hankele, G. Klamke, and D. Zeppenfeld. "Higgs + 2 jets as a probe for CP properties". In: *Meeting on CP Violation and Non-standard Higgs Physics*. May 2006. arXiv: hep-ph/0605117.

[143] T. Sjöstrand et al. "A Brief Introduction to PYTHIA 8.1". In: *Comput. Phys. Commun.* 178 (2008), pp. 852–867. DOI: 10.1016/j.cpc.2008.01.036. arXiv: 0710.3820 [hep-ph].

[144] ATLAS Collaboration. "Measurements of Higgs boson properties in the diphoton decay channel with 36 fb^{-1} of pp collision data at $\sqrt{s} = 13$ TeV with the ATLAS detector". In: *Phys. Rev. D* 98 (2018), p. 052005. DOI: 10.1103/PhysRevD.98.052005. arXiv: 1802.04146 [hep-ex].

[145] CMS Collaboration. "Constraints on anomalous Higgs boson couplings to vector bosons and fermions in its production and decay using the four-lepton final state". In: *Phys. Rev. D* 104.5 (2021), p. 052004. DOI: 10.1103/PhysRevD.104.052004. arXiv: 2104.12152 [hep-ex].

[146] ATLAS Collaboration. "Constraints on non-Standard Model Higgs boson interactions in an effective Lagrangian using differential cross sections measured in the $H \to \gamma\gamma$ decay channel at $\sqrt{s} = 8$TeV with the ATLAS detector". In: *Phys. Lett. B* 753 (2016), pp. 69–85. DOI: 10.1016/j.physletb.2015.11.071. arXiv: 1508.02507 [hep-ex].

[147] H. Bahl et al. "Constraining the $\mathcal{CP}$ structure of Higgs-fermion couplings with a global LHC fit, the electron EDM and baryogenesis". In: *Eur. Phys. J. C* 82.7 (2022), p. 604. DOI: 10.1140/epjc/s10052-022-10528-1. arXiv: 2202.11753 [hep-ph].

[148] M. Baak et al. "Interpolation between multi-dimensional histograms using a new non-linear moment morphing method". In: *Nucl. Instrum. Meth. A* 771 (2015), pp. 39–48. DOI: 10.1016/j.nima.2014.10.033. arXiv: 1410.7388 [physics.data-an].

[149] ATLAS Collaboration. *A morphing technique for signal modelling in a multidimensional space of coupling parameters*. Tech. rep. CERN. URL: https://cds.cern.ch/record/2066980.

[150] ATLAS Collaboration. *Soft b-hadron tagging for compressed SUSY scenarios*. Tech. rep. CERN. URL: https://cds.cern.ch/record/2682131.

[151] ATLAS Collaboration. *Expected tracking and related performance with the updated ATLAS Inner Tracker layout at the High-Luminosity LHC*. Tech. rep. 2021. URL: https://cds.cern.ch/record/2776651.

[152] CMS Collaboration. "Measurements of Higgs boson production in the decay channel with a pair of τ leptons in proton-proton collisions at $\sqrt{s}$ = 13 TeV". In: (Apr. 2022). arXiv: 2204.12957 [hep-ex].

[153] D. B. Kaplan and H. Georgi. "SU(2) x U(1) Breaking by Vacuum Misalignment". In: *Phys. Lett. B* 136 (1984), pp. 183–186. DOI: 10.1016/0370-2693(84)91177-8.

[154] D. B. Kaplan, H. Georgi, and S. Dimopoulos. "Composite Higgs Scalars". In: *Phys. Lett. B* 136 (1984), pp. 187–190. DOI: 10.1016/0370-2693(84)91178-X.

[155] J. Brehmer et al. "Polarized WW scattering on the Higgs pole". In: *Phys. Rev. D* 90.5 (2014), p. 054023. DOI: 10.1103/PhysRevD.90.054023. arXiv: 1404.5951 [hep-ph].

[156] A. Greljo et al. "Electroweak Higgs production with HIGGSPO at NLO QCD". In: *Eur. Phys. J. C* 77.12 (2017), p. 838. DOI: 10.1140/epjc/s10052-017-5422-4. arXiv: 1710.04143 [hep-ph].

[157] ATLAS Collaboration. "Measurement of the cross-section for electroweak production of dijets in association with a Z boson in pp collisions at $\sqrt{s}$ = 13 TeV with the ATLAS detector". In: *Phys. Lett. B* 775 (2017), pp. 206–228. DOI: 10.1016/j.physletb.2017.10.040. arXiv: 1709.10264 [hep-ex].

[158] ATLAS Collaboration. "A search for the dimuon decay of the Standard Model Higgs boson with the ATLAS detector". In: *Phys. Lett. B* 812 (2021), p. 135980. DOI: 10.1016/j.physletb.2020.135980. arXiv: 2007.07830 [hep-ex].

[159] CMS Collaboration. "Evidence for Higgs boson decay to a pair of muons". In: *JHEP* 01 (2021), p. 148. DOI: 10.1007/JHEP01(2021)148. arXiv: 2009.04363 [hep-ex].

[160] ATLAS Collaboration. "Measurements of WH and ZH production in the $H \to b\bar{b}$ decay channel in pp collisions at 13 TeV with the ATLAS detector". In: *Eur. Phys. J. C* 81.2 (2021), p. 178. DOI: 10.1140/epjc/s10052-020-08677-2. arXiv: 2007.02873 [hep-ex].

[161] ATLAS Collaboration. "Measurements of Higgs bosons decaying to bottom quarks from vector boson fusion production with the ATLAS experiment at $\sqrt{s} = 13$ TeV". In: *Eur. Phys. J. C* 81.6 (2021), p. 537. DOI: 10.1140/epjc/s10052-021-09192-8. arXiv: 2011.08280 [hep-ex].

[162] ATLAS Collaboration. "Measurement of Higgs boson decay into b-quarks in associated production with a top-quark pair in pp collisions at $\sqrt{s} = 13$ TeV with the ATLAS detector". In: *JHEP* 06 (2022), p. 097. DOI: 10.1007/JHEP06(2022)097. arXiv: 2111.06712 [hep-ex].

[163] ATLAS Collaboration. “Constraints on Higgs boson production with large transverse momentum using H→bb¯ decays in the ATLAS detector”. In: *Phys. Rev. D* 105.9 (2022), p. 092003. DOI: 10.1103/PhysRevD.105.092003. arXiv: 2111.08340 [hep-ex].

[164] ATLAS Collaboration. “A search for the $Z\gamma$ decay mode of the Higgs boson in pp collisions at $\sqrt{s}$ = 13 TeV with the ATLAS detector”. In: *Phys. Lett. B* 809 (2020), p. 135754. DOI: 10.1016/j.physletb.2020.135754. arXiv: 2005.05382 [hep-ex].

[165] ATLAS Collaboration. “Combined measurements of Higgs boson production and decay using up to 80 fb^{-1} of proton-proton collision data at $\sqrt{s}$ = 13 TeV collected with the ATLAS experiment”. In: *Phys. Rev. D* 101.1 (2020), p. 012002. DOI: 10.1103/PhysRevD.101.012002. arXiv: 1909.02845 [hep-ex].

[166] M. Grazzini, A. Ilnicka, M. Spira, and M. Wiesemann. “Modeling BSM effects on the Higgs transverse-momentum spectrum in an EFT approach”. In: *JHEP* 03 (2017), p. 115. DOI: 10.1007/JHEP03(2017)115. arXiv: 1612.00283 [hep-ph].

[167] ATLAS Collaboration. “Interpretations of the ATLAS measurements of Higgs boson production and decay rates and differential cross-sections in pp collisions at $\sqrt{s}$ = 13 TeV”. In: (Feb. 2024). arXiv: 2402.05742 [hep-ex].

[168] R. Contino, D. Marzocca, D. Pappadopulo, and R. Rattazzi. “On the effect of resonances in composite Higgs phenomenology”. In: *JHEP* 10 (2011), p. 081. DOI: 10.1007/JHEP10(2011)081. arXiv: 1109.1570 [hep-ph].

[169] K. Agashe et al. “The minimal composite Higgs model”. In: *Nucl. Phys. B* 719 (2005), pp. 165–187. DOI: 10.1016/j.nuclphysb.2005.04.035. arXiv: hep-ph/0412089 [hep-ph].

[170] R. Foadi et al. “Minimal walking technicolor: Setup for collider physics”. In: *Phys. Rev. D* 76 (2007), p. 055005. DOI: 10.1103/PhysRevD.76.055005. arXiv: 0706.1696 [hep-ph].

[171] A. Belyaev et al. “Technicolor walks at the LHC”. In: *Phys. Rev. D* 79 (2009), p. 035006. DOI: 10.1103/PhysRevD.79.035006. arXiv: 0809.0793 [hep-ph].

[172] A. Oliveira. “Gravity particles from Warped Extra Dimensions, predictions for LHC”. In: (Mar. 2014). arXiv: 1404.0102 [hep-ph].

[173] L. Randall and R. Sundrum. “A Large mass hierarchy from a small extra dimension”. In: *Phys. Rev. Lett.* 83 (1999), pp. 3370–3373. DOI: 10.1103/PhysRevLett.83.3370. arXiv: hep-ph/9905221.

[174] H. Georgi and M. Machacek. “Doubly Charged Higgs Bosons”. In: *Nucl. Phys. B* 262 (1985), pp. 463–477. DOI: 10.1016/0550-3213(85)90325-6.

[175] ATLAS Collaboration. *Summary of Diboson Resonance Searches at the ATLAS experiment using full run-2 data*. Tech. rep. Geneva: CERN, 2023. URL: https://cds.cern.ch/record/2853753.

[176] ATLAS Collaboration. “Search for heavy resonances decaying into a pair of Z bosons in the $\ell^+\ell^-\ell'^+\ell'^-$ and $\ell^+\ell^-\nu\bar{\nu}$ final states using 139 fb^{-1} of proton–proton collisions at $\sqrt{s}$ = 13 TeV with the ATLAS detector”. In: *Eur. Phys. J. C* 81.4 (2021), p. 332. DOI: 10.1140/epjc/s10052-021-09013-y. arXiv: 2009.14791 [hep-ex].

[177] CMS Collaboration. “Search for a new scalar resonance decaying to a pair of Z bosons in proton-proton collisions at $\sqrt{s}$ = 13 TeV”. In: *JHEP* 06 (2018). [Erratum: JHEP 03, 128 (2019)], p. 127. DOI: 10.1007/JHEP06(2018)127. arXiv: 1804.01939 [hep-ex].

[178] ATLAS Collaboration. *Search for heavy resonances in the decay channel $W^+W^- \to e\nu\mu\nu$ in pp Collisions at $\sqrt{s} = 13$ TeV using 139 fb^{-1} of data with the ATLAS detector*. 2022. URL: https://cds.cern.ch/record/2842518.

[179] CMS Collaboration. "Search for a heavy Higgs boson decaying to a pair of W bosons in proton-proton collisions at $\sqrt{s} = 13$ TeV". In: *JHEP* 03 (2020), p. 034. DOI: 10.1007/JHEP03(2020)034. arXiv: 1912.01594 [hep-ex].

[180] CMS Collaboration. "Search for charged Higgs bosons produced in vector boson fusion processes and decaying into vector boson pairs in proton–proton collisions at $\sqrt{s} = 13$ TeV". In: *Eur. Phys. J. C* 81.8 (2021), p. 723. DOI: 10.1140/epjc/s10052-021-09472-3. arXiv: 2104.04762 [hep-ex].

[181] ATLAS Collaboration. "Search for resonant WZ production in the fully leptonic final state in proton–proton collisions at $\sqrt{s} = \mathbf{13}$ TeV with the ATLAS detector". In: *Eur. Phys. J. C* 83.7 (2023), p. 633. DOI: 10.1140/epjc/s10052-023-11437-7. arXiv: 2207.03925 [hep-ex].

[182] ATLAS Collaboration. "Search for diboson resonances in hadronic final states in 139 fb^{-1} of *pp* collisions at $\sqrt{s} = 13$ TeV with the ATLAS detector". In: *JHEP* 09 (2019), p. 091. DOI: 10.1007/JHEP09(2019)091. arXiv: 1906.08589 [hep-ex].

[183] ATLAS Collaboration. "Dijet Resonance Search with Weak Supervision Using $\sqrt{s} = 13$ TeV *pp* collisions in the ATLAS detector". In: *Phys. Rev. Lett.* 125 (2020), p. 131801. DOI: 10.1103/PhysRevLett.125.131801. arXiv: 2005.02983 [hep-ex].

[184] CMS Collaboration. "Search for new heavy resonances decaying to WW, WZ, ZZ, WH, or ZH boson pairs in the all-jets final state in proton-proton collisions at $\sqrt{s} = 13$ TeV". In: *Phys. Lett. B* 844 (2023), p. 137813. DOI: 10.1016/j.physletb.2023.137813. arXiv: 2210.00043 [hep-ex].

[185] ATLAS Collaboration. "Search for heavy diboson resonances in semileptonic final states in *pp* collisions at $\sqrt{s} = 13$ TeV with the ATLAS detector". In: *Eur. Phys. J. C* 80 (2020), p. 1165. DOI: 10.1140/epjc/s10052-020-08554-y. arXiv: 2004.14636 [hep-ex].

[186] CMS Collaboration. "Search for heavy resonances decaying to $Z(\nu\bar{\nu})V(q\bar{q}')$ in proton-proton collisions at $\sqrt{s} = 13$ TeV". In: *Phys. Rev. D* 106.1 (2022), p. 012004. DOI: 10.1103/PhysRevD.106.012004. arXiv: 2109.08268 [hep-ex].

[187] ATLAS Collaboration. "A search for heavy Higgs bosons decaying into vector bosons in same-sign two-lepton final states in *pp* collisions at $\sqrt{s} = 13$ TeV with the ATLAS detector". In: (Nov. 2022). arXiv: 2211.02617 [hep-ex].

[188] CMS Collaboration. "Search for heavy resonances decaying to WW, WZ, or WH boson pairs in a final state consisting of a lepton and a large-radius jet in proton-proton collisions at $\sqrt{s} = 13$ TeV". In: *Phys. Rev. D* 105.3 (2022), p. 032008. DOI: 10.1103/PhysRevD.105.032008. arXiv: 2109.06055 [hep-ex].

[189] ATLAS Collaboration. "Search for resonances decaying into a weak vector boson and a Higgs boson in the fully hadronic final state produced in proton–proton collisions at $\sqrt{s} = 13$ TeV with the ATLAS detector". In: *Phys. Rev. D* 102 (2020), p. 112008. DOI: 10.1103/PhysRevD.102.112008. arXiv: 2007.05293 [hep-ex].

[190] ATLAS Collaboration. "Search for heavy resonances decaying into a Z or W boson and a Higgs boson in final states with leptons and b-jets in 139 fb^{-1} of pp collisions at $\sqrt{s} = 13$ TeV with the ATLAS detector". In: *JHEP* 06 (2023), p. 016. DOI: 10.1007/JHEP06(2023)016. arXiv: 2207.00230 [hep-ex].

[191] CMS Collaboration. "Search for a heavy vector resonance decaying to a Z boson and a Higgs boson in proton-proton collisions at $\sqrt{s} = 13$ TeV". In: *Eur. Phys. J. C* 81.8 (2021), p. 688. DOI: 10.1140/epjc/s10052-021-09348-6. arXiv: 2102.08198 [hep-ex].

[192] CMS Collaboration. "Search for a heavy pseudoscalar Higgs boson decaying into a 125 GeV Higgs boson and a Z boson in final states with two tau and two light leptons at $\sqrt{s} = 13$ TeV". In: *JHEP* 03 (2020), p. 065. DOI: 10.1007/JHEP03(2020)065. arXiv: 1910.11634 [hep-ex].

[193] ATLAS Collaboration. "Search for boosted diphoton resonances in the 10 to 70 GeV mass range using 138 fb^{-1} of 13 TeV pp collisions with the ATLAS detector". In: (Nov. 2022). arXiv: 2211.04172 [hep-ex].

[194] ATLAS Collaboration. "Search for resonances decaying into photon pairs in 139 fb^{-1} of pp collisions at $\sqrt{s}$=13 TeV with the ATLAS detector". In: *Phys. Lett. B* 822 (2021), p. 136651. DOI: 10.1016/j.physletb.2021.136651. arXiv: 2102.13405 [hep-ex].

[195] CMS Collaboration. "Search for a standard model-like Higgs boson in the mass range between 70 and 110 GeV in the diphoton final state in proton-proton collisions at $\sqrt{s} = 8$ and 13 TeV". In: *Phys. Lett. B* 793 (2019), pp. 320–347. DOI: 10.1016/j.physletb.2019.03.064. arXiv: 1811.08459 [hep-ex].

[196] ATLAS Collaboration. *Search for the $Z\gamma$ decay mode of new high-mass resonances in pp collisions at $\sqrt{s} = 13$ TeV with the ATLAS detector*. Tech. rep. URL: http://cds.cern.ch/record/2861557.

[197] ATLAS Collaboration. "Search for high-mass Wγ and Zγ resonances using hadronic W/Z boson decays from 139 fb^{-1} of pp collisions at $\sqrt{s}$ = 13 TeV with the ATLAS detector". In: *JHEP* 07 (2023), p. 125. DOI: 10.1007/JHEP07(2023)125. arXiv: 2304.11962 [hep-ex].

[198] CMS Collaboration. "Search for Wγ resonances in proton-proton collisions at $\sqrt{s} = 13$ TeV using hadronic decays of Lorentz-boosted W bosons". In: *Phys. Lett. B* 826 (2022), p. 136888. DOI: 10.1016/j.physletb.2022.136888. arXiv: 2106.10509 [hep-ex].

[199] ATLAS Collaboration. "Search for Heavy Resonances Decaying into a Photon and a Hadronically Decaying Higgs Boson in pp Collisions at $\sqrt{s} = 13$ TeV with the ATLAS Detector". In: *Phys. Rev. Lett.* 125 (2020), p. 251802. DOI: 10.1103/PhysRevLett.125.251802. arXiv: 2008.05928 [hep-ex].

[200] CMS Collaboration. "Search for narrow Hγ resonances in proton-proton collisions at $\sqrt{s} = 13$ TeV". In: *Phys. Rev. Lett.* 122.8 (2019), p. 081804. DOI: 10.1103/PhysRevLett.122.081804. arXiv: 1808.01257 [hep-ex].

[201] A. L. Read. "Presentation of search results: The CL$_s$ technique". In: *J. Phys. G* 28 (2002), pp. 2693–2704. DOI: 10.1088/0954-3899/28/10/313.

[202] G. Cowan et al. "Asymptotic formulae for likelihood-based tests of new physics". In: *Eur. Phys. J. C* 71 (2011). [Erratum: Eur. Phys. J. C **73** (2013) 2501], p. 1554. DOI: 10.1140/epjc/s10052-011-1554-0. arXiv: 1007.1727 [physics.data-an].

[203] P. W. Higgs. "Broken Symmetries and the Masses of Gauge Bosons". In: *Phys. Rev. Lett.* 13 (1964), pp. 508–509. DOI: 10.1103/PhysRevLett.13.508.

[204] F. Englert, and R. Brout. “Broken Symmetry and the Mass of Gauge Vector Mesons”. In: *Phys. Rev. Lett.* 13 (1964), pp. 321–323. DOI: 10.1103/PhysRevLett.13.321.

[205] A. G. Cohen, D. B. Kaplan, and A. E. Nelson. “Progress in electroweak baryogenesis”. In: *Ann. Rev. Nucl. Part. Sci.* 43 (1993), pp. 27–70. DOI: 10.1146/annurev.ns.43.120193.000331. arXiv: hep-ph/9302210.

[206] J. E. Kim, and G. Carosi. “Axions and the Strong CP Problem”. In: *Rev. Mod. Phys.* 82 (2010). [Erratum: Rev.Mod.Phys. 91, 049902 (2019)], pp. 557–602. DOI: 10.1103/RevModPhys.82.557. arXiv: 0807.3125 [hep-ph].

[207] M. E. Peskin. “Supersymmetry in Elementary Particle Physics”. In: *Theoretical Advanced Study Institute in Elementary Particle Physics: Exploring New Frontiers Using Colliders and Neutrinos*. Jan. 2008, pp. 609–704. arXiv: 0801.1928 [hep-ph].

[208] E. Bagnaschi et al. “MSSM Higgs Boson Searches at the LHC: Benchmark Scenarios for Run 2 and Beyond”. In: *Eur. Phys. J. C* 79.7 (2019), p. 617. DOI: 10.1140/epjc/s10052-019-7114-8. arXiv: 1808.07542 [hep-ph].

[209] P. Fileviez Perez et al. “Testing a Neutrino Mass Generation Mechanism at the LHC”. In: *Phys. Rev. D* 78 (2008), p. 071301. DOI: 10.1103/PhysRevD.78.071301. arXiv: 0803.3450 [hep-ph].

[210] Y. Cai, T. Han, T. Li, and R. Ruiz. “Lepton Number Violation: Seesaw Models and Their Collider Tests”. In: *Front. in Phys.* 6 (2018), p. 40. DOI: 10.3389/fphy.2018.00040. arXiv: 1711.02180 [hep-ph].

[211] W. Chao, Z. G. Si, Z. Z. Xing, and S. Zhou. “Correlative signatures of heavy Majorana neutrinos and doubly-charged Higgs bosons at the Large Hadron Collider”. In: *Phys. Lett. B* 666 (2008), pp. 451–454. DOI: 10.1016/j.physletb.2008.08.003. arXiv: 0804.1265 [hep-ph].

[212] D. Fontes, J. C. Romão, R. Santos, and J. Silva. “Undoubtable signs of CP-violation in Higgs boson decays at the LHC run 2”. In: *Phys. Rev. D* 92.5 (2015), p. 055014. DOI: 10.1103/PhysRevD.92.055014. arXiv: 1506.06755 [hep-ph].

[213] D. Fontes, J. C. Romão, and J. Silva. “$h \to Z\gamma$ in the complex two Higgs doublet model”. In: *JHEP* 12 (2014), p. 043. DOI: 10.1007/JHEP12(2014)043. arXiv: 1408.2534 [hep-ph].

[214] S. Gori, C. Grojean, A. Juste, and A. Paul. “Heavy Higgs Searches: Flavour Matters”. In: *JHEP* 01 (2018), p. 108. DOI: 10.1007/JHEP01(2018)108. arXiv: 1710.03752 [hep-ph].

[215] F. J. Botella, G. C. Branco, M. Nebot, and M. N. Rebelo. “Flavour Changing Higgs Couplings in a Class of Two Higgs Doublet Models”. In: *Eur. Phys. J. C* 76.3 (2016), p. 161. DOI: 10.1140/epjc/s10052-016-3993-0. arXiv: 1508.05101 [hep-ph].

[216] M. Muhlleitner, and M. Spira. “A Note on doubly charged Higgs pair production at hadron colliders”. In: *Phys. Rev. D* 68 (2003), p. 117701. DOI: 10.1103/PhysRevD.68.117701. arXiv: hep-ph/0305288.

[217] M. S. Chanowitz and M. Golden. “Higgs Boson Triplets With M (W) = M $(Z)\cos\theta\omega$”. In: *Phys. Lett. B* 165 (1985), pp. 105–108. DOI: 10.1016/0370-2693(85)90700-2.

[218] K. Hartling, K. Kumar, and H. E. Logan. “GMCALC: a calculator for the Georgi-Machacek model”. In: (Dec. 2014). arXiv: 1412.7387 [hep-ph].

[219] K. Hartling, K. Kumar, and H. E. Logan. “The decoupling limit in the Georgi-Machacek model”. In: *Phys. Rev. D* 90.1 (2014), p. 015007. DOI: 10.1103/PhysRevD.90.015007. arXiv: 1404.2640 [hep-ph].

[220] R. M. Schabinger, and J. D. Wells. "A Minimal spontaneously broken hidden sector and its impact on Higgs boson physics at the large hadron collider". In: *Phys. Rev. D* 72 (2005), p. 093007. DOI: 10.1103/PhysRevD.72.093007. arXiv: hep-ph/0509209.

[221] D. Pappadopulo, A. Thamm, R. Torre, and A. Wulzer. "Heavy Vector Triplets: Bridging Theory and Data". In: *JHEP* 09 (2014), p. 060. DOI: 10.1007/JHEP09(2014)060. arXiv: 1402.4431 [hep-ph].

[222] J. M. Cornwall, D. N. Levin, and G. Tiktopoulos. "Derivation of Gauge Invariance from High-Energy Unitarity Bounds on the s Matrix". In: *Phys. Rev. D* 10 (1974). [Erratum: Phys.Rev.D 11, 972 (1975)], p. 1145. DOI: 10.1103/PhysRevD.10.1145.

[223] V. Barger, W. Y. Keung, and E. Ma. "Gauge model with light W and Z bosons". In: *Phys. Rev. D* 22 (1980), pp. 727–737. DOI: 10.1103/PhysRevD.22.727.

[224] W. D. Goldberger and M. B. Wise. "Modulus stabilization with bulk fields". In: *Phys. Rev. Lett.* 83 (1999), pp. 4922–4925. DOI: 10.1103/PhysRevLett.83.4922. arXiv: hep-ph/9907447.

[225] W. D. Goldberger and M. B. Wise. "Phenomenology of a stabilized modulus". In: *Phys. Lett. B* 475 (2000), pp. 275–279. DOI: 10.1016/S0370-2693(00)00099-X. arXiv: hep-ph/9911457.

[226] CMS Collaboration. "Searches for Higgs Boson Production through Decays of Heavy Resonances". In: (Mar. 2024). arXiv: 2403.16926 [hep-ex].

[227] F. Sannino et al. "Orientifold theory dynamics and symmetry breaking". In: *Phys. Rev. D* 71 (2005), p. 051901. DOI: 10.1103/PhysRevD.71.051901. arXiv: hep-ph/0405209 [hep-ph].

[228] M. Schmaltz et al. "LITTLE HIGGS THEORIES". In: *Ann. Rev. Nucl. Part. Sci.* 55 (2005), pp. 229–270. DOI: 10.1146/annurev.nucl.55.090704.151502. arXiv: hep-ph/0502182 [hep-ph].

[229] M. J. Dugan et al. "Anatomy of a composite Higgs model". In: *Nucl. Phys. B* 254 (1985), p. 299. DOI: 10.1016/0550-3213(85)90221-4.

[230] H. Davoudiasl et al. "Bulk gauge fields in the Randall-Sundrum model". In: *Phys. Lett. B* 473 (2000), pp. 43–49. DOI: 10.1016/S0370-2693(99)01430-6. arXiv: hep-ph/9911262.

[231] J. F. Gunion and H. E. Haber. "The CP conserving two Higgs doublet model: The Approach to the decoupling limit". In: *Phys. Rev. D* 67 (2003), p. 075019. DOI: 10.1103/PhysRevD.67.075019. arXiv: hep-ph/0207010.

[232] V. Keus et al. "Three-Higgs-doublet models: symmetries, potentials and Higgs boson masses". In: *JHEP* 01 (2014), p. 052. DOI: 10.1007/JHEP01(2014)052. arXiv: 1310.8253 [hep-ph].

[233] T.P Cheng and L Li. "Neutrino masses, mixings, and oscillations in SU(2)×U(1) models of electroweak interactions". In: *Phys. Rev. D* 22 (11 Dec. 1980), pp. 2860–2868. DOI: 10.1103/PhysRevD.22.2860. URL: https://link.aps.org/doi/10.1103/PhysRevD.22.2860.

[234] J. Schechter and J. W. F. Valle. "Neutrino masses in SU(2) $\bigotimes$ U(1) theories". In: *Phys. Rev. D* 22 (9 Nov. 1980), pp. 2227–2235. DOI: 10.1103/PhysRevD.22.2227. URL: https://link.aps.org/doi/10.1103/PhysRevD.22.2227.

[235] M. S. Chanowitz and M. Golden. "Higgs boson triplets with Mw=Mzcos θ_w". In: *Physics Letters B* 165.1 (1985), pp. 105–108. ISSN: 0370-2693. DOI: https://doi.org/10.1016/0370-2693(85)90700-2. URL: https://www.sciencedirect.com/science/article/pii/0370269385907002.

[236] R. Vega J. F. Gunion and J. Wudka. “Higgs triplets in the standard model”. In: *Phys. Rev. D* 42 (5 Sept. 1990), pp. 1673–1691. DOI: 10.1103/PhysRevD.42.1673. URL: https://link.aps.org/doi/10.1103/PhysRevD.42.1673.

[237] ATLAS Collaboration. “Performance of the missing transverse momentum triggers for the ATLAS detector during Run 2 data taking”. In: *JHEP* 08 (2020), p. 080. DOI: 10.1007/JHEP08(2020)080. arXiv: 2005.09554 [hep-ex].

[238] ATLAS Collaboration. “Performance of electron and photon triggers in ATLAS during LHC Run 2”. In: *Eur. Phys. J. C* 80 (2020), p. 47. DOI: 10.1140/epjc/s10052-019-7500-2. arXiv: 1909.00761 [hep-ex].

[239] ATLAS Collaboration. “Performance of the ATLAS muon triggers in Run 2”. In: *JINST* 15 (2020), P09015. DOI: 10.1088/1748-0221/15/09/p09015. arXiv: 2004.13447 [hep-ex].

[240] A. Honle. “Searches for new resonances decaying to a Higgs and a vector boson with the ATLAS detector at the LHC”. 2021. URL: https://cds.cern.ch/record/2779497.

[241] ATLAS Collaboration. “Observation of $H \to b\bar{b}$ decays and VH production with the ATLAS detector”. In: *Phys. Lett. B* 786 (2018), pp. 59–86. DOI: 10.1016/j.physletb.2018.09.013. arXiv: 1808.08238 [hep-ex].

[242] ATLAS Collaboration. “Measurement of cross-sections for production of a Z boson in association with a flavor-inclusive or doubly b-tagged large-radius jet in proton-proton collisions at $\sqrt{s} = 13$ TeV with the ATLAS experiment”. In: (Apr. 2022). arXiv: 2204.12355 [hep-ex].

[243] ATLAS Collaboration. “Search for heavy resonances decaying into a W or Z boson and a Higgs boson in final states with leptons and b-jets in 36 fb^{-1} of $\sqrt{s} = 13$ TeV pp collisions with the ATLAS detector”. In: *JHEP* 03 (2018). [Erratum: JHEP 11, 051 (2018)], p. 174. DOI: 10.1007/JHEP03(2018)174. arXiv: 1712.06518 [hep-ex].

[244] CMS Collaboration. “Search for a heavy pseudoscalar Higgs boson decaying into a 125 GeV Higgs boson and a Z boson in final states with two tau and two light leptons at $\sqrt{s} = 13$ TeV”. In: *JHEP* 03 (2020), p. 065. DOI: 10.1007/JHEP03(2020)065. arXiv: 1910.11634 [hep-ex].

[245] CMS Collaboration. “Identification of heavy-flavour jets with the CMS detector in pp collisions at 13 TeV”. In: *JINST* 13.05 (2018), P05011. DOI: 10.1088/1748-0221/13/05/P05011. arXiv: 1712.07158 [physics.ins-det].

[246] S. R. Maschek. “Search for heavy Zh and Wh resonances in 13 TeV proton-proton collisions with the ATLAS detector at the LHC”. 2021. URL: https://cds.cern.ch/record/2797577.

[247] T. Qiu. “Search for heavy resonances decaying into a Z boson and a Higgs boson with the ATLAS detector”. 2022. URL: https://cds.cern.ch/record/2850728.

[248] M. A. Vessella. “Do Dibosons Dream of Semileptonic Sheep? Searching for heavy Wh resonances and optimizing track reconstruction with the ATLAS detector”. 2024. URL: https://cds.cern.ch/record/2910311.

[249] ATLAS Collaboration. “Modelling and computational improvements to the simulation of single vector-boson plus jet processes for the ATLAS experiment”. In: *JHEP* 08 (2022), p. 089. DOI: 10.1007/JHEP08(2022)089. arXiv: 2112.09588 [hep-ex].

[250] M.P. Wand and M.C. Jones. *Kernel Smoothing*. CRC Press, 1994. ISBN: 9780412552700. URL: https://books.google.ch/books?id=GTOOi5yE008C.

[251] ATLAS Collaboration. *Optimisation of the smoothing of b-jet identification efficiency and mistag rate simulation-to-data scale factors in ATLAS*. Tech. rep. 2020. URL: https://cds.cern.ch/record/2710598.

[252] CMS Collaboration. *Transformer Neural Networks for Identifying Boosted Higgs Bosons decaying into $b\bar{b}$ and $c\bar{c}$ in ATLAS*. Tech. rep. CERN, 2023. URL: https://cds.cern.ch/record/2866601.

[253] M. B. Gavela, J. M. No, V. Sanz, and J. F. de Trocóniz. "Nonresonant Searches for Axionlike Particles at the LHC". In: *Phys. Rev. Lett.* 124.5 (2020), p. 051802. DOI: 10.1103/PhysRevLett.124.051802. arXiv: 1905.12953 [hep-ph].

[254] N. Craig et al. "Heavy Higgs bosons at low $\tan\beta$: from the LHC to 100 TeV". In: *JHEP* 01 (2017), p. 018. DOI: 10.1007/JHEP01(2017)018. arXiv: 1605.08744 [hep-ph].

[255] ATLAS Collaboration. "Search for $t\bar{t}H/A \to t\bar{t}t\bar{t}$ production in the multilepton final state in proton–proton collisions at $\sqrt{s}$ = 13 TeV with the ATLAS detector". In: *JHEP* 07 (2023), p. 203. DOI: 10.1007/JHEP07(2023)203. arXiv: 2211.01136 [hep-ex].

[256] ATLAS Collaboration. "Search for the standard model Higgs boson produced in association with top quarks and decaying into a $b\bar{b}$ pair in pp collisions at $\sqrt{s}$ = 13 TeV with the ATLAS detector". In: *Phys. Rev. D* 97.7 (2018), p. 072016. DOI: 10.1103/PhysRevD.97.072016. arXiv: 1712.08895 [hep-ex].

[257] CMS Collaboration. "Search for a heavy pseudoscalar boson decaying to a Z and a Higgs boson at $\sqrt{s}$ = 13 TeV". In: *Eur. Phys. J. C* 79.7 (2019), p. 564. DOI: 10.1140/epjc/s10052-019-7058-z. arXiv: 1903.00941 [hep-ex].

[258] CMS Collaboration. "Search for a heavy pseudoscalar Higgs boson decaying into a 125 GeV Higgs boson and a Z boson in final states with two tau and two light leptons at $\sqrt{s}$ = 13 TeV". In: *JHEP* 03 (2020), p. 065. DOI: 10.1007/JHEP03(2020)065. arXiv: 1910.11634 [hep-ex].

[259] ATLAS Collaboration. "Search for heavy Higgs bosons decaying into two tau leptons with the ATLAS detector using pp collisions at $\sqrt{s} = 13$ TeV". In: *Phys. Rev. Lett.* 125.5 (2020), p. 051801. DOI: 10.1103/PhysRevLett.125.051801. arXiv: 2002.12223 [hep-ex].

[260] ATLAS Collaboration. "Search for Heavy Higgs Bosons A/H Decaying to a Top Quark Pair in pp Collisions at $\sqrt{s} = 8$ TeV with the ATLAS Detector". In: *Phys. Rev. Lett.* 119.19 (2017), p. 191803. DOI: 10.1103/PhysRevLett.119.191803. arXiv: 1707.06025 [hep-ex].

[261] Y. Gao et al. "Spin Determination of Single-Produced Resonances at Hadron Colliders". In: *Phys. Rev. D* 81 (2010), p. 075022. DOI: 10.1103/PhysRevD.81.075022. arXiv: 1001.3396 [hep-ph].

[262] A. Berlin, T. Lin, and L. T. Wang. "Mono-Higgs Detection of Dark Matter at the LHC". In: *JHEP* 06 (2014), p. 078. DOI: 10.1007/JHEP06(2014)078. arXiv: 1402.7074 [hep-ph].

[263] M. Muhlleitner, S. Margarete, P. Marco, R. Santos, and J. Wittbrodt. "The N2HDM under Theoretical and Experimental Scrutiny". In: *JHEP* 03 (2017), p. 094. DOI: 10.1007/JHEP03(2017)094. arXiv: 1612.01309 [hep-ph].

[264] R. Boto, J. C. Romão, and J. P. Silva. "Current bounds on the type-Z Z3 three-Higgs-doublet model". In: *Phys. Rev. D* 104.9 (2021), p. 095006. DOI: 10.1103/PhysRevD.104.095006. arXiv: 2106.11977 [hep-ph].

[265] G. Lazarides, Q. Shafi, and C. Wetterich. "Proton lifetime and fermion masses in an SO(10) model". In: *Nuclear Physics B* 181.2 (1981), pp. 287–300. ISSN: 0550-3213. DOI: https://doi.org/10.1016/0550-3213(81)90354-0. URL: https://www.sciencedirect.com/science/article/pii/0550321381903540.

[266] N. Ghosh, S. Ghosh, and I. Saha. "Charged Higgs boson searches in the Georgi-Machacek model at the LHC". In: *Phys. Rev. D* 101.1 (2020), p. 015029. DOI: 10.1103/PhysRevD.101.015029. arXiv: 1908.00396 [hep-ph].

[267] T Biekötter, H. Chakraborti, and S. Heinemeyer. "The "96 GeV excess" in the N2HDM". In: *31st Rencontres de Blois on Particle Physics and Cosmology*. Oct. 2019. arXiv: 1910.06858 [hep-ph].

[268] S. G. Grewe. "Search for Charged Higgs Bosons in $H^+ \to W^+h$ Decays with the ATLAS Detector". 2021. URL: https://cds.cern.ch/record/2776405.

[269] H. Bahl et al. "The forgotten channels: charged Higgs boson decays to a $W^\pm$ and a non-SM-like Higgs boson". In: *JHEP* 06 (2021), p. 183. DOI: 10.1007/JHEP06(2021)183. arXiv: 2103.07484 [hep-ph].

[270] ATLAS Collaboration. *Search for diphoton resonances in the 66 to 110 GeV mass range using 140 fb^{-1} of 13 TeV pp collisions collected with the ATLAS detector*. Tech. rep. 2023. URL: https://cds.cern.ch/record/2862024.

[271] ATLAS Collaboration. "Search for the $Z\gamma$ decay mode of new high-mass resonances in pp collisions at $\sqrt{s} = 13$ TeV with the ATLAS detector". In: (Sept. 2023). arXiv: 2309.04364 [hep-ex].

[272] S. Catani, Y. L. Dokshitzer, M. Olsson, G. Turnock, and B. R. Webber. "New clustering algorithm for multi - jet cross-sections in e+ e- annihilation". In: *Phys. Lett. B* 269 (1991), pp. 432–438. DOI: 10.1016/0370-2693(91)90196-W.

[273] C. Chen. "Identification of a bottom quark-antiquark pair in a single jet with high transverse momentum and its application". In: *Phys. Rev. D* 92.9 (2015), p. 093010. DOI: 10.1103/PhysRevD.92.093010. arXiv: 1507.06913 [hep-ph].

[274] M. Oreglia. "A Study of the Reactions $\psi' \to \gamma\gamma\psi$". MA thesis. Dec. 1980.

[275] H. Abouabid et al. "Benchmarking di-Higgs production in various extended Higgs sector models". In: *JHEP* 09 (2022), p. 011. DOI: 10.1007/JHEP09(2022)011. arXiv: 2112.12515 [hep-ph].

[276] W. Zhang et al. "Double Higgs boson production and decay in Randall-Sundrum model at hadron colliders". In: *Phys. Rev. D* 92 (2015), p. 116005. DOI: 10.1103/PhysRevD.92.116005. arXiv: 1512.01766 [hep-ph].

[277] ATLAS Collaboration. "Combination of searches for resonant Higgs boson pair production using pp collisions at $\sqrt{s} = 13$ TeV with the ATLAS detector". In: (Nov. 2023). arXiv: 2311.15956 [hep-ex].

[278] ATLAS Collaboration. "Anomaly detection search for new resonances decaying into a Higgs boson and a generic new particle X in hadronic final states using $\sqrt{s} = 13$ TeV pp collisions with the ATLAS detector". In: (June 2023). arXiv: 2306.03637 [hep-ex].

[279] ATLAS Collaboration. "Dijet resonance search with weak supervision using $\sqrt{s} = 13$ TeV pp collisions in the ATLAS detector". In: *Phys. Rev. Lett.* 125.13 (2020), p. 131801. DOI: 10.1103/PhysRevLett.125.131801. arXiv: 2005.02983 [hep-ex].

[280] J. Chung et al. "A Recurrent Latent Variable Model for Sequential Data". In: (2015). arXiv: 1506.02216 [cs.LG]. URL: https://arxiv.org/abs/1506.02216.

[281] ATLAS Collaboration. “Combination of searches for heavy resonances decaying into bosonic and leptonic final states using 36 fb^{-1} of proton-proton collision data at $\sqrt{s} = 13$ TeV with the ATLAS detector”. In: *Phys. Rev. D* 98.5 (2018), p. 052008. DOI: 10.1103/PhysRevD.98.052008. arXiv: 1808.02380 [hep-ex].

[282] CMS Collaboration. “Combination of CMS searches for heavy resonances decaying to pairs of bosons or leptons”. In: *Phys. Lett. B* 798 (2019), p. 134952. DOI: 10.1016/j.physletb.2019.134952. arXiv: 1906.00057 [hep-ex].

[283] ATLAS Collaboration. “Combination and summary of ATLAS dark matter searches interpreted in a 2HDM with a pseudo-scalar mediator using 139 fb^{-1} of $\sqrt{s} = 13$ TeV pp collision data”. In: (June 2023). arXiv: 2306.00641 [hep-ex].

[284] ATLAS Collaboration. “Constraints on spin-0 dark matter mediators and invisible Higgs decays using ATLAS 13 TeV pp collision data with two top quarks and missing transverse momentum in the final state”. In: *Eur. Phys. J. C* 83.6 (2023), p. 503. DOI: 10.1140/epjc/s10052-023-11477-z. arXiv: 2211.05426 [hep-ex].

[285] ATLAS Collaboration. “A statistical combination of ATLAS Run 2 searches for charginos and neutralinos at the LHC”. In: (Feb. 2024). arXiv: 2402.08347 [hep-ex].

[286] CMS Collaboration. “Combined search for electroweak production of winos, binos, higgsinos, and sleptons in proton-proton collisions at $\sqrt{s}$ = 13 TeV”. In: (Feb. 2024). arXiv: 2402.01888 [hep-ex].

[287] CMS Collaboration. “Combined searches for the production of supersymmetric top quark partners in proton–proton collisions at $\sqrt{s} = 13$ TeV”. In: *Eur. Phys. J. C* 81.11 (2021), p. 970. DOI: 10.1140/epjc/s10052-021-09721-5. arXiv: 2107.10892 [hep-ex].

[288] CMS Collaboration. “Combined search for supersymmetry with photons in proton-proton collisions at $\sqrt{s}$ = 13 TeV”. In: *Phys. Lett. B* 801 (2020), p. 135183. DOI: 10.1016/j.physletb.2019.135183. arXiv: 1907.00857 [hep-ex].

[289] ATLAS Collaboration. “Combination of searches for heavy spin–1 resonances using 139 fb^{-1} of proton–proton collision data at $\sqrt{s} = 13$ TeV with the ATLAS detector”. In: (Feb. 2024).

[290] ATLAS Collaboration. “Search for a heavy charged boson in events with a charged lepton and missing transverse momentum from pp collisions at $\sqrt{s} = 13$ TeV with the ATLAS detector”. In: *Phys. Rev. D* 100.5 (2019), p. 052013. DOI: 10.1103/PhysRevD.100.052013. arXiv: 1906.05609 [hep-ex].

[291] ATLAS Collaboration. *Search for high-mass resonances in final states with a tau lepton and missing transverse momentum with the ATLAS detector*. CERN-EP-2023-298. 2024.

[292] ATLAS Collaboration. “Search for high-mass dilepton resonances using 139 fb^{-1} of pp collision data collected at $\sqrt{s}$ =13 TeV with the ATLAS detector”. In: *Phys. Lett. B* 796 (2019), pp. 68–87. DOI: 10.1016/j.physletb.2019.07.016. arXiv: 1903.06248 [hep-ex].

[293] ATLAS Collaboration. “Search for $t\bar{t}$ resonances in fully hadronic final states in pp collisions at $\sqrt{s}$ = 13 TeV with the ATLAS detector”. In: *JHEP* 10 (2020), p. 061. DOI: 10.1007/JHEP10(2020)061. arXiv: 2005.05138 [hep-ex].

[294] ATLAS Collaboration. “Search for vector-boson resonances decaying into a top quark and a bottom quark using pp collisions at $\sqrt{s}$ = 13 TeV with the ATLAS detector”. In: *JHEP* 12 (2023), p. 073. DOI: 10.1007/JHEP12(2023)073. arXiv: 2308.08521 [hep-ex].

[295] ATLAS Collaboration. “Search for new resonances in mass distributions of jet pairs using 139 fb^{-1} of pp collisions at $\sqrt{s} = 13$ TeV with the ATLAS detector”. In: *JHEP* 03 (2020), p. 145. DOI: 10.1007/JHEP03(2020)145. arXiv: 1910.08447 [hep-ex].

[296] A. Djouadi, L. Maiani, A. Polosa, J. Quevillon, and V. Riquer. “Fully covering the MSSM Higgs sector at the LHC”. In: *JHEP* 06 (2015), p. 168. DOI: 10.1007/JHEP06(2015)168. arXiv: 1502.05653 [hep-ph].

[297] D. Duda. *Searching for new symmetries in the Higgs sector with the ATLAS detector*. Tech. rep. 2023. URL: https://cds.cern.ch/record/2846501.

[298] ATLAS Collaboration. “Search for heavy resonances decaying into a pair of Z bosons in the $\ell^+\ell^-\ell'^+\ell'^-$ and $\ell^+\ell^-\nu\bar{\nu}$ final states using 139 fb^{-1} of proton–proton collisions at $\sqrt{s} = 13$ TeV with the ATLAS detector”. In: *Eur. Phys. J. C* 81.4 (2021), p. 332. DOI: 10.1140/epjc/s10052-021-09013-y. arXiv: 2009.14791 [hep-ex].

[299] ATLAS Collaboration. “Search for a heavy Higgs boson decaying into a Z boson and another heavy Higgs boson in the $\ell\ell bb$ and $\ell\ell WW$ final states in pp collisions at $\sqrt{s} = 13$ TeV with the ATLAS detector”. In: *Eur. Phys. J. C* 81 (2020), p. 396. DOI: 10.1140/epjc/s10052-021-09117-5. arXiv: 2011.05639 [hep-ex].

[300] ATLAS Collaboration. “Search for Higgs boson pair production in association with a vector boson in pp collisions at $\sqrt{s} = 13$ TeV with the ATLAS detector”. In: (Oct. 2022). arXiv: 2210.05415 [hep-ex].

[301] ATLAS Collaboration. *Combination of searches for non-resonant and resonant Higgs boson pair production in the $b\bar{b}\gamma\gamma$, $b\bar{b}\tau^+\tau^-$ and $b\bar{b}b\bar{b}$ decay channels using pp collisions at $\sqrt{s} = 13$ TeV with the ATLAS detector*. Tech. rep. 2021. URL: https://cds.cern.ch/record/2786865.

[302] ATLAS Collaboration. *Search for heavy Higgs bosons from a g2HDM in multilepton plus b-jets final states in pp collisions at* 13 TeV *with the ATLAS detector*. Tech. rep. 2022. URL: https://cds.cern.ch/record/2815674.

[303] ATLAS Collaboration. “Search for heavy neutral Higgs bosons produced in association with b-quarks and decaying into b-quarks at $\sqrt{s} = 13$ TeV with the ATLAS detector”. In: *Phys. Rev. D* 102.3 (2020), p. 032004. DOI: 10.1103/PhysRevD.102.032004. arXiv: 1907.02749 [hep-ex].

[304] ATLAS Collaboration. “Search for a light charged Higgs boson in $t \to H^{\pm}b$ decays, with $H^{\pm} \to cb$, in the lepton+jets final state in proton-proton collisions at $\sqrt{s} = 13$ TeV with the ATLAS detector”. In: (Feb. 2023). arXiv: 2302.11739 [hep-ex].

[305] ATLAS Collaboration. “Search for charged Higgs bosons decaying via $H^{\pm} \to \tau^{\pm}\nu_{\tau}$ in the τ+jets and τ+lepton final states with 36 fb^{-1} of pp collision data recorded at $\sqrt{s} = 13$ TeV with the ATLAS experiment”. In: *JHEP* 09 (2018), p. 139. DOI: 10.1007/JHEP09(2018)139. arXiv: 1807.07915 [hep-ex].

[306] ATLAS Collaboration. “Search for charged Higgs bosons decaying into a top quark and a bottom quark at $\sqrt{s} = 13$ TeV with the ATLAS detector”. In: *JHEP* 06 (2021), p. 145. DOI: 10.1007/JHEP06(2021)145. arXiv: 2102.10076 [hep-ex].

[307] ATLAS Collaboration. “Search for doubly charged Higgs boson production in multi-lepton final states using 139 fb^{-1} of proton-proton collisions at $\sqrt{s} = 13$ TeV with the ATLAS detector”. In: (Nov. 2022). arXiv: 2211.07505 [hep-ex].

[308] ATLAS Collaboration. "Search for doubly and singly charged Higgs bosons decaying into vector bosons in multi-lepton final states with the ATLAS detector using proton-proton collisions at $\sqrt{s}$ = 13 TeV". In: *JHEP* 06 (2021), p. 146. DOI: 10.1007/JHEP06(2021)146. arXiv: 2101.11961 [hep-ex].

[309] ATLAS Collaboration. "Summary plots for beyond Standard Model Higgs boson benchmarks for direct and indirect searches". In: (2022). URL: https://cds.cern.ch/record/2827098/.

[310] ATLAS Collaboration. *Summary plot for the interpretation of heavy Higgs boson searches in the Georgi-Machacek model*. Tech. rep. 2022. URL: https://cds.cern.ch/record/2803996.

[311] C. Gao et al. "Searching for Additional Higgs Bosons via Higgs Cascades". In: *Phys. Rev. D* 97.7 (2018), p. 075040. DOI: 10.1103/PhysRevD.97.075040. arXiv: 1604.03108 [hep-ph].

[312] ATLAS Collaboration. "Observation of $W\gamma\gamma$ triboson production in proton-proton collisions at $\sqrt{s} = 13$ TeV with the ATLAS detector". In: (Aug. 2023). arXiv: 2308.03041 [hep-ex].

[313] ATLAS Collaboration. "Observation of $WZ\gamma$ production in pp collisions at $\sqrt{s} = 13$ TeV with the ATLAS detector". In: (May 2023). arXiv: 2305.16994 [hep-ex].

[314] ATLAS Collaboration. "Measurement of $Z\gamma\gamma$ production in pp collisions at $\sqrt{s} = 13$ TeV with the ATLAS detector". In: *Eur. Phys. J. C* 83.6 (2023), p. 539. DOI: 10.1140/epjc/s10052-023-11579-8. arXiv: 2211.14171 [hep-ex].

[315] ATLAS Collaboration. "Observation of WWW Production in pp Collisions at $\sqrt{s}$ =13 TeV with the ATLAS Detector". In: *Phys. Rev. Lett.* 129.6 (2022), p. 061803. DOI: 10.1103/PhysRevLett.129.061803. arXiv: 2201.13045 [hep-ex].

[316] ATLAS Collaboration. "Search for heavy resonances decaying into WW in the $e\nu\mu\nu$ final state in pp collisions at $\sqrt{s} = 13$ TeV with the ATLAS detector". In: *Eur. Phys. J. C* 78.1 (2018), p. 24. DOI: 10.1140/epjc/s10052-017-5491-4. arXiv: 1710.01123 [hep-ex].

[317] Z. Berezhiani, L. Gianfagna, and M. Giannotti. "Strong CP problem and mirror world: The Weinberg-Wilczek axion revisited". In: *Phys. Lett. B* 500 (2001), pp. 286–296. DOI: 10.1016/S0370-2693(00)01392-7. arXiv: hep-ph/0009290.

[318] A. Chatrchyan et al. "ALP dark matter with non-periodic potentials: parametric resonance, halo formation and gravitational signatures". In: *JCAP* 10 (2023), p. 068. DOI: 10.1088/1475-7516/2023/10/068. arXiv: 2305.03756 [hep-ph].

[319] C. Eröncel et al. "ALP dark matter from kinetic fragmentation: opening up the parameter window". In: *JCAP* 10 (2022), p. 053. DOI: 10.1088/1475-7516/2022/10/053. arXiv: 2206.14259 [hep-ph].

[320] N. Craig, A. Hook, and S. Kasko. "The Photophobic ALP". In: *JHEP* 09 (2018), p. 028. DOI: 10.1007/JHEP09(2018)028. arXiv: 1805.06538 [hep-ph].

[321] K. Agashe et al. "Dedicated Strategies for Triboson Signals from Cascade Decays of Vector Resonances". In: *Phys. Rev. D* 99.7 (2019), p. 075016. DOI: 10.1103/PhysRevD.99.075016. arXiv: 1711.09920 [hep-ph].

[322] K. S. Agashe et al. "LHC Signals from Cascade Decays of Warped Vector Resonances". In: *JHEP* 05 (2017), p. 078. DOI: 10.1007/JHEP05(2017)078. arXiv: 1612.00047 [hep-ph].

[323] C. Englert et al. "Sensing Higgs boson cascade decays through memory". In: *Phys. Rev. D* 102.9 (2020), p. 095027. DOI: 10.1103/PhysRevD.102.095027. arXiv: 2008.08611 [hep-ph].

[324] J. A. Aguilar-Saavedra, and F. R. Joaquim. "Multiboson production in W' decays". In: *JHEP* 01 (2016), p. 183. DOI: 10.1007/JHEP01(2016)183. arXiv: 1512.00396 [hep-ph].

[325] ATLAS Collaboration. *Performance of W/Z taggers using UFO jets in ATLAS*. Tech. rep. Geneva: CERN, 2021. URL: https://cds.cern.ch/record/2777009.

[326] CMS Collaboration. "Identification of heavy, energetic, hadronically decaying particles using machine-learning techniques". In: *JINST* 15.06 (2020), P06005. DOI: 10.1088/1748-0221/15/06/P06005. arXiv: 2004.08262 [hep-ex].

[327] ATLAS Collaboration. "Reconstruction and identification of boosted di-τ systems in a search for Higgs boson pairs using 13 TeV proton-proton collision data in ATLAS". In: *JHEP* 11 (2020), p. 163. DOI: 10.1007/JHEP11(2020)163. arXiv: 2007.14811 [hep-ex].

[328] ATLAS Collaboration. *Identification of highly boosted $Z \to e^+e^-$ decays with the ATLAS detector using deep neural networks*. Tech. rep. Geneva, 2022. URL: https://cds.cern.ch/record/2845238.

[329] J. Neyman and E. S. Pearson. "On the Problem of the Most Efficient Tests of Statistical Hypotheses". In: New York, NY: Springer New York, 1992, pp. 73–108. ISBN: 978-1-4612-0919-5. DOI: 10.1007/978-1-4612-0919-5_6. URL: https://doi.org/10.1007/978-1-4612-0919-5_6.

[330] F. J. Kiwit. "A new algorithm for the identification of boosted $Z \to e^+e^-$ decays for heavy resonance searches with the ATLAS detector at the LHC". 2022. URL: https://cds.cern.ch/record/2851190.

[331] N. Hey. "Identification of highly boosted $H \to \gamma\gamma$ decays with the ATLAS detector using deep neural networks". 2023. URL: https://cds.cern.ch/record/2878576.

[332] M. Bauer, M. Neubert, and A. Thamm. "Collider Probes of Axion-Like Particles". In: *JHEP* 12 (2017), p. 044. DOI: 10.1007/JHEP12(2017)044. arXiv: 1708.00443 [hep-ph].

[333] D. Curtin, R. Essig, S. Gori, and J. Shelton. "Illuminating Dark Photons with High-Energy Colliders". In: *JHEP* 02 (2015), p. 157. DOI: 10.1007/JHEP02(2015)157. arXiv: 1412.0018 [hep-ph].

[334] CMS Collaboration. *Search for a standard model-like Higgs boson in the mass range between 70 and 110* GeV *in the diphoton final state in proton-proton collisions at* $\sqrt{s} = 13$ TeV. Tech. rep. 2023. URL: https://cds.cern.ch/record/2852907.

[335] T. Biekötter, S. Heinemeyer, and G. Weiglein. "Mounting evidence for a 95 GeV Higgs boson". In: *JHEP* 08 (2022), p. 201. DOI: 10.1007/JHEP08(2022)201. arXiv: 2203.13180 [hep-ph].

[336] CMS Collaboration. "Search for Higgs Boson Decay to a Charm Quark-Antiquark Pair in Proton-Proton Collisions at s=13 TeV". In: *Phys. Rev. Lett.* 131.6 (2023), p. 061801. DOI: 10.1103/PhysRevLett.131.061801. arXiv: 2205.05550 [hep-ex].

[337] ATLAS Collaboration. "Search for $t\bar{t}$ resonances in the lepton plus jets final state with ATLAS using 4.7 fb^{-1} of pp collisions at $\sqrt{s} = 7$ TeV". In: *Phys. Rev. D* 88.1 (2013), p. 012004. DOI: 10.1103/PhysRevD.88.012004. arXiv: 1305.2756 [hep-ex].

[338] ATLAS Collaboration. "A search for $t\bar{t}$ resonances using lepton-plus-jets events in proton-proton collisions at $\sqrt{s} = 8$ TeV with the ATLAS detector". In: *JHEP* 08 (2015), p. 148. DOI: 10.1007/JHEP08(2015)148. arXiv: 1505.07018 [hep-ex].

[339] ATLAS Collaboration. "Searches for heavy diboson resonances in pp collisions at $\sqrt{s} = 13$ TeV with the ATLAS detector". In: *JHEP* 09 (2016), p. 173. DOI: 10.1007/JHEP09(2016)173. arXiv: 1606.04833 [hep-ex].

[340] ATLAS Collaboration. "Performance of b-Jet Identification in the ATLAS Experiment". In: *JINST* 11.04 (2016), P04008. DOI: 10.1088/1748-0221/11/04/P04008. arXiv: 1512.01094 [hep-ex].

[341] ATLAS Collaboration. *Calibration of ATLAS b-tagging algorithms in dense jet environments*. Tech. rep. 2016. URL: https://cds.cern.ch/record/2127958.

[342] ATLAS Collaboration. *Multi-Boson Simulation for 13 TeV ATLAS Analyses*. Tech. rep. Geneva: CERN, 2017. URL: https://cds.cern.ch/record/2261933.

[343] D. Duda. *Searches for neutral heavy Higgs bosons decaying into a diboson system*. Tech. rep. 2020. URL: https://cds.cern.ch/record/2743421.

[344] D. Duda. *Search for heavy resonances at the LHC*. Tech. rep. 2021. URL: https://cds.cern.ch/record/2780687.

[345] D. Duda. *Searching for new symmetries in the Higgs sector with the ATLAS detector*. Tech. rep. 2022. URL: https://cds.cern.ch/record/2841081.

[346] D. Duda. "Overview of ATLAS and CMS results at the LHC". In: (2024). URL: https://cds.cern.ch/record/2887816.

[347] D. Duda. *Direct searches for new resonances in multi-boson events*. Tech. rep. 2021. URL: https://cds.cern.ch/record/2779446.

[348] ATLAS Collaboration. "ATLAS b-jet identification performance and efficiency measurement with $t\bar{t}$ events in pp collisions at $\sqrt{s} = 13$ TeV". In: *Eur. Phys. J. C* 79 (2019), p. 970. DOI: 10.1140/epjc/s10052-019-7450-8. arXiv: 1907.05120 [hep-ex].

[349] ATLAS Collaboration. "A search for new resonances in multiple final states with a high transverse momentum Z boson in $\sqrt{s} = 13$ TeV pp collisions with the ATLAS detector". In: (Sept. 2022). arXiv: 2209.15345 [hep-ex].

[350] Urknall, Weltall und das Leben. *10 Jahre Higgs Boson • Was wissen wir heute und wie gehts weiter? by Dominik Duda*. Youtube. 2022. URL: https://www.youtube.com/watch?v=z6prXrYD47w&t=472s.

A Related Scientific and Academic Activities

A.1 Contributions to the efforts of the ATLAS collaboration

Over the past few years of my habilitation, I have built a strong profile in the field of particle physics by leading eight different analysis efforts of the ATLAS collaboration and by contributing significantly to several others.

In particular, I have worked on searches for new heavy particles decaying into top-quark pairs [337, 338], pairs of vector bosons [316, 339], or a vector boson and a Higgs boson [190, 299]. I have also worked on searches for anomalies in the Higgs boson production process [107], and measurements of Higgs boson properties [103, 104, 105, 111]. Additionally, I have made essential contributions to the development and calibration of flavor-tagging algorithms [52, 55, 340, 341], the development of improved simulations of vector boson or Higgs boson production in association with jets [342], and to the development of an algorithm dedicated to the reconstruction and identification of highly boosted $Z \to e^+e^-$ [328, 330] and $h \to \gamma\gamma$ decays [331].

This work led so far to 17 journal publications, 17 conference notes, and 6 public notes[52]. My strong contributions in the field have been acknowledged by several invitations to give high-profile presentations at national and international conferences. Since the beginning of my habilitation, I gave the following public presentations:

- Invited by the ATLAS Speaker Committee:
  - "Searches for neutral heavy Higgs bosons decaying into a diboson system" [343] presented at the Higgs 2020 conference.
  - "Search for heavy resonances at the LHC" [344] presented at the Particles and Nuclei International Conference 2021.
  - "Searching for new symmetries in the Higgs sector with the ATLAS detector" [345] presented at 8th Symposium on Prospects in the Physics of Discrete Symmetries.
  - "Overview of ATLAS and CMS results at the LHC" [346] presented at the IAS2024 conference.
- Invited by the Organising Committee of the corresponding conference:
  - "Direct searches for new resonances in multi-boson events" [347] presented at the Multi-Boson Interactions 2021 conference.
  - "Searches for new scalar particles at the LHC" presented at the DPG Spring Meeting in Heidelberg 2022.

Furthermore, I developed my leadership and managment skills by accepting various coordination roles within the ATLAS collaboration. I have been the coordinator for three working groups dedicated to the calibration of flavour-tagging algorithms (April 2018 - January 2020), the search for resonances decaying into pairs of bosons[53] (October 2019 - October 2021), and the development and calibration of photon identification algorithms (since October 2023). These coordination roles involved steering the various data analysis

[52] This series of notes covers mostly results using simulated data and interpretations of data analyses.

[53] This group performs searches for heavy Higgs bosons, heavy vector bosons, and other exotic particles.

efforts and editorial work for the corresponding publications. Another responsibility was to communicate new developments in the collaboration to the various analysis teams. In total, I was responsible for a dozen analysis teams with about 150 international researchers. In total, these efforts have led to ten publications [181, 183, 185, 187, 189, 199, 299, 300, 348, 349]. Between September 2021 and September 2024, I was the coordinator for Higgs-physics of the german ATLAS community. This role involves the review of presentations for national conferences and the writing of research summaries for the German funding agencies. In addition, I have been planning the scientific programme for several ATLAS workshops and topical meetings focusing either on the flavour-tagging techniques or the search for new heavy resonances.

I have gained high visibility as an expert reviewer for the ATLAS Higgs physics and Higgs and Diboson Search working groups. In these roles, I am regularly reviewing conference talks and documentation of other collaboration members. I have also chaired several editorial boards within the ATLAS collaboration. In this context, I lead the review of analyses focusing on the calibration of flavour-tagging algorithms [49] and searches for exotic Higgs boson decays into axion-like particles.

A.2 Supervision of students

Supervising students is one of the most favorite aspects of my job. I enjoy supporting young people in their and development into independent researchers. To help my students succeed, I create an inclusive and open working environment.

I believe that successful supervision requires a high level of commitment to the student's advancement and a willingness to be flexible. When working in large collaborations such as ATLAS, gaining visibility is one of the biggest challenges for students. As a mentor and supervisor, I strive to give my students ample opportunities to present their work to the working group from an early stage in their research careers. By assigning them tasks that will make a significant contribution to the overall research progress, I help them establish themselves in the collaboration and the international particle physics community. Under my supervision, the students have made crucial contributions to numerous publications of the ATLAS collaboration.

Over the past years I have been a mentor and daily supervisor to several bachelor, master, and Ph.D. students. I have been responsible for finding and formulating their thesis topics, the steering of their data analysis efforts, and their thesis writing. During my habilitation, I have supervised the following Ph.D., M.Sc, and B.Sc. projects:

- Ph.D. theses:
  - "Searches for new resonances decaying to a Higgs and a vector boson with the ATLAS detector at the LHC" [240], accepted in July 2021.
  - "Search for heavy Zh and Wh resonances in 13 TeV proton-proton collisions with the ATLAS detector at the LHC" [246], accepted in December 2021.
  - "Search for charged Higgs bosons with the ATLAS detector at the LHC", since November 2021.
- M.Sc. theses:
  - "Search for Charged Higgs Bosons in $H^+ \to W^+h$ Decays with the ATLAS Detector" [268], accepted in July 2021.

- "A new algorithm for the identification of boosted $Z \to e^+e^-$ decays for heavy resonance searches with the ATLAS detector at the LHC" [330], accepted in November 2022.
- "Identification of highly boosted $h \to \gamma\gamma$ decays with the ATLAS detector using deep neural networks" [331], accepted in September 2023.
- "Feasibility Study to Search for Higgs Boson Decays to Gluons at the LHC Using Machine Learning", accepted in August 2024.

- B.Sc. theses:
  - "Identification of boosted $Z \to e^+e^-$ decays using a machine learning approach", accepted in September 2020.
  - "Search for charged Higgs bosons with the ATLAS detector at a center of mass energy of 13 TeV at the LHC", accepted in September 2020.
  - "Suche nach geladenen Higgs-Bosonen in $\ell\nu\ell\nu bbbb$-Endzuständen mit dem ATLAS-Detektor am LHC unter Einsatz von Machine-Learning-Methoden", accepted in March 2021.
  - "Search for Doubly Charged Higgs Bosons via the Vector Boson Fusion Production Mode", accepted in October 2021.
  - "Background rejection studies to improve the search for CP violation in the effective Higgs-gluon coupling", accepted in October 2022.
  - "Identification of highly boosted $H \to gg$ decays using deep neural networks", accepted in November 2023.

A.3 Teaching at TU Munich

In addition to the supervision of the research of Bachelor, Master and PhD students, I took responsibilities in the physics-education programme at the TU Munich through the following activities:

- Preparation and supervision of a seminar course on "Physics at the Large Hadron Collider" (winter semester 2019/2020 until winter semester 2021/2022)
- Supervision of tutorials accompanying the lecture course "Testing the Standard Model of Elementary Particle Physics I" (winter semester 2019/2020)
- Supervision of tutorials accompanying the lecture course "Testing the Standard Model of Elementary Particle Physics II" (summer semester 2020)
- Lecturer of the course "Testing the Standard Model of Elementary Particle Physics I" (winter semester 2020/2021)
- Lecturer of the course "Testing the Standard Model of Elementary Particle Physics II" (summer semester 2021)

A.4 Public outreach engagement

Over the past few years, I have contributed to numerous outreach activities as a lecturer and supervisor, engaging young students in particle physics. For example, I have been involved in the international CERN masterclasses organised by the International Particle Physics Outreach Group, and the national masterclasses organised by the "Netzwerk Teilchenwelt". These two projects give high school students the opportunity to learn about particle physics and to participate in hands-on data analysis sessions. Furthermore, I organised and led two workshops on assembling self-made cloud chambers. The first workshop was held at the Max-Planck Institute during a Girls' Day event, and the second workshop was held at a high school in Ingolstadt. I have also visited high schools to support other projects, such as the CERN "Beamline for Schools" competition. In this competition, I helped a small group of students design an experiment and write a project proposal for that experiment.

On another occasion I participated in the CERN project weeks organised by the "Netzwerk Teilchenwelt", where I supervised a high school student for two weeks at CERN. During this time, the student conducted initial studies on a machine learning-based identification of strongly Lorentz-boosted $Z \to e^+e^-$ decays. The student later entered the regional youth science competition "Jugend forscht" and won in the special category "Sonderpreis Technologie" of the Bavarian Academy of Sciences.

On the occasion of the 10th anniversary of the Higgs boson discovery, I gave a public lecture on the Higgs boson as part of the "Café & Kosmos" series organised by the Excellence Cluster ORIGINS [350].

B Selected Publications

The following publications are the core of my habilitation work:

- "Constraints on Higgs boson properties using $WW^*(\to e\nu\mu\nu)jj$ production in $36.1\,\text{fb}^{-1}$ of $\sqrt{s} = 13$ TeV pp collisions with the ATLAS detector", Eur. Phys. J. C 82 (2022) 7, 622.
- "Measurements of Higgs boson production by gluon–gluon fusion and vector-boson fusion using $H \to WW^* \to e\nu\mu\nu$ decays in pp collisions at $\sqrt{s} = 13$ TeV with the ATLAS detector", Phys. Rev. D 108 (2023) 032005.
- "Search for heavy resonances decaying into a Z or W boson and a Higgs boson in final states with leptons and b-jets in $139\,\text{fb}^{-1}$ of pp collisions at $\sqrt{s} = 13$ TeV with the ATLAS detector", JHEP 06 (2023) 016.
- "Combination of searches for heavy spin-1 resonances using $139\,\text{fb}^{-1}$ of proton–proton collision data at $\sqrt{s} = 13$ TeV with the ATLAS detector", JHEP 04 (2024) 118.